Final Report
Covering Period: October 1, 2008– September 30, 2013
Date of Report: December 10, 2013

Award Number:	DE-FC26-08NT01922
Project Title:	**Production and Utilization of Next Generation Fuels for Clean Power**
Project Period:	10/1/2008-9/30/2013
Recipient Organization:	Primary- Nicholls State University Subcontracts-Louisiana State University, University of New Orleans, Tulane University, Southern University, University of Louisiana Lafayette.
Technical Contact (Primary):	Dr. Ramaraj Boopathy, (985) 448-4716; ramaraj.boopathy@nicholls.edu
Business Contact (Primary):	Debi Benoit; (985) 488-2563; debi.benoit@nicholls.edu
DOE Project Officer:	Dr. Judith Dyer Judith.Dyer@netl.doe.gov
DOE HQ Contact:	Bob Gemmer, (202) 586-5585

Project Objective: The project goals are to develop technologies and the scientific understanding related to the effective production and utilization of next generation fuels for clean power and energy production.

Summary: CPERC's activities focused on two major themes: (a) cost-effective production of next-generation fuels with a focus on hydrogen from gasification and biofuels (primarily ethanol and butanol), and (b) efficient utilization of hydrogen and biofuels for power generation with a focus on improved performance, greater reliability and reduced energy costs.

CPERC consists of six Louisiana schools that addressed the above research in a synergistic fashion. University of New Orleans (UNO) explored improvements to gasification of coal (and other feedstock) leading to syngas (primarily hydrogen with CO, CH_4, CO_2, etc as other constituents) while Louisiana State University (LSU) examined strategies for efficient premixed combustion of syngas, and the effect of fuel composition variability. Nicholls State University, University of Louisiana (ULL) and Tulane examined cost-effective strategies for biofuel production, while LSU and UNO developed techniques for increasing the energy density of the biofuels, and examining their combustion characteristics. To address reliability and performance issues of the energy producing system (e.g., gas turbines) pertaining to the use of the next-generation fuels, improved cooling strategies was explored by LSU and improved material coatings was examined by Southern University in Baton Rouge (SUBR).

Executive Summary

This project is an effort of six different universities in Louisiana, who are the members of the Clean Power and Energy Research Consortium (CPERC). The CPERC members include Nicholls State University, Louisiana State University, University of New Orleans, Tulane University, University of Louisiana at Lafayette, and Southern University in Baton Rouge. Each university had its own individual research task. The CPERC consortium's activities centered on two themes, namely, cost-effective production of next-generation fuels with a focus on hydrogen from gasification and biofuels and efficient utilization of hydrogen and biofuels for power generation with a focus on improved performance, greater reliability and reduced energy costs. University of New Orleans (UNO) explored improvements to gasification of coal (and other feedstock) leading to syngas (primarily hydrogen with CO, CH_4, CO_2, etc as other constituents) while Louisiana State University (LSU) examined strategies for efficient premixed combustion of syngas, and the effect of fuel composition variability. Nicholls State University, University of Louisiana (ULL) and Tulane examined cost-effective strategies for biofuel production, while LSU and UNO developed techniques for increasing the energy density of the biofuels, and examining their combustion characteristics. To address reliability and performance issues of the energy producing system (e.g., gas turbines) pertaining to the use of the next-generation fuels, improved cooling strategies was explored by LSU and improved material coatings was examined by Southern University in Baton Rouge (SUBR). This report contains six chapters pertaining to six universities. Each chapter describes the individual task, summary of the project, background information, research methods, results and discussion, and conclusions. The list of peer-reviewed publications and conference presentations are also listed at the end of each chapter.

Table of Contents

Chapter 1

Nicholls State University

Task 1: Ethanol Production

Summary

Approximately half of the 80 billion tons of crop produced annually around the world remains as residue that could serve as a renewable resource to produce valuable products such as ethanol and butanol. Ethanol produced from lignocellulosic biomass is a promising renewable alternative to diminishing oil and gas liquid fuels. Sugarcane is an important industry in Louisiana. The recently released variety of "energy cane" has great potential to sustain a competitive sugarcane industry. It has been demonstrated that fuel-grade ethanol can be produced from post harvest sugar cane residue in the past, but optimized ethanol production was not achieved. Optimization of the fermentation process requires efficient pretreatment to release cellulose and hemicellulose from lignocellulosic complex of plant fiber. Determining optimal pretreatment techniques for fermentation is essential for the success of lignocellulosic ethanol production process. The purpose of this study was to evaluate three pretreatment methods for the energy cane variety L 79-1002 for maximum lignocellulosic ethanol production. The pretreatments include alkaline pretreatment, dilute acid hydrolysis, and solid-state fungal pretreatment process using brown rot and white rot fungi. Pretreated biomass was enzymatically saccharified and subjected to fermentation using a recombinant *Escherichia coli* FBR5. The results revealed that all pretreatment processes produced ethanol. However, the best result was observed in dilute acid hydrolysis followed by alkaline pretreatment and solid-state fungal pretreatment. Combination of fungal pretreatment with dilute acid hydrolysis reduced the acid requirement from 3% to 1% and this combined process could be more economical in a large-scale production system.

Introduction

Concerns over the United States' dependency on other countries for fuel and the negative influence that modern day fuels have on environmental issues such as global warming have sparked interests in finding a more efficient and cleaner way to produce fuel (Jeffries, 2006). A potential solution is the production of ethanol from cellulosic and hemicellulosic waste products. These agricultural residues are composed of high-energy bonds and could be used to make value added products such as ethanol and butanol, but instead they are commonly disposed by open air burning (Dawson and Boopathy, 2007).

The U.S Government's Advanced Energy Initiative began an effort to reduce America's dependence on foreign oil by establishing domestic renewable alternatives to liquid fuels. Lignocellulosic biomass is a promising alternative source of energy because of a national abundance of renewable and sustainable feedstocks (U.S. DOE, 2006; U.S. DOE, 2009). Biofuels produced from lignocellulosic biomass will, not only enhance national security, but also stimulate the economy, create jobs, and reduce global climate

change. Biomass refers to grasses, agricultural and woody residues and wastes that can be converted to fuels, chemicals, and electricity (U.S. DOE, 2009). Sugarcane is one of the most efficient crops in converting sunlight energy to chemical energy for fuel (Tew and Cobill, 2008). Brazil uses sugarcane as an important energy crop, converting the raw sugar into ethanol. Sugarcane is Louisiana's leading agricultural row crop, worth over $600 million in 2008 (Salassi et al. 2009). The introduction of energy cane varieties to Louisiana sugarcane farmers could be the forefront of a competitive edge of the sugarcane industry.

The new energy cane varieties are a promising development for cellulosic ethanol production. Energy cane produces large amounts of biomass that can be easily transported, and production does not compete with food supply and prices (Cobill, 2007) because energy cane can be grown on marginal land instead of land for food crops. In 2007, three energy cane varieties were released, namely, L 79-1002 (Tew et al. 2007c), HoCP 91-552 (Tew et al. 2007b), and Ho 00-961 (Tew et al. 2007a).

Lignocellulosic biomass consists of a network of cellulose and hemicellulose bound by lignin. The process of converting biomass to ethanol involves pretreatment to remove lignin and free sugars followed by enzymatic saccharification and fermentation. The lignin sheath as well as the crystallinity of cellulose presents major challenges to these pre-treatment techniques (Cowling and Kirk 1976). However, alkaline (Gould,1984; 1985; Gould and Freer, 1984; Dawson and Boopathy 2007; 2008) and weak acid solutions (Knappert et al. 1981; Grohmann et al. 1986; Dawson and Boopathy, 2007; 2008) can effectively remove lignin and reduce cellulose crystallinity. Determining the optimal pretreatment for energy cane is necessary to develop efficient fermentation for ethanol production.

The release of cellulose and hemicellulose allows for post-treatment enzymatic saccharification of these carbohydrates to simple sugars for fermentation. The more effective the pretreatment is at loosening the cyrstallinity of lignocellulosic biomass, more carbohydrates will be available for enzymatic saccharification, thereby increasing ethanol yield from fermentation (Krishna and Chowdry, 2000; Chapple et al. 2007). In this project, the biomass used was sugarcane leaf from the energy cane. Every year after sugarcane is harvested, farmers typically reduce residue by open air burning. This is a cost-effective way to remove the fibrous content that would otherwise significantly reduce milling efficiency and decrease profits, as well as to clear residue from the field that hinders farming (Dawson and Boopathy 2007). The open air burning practice not only affects the quality of air but also the quality of life to those who live in the area. One alternative to open air burning is the production of ethanol from sugarcane residue. Ethanol is a clean burning, renewable resource that can be produced from cellulosic biomass. The purpose of this study was to evaluate three pretreatment methods, namely, dilute acid hydrolysis, alkaline pretreatment, and fungal pretreatment for energy cane variety L 79-1002 for lignocellulosic ethanol production. The results showed that dilute acid hydrolysis is the best pretreatment method for maximum ethanol yield for the energy cane variety L 79-1002. The other biomass tested including commercial sugarcane, gamma grass, and switch grass yielded similar results.

Methods

Materials

Leaves of energy cane varieties L 79-1002 was collected in May and June of 2010 from the United States Department of Agriculture (USDA) sugarcane research unit in Houma, LA. Leaf tops were cut in three to five centimeter pieces and stored in muck buckets in the laboratory. The other biomass including commercial sugarcane, gamma grass, and switch grass were collected from Nicholls Farm. A recombinant *Escherichia coli* FBR 5 was kindly provided by Dr. Mike Cotta of National Center for Agricultural Utilization Research of USDA, Peoria, IL, USA. This recombinant *E. coli* is known to ferment both glucose and xylosic sugars from cellulose and hemicellulose of wheat hydrolysate (Saha and Cotta, 2011). Brown rot and white rot fungi, namely, *Cerioporiopsis pannocinta* (ATCC 9409) and *Phanerochaete chrysosporium* (ATCC 32629*)* were obtained from the American Type Culture Collection (ATCC; Manassas, VA). All chemicals used in the study were of reagent grade. *E.coli* was maintained in LB broth medium and the fungi were maintained in potato dextrose agar (PDA) medium. Cellulase, ß-glucanase, and endo-1,4-ß-xylanase enzymes were from Sigma chemicals, St. Louis, MO.

Alkaline Pretreatment

Previous study showed that 2% hydrogen peroxide at alkaline pH removed lignin from commercial sugarcane biomass (Dawson and Boopathy, 2007; 2008). Energy cane variety L 79-1002 was treated with 2% hydrogen peroxide solution at various alkaline pHs of 8, 10, 12, and 13. Deionized (DI) water was used as control. Potassium hydroxide stock solution was added to 2% hydrogen peroxide solution to increase the pH to 8, 10, 12, and 13.

Energy cane L 79-1002 was cut into 2-5 cm pieces and dried in an oven at 100°C to remove any moisture. Ten grams of the dry energy cane were placed into each labeled flask. Two percent hydrogen peroxide solution with different pHs was added so that the energy cane was submerged (150mL). After 24 hours of soaking, the alkaline peroxide solutions were removed through cheesecloth to retain the biomass. The treated mass was then triple rinsed with DI water for a total of 30 minutes to remove alkaline traces. The washed sample was then placed in 250 ml reactor for saccharification and fermentation as described in section 2.5.

Dilute Acid Hydrolysis

Dilute acid pretreatments at moderate temperatures free hemicellulose and cellulose (Knappert et al., 1981) and disrupt lignin, thereby releasing cellulose for enzymatic reactions (Yang and Wyman, 2004). In this study 0, 1, 2, 3, and 4% H_2SO_4 solutions were used for pretreatment of energy cane biomass.

Energy cane L 79-1002 was cut into 2-5 cm pieces and dried in an oven at 100°C to remove any moisture. Ten grams of the dry energy cane were placed into each labeled flask. Different concentrations of H_2SO_4 solution were added so that the energy cane was submerged (150mL). All acid treatments were done in triplicate as well as the control, which used DI water. Each sample was soaked for 24 hours in respective concentrations

of H_2SO_4 and then autoclaved at 121°C for 20 minutes. The H_2SO_4 solution was removed, and each sample was triple rinsed with DI water for a total of three hours (one rinse per hour).

Fungal Pretreatment

The fungal pretreatment was performed in solid state using a sterile Ziploc bag filled with 10 gram of energy cane cut into 2-5 cm pieces as described in detail by Lyn et al. (2010). Fungal treatment includes individual fungus alone, namely, *Cerioporiopsis pannocinta* (ATCC 9409) and *Phanerochaete chrysosporium* (ATCC 32629*)* and combination of both fungi together with a total of three treatments and each treatment had triplicates. Pre-grown fungi were inoculated into the Ziploc bags as an agar plug grown on PDA for three days with 100% coverage of mycelium on the agar surface. A 5% (W/W) agar plug was used as inoculum. The bags were maintained with 70% moisture and incubated for 10 days at room temperature (20-22°C) to simulate the biomass storage conditions prior to processing for biofuel in a large-scale production unit. A control was maintained in triplicate without any addition of fungus.

Combination of Fungal and Acid Pre-Treatment

An experiment was conducted with a fungal pretreated biomass with both fungi as described above. The fungal pretreated biomass was subjected to dilute acid pretreatment with low concentrations of acids, namely, 0.25, 0.5, 1, 1.5, and 2% sulfuric acid as described above. These various combined pretreated biomasses underwent enzymatic saccharification and fermentation as described below.

Enzymatic Saccharification and Fermentation

The pretreated biomass from alkaline, dilute acid and fungal pretreatments were subjected to simultaneous saccharification and fermentation (SSF). Pretreated samples underwent SSF with enzymatic saccahrification for 18 hours at 30°C with the addition of cellulase enzymes (Sigma C9748), ß-glucanase (Sigma G4423), and hemicellulose enzyme 1,4-ß-xylanase (Sigma X2629) at 10% protein of enzyme dosing of each enzyme as described by Shields and Boopathy (2011). After 18 hours of enzyme reaction, a 5% recombinant *E.coli* FBR 5 pregrown in LB medium with the optical density of 1.2 at 600nm was introduced into individual fermentor to start the fermentation. The fermentation medium was basic mineral salt medium with the volume of 150 ml in 250 ml fermentor as described by Shields and Boopathy (2011). The initial pH of the medium was 6.0 and the fermentation temperature was 30°C. Samples were periodically drawn for ethanol analysis. The fermentation lasted for six days.

Sugar and Ethanol Analysis

Prior to fermentation, the pretreated hydrolysates were analyzed for glucose and xylose using the same method described below for ethanol. The organic acid column used in the analysis was able to separate all sugars as well as ethanol. All fermentation samples were analyzed for ethanol production using high performance liquid chromatography (HPLC) as described by Dawson and Boopathy (2007) and Shields and Boopathy (2011). A Varian Pro Star Autosampler Model 410 liquid chromatograph equipped with two solvent pumps and Infinity UV and diode array detector with a data module, and a model

320 system controller were used. The mobile phase was 0.0025 N H_2SO_4. Aliquots of 10 μL were injected into an organic acid column (Varian organic acid column, Cat #SN 035061) at 22°C. The flow rate of the mobile phase was 0.6 mL/min, and the analysis was done under isocratic mode. An ethanol standard was used for quantification of ethanol in the sample. Glucose and xylose sugars were used as standards for sugar quantification.

Statistical Analysis

Analysis of variance (ANOVA), followed by a Tukey *post-hoc* range test ($p < 0.05$; Neter et al. 1990), was used to analyze sugar and ethanol production data.

Results and Discussion

Effect of Pretreatment on release of free sugars

The biomass of energy cane was subjected to three different pretreatment methods as described in method section. After the pretreatment, the hydrolysate underwent enzymatic saccharification step. Cellulose in the biomass was broken down to glucose by cellulase and ß-glucanase and the hemicellulose was broken down to various pentose and hexose sugars namely, glucose, arabinose, glucuronic acid, mannose, and xylose by the enzyme endo-1,4-ß-xylanase. The total free sugar released after enzymatic saccharification was given in Table 1. The saccharification step depends on the availability of cellulose and hemicellulose for enzyme reaction and this availability further depends on the effectiveness of the chemical and biological pretreatments used in this study. Among the various alkaline pretreatments, maximum glucose of 2002 mg/l and xylose of 901 mg/l was obtained in pH 13 followed by pH 12, 10, and 8. There was no statistical difference in sugar release between pH 12 and 13. These two pHs yielded almost similar amount of glucose and xylose. Based on this result, the lower pH of 12 is recommended for pretreatment of energy cane.

Table 1. Effect of pretreatments on release of free sugars after enzymatic saccharification

Treatment	Glucose (mg/l)	Xylose (mg/l)
Control (no pretreatment)	5 $\pm$ 0.23	3.4 $\pm$ 0.11
Alkaline Pretreatment:		
pH 8	199 + 12.4	102 + 9.7
pH 10	1276 + 21.9^{A}	678 + 5.7^{A}
pH 12	1998 + 33.1^{B}	895 + 11.8^{B}
pH 13	2002 + 42.3^{B}	901 + 23.6^{B}
Dilute Acid Hydrolysis:		
1% sulfuric acid	1324 + 22.3^{A}	543 + 10.1
2% sulfuric acid	2147 + 34.2^{B}	998 + 9.8^{A}
3% sulfuric acid	3786 + 29.9^{C}	1198 + 18.7^{A}
4% sulfuric acid	3987 + 31.9^{C}	1234 + 13.3^{A}

Fungal Pretreatment:		
Cerioporiopsis alone	1055 + 16.8[A]	608 + 5.6[A]
Phanerochaete alone	1119 + 29.6[A]	639 + 8.9[A]
Cerioporiopsis + *Phanerochaete*	1636 + 11.4[B]	799 + 12.5[B]

Results are average of triplicates in each treatment with S.D. Data with similar letters are not significantly different from each other under each treatment condition for two different sugars based on ANOVA.
All pretreated biomass were treated with a cocktail of cellulases and xylonase enzymes as described in the method section.
Xylose sugars include the sum of the following sugars: mannose, arabinose, xylose, and glucuronic acid.

The sugar release among various dilute acid hydrolysis varied among the acid concentrations. The maximum sugar release was observed in the dilute acid concentrations of 3% and 4%. Even though the 4% acid produced slightly higher sugar concentration than 3% dilute acid, the statistical analysis showed no difference in these two treatments. The lower dilutions of 1 and 2% produced significantly lesser sugar than 3 and 4% acid treated biomass (Table 1). This result showed 3% dilute acid pretreatment could be economical and may be used in ethanol production from energy cane L 79-1002.

The fungal pretreated biomass also released sugar and the best fungal treatment was the combination of both *Cerioporiopsis* and *Phanerochaete*, which produced 1636 mg/l glucose and 799 mg/l xylose (Table 1). The individual fungal treatments produced sugars, but they were significantly lower than the combined treatment. Among the individual treatments, there was no statistical significance, both fungi yielded almost similar sugar concentration. This result suggested the use of combined *Cerioporiopsis* and *Phanerochaete* treatment for higher sugar yield for ethanol production from the energy cane.

Ethanol production in alkaline pretreated energy cane

Results from previous studies demonstrated that the sugarcane residue treated with 2% hydrogen peroxide under alkaline pH removed lignin and released cellulose and hemiceullulose for enzymatic reaction (Dawson and Boopathy, 2007; 2008; Shields and Boopathy, 2011). In this study, an attempt was made to find the optimum alkaline pH for 2% hydrogen peroxide solution to enhance the liberation of cellulose and hemicellulose from energy cane biomass for enzymatic reaction. The results suggested that the elevated pH of 12 and 13 produced maximum ethanol of 1,455 and 1475 mg/l respectively. There was no statistical difference between these two pHs in terms of ethanol yield. However, the ethanol production was significantly less in pH 8 and 10 (Fig. 1A). The Recombinant *E.coli FBR 5* used in this study is known to produce ethanol from both pentose and hexosic sugars of cellulose and hemicellulose (Dien et al. 1998; 2000; Saha and Cotta, 2011). The mass balance of sugar to ethanol showed close to theoretical yield of ethanol, which is 0.51 g of ethanol per gram of sugar (Saha and Cotta, 2011; Dien et al 2000). The available sugar from alkaline pretreatment was 2002 mg/ glucose and 901 mg/l xylose in pH 13, which is added up to a total sugar of 2,903 mg/l available for ethanol fermentation (Table 1). From this sugar, maximum ethanol yield obtained was 1,455 mg/l in pH 12 and 13 (Fig. 1A). This study showed that the for the energy cane L

79-1002 variety, alkaline pretreatment at pH 12 will be the optimum alkaline treatment for maximum ethanol production. Because lignin is the primary site of alkaline peroxide reaction (Gould 1985), alkaline pretreatment can remove lignin, making sugars more available for enzymatic saccharification and fermentation (Dawson and Boopathy, 2007; 2008). Gould (1984) determined that pH 11.5 pretreatment could remove half of the total lignin in agricultural residues after 24 hours of soaking at room temperature. Alkaline peroxide treatments can effectively remove enough lignin so that enzymes convert almost 100% of cellulose to glucose (Gould,1984). An advantage of alkaline peroxide pretreatment is that the byproducts released during lignin degradation by alkaline peroxide pretreatment are not inhibitory or toxic to *S. cerevisiae* (Gould and Freer, 1984) unlike the toxic byproducts released during acid pretreatment.

Ethanol production in dilute acid pretreated energy cane

Fig. 1B shows ethanol production from dilute acid pretreated energy cane biomass. The result showed maximum ethanol production in 3 and 4% sulfuric acid treated biomass. A maximum ethanol yield of 2,601 mg/l was observed in 4% sulfuric acid treatment. The ethanol yield in 3 and 4% sulfuric acid treatment showed no difference in statistical significance. However, there was lower ethanol yield in 1 and 2% sulfuric acid treatments. Comparing the sugar production in dilute acid treatments (Table 1) and ethanol yield shown in Fig. 1B demonstrated that the recombinant *E.coil FBR 5* produced maximum possible theoretical yield of ethanol from total free sugars available after enzymatic saccharification of dilute acid pretreated biomass of energy cane L 79-1002. The pretreatment method using acid hydrolysis and enzymatic catalysis proved effective in increasing the ethanol yield using both cellulose and pentose-sugar fermenting recombinant *E.coli.* It has been shown that recombinant plasmids can be used to produce strains of *Saccharomyces* that are capable of fermenting sugars. This process involves the use of three xylose-metabolizing genes, xylose reductase, xylitol dehydrogenase, and xylulokinase to convert xylose to xylitol, xylitol to xylulose, and xylulose to xylulose-5-phosphate, respectively (Ho, et al., 1998). Once xylose is converted to xylulose-5-phosphate, it is readily accessible by many bacteria and fungi for metabolism using the non-oxidative phase of the pentose phosphate pathway (Jeffries 2006). In addition to providing the enzymatic capability to proceed in the first step of xylose fermentation, xylose reductase has also been shown to aid *S. cerevisiae* in the reduction of inhibitory furaldehyde compounds released during acid hydrolysis (Almeida et al., 2008). Compared to available literature on lignocellulosic ethanol production, the recombinant *E.coli FBR 5* used in this study effectively produced ethanol from both cellulosic and hemicellulosic sugars and the yield was close to theoretical maximum. Even though the 4% dilute acid treatment produced higher sugar content than 3% dilute acid treatment, the ethanol yields in these two treatments were almost similar. This may be due to the production of inhibitory compounds such as furfural and 5-hydroxymethyl furfural in higher acid concentration as reported by Almeida et al. 2008 and Boopathy, 2009.

A

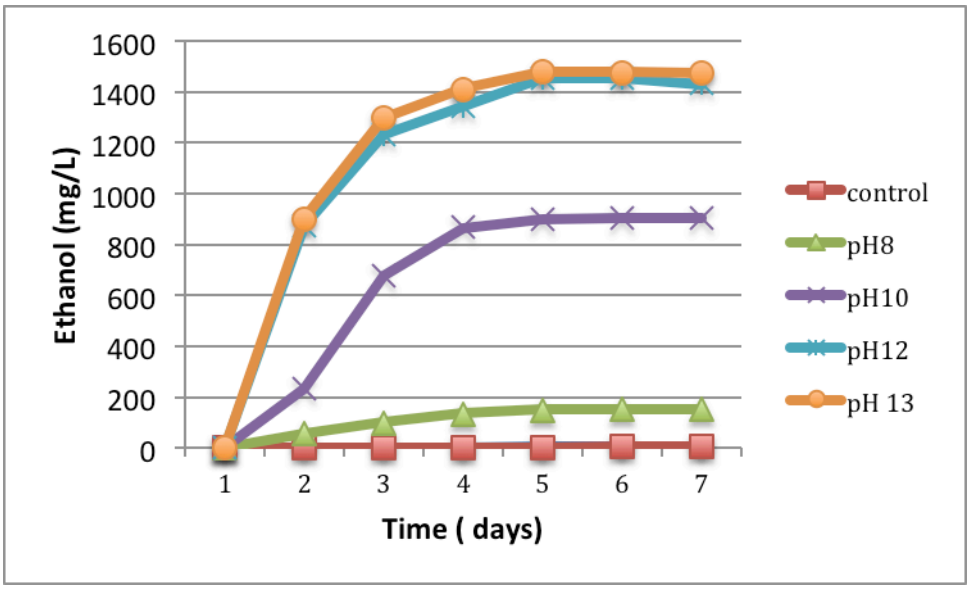

Figure 1A. Effect of alkaline pretreatment of energy cane L 79-1002 biomass on ethanol production. Data represent mean of triplicates in each treatment. ANOVA and Tukey groupings showed significant difference in pH 12 and pH 13 compared to rest of the treatments.

B

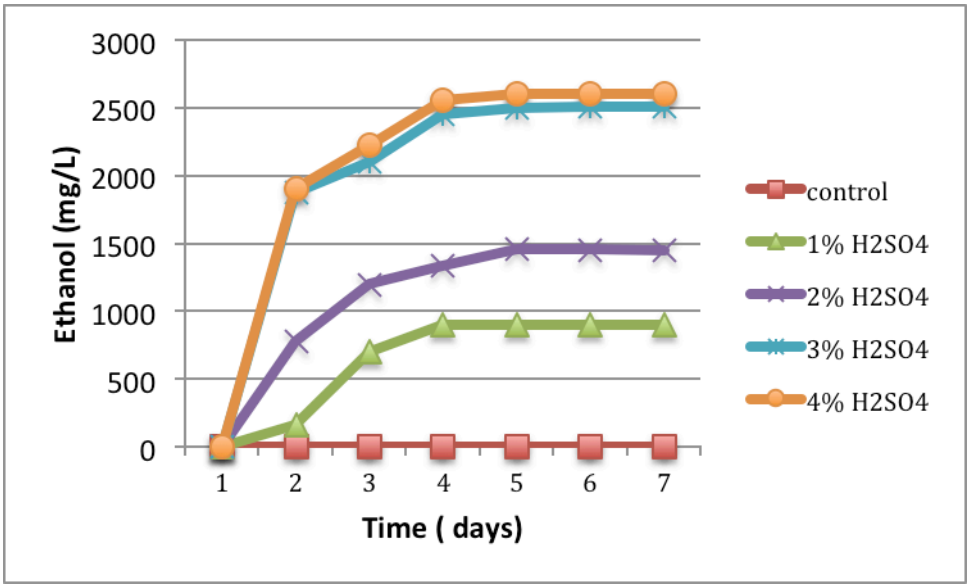

Figure. 1B. Effect of dilute acid pretreatment of energy cane L 79-1002 biomass on ethanol production. Data represent mean of triplicates in each treatment. ANOVA and Tukey groupings showed significant difference in 3 and 4% sulfuric acid treatments compared to rest of the treatments.

Ethanol production from fungal pretreated energy cane

Fungal Pretreatment of energy cane L 79-1002 yielded significant amount of total free sugar (Table 1) and when this sugar was subjected to fermentation by recombinant *E. coli FBR 5*, the ethanol yield was close to theoretical maximum (Fig. 1C). Maximum ethanol was obtained in the combined pretreatment of both fungi, *Cerioporiopsis* and *Phanerochaete,* which produced 1,299 mg/l ethanol in six days of fermentation, which is statistically significant compared to individual fungal pretreatment (ethanol yield of around 900 mg/l). In natural systems, fungi especially, the brown rot and white rot fungi are known to decompose fallen leaves from trees and other plants to humic and water soluble compounds (Lyn et al. 2010). These fungi produce various enzymes such as lignin peroxidase, phenol oxidase, manganese peroxidase, and laccase (Kuhad et al. 1997; Leonowicsz et al. 1999; Howard et al. 2003). These enzymes can be produced both under submerged fermentation (SmF) and solid-state fermentation (SSF) (Osma et al. 2007). In this study, the SSF pretreatment showed effective removal of lignin, which resulted in significantly higher ethanol production in the fungal pretreated energy cane compared to control.

C

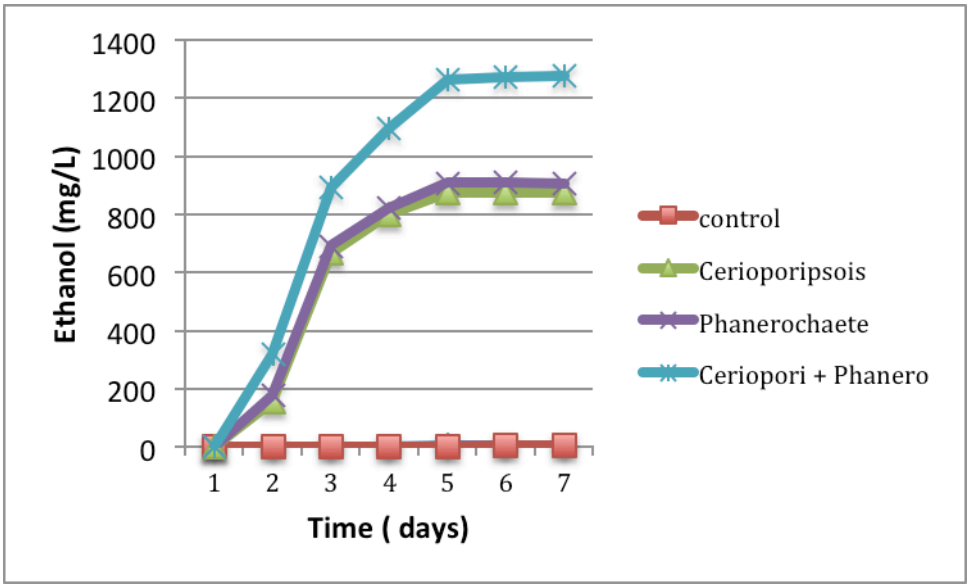

Figure. 1C. Effect of fungal pretreatment of energy cane L 79-1002 biomass on ethanol production. Data represent mean of triplicates in each treatment. ANOVA and Tukey groupings showed significant difference in combined pretreatment of *Cerioporiopsis* and *Phanerochaete* compared to individual fungal pretreatments.

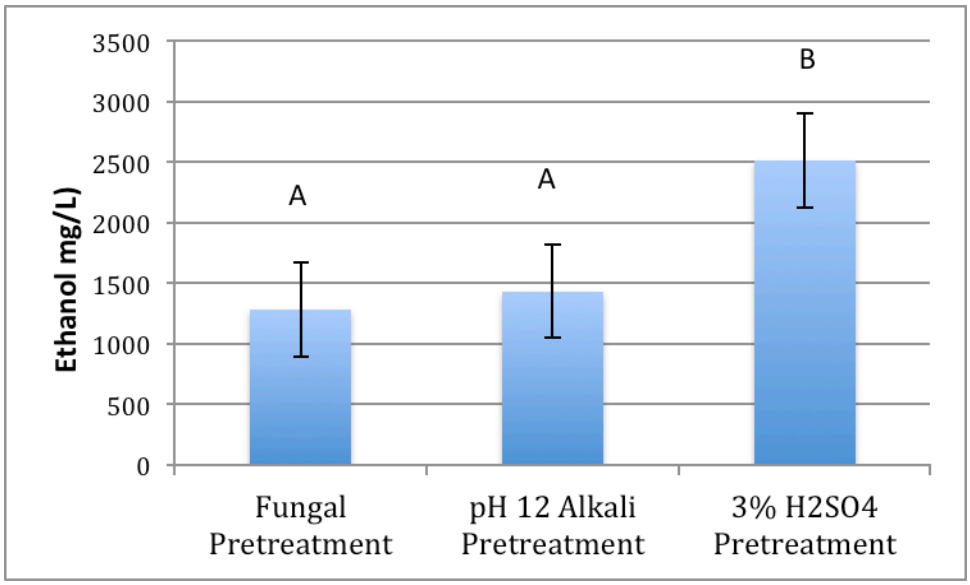

Figure 2. Comparison of best results from three pretreatments in ethanol production after six days of fermentation. Data represent mean of triplicates with S.D. Letters above samples represent Tukey groupings based ANOVA results. Data with similar letters are not significantly different from each other.

Comparison of all pretreatments

The best conditions under each of the pretreatment studied were compared and the result is presented in Fig. 2. The best pretreatment of energy cane L79-1002 is 3% sulfuric acid, which is statistically significant compared to pH 12 alkaline hydroxide pretreatment and combined fungal pretreatment of *Cerioporiopsis* and *Phanerochaete.* Among the fungal and alkaline pretreatments, the ethanol production showed no difference in significance. Pretreatment of lignocellulosic biomass is a costly step (Lynd et al. 1996), but is essential for high ethanol yields on a commercial level. Efficient pretreatment can affect downstream process costs by reducing the use of enzymes or fermentation time (Lynd et al. 1996). In our previous studies, we reported acid pretreatment was better than alkaline pretreatment in removing lignin from commercial sugarcane residues such as leaf and bagasse (Dawson and Boopathy, 2007; 2008; Shields and Boopathy, 2011). In the current study, based on the results obtained from three different pretreatments, dilute acid pretreatment with 3% sulfuric acid could be used as an effective pretreatment method for energy cane L 79-1002. Further experiments should be carried out to combine the dilute acid pretreatment with fungal pretreatment in order to reduce the use of acid, which will be a big cost factor in large scale biofuel production systems. Combining the fungal treatment with dilute acid treatment could significantly lower the volume of acid that is needed for pretreatment of energy cane for ethanol production. This combined pretreatment makes practical sense as the biomass can be treated with fungi during storage period prior to biomass processing. Biofuels are a potential sustainable solution to the global fuel crisis that is depleting natural resources as it contributes to climate change. The development of energy cane varieties for ethanol production has both environmental and economic significance. For Louisiana, the advent of new sugarcane varieties could help sustain the sugarcane industry while providing a new niche of jobs and capital. The advantage of producing an efficient source of ethanol could lead to greater net benefit with regard to carbon dioxide emissions as well as a smaller ecological footprint.

Combination of Fungal and Acid Pre-Treatment

Based on the results obtained from two different pretreatments, further experiments were carried out to combine the dilute acid pretreatment with fungal pretreatment in order to reduce the use of acid, which will be a big cost factor in large scale biofuel production systems. Energy cane was subjected to a pretreatment condition with *Cerioporiopsis* and *Phanerochaete* together, which yielded higher ethanol yield among various fungal pretreatments as detailed in method section. Following ten days of fungal pretreatment, the energy cane was pretreated with various low concentrations of sulfuric acid (0, 0.25, 0.5, 1, 1.5, and 2%). The pretreated biomass was enzymatically saccharified and subjected to fermentation using recombinant *E.coli* FBR 5. The results from this study are given in Table 2. The energy cane with 0% sulfuric acid after 10 days of fungal treatment produced ethanol concentration of 1266 mg/L compared to 2% sulfuric acid treatment of fungal pretreated biomass, which produced 3055 mg/L of ethanol (p value or 0.01). However, the lower dilution of 1 and 1.5% produced equally

good amount of ethanol, namely, 2876 and 2956 mg/L, respectively. Statistical analysis showed no significant difference among 1, 1.5, and 2% dilute acid treatment of fungal pretreated energy cane with a p value of 0.32.

Table 2. Effect of Fungal Pretreatment on Dilute Acid Pretreatments in Ethanol Production after Six Days of Fermentation

Treatment	Ethanol Production (mg/L)
0% sulfuric acid	1266 $\pm$ 11.5^{A}
0.25% sulfuric acid	1325 $\pm$ 22.7^{A}
0.5% sulfuric acid	1971 $\pm$ 29.5^{A}
1% sulfuric acid	2876 $\pm$ 39.2^{AB}
1.5% sulfuric acid	2956 $\pm$ 41.2^{AB}
2% sulfuric acid	3055 $\pm$ 25.3^{AB}

Results are average of triplicates in each treatment with S.D. Data with similar letters are not significantly different from each other.
Energy cane was pretreated with *Cerioporiopsis and Phanerochaete* for 10 days followed by various dilute acid treatments before the hydrolysate was subjected to enzymatic saccharification and fermentation with recombinant *E.coli* FBR 5 as detailed in methods section.

Other Biomass

Similar studies described above were conducted with other biomass such as commercial sugarcane (three cultivars), gamma grass, and switch grass. The optimization of pretreatment method was very similar to energy cane as described above. The best pretreatment for all the biomass was the combination of fungal and dilute acid pretreatment. Almost theoretical yield of ethanol was achieved in all biomass used in this study with the combination pretreatment of fungi and dilute acid.

Conclusions

1. This study shows that dilute acid pretreatment released cellulose and hemicellulose, which are available for enzymatic saccharification and fermentation. The best dilute acid pretreatment was 3% sulfuric acid.
2. The use of fungal pretreatment enhanced ethanol production. Brown rot and white rot fungi produced almost similar ethanol yield. The combined treatment of brown rot and white rot fungi together produced significantly higher ethanol yield compared to control, however, produced less ethanol compared to 3% dilute sulfuric acid pretreatment.
3. The combination of fungal pretreatment with lower dilute acid pretreatment produced the best result of this study. A 10 day fungal pretreated energy cane with both brown rot and white rot fungi together treated with 1% sulfuric acid showed ethanol production of 2876 mg/L, which is comparable to ethanol production in 3% dilute

acid treatment without fungal pretreatment and thus combining the fungal pretreatment with acid pretreatment makes practical sense.

References

Almeida, J.R., Modig, M.T., Röder, A., Lidén, G., Gorwa-Grauslund.M., 2008. *Pichia stipitis* xylose reductase helps detoxifying lignocellulosic hydrolysate by reducing 5-hydroxymethyl-furfural (HMF). Biotechnology and Biofuels 1, 1-12.

Boopathy, R., 2009. Anaerobic Biotransformation of furfural and Furfuryl Alcohol by a Methanogenic Archaebacterium. International Journal of Biodeterioration & Biodegradation 63, 1070-1072.

Chapple, C., Ladisch, M., Meilan, R., 2007. Loosening lignin's grip on biofuel production. *Nature Biotechnology* 25, 746-748.

Cobill, R.M., 2007. Development of energy canes for an expanding biofuels industry. Sugar Journal 70, 6.

Cowling, E.B., Kirk, T.K., 1976. Properties of cellulose and lignocellulosic materials as substrates for enzymatic conversion processes. Biotechnology and Bioengineering Symposium 6, 95–123.

Dien, B.S., Hespell, R.B., Wyckoff, H.A., Bothast, R.J., 1998. Fermentation of hexose and pentose sugars using a novel ethanologenic *Escherichia coli* strain. Enzyme and Microbial Technology 23, 336-371.

Dien, B.S., Nicholas, N.N., O'Bryan, P.J., Bothast, R.J., 2000. Development of new ethanologenic *Esherichia coli* strains fro fermentation of lignocellulosic biomass. Applied Biochemistry and Biotechnology 84, 181-186.

Dawson, L., Boopathy, R., 2007. Use of post-harvest sugarcane residue for ethanol production. Bioresource Technology 98, 1695-1699.

Dawson, L., Boopathy, R., 2008. Cellulosic ethanol production from sugarcane bagasse without enzymatic saccharification. BioResources 3, 452-460.

Gould, J.M. 1984. Alkaline peroxide delignification of agricultural residues to enhance enzymatic saccharification. Biotechnology and Bioengineering 26, 46-52.

Gould, J.M., 1985. Studies on the mechanism of alkaline peroxide delignification of agricultural residues. Biotechnology and Bioengineering 26, 225-231.

Gould J.M., S.N. Freer., 1984. High-efficiency ethanol production from lignocellulosic residues pretreated with alkaline H_2O_2. Biotechnology and Bioengineering 26, 628-631.

Grohmann, K., Torget, R., Himmel, M., 1986. Dilute acid pretreatment of biomass at high solids concentration. Biotechnology and Bioengineering Symposium 17, 135-151.

Howard, R.L., Abotsi, E., Rensburg, J.E.L., Howard, S., 2003. Lignocellulosic biotechnology: issues of bioconversion and enzyme production. African Journal of Biotechnology 2, 602-619.

Ho, N., Chen, W.Y.Z., Brainard, A.P., 1998. Genetically Engineered *Saccharomyces* Yeast Capable of Effective Cofermentation of Glucose and Xylose. Applied and Environmental Microbiology 64, 1852-1859

Jeffries, T., 2006. Engineering yeasts for xylose metabolism. Biotechnology 17, 320-326.

Knappert, D.R., Grethlein, H.E., Converse, A.O., 1981. Partial acid hydrolysis of poplar wood as a pretreatment for enzymatic hydrolysis. Biotechnology Bioengineering 11, 67–77.

Krishna, S., Chowdry, G.V., 2000. Optimization of simultaneous saccharification and fermentation for the production of ethanol from lignocellulosic biomass. Journal of Agriculture and Food Chemistry 48, 1971-1976.

Kuhad, R.C., Singh, A., Ericsson, K.E.L., 1997. Microorganisms and enzymes involved in the plant fiber cell walls. Advances in Biochemical Engineering and Bioechnology 57, 45-125.

Lenowicsz, A., Matuszewska, A., Luterek, J., Ziegenhagen, D., Wasilewska, W.M., Cho, N.S., 1999. Biodegradation of lignin by white rot fungi. Fungal Genetics and Biology 27, 175-185.

Lynd, L.R., Elander, R.T., Wyman, C.E., 1996. Likely features and costs of mature biomass ethanol technology. Applied Biochemistry and Biotechnology 57/58 741-761.

Lynn, M., Boopathy, R., Boykin, D., Weaver, M.A., Viator, R., Johnson, R., 2010. Sugarcane residue decomposition by white rot and brown rot microorganisms. Sugarcane International Journal 28, 37-42.

Neter, J., Wasserman, W., Kutner, M.H., 1990. Applied linear statistical models: regression, analysis of variance, and experimental designs". 3rd ed. IRWIN. Burr Ridge, Illinois.

Osma, J.F., Herrera, J.L.T., Couto, S.R., 2007. Banana skin; A novel waste for laccase production by Trametes pubescens under solid state conditions application to synthetic dye decoloration. Dyes and Pigments 75, 32-37.

Saha, B.C., Cotta, M.A., 2011. Continuous ethanol production from wheat straw hydrolysate by recombinant ethanologenic *Escherichia coli* strain FBR5. Applied Microbiology & Biotechnology 90, 477-487.

Shields, S., Boopathy, R., 2011. Ethanol production from lignocellulosic biomass of energy cane. International Journal of Biodeterioration & Biodegradation 65, 142-146.

Salassi, M., Deliberto, M., Legendre, B., 2009. Economic importance of Louisiana sugarcane production in 2008. LSU AGCenter. Available http://www.lsuagcenter.com/MCMS/RelatedFiles/%7BD2E200B1-74C8-4AD7-AB33-CFDD6EDB0839%7D/2008+SUMMARY.pdf

Tew, T., Cobill, R., 2008. Genetic improvement of sugarcane (*Saccharum* spp.) as an energy crop". In: Vermerris, W. (Ed.), Genetic Improvement of Bioenergy Crops. Springer Science + Business Media, LLC, Newy York, NY, pp. 249-272.

Tew, T.L., Dufrene, E.O., Garrison, D.D., White, W.H., Grisham, M.P., Pan, Y., Richard, E.P., Legendre, B.L., Miller, J.D., 2007a. Notice of release of high-fiber sugarcane variety Ho 00-961. Sugar Bulletin 85, 23-24.

Tew, T.L., Dufrene, E.O., Garrison, D.D., White, W.H., Grisham, M.P., Pan, Y., Richard, E.P., Legendre, B.L., Miller, J.D., 2007b. Notice of release of high-fiber sugarcane variety HoCP 91-552. Sugar Bulletin 85, 25-26.

Tew, T.L., Dufrene, E.O., Garrison, D.D., White, W.H., Grisham, M.P., Pan, Y., Richard, E.P., Legendre, B.L., Miller, J.D.,. 2007c. Notice of release of high-fiber sugarcane variety L 79-1002. Sugar Bulletin 85, 21-22.

U.S. DOE., 2006. Breaking the biological barriers to cellulosic ethanol: a joint research agenda, DOE/SC/EE-0095, U.S. Department of Energy Office of Science and Office of Energy Efficiency and Renewable Energy. Available http://genomicscience.energy.gov/biofuels/b2bworkshop.shtml

U.S. DOE., 2009. Biomass: multi-year program plan. U.S. Department of Energy Office of Energy Efficiency and Renewable Energy. Available http://www1.eere.energy.gov/biomass/pdfs/mypp.pdf

Yang, B., Wyman, C.E., 2004. Effect of xylan and lignin removal by batch and flow through pretreatment on the enzymatic digestibility of corn stover cellulose. Biotechnology and Bioengineering 86, 88-95.

Patents: None.

Publications / Presentations:

Peer Reviewed Journals

Suhardi, V.S.H., B. Prasai, D. Samaha, and R. Boopathy. 2013. Combined biological and chemical pretreatment method for lignocellulosic ethanol production from energy cane. **Renewable Bioresources**. 1: 1-5.

Suhardi, V.S.H., B. Prasai, D. Samaha, and R. Boopathy. 2013. Evaluation of Pretreatment methods for lignocellulosic ethanol production from energy cane Variety L 79-1002. **International Journal of Biodeterioration & Biodegradation**. 85: 683-687.

Shields, S., and R. Boopathy. 2011. Ethanol Production from Lignocellulosic Biomass of Energy Cane. **International Journal of Biodeterioration & Biodegradation.** 65: 142-146.

Lynn, M., R. Boopathy, D. Boykin, M.A. Weaver, R. Viator, and R. Johnson. 2010. Sugarcane Residue Decomposition by White Rot and Brown Rot microorganisms. **Sugarcane International Journal.** 28: 37-42.

Johnson, R.M., R.P. Viator, M.P. Grisham, E.P. Richard, and R. Boopathy. 2008. Microbial Degradation of Post-Harvest Residues. **Proceedings of International Sugar Cane Technology**. 26: 365-373.

Conference Presentations

Boopathy, R. 2013. Biological Pretreatment of Lignocellulosic Biomass from Sugarcane for Ethanol Production. Paper Presented at the Annual Meeting of the Society for Industrial Microbiology and Biotechnology. San Diego, CA. August 11-15, 2013.

Boopathy, R. 2013. Biological and Chemical Pretreatment Method for Lignocellulosic Ethanol Production from Energy Cane. Paper Presented at the 113th Annual Meeting of the American Society for Microbiology. Denver, CO. May 18-21, 2013.

Samaha, D. and R. Boopathy. 2013. Combined Biological and Chemical Pretreatment Methods for Lignocellulosic Ethanol Production from Energy Cane. Paper Presented at the 87th Annual Meeting of the Louisiana Academy of Sciences. Grambling, LA March 9th, 2013.

Boopathy, R. 2012. Use of White Rot and Brown Rot Fungi in Lignin Removal from Agricultural Residues for Ethanol Production. Paper Presented at the 5th Annual Conference on the Challenges in Environmental Science and Engineering. Melbourne, Australia, September 9th to 13th, 2012.

Boopathy, R. 2012. Biological Deliginification of Sugarcane Biomass for Ethanol Production. Paper Presented at the Society for Industrial Microbiology and Biotechnology Conference. Washington DC. August 12 – 16, 2012.

Boopathy, R. 2012. Use of Local Louisiana Cultivar of Gamagrass for Bioethanol Production. Paper Presented at the 34th Industrial Energy Technology Conference. New Orleans, LA. May 29th to June 1st, 2012.

Samaha, D. and R. Boopathy. 2012. Evaluation of Local Louisiana Cultivars of Gamagrass and Switchgrass for Bio-ethanol Production. Paper Presented at the 34th Symposium on Biotechnology for Fuels and Chemicals. New Orleans, LA. April 30th – May 3rd, 2012.

Samaha, D. and R. Boopathy. 2012. Fuel Grade Ethanol Production from Eastern Gamagrass. Paper Presented at the 86th Annual Meeting of the Louisiana Academy of Sciences. Alexandria, LA. March 3rd, 2012.

Boopathy, R. 2011. Bioethanol Prodcution from Agricultural Residues. Paper Presented at the Industrial Energy Technology Conference. New Orleans, LA. May 17-19, 2011.

Shields, S. and R. Boopathy. 2011. Optimization of Ethanol Production from the Biomass of Energy Cane L79-1002. Paper Presented at the 111th General Meeting of American Society for Microbiology. New Orleans, LA. May 21 -24, 2011.

Boopathy, R. 2010. Ethanol Production from Agricultural Residues and Energy Canes. Paper presented at the 7th International Conference of the Biotechnology Research Society of India. Madurai, India. Nov. 12-14, 2010.

Shields, S., and R. Boopathy. 2010. Evaluation of Type II Energy Cane L79-1002 for Lignocellulosic Ethanol Production. Paper Presented at the ASM South Central Branch Annual Meeting. Hattiesburg, MS. Oct. 29-30, 2010.

Shields, S. and R. Boopathy. 2010. Use of Energy Cane in Louisiana for Energy Production. Paper Presented at the 84th Annual Meeting of the Louisiana Academy of Sciences. Alexandria, LA. Feb. 27th, 2010.

CHAPTER Two
Tulane University

Technical Contact: Professor Victor Law, (504) 865-5773, law@tulane.edu
Business Contact: Ken Bode, (504)865-5272, kbode@tulane.edu

Task 2: Bio-butanol Production

SUMMARY

Tulane University pursued three projects related the Clean Power Energy Research Consortium during the period 2008-2010. These include the utilization of sugar mill wastes to produce biobutanol, the process design and pilot scale experiments for biobutanol purification into fuel grade products, the supply chain economic analysis of biobutanol, and the analysis of integrating intermittent power into the power grid.

WORK STATEMENT

The Tulane project follows three parallel tasks:

1. Utilization of sugar mill wastes to produce butanol via a variety of microbial pathways.
2. Process design and pilot scale experiments for the purification of butanol [from the products of item (1)] into a fuels grade product.
3. Biobutanol supply chain economic analysis and renewable power integration into the grid

We propose an incremental approach to development of a commercially viable process from (eventually) cellulosic material. The process for the manufacture of fuel-grade butanol from sugar mill waste material is comprised of two steps: 1) biological production of a butanol/water mixture; and 2) purification and separation of butanol from the reaction mass.

Three major steps or phases are envisioned. In each phase, parallel efforts dealing with both the bioproduction of butanol and the process design/development will be performed.

*Phase 1 (*year 1*):*Fermentation efforts will focus on identifying yeast strains that maximize butanol production from sugar mill waste while minimizing creation of other species. Laboratory fermentation studies will be performed to determine the optimum conditions (*e.g.* waste particle size, temperature, pH, etc.) for each strain. High-throughput screening techniques will be applied to rapidly obtain this data on multiple strains.

Process design efforts during the initial phase involves a study of numerous butanol purification schemes. Each purification option's sensitivity to butanol and fermentation by-product (*e.g.* ethanol, acetone, etc.) concentration will be studied. Each scheme will be investigated based on capital investment, energy-efficiency, and environmental impact. Much of this effort has already begun. Detailed process simulations for four purification alternatives have been developed for a 2 wt% butanol-in-water feed composition.

Sensitivity and optimization studies for these process options must be completed. Computer simulations for other alternatives must be developed.
The fermentation and simulation efforts will affect each other in a cyclical fashion during this phase. The laboratory fermentation results will be incorporated into the detailed simulations for each purification alternative. Additional process simulation work will be performed to guide future laboratory studies to the overall process optimum.
At the conclusion of Phase 1, our laboratory and process simulation studies will have identified the optimal process for Phase 2. Other researchers at the business school will also have completed a commercial/economic analysis of the overall market for alcohol based fuels and will have made a preliminary estimate of the potential for penetration of that market by Butanol.
In Phase 2, the focus will be on scaling up the optimal process developed from Phase I. Fermentation vessels on the order of 10-20 liters will be employed during this phase. The purification section will be scaled to match the butanol production rate from fermentation. Once operational, we will use this small pilot-plant to confirm our laboratory findings. Overall material balances will be obtained and additional optimization will be performed. All pilot-scale operation data will be used to determine capital investment requirements and rates-of-return for incorporating the optimal biobutanol process into a typical Louisiana sugar mill.
Fermentation studies during Phase 2 will focus on screening a number of biological organisms for production of butanol from cellulose. This study will begin with naturally occurring organisms that are known to digest cellulosic material (*e.g.* bacteria from bovine gut and termites, fungus from rotting trees, etc.). It is unlikely that these organisms' metabolic pathways will produce significant quantities of butanol without genetic modification. Hence, pathways for organisms that have already been mapped will be analyzed to determine whether genetic modifications would increase their likelihood of producing feed for another butanol-producing organism (*i.e*. glucose or butyric acid) or butanol directly from cellulose.As new biological candidates are identified during Phase II, their results will be incorporated into simulations of the optimal process to determine their impact. Additional studies on the pilot-scale may be warranted if the feed composition to the purification section is expected to change significantly when the cellulose-digesting organisms replace their glucose-digesting counterparts.At the conclusion of this second phase, we will have determined the following:

1. Economics for incorporating the optimal glucose-to-butanol process into a typical Louisiana sugar mill or ethanol plant. These results will be transmitted to the Tulane business school researchers analyzing the economic aspects of this proposal.
2. Reliable operating conditions for the optimal glucose-to-butanol process.
3. Several biological candidates for producing butanol from cellulose.

During the last phase, we intend to partner with a sugar mill to commercialize the piloted process. During this phase, the proposed commercial process will contain those organisms which have been piloted from Phase 1. We have identified the Audubon Sugar Institute as a partner to assist us in finding a candidate. We will work closely with the candidate to transfer the technology and will provide process assistance during start-up. A further increase in scale will occur at this phase. Hence, some additional pilot-scale

studies may be required to convince our sugar mill partners of the reliability of our claims.

Phase 3a of the research project investigates the economic viability of bio-butanol as an alternative liquid transportation fuel. This work seeks to model and optimize critical decision variables while considering multiple objectives that are important to policy makers, investors and citizens under conditions where a competitive bio-butanol industry is emerging. A key issue motivating the study is the concern that policy makers moved forward with the build-out of an ethanol infrastructure without a complete understanding of the impact of long-term decisions. We posit that, without proper studies, there is a risk of locking the country into an inferior market design that will be costly to change and the true social benefits from this emerging technology will not be fully realized. To this end, we examine the commercial/economic viability of the large-scale production of bio-butanol, first as an industrial solvent, second as a fuel additive, and third as a potential replacement for gasoline. Specifically, we attempt to quantify the risks venture capitalists face in their investment decisions and speculate on future policy decisions that may affect their choice to participate. We also examine the domestic labor benefits and potential environmental impact of this emerging bio-butanol industry.

Phase 3b of the project: Professors Jiang, Parker and Shittu examine electricity capacity markets to see how well they accommodate renewable energy resources that tend to be more intermittent than their fossil fuel counterparts. The original intention of capacity markets is to ensure capacity adequacy. In particular, performance incentive mechanisms are often included as an integrated part of capacity market designs. The underlying logic is based on the perspective that adequate capacity induces adequate system reliability. Therefore, the same capacity measure that is used for compensating the suppliers' contribution to system capacity can be also used for evaluating their contribution (or damage) to system reliability. While the logic is qualitatively sound, the quantitative relationship between capacity and reliability is not seen in practice. Based on historical data, an analysis of 18 years of data from ISO New England shows little correlation between installed capacity and the annual duration of the scarcity period. Such an observation suggests a more complicated relationship between capacity and reliability than what the current capacity market design assumes. In particular, the current market design treats derating (reductions from the maximum installed capacity) and unplanned outages (percentage of time a resource is unavailable) in the same way. In practice, however, derating has a much smaller impact on system reliability than an unplanned outage.

Task 2: Butanol production via a variety of microbial pathways

July 2011 Overview:

In this quarter we investigated the ability of strain TU-103 to metabolize starch and cellulose and produce butanol and acetone as end products, and we determined the nucleotide sequence of the genome of TU-103.

Bottle level fermentations	**Incubation conditions**	**Results**
Starch	P2Y medium, 32^{o}C, 200 rpm, Duration 1-8 days	Maximum butanol levels produced were in the range of 1.5 - 2.0 gl^{-1} Incubation period: 7-8 days
Paper waste (whatman paper pulp		Maximum butanol levels produced were in the range of 1.0 - 1.7 gl^{-1} Incubation period; 8-10 days
Paper waste (filter paper pulp		Maximum butanol levels produced were in the range of 1.0 - 2.0 gl^{-1} Incubation period; 8-10 days
Paper waste (newspaper pulp)		Maximum butanol levels produced were in the range of 0.7 - 2.2 gl^{-1} Incubation period; 8-10 days

Observations:

1) Strain TU-103 produces amylases that allow it to utilize starch as a source of carbon and produce butanol.
2) Strain TU-103 can also utilize paper waste as the source of carbon, and butanol is produced as an end product of metabolism. Different sources of papers were converted into pulp by the process of soaking, drying and size reduction, and added as substrates to fermentations.
3) Complete utilization of the substrates was not observed.

Bioreactor studies: Fermentations were conducted in a 10 l Fermentor by using starch and cellulosic substrates

Bioreactor fermentations	Incubation conditions	Results
Starch fermentation	P2Y medium, 32^{o}C, 400rpm, Duration 1-8 days	Maximum butanol levels produced were in the range of 2.3 gl^{-1} Incubation period: 8 days
Paper waste (newspaper pulp)		Fermentation is in progress.

Determination of Amylolytic enzymes in bacterial cultures:
For determining the concentrations of Amylolytic enzymes in bacterial cultures, samples taken from bacterial cultures were centrifuged and the supernatant was tested for Amylolytic activity. The disc plate method (**Harshad: put in a reference**) was used to determine the Amylolytic activities in culture supernatants.

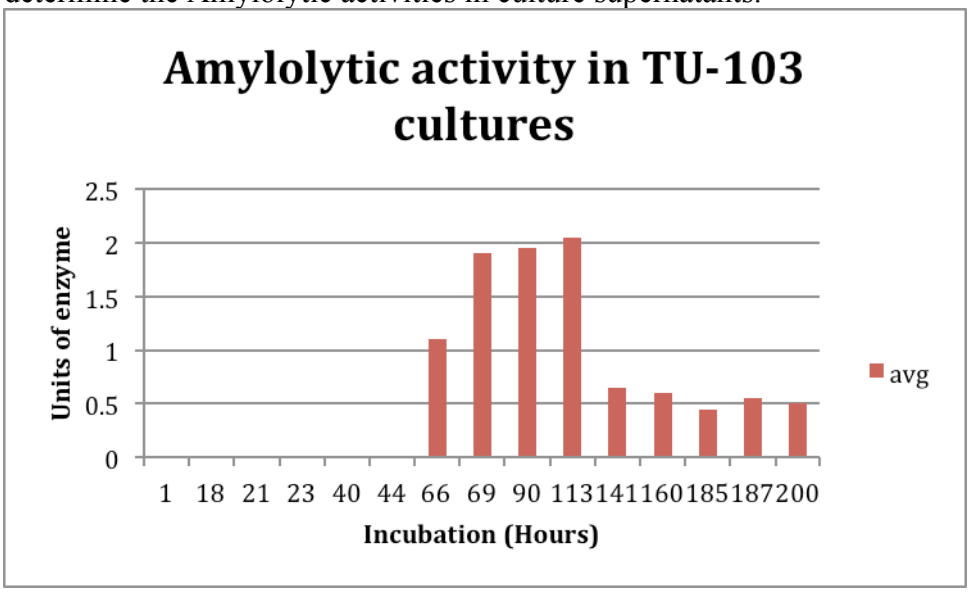

Observations

1) Maximum concentrations of Amylolytic activity of 2 U/ml was observed around the 66 hr post inoculation.

Separation of proteins with cellulolytic activity in TU-103 cultures

Spent broth of strain TU-103 were used as source of cellulase protein for purification. Broth samples were centrifuged to remove cells and particulate matter and the proteins were precipitated with acetone or ammonium sulfate.

Protein pellets were resuspended in buffer, desalted by gel filtration, and eluted a DEAE ion exchange column. Fractions from the column were assayed for cellulolytic activity by using carboxymethyl cellulose or filter paper as the substrates and then the fractions with peak activity were pooled and proteins were fractionated by gel filtration chromatography gel chromatography.

The results of this protein purification scheme allowed the cellulase activity of strain TU-103 to be purified though not yet to homogeneity. Further purification steps will needed to obtain homogeneously pure protein for enzymology studies and structure study by X-ray crystallography.

Genome sequencing

We have assembled the nucleotide sequence of the genome of TU-103 and we are in the process of annotating the genome.

Task 2a: Biobutanol Supply Chain Economics

10/1/2008 -9/30/2009

During the period from September 2008 through August 2009, business school researchers (Eric Smith, Geoffrey Parker, and visiting associate professor Paul Bergey) developed an economic model of the bio-butanol production and supply chain. The economics and supply chain research was presented at the 32nd Annual Meeting of the International Association for Energy Economics (June 24, 2009) in San Francisco, CA.

In addition to the model development that has taken place at Tulane, the work has led to several collaborative research opportunities with North Carolina State University. Dr. Vivek Felner in the Animal Science Department at NCSU provided biological samples of cow rumen to the molecular biologists at Tulane University, who are working on genetically modifying the bacteria that live in the cow rumen for optimizing bio-butanol production. As a result, Dr. Felner and Paul Bergey (among others) submitted a grant proposal to DOE/USDA for a multi-year research project in April, 2009 for a new biorefinery concept.

Dr. Prema Arasu (Professor – CVM, Molecular Biomedical Science, Associate Vice Provost - International Academics, and Director – NCSU Global Health Initiative), invited Paul Bergey to participate in the “Biofuels-Livestock-Health Interest Group” at NCSU, aimed at exploring the diverse interests of NCSU faculty and defining opportunities for collaboration. Bergey presented a sample of the research on "Biobutanol

and supply chain economics," at the CVM on September 28th, 2009. The work with this group has already led to new research opportunities with BioEconomics Inc., an incubator company on the Centennial Campus at NCSU.

In October 2009, initial result from the bio-butanol research were featured in an article "Researchers looking to biological methods to produce butanol" that appeared on page 20 in the Business and Industry Connection (BIC) Magazine (www.bicalliance.com).

To date, there is only one biobutanol plant in production in the United States, which is owned and operated by Butyfuels, Inc. in Blacklick, Ohio. The plant is designed for a maximum production capacity of 5 million gallons per year with a second plant of equal capacity under construction. The details of the plant's economics are outlined in Ramey, D., Yang, S., "Production of Butyric Acid and Butanol from Biomass," Department of Energy Final Report: Contract No.: DE-F-G02-00ER86106, 2004.

Task 2b: Renewable Power Integration
10/1/2009 -12/31/2012

The renewable power integration phase was launched in September 2009. In this project, Professors Jiang, Parker, Sheffrin, Shittu with PhD student Dmitry Kurochkin examine electricity capacity markets to see how well they accommodate renewable energy resources that tend to be more intermittent than their fossil fuel counterparts. The original intention of capacity markets is to ensure capacity adequacy. In particular, performance incentive mechanisms are often included as an integrated part of capacity market designs. The underlying logic is based on the perspective that adequate capacity induces adequate system reliability. Therefore, the same capacity measure that is used for compensating the suppliers' contribution to system capacity can be also used for evaluating their contribution (or damage) to system reliability. While the logic is qualitatively sound, the quantitative relationship between capacity and reliability is not seen in practice. Based on historical data, an analysis of 18 years of data from ISO New England shows little correlation between installed capacity and the annual duration of the scarcity period. Such an observation suggests a more complicated relationship between capacity and reliability than what the current capacity market design assumes. In particular, the current market design treats derating (reductions from the maximum installed capacity) and unplanned outages (percentage of time a resource is unavailable) in the same way. In practice, however, derating has a much smaller impact on system reliability than an unplanned outage.

Subtask 2.1 Supply Chain Economics

BIO-BUTANOL PRODUCTION AND SUPPLY CHAIN ECONOMICS

Technical Contact: Geoff Parker, Tulane University
Phone (504) 865-5472, Email: gparker@tulane.edu

Project Summary

In an era of increasing price volatility and concerns over global warming, diversifying the energy supply base through reducing dependence on foreign oil and expanding domestic sources of environmentally friendly alternative energy sources have become pressing national priorities. One potential step toward this diversification is to expand the role of biofuels industry in the US economy. Before expanding existing ethanol programs, however, we suggest that there might be superior alternatives such as biobutanol.

Biobutanol is an alcohol-based biofuel that has many advantages over ethanol. Among the notable benefits of biobutanol are as follows. 1. It has a higher energy density per unit volume than ethanol. 2. It can be produced with significantly less energy than ethanol. 3. It is compatible with the existing distribution infrastructure for petroleum based fuels, and thus, can be distributed via the national pipeline network, unlike ethanol. 4. It is highly resistant to moisture absorption and therefore has potential as an aviation fuel. 5. It can be burned in existing automobile engines in any blended proportion (up to 100%) without significant performance degradation or engine modification. 6. It is cleaner burning than gasoline or ethanol and therefore yields a reduction in carbon emissions when consumed.

We are concerned that policy makers are moving forward with the build out of an ethanol infrastructure without a complete understanding of the impact of long term decisions. We posit that without proper studies there is a risk of being locked into an inferior market design which will be costly to change and the true social benefits from this emerging technology will not be fully realized. To this end, we examine the commercial/economic viability of the large scale production of biobutanol, first as an industrial solvent, second as a fuel additive, and third as a potential replacement for gasoline. Specifically, we attempt to quantify the risks venture capitalists face in their investment decisions and speculate on future policy decisions that may affect their choice to participate. We also examine the domestic labor benefits and potential environmental impact of this emerging biobutanol industry.

Technical Merit

To attract private capital investment, we have developed a high level simulation model to characterize the investment risks for market participants interested in engaging in the emerging biobutanol industry. Using actual data that we have collected from the Reuters commodity trading system, we have constructed a preliminary monte-carlo simulation of price spreads between ethanol and conventional gasoline. Using ethanol price levels and correlations as a proxy for other biofuels such as butanol, we calibrated our simulation model to provide an estimate for a free market equilibrium price of carbon

emissions for fossil fuels vs biofuels. We then examined the impact of incremental movements in the blend wall beyond 10%. Our cost estimation method is based upon the displacement volume of conventional gasoline with biofuels and the corresponding reduction in carbon footprint of the target biofuel as determined by the GREET model for life cycle analysis of carbon emissions, the government standard for carbon footprint analysis. Our preliminary model shows that a policy change moving the blend wall for reformulated gasoline from 10% (ethanol) to 20% (10% ethanol, 10% butanol), would displace approximately 11 billion gallons of conventional gasoline and result in a reduction of 3.6 to 14.3 million tons of greenhouse gas emissions per year. The expected costs of this change would be a price spread of approximately 23% between conventional gasoline and the biofuel alternatives, reflecting a free market price of mitigated carbon emissions of approximately $18.5 per ton CO_2.

Using data from the first edition of the Biomass Energy Databook, we have constructed a preliminary model for estimating the number of new plant jobs created and the number of supply chain jobs supported by the startup (or conversion) of a corn ethanol plant to a biobutanol plant. A movement of the blend wall in reformulated gasoline from 10% (ethanol) to 12.35% (10% ethanol, 2.35% butanol), could be achieved by retrofitting the 24 idle ethanol plants taken out of service in the past three months (2 billion gallons per year capacity) , which would save between 135,000 to 142,000 supply chain jobs and create an estimated 8,000 new butanol plant jobs, while simultaneously serving our environment and reducing our dependency on foreign oil.

Preliminary results suggest that the investment risk for a startup biobutanol plant is high. Policy decisions such as the introduction of a carbon tax or a cap & trade system would mitigate the risk. Large scale production of biobutanol (in lieu of ethanol) would likely have a positive impact on the environment, particularly with regard to reduced carbon emissions in the supply chain. A key factor to improving the environmental benefit of butanol over ethanol lies with scientific advancement of the production processes, whereby the percentage of acetone produced as a co-product is reduced.

Broader Impact

Environmental: Clean air is the social and political priority around the world. A rumen-based bioreactor used to produce biobutanol with genetically modified and optimized microbial enzymes has the potential to mitigate several environmental concerns. First, breaking down complex molecules into simpler building blocks will lead to increased production of biofuels and offsetting petroleum productions with the resultant ***decrease in exhaust and greenhouse gas emissions***. Second, by providing for controlled decomposition of cellulosic plant matter in a closed loop bioreactor it will ***reduce the overall risk of airborne contaminants.*** This will reduce level of methane gas that would otherwise be generated during landfill decomposition or natural decomposition in the greater environment.

Economic: A rumen-based bioreactor used to produce biobutanol will provide several desirable economic advantages over other state-of-the-art approaches to biofuel production. First, GM organisms are considerably ***more efficient*** at breaking down complex cell structures that exist in lignin rich cellulosic feedstocks. Second, increased biofuel production ***will lead to primary and secondary domestic job creation*** at a time when initial jobless claims have increased for 18 consecutive months and the economy is

losing jobs at the rate of 350-650 million jobs per month. These models may impact the efficacy of venture capitalists and guide policy makers on the timing and intensity of policy decisions. Finally, our economic models allow for inferences of policy decisions on the emergence of a free-market driven price for carbon emission from alternative transportation fuels based upon their displacement rate of conventional gasoline.
Energy Independence: A rumen-based bioreactor used to produce biobutanol **would convert non-food sources of feedstock to liquid transportation fuels**, reducing U.S. dependence on foreign oil. Biobutanol is compatible with the existing distribution infrastructure and automobile engines, unlike ethanol, which avoids the costly development of a parallel distribution system necessary for the E85 program currently used in selected regions of the country. Butanol, has a higher energy density, lower volatility and higher resistance to water absorption, making it highly desirable as an alternative transportation fuel.

Background

America's current dependence on fossil fuels poses a number of problems, including environmental pollution, global warming, unfavorable balance of trade, and the need for a worldwide transport system for both crude oil and refined petroleum products. To remedy these problems, new, clean, sustainable, domestic sources of energy are needed [3]. Biofuels, which are produced from biological sources, provide a potential solution to these problems. With certain exceptions, environmental pollution from biofuels is lower than for fossil fuels. The natural carbon cycle results in lower net production of greenhouse gases than for the sequestered carbon in petroleum. In addition, biofuels hold the promise of a renewable, domestic supply of fuel.

Currently, the availability of biofuels is limited by the supply of feedstocks. In addition, biofuel production has the demonstrated potential to adversely impact food prices and to disrupt food supply. For these reasons, there is great interest in the development of biofuels from organic wastes and plant matter that is not part of the human food chain. Also, there is a considerable advantage to biofuel production methods that can utilize a variety of fuelstocks.

Because they make use of stored energy in the form of sugars and fats, first-generation biofuels, such as ethanol and biodiesel, compete with the human food supply. The next generation of biofuels will take advantage of more complex molecules such as cellulose. However, it is much more difficult to convert these non-food sources into fuel. A novel scientific approach is to break down these complex molecules into simple sugars by enzymatic processes, or fermentations involving genetically-modified organisms (GM) that thrive in a bio-reactor. The benefit of this approach is that it can be optimized for high yields for fuelstock- and product-specific targets, such as converting sugar mill waste products to biobutanol. The drawbacks of this approach is that it can be expensive, the genetically modified organisms can be hard to maintain, and they may pose a risk to the environment.

Model Development

The project team has taken a multidisciplinary approach to the investigation of the bio-reactor concept, including adaptability to various feedstocks, and genetically modified pathways of bacteria commonly found in the rumen of a cow stomach, to biobased end products such as biobutanol. Essential to this evaluation is the development of in-house, stochastic economic models to assess the merits of various production

process alternatives in light of market conditions and the regulatory environment. In our view, the economic viability of the bio-reactor approach depends upon our ability to optimize the output mix of biofuel products for commercial production

Venture Capital Model

To attract private capital investment, we have developed a high level simulation model to characterize the investment risks for market participants interested in engaging in a biobutanol investment project. In this section, we discuss the application of our model to the emerging biobutanol industry to add context to our bioreactor concept.

A typical venture capital model will assess the viability of an investment using a discounted cash flow measure known as Net Present Value. Figure 1 shows an influence diagram of our NPV Model. An influence diagram is a relatively common tool used to visualize and organize the variables in a stochastic model (such as a monte-carlo simulation) without showing the complexity of the mathematical relationships that connect the variables. The influence diagram in Figure 1 uses the following conventions:

1. A Diamond shape indicates an objective function. The shape is painted blue to indicate that it is an output variable of the simulation model that will have probability characteristics of interest. For example, the probability of a positive NPV is a key objective measure for VC investors, as is the expected NPV and 95% Confidence intervals encasing the expected NPV.
2. A Double lined oval shape indicates an exogenous variable having a fixed input value. It is an assumption that is held constant in the model, but can be manipulated using senstivitiy analysis to investigate various scenarios. For example, various corporate tax rates or borrowing costs (cost of debt).
3. A Single lined oval shape indicates an endogenous variable, which means that it is constructed entirely from other variables in the model. For example, Annual Income is an accounting measure taken from the corporate balance sheet. It is constructed entirely of other accounting input measures. Generally speaking, endogenous variables serve as a transformation function toward a higher level objective function.
4. A Single lined rectangle indicates an exogenous variable with a random input value drawn from a probability distribution. These act as sources of uncertainty for the monte-carlo simulation. The selection of distribution parameters may come from a range of approaches that incorporate any combination of historical data analysis, probability estimates from experts, and prior estimates grounded in the extant literature. For example, we examine the scenario of Butanol Price = Ethanol Historical Price as a baseline for our simulation analysis.

Figure 1 – Influence Diagram for NPV

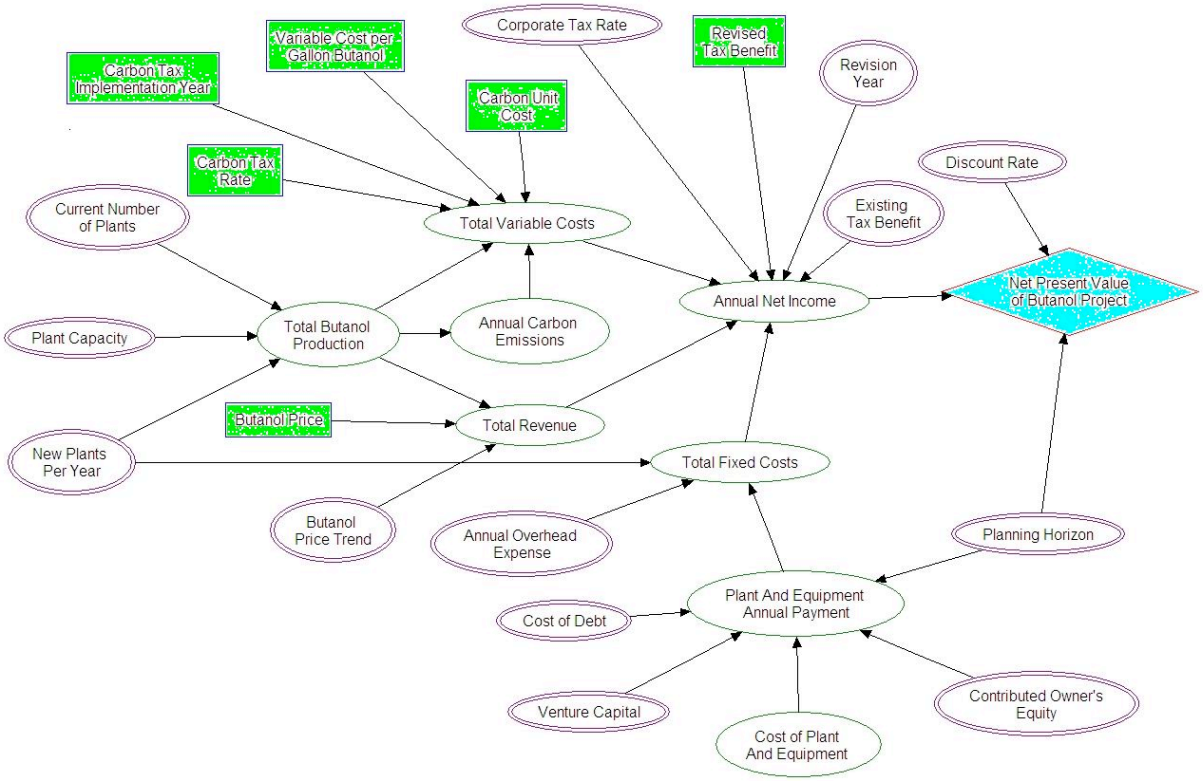

Grounding Our Model in Prior Research

To date, there is only one biobutanol plant in production in the United States, which is owned and operated by Butyfuels, Inc. in Blacklick, Ohio. The plant is designed for a maximum production capacity of 5 million gallons per year with a second plant of equal capacity under construction. The details of the venture capital model are outlined in Ramey and Yang [4]. In short, Ramey's venture capital model provided investors with an exit opportunity via initial public offering (IPO) in the seventh year of the project. A shortcoming of Ramey's venture capital model is that it is deterministic, and therefore, does not capture the risk associate with various input assumptions. Furthermore, Ramey's choice of investment metrics relied upon the project's internal rate of return (IRR) rather than NPV. Our approach to the venture capital model uses similar base assumptions, but implements stochastic inputs to appropriately characterize the risk. To this end, we replicated Ramey's investment model to provide stochastic output measures of both IRR and NPV, although we believe NPV to be a superior metric for evaluating the viability of a venture capital investment. Figure 2 shows that the expected NPV for a single 5 million gallon per year plant is approximately 28 Million and the probability of a positive NPV is 91.54%.

Figure 2 – Stochastic NPV metric

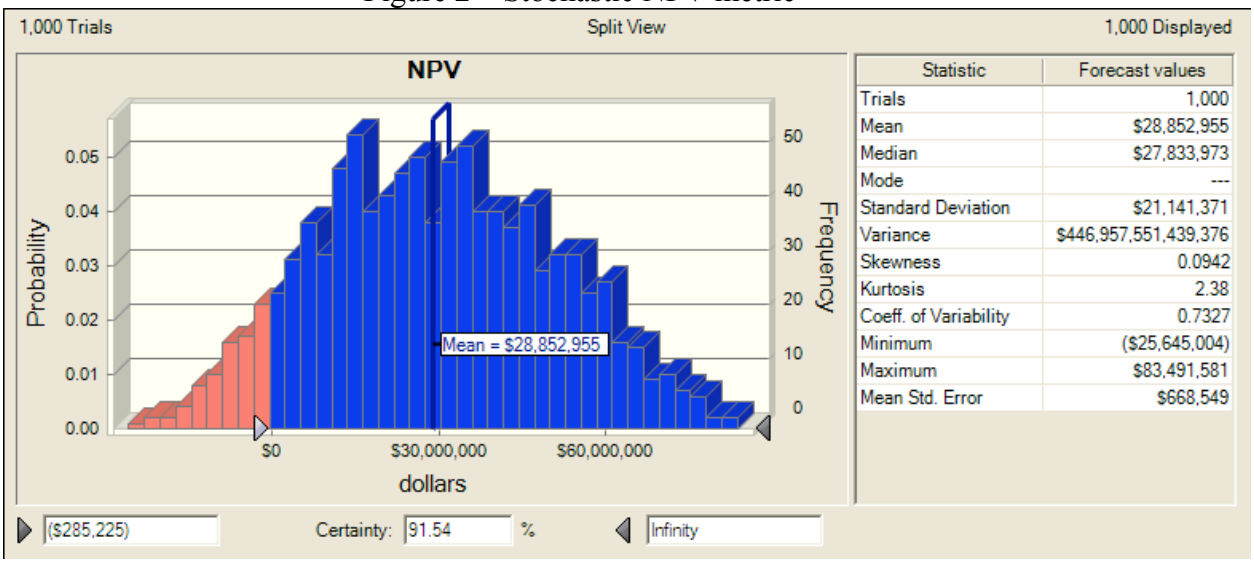

While Figure 1 shows that a VC investor should expect the project to be profitable (i.e. positive NPV), it also illuminates that there is roughly an 8.46% chance that they will regret the decision to move forward. Furthermore, in reviewing the baseline assumptions used by Ramey, our opinion differed on the values of some inputs. We reconfigured the parameters of the model to reflect what we believed to be appropriately conservative. Figure 3 shows the results of our reconfigured model compared to the replicated model reported in NPV terms via Ramey [4]. Our model assumptions produced an NPV distribution with a lower expected NPV (16.4 million vs 27.3 million), but also reduced the variance of the NPV distribution.

Figure 3 – Overlay of NPV for Ramey's Baseline Assumptions vs. our Parameter Estimates

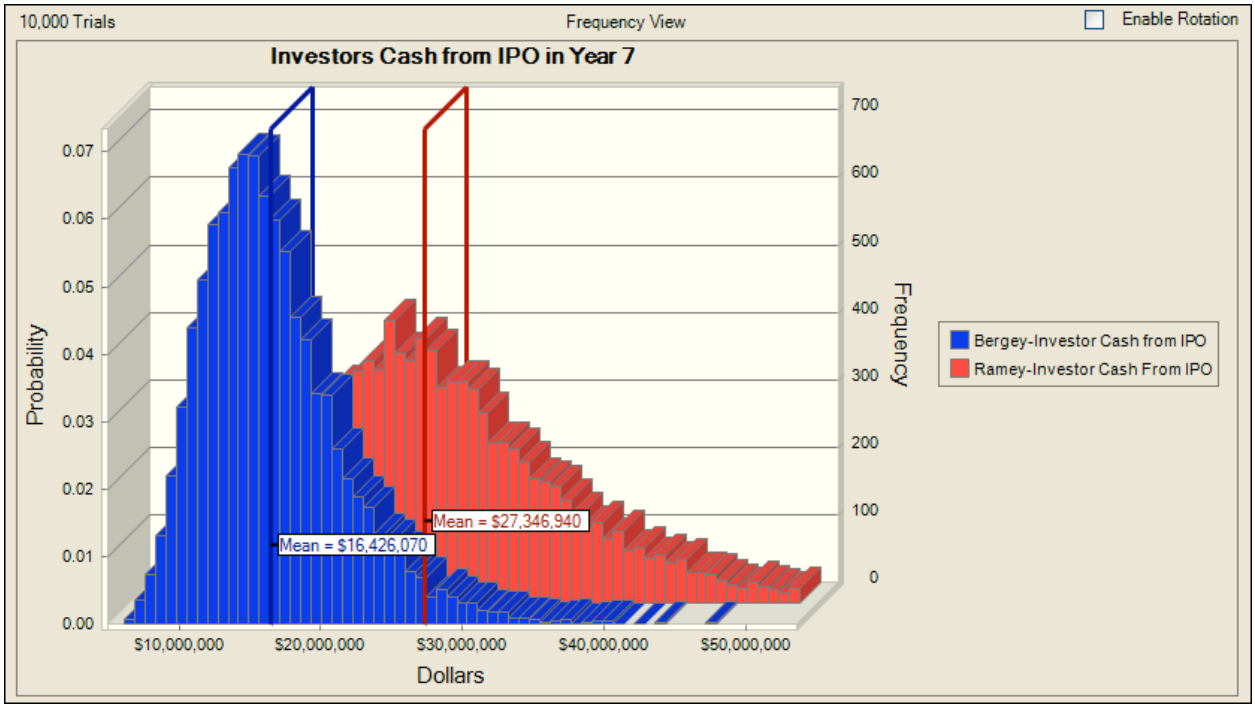

Our model comparison would not be complete without addressing the baseline metric proposed in Ramey [4], which used IRR as the investor's performance metric. Thus, we also reconstructed the IRR model using the published baseline assumptions and then performed a sensitivity analysis upon the IRR metric by applying perturbations of +/- 10% to the input parameters of the model. Figure 4 shows the results of the sensitivity analysis in the form of a tornado diagram. The results clearly indicate that the assumed price of butanol is the single most significant input affecting the project's IRR. Not surprisingly, the variables having the second biggest impact are investor equity (capital gain) and investor contribution (original cash infusion).

Figure 4 – Tornado Sensitivity Chart

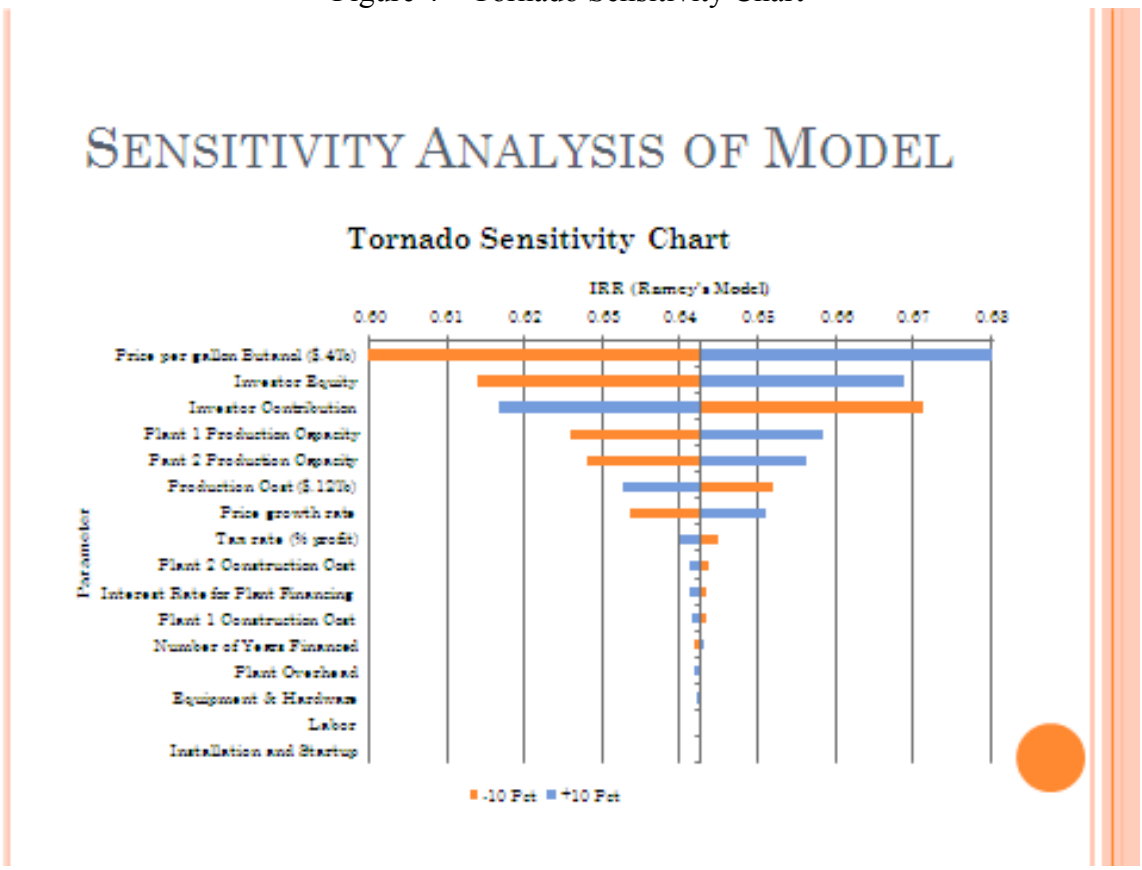

Once again we compare our more conservative estimates for the IRR metric to the assumptions provided in Ramey's model and found an IRR of 41% on an annualized basis versus 54% annualized basis for our replication of Ramey's model. While the former is not as impressive as the latter, either set of assumptions show a substantial return on investment. See Figure 5.

Figure 5 - Overlay of IRR for Ramey's Baseline Assumptions vs. our Parameter Estimates

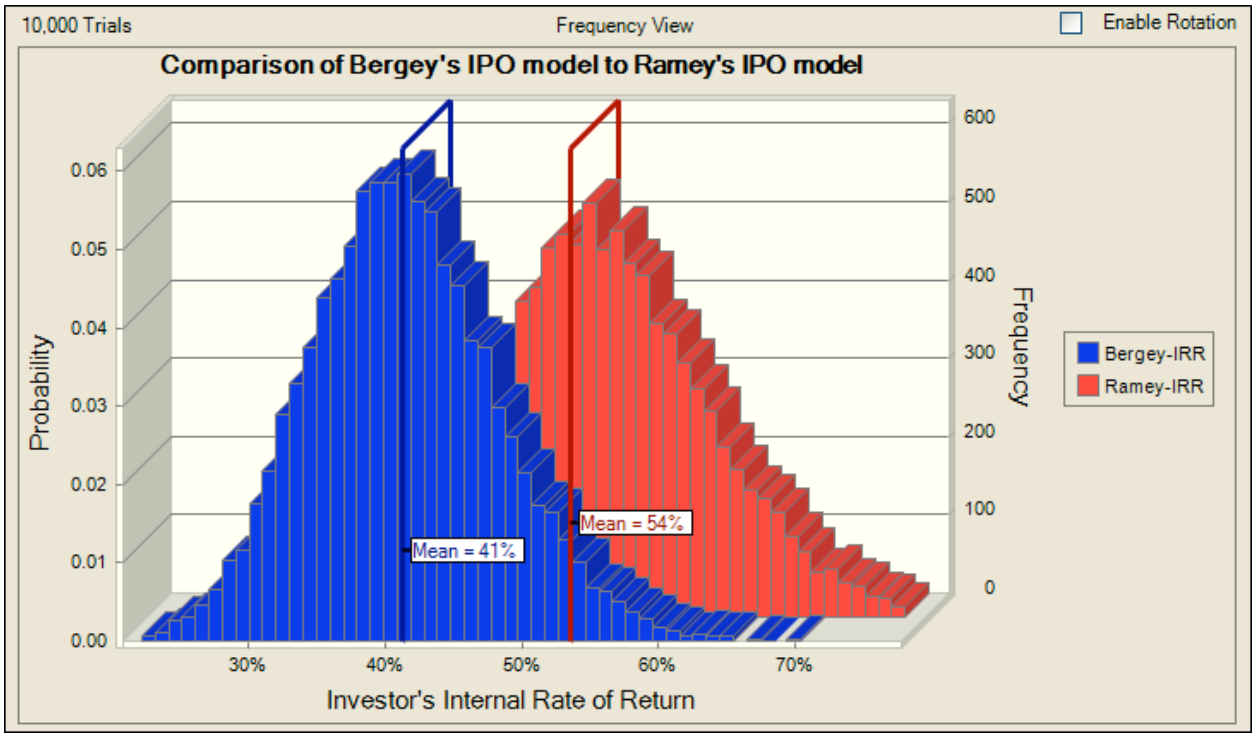

Investigating Policy Changes to the Blend Wall Limits

Using recent historical data that we have collected from the Reuters commodity trading system, we have analyzed the price levels and spreads between ethanol and conventional gasoline. Figure 6 shows the average weekly spot price levels for ethanol, conventional gasoline, and reformulated gasoline (approximately 10% ethanol, 90% conventional gasoline).

Figure 6 – Wholesale Fuel Prices

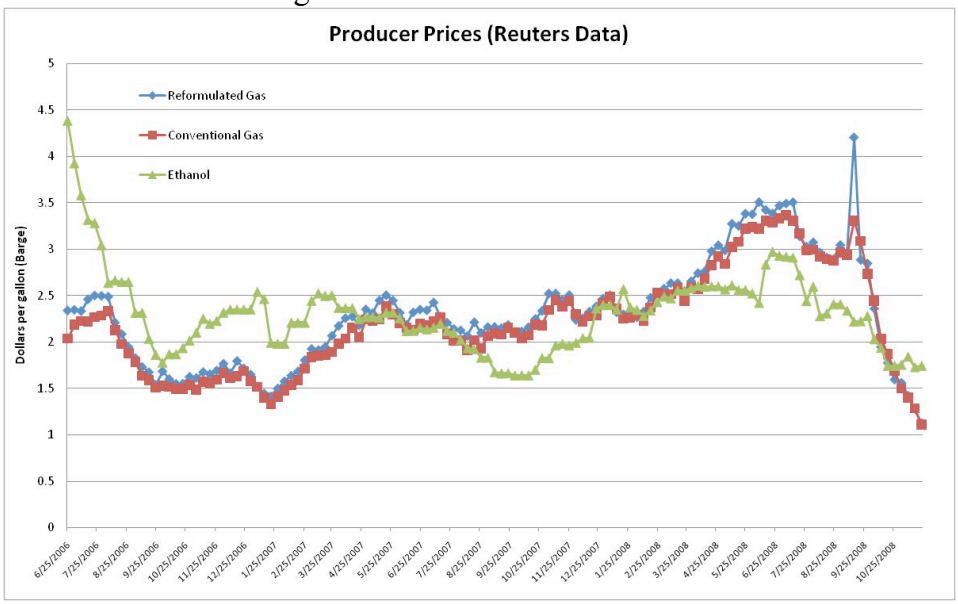

We use ethanol price levels and correlations as a proxy for other biofuels such as butanol. We calibrated our simulation model to provide an estimate for a free market equilibrium price of butanol that is consistent with the current policy mandate of 10% oxegenates (ethanol, MTBE, or Butanol). We then used the calibrated simulation to examine policy changes such as a movement of the blend wall for reformulated gasoline beyond 10% oxegenates. Because ethanol blends beyond 10% require modification to automobile engines and fuel distribution infrastructure, butanol blends offer a practical solution to extend the blend wall limit for reformulated gasoline beyond its current level of 10%. The result would be an immediate demand for butanol in the fuel oxegenate market, which results in a cleaner burning fuel with higher fuel density and oxygen content than lower blends.

The simulation model can also be used to forecast an expected free market price for Butanol that would support the new demand created by the movement in the blend wall. The inferred market price is based upon the simulation model's calibration to historical market pricing data. Figure 7 shows the historical price correlations for the data provided in Figure 6. The correlations shown are Spearman correlations that allow for non-linear relationships rather than the more typical Pearson correlation which assumes only a linear relashionship between the variable pair.

Figure 7 – Variable Price Correlations

PRICE CORRELATIONS

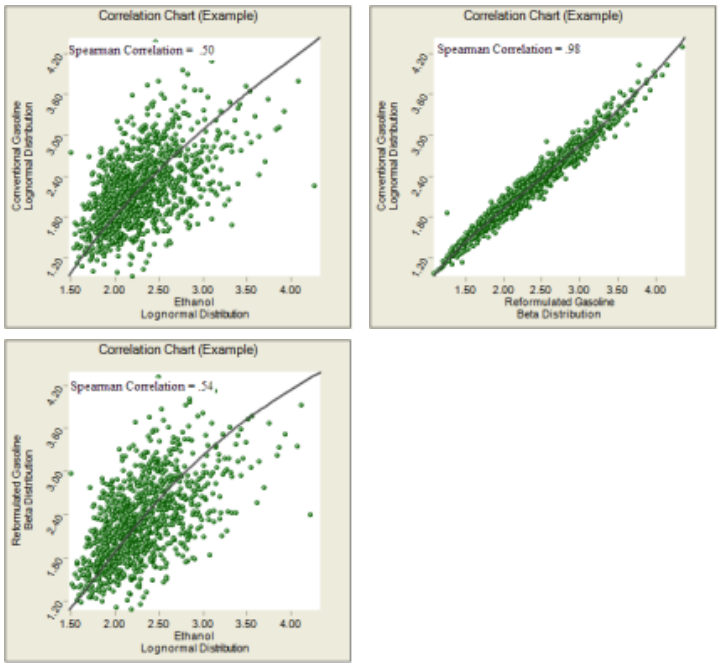

Carbon Emissions Model

$/ton 18.5 Free Market Carbon Price

We are interested in movements of the blend wall for reformulated gasoline because it represents a gallon for gallon displacement of conventional gasoline derived from imported foreign oil with a gallon of domestically produced environmentally friendly bio-fuel with a reduced global carbon footprint. If made to be cost effective, it would represent a Pareto move with regard to environmental policy, national security policy and economic policy. Therefore, our cost estimation method is based upon the displacement volume of conventional gasoline with biofuels and the corresponding reduction in carbon footprint of the target biofuel as determined by the GREET model for life cycle analysis of carbon emissions, the government standard for carbon footprint analysis [5]. Our preliminary model shows that a policy change moving the blend wall for reformulated gasoline from 10% (ethanol) to 20% (10% ethanol, 10% butanol), would displace approximately 11 billion gallons of conventional gasoline and result in a **reduction of 3.6 to 14.3 million tons of greenhouse gas emissions per year**. The expected costs of this change would be a price spread of approximately 23% between conventional gasoline and the biofuel alternatives, reflecting a free market price of mitigated carbon emissions of approximately $18.5 per ton CO_2. See Figure 8.

Figure 8 – Carbon Pricing, Butanol Production, & Energy Policy

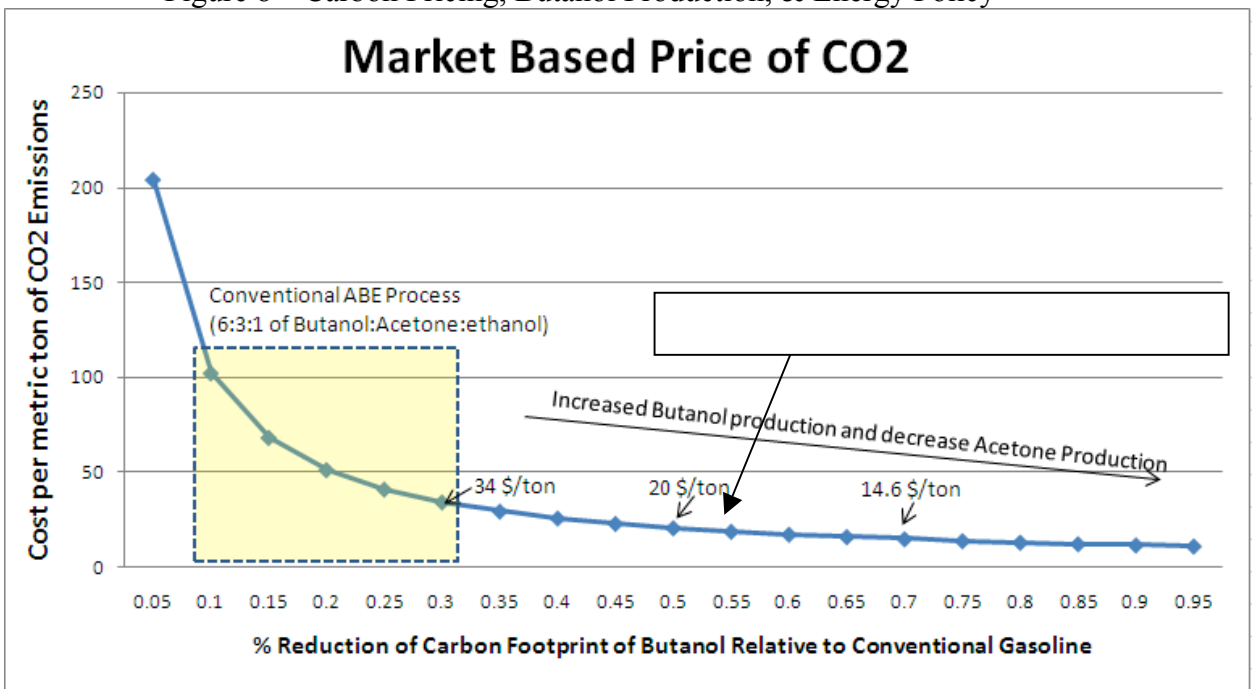

Figure 8 shows that the free market price for carbon calculated as gallon for gallon displacement of conventional gasoline with butanol is highly dependent upon the production process employed to create the butanol. ABE fermentation is a process that is well known and heavily studied for producing butanol, acetone, and ethanol in proportions of approximately 6:3:1 respectively [5]. In the best case scenario, the cost of carbon for a gallon of conventional gasoline displaced by butanol produced from the ABE process could be as little as 34.00 $/ton. In the worst case scenario, the cost of carbon for the same gallon could be as much as 100.00 $/ton. The obvious question to us was, 'how do we move down the curve using economics to guide the science?' Our economic model suggests that the profitability of our bioreactor process is significantly

improved if the production ratio is adjusted in favor of biobutanol production and simultaneously less favorable toward acetone production. We believe that this can be accomplished using genetically modified microbial enzymes potentially derived from the rumen of cow stomach.

Creating and/or Saving Jobs

Revitalizing the labor market has become a pressing national priority. Using data from the first edition of the Biomass Energy Databook [1] and the most recent issue of the Transportation Energy Data Book [2], we have constructed a preliminary model for estimating the number of new plant jobs created (first order effects) and the number of supply chain jobs supported by the startup (or conversion) of a corn ethanol plant to a biobutanol plant (second order effects). See Figure 9.

Figure 9 – Influence Diagram for Butanol Jobs

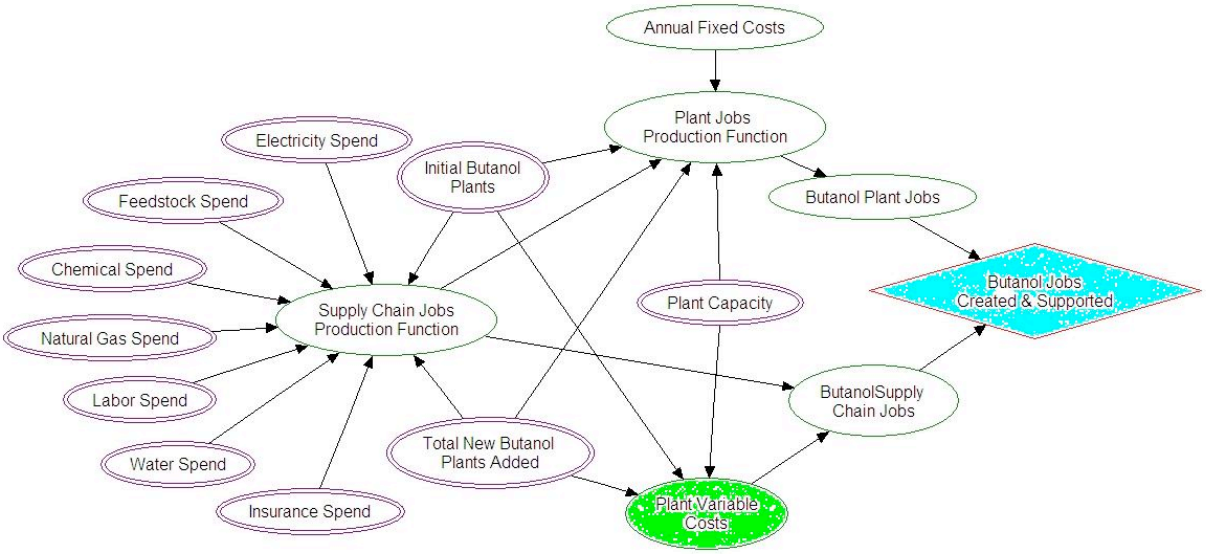

Our model shows that a movement of the blend wall in reformulated gasoline from 10% (ethanol) to 12.35% (10% ethanol, 2.35% butanol), could be achieved by retrofitting the 24 idle ethanol plants taken out of service in the first three months of 2009 (2 billion gallons per year capacity), which would **save between 135,000 to 142,000 supply chain jobs and create an estimated 8,000 new butanol plant jobs**, while simultaneously serving our environment and reducing our dependency on foreign oil.

Future work

Despite its long history and the many favorable characteristics of biobutanol, it has remained a relatively obscure alternative transportation fuel. Only recently has it been recognized by federal and state funding agencies as an "advanced biofuel" which has the potential to meet the many domestic needs of our economy [6]. Considerable funding has been made available to perform basic and applied research to meet the growing energy demand in the US. The results achieved with the American Recovery and Reinvestment Act (ARRA) funding are assessed according to the following performance metrics: 1) Jobs created. 2) Energy saved. 3) Renewable energy installed capacity and generated. 4) GHG emissions reduced. 5) Energy cost savings. 6) Funds leveraged [7].

The work presented herein represents an initial attempt to independently model three of the key performance metrics by which future projects of this genre will be judged. Clearly, the individual objectives have some level of inter-dependence which would be meaningful to include in future models. As we move forward in our modeling work, we will continue to refine our existing models and attempt to quantify the inter-dependencies that will arise under various policy decision scenarios. Figure 10 shows an example of the nature of dependence among the variables and objectives we have discussed in this report.

Figure 10 – Integrated Model Inter-dependencies

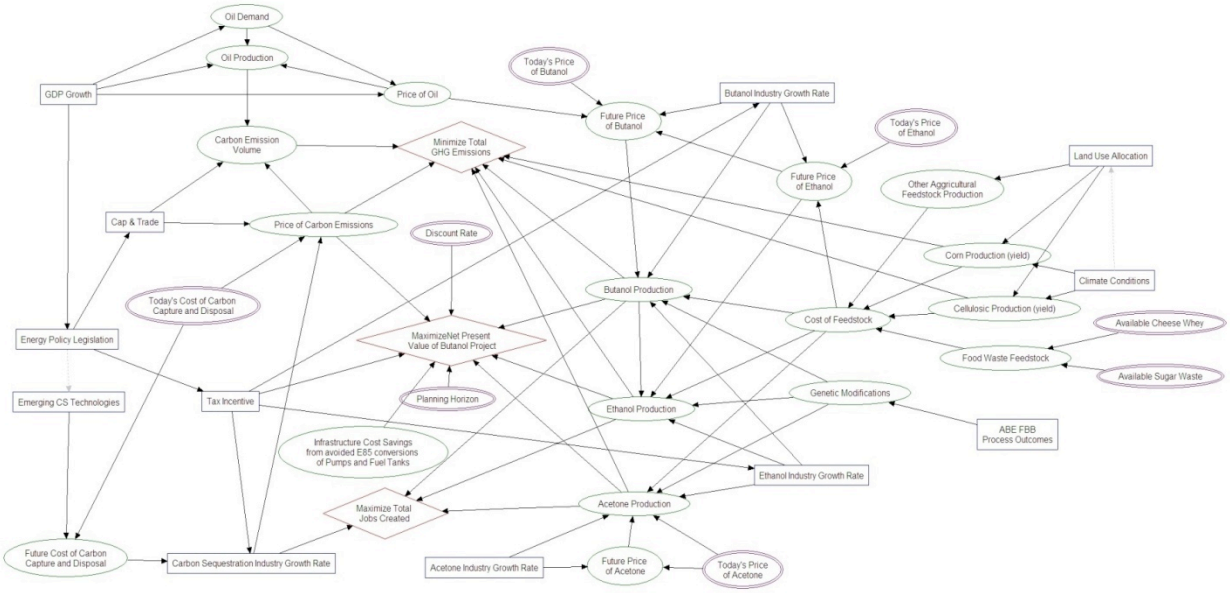

References

[1] Davis, Stacey, C., Nguyen, Tien, Biomass Energy Databook, Edition 1, 2008. US Department of Energy, Oak Ridge National Laboratory. Available at: cta.ornl.gov/bedb.
[2] Davis, Stacey, C., Diegel, Susan, W., Boundy, Robert, G., Transportation Energy Data Book: Edition 28. Oak Ridge National Laboratory – ORNL-5198. 2009.
[3] Matos, Stelvia, and Hall, Jeremy, "Integrating sustainable development in the supply chain: The case of life cycle assessment in oil and gas and agricultural biotechnology" *Journal of Operations Management,* 25 pp1083-1102, 2007.
[4] Ramey, D., Yang, S., "Production of Butyric Acid and Butanol from Biomass," Department of Energy Final Report: Contract No.: DE-F-G02-00ER86106, 2004.
[5] Wu, M., Wang, M., Liu, J. and Huo H., "Life-Cycle Assessment of Corn-Based Butanol as a Potential Transportation Fuel," This report is available at http://www.osti.gov/bridge.
ANL/ESD/07-10, November, 2007.
[6]Demonstration of Integrated Biorefinery Operations, Funding Opportunity Announcement Number: DE-PS36-09GO99038, Announcement Type: Modification 005, CFDA Number: 81.087, Renewable Energy Research and Development, Issue Date: pp. 22. December 22, 2008.

[7]U. S. Department of Energy, National Energy Technology Laboratory, "State Energy Program (SEP) PY 2009 Formula Award Funding Opportunity Announcement," Funding Opportunity Number: DE-FOA-0000073, Announcement Type: Initial, CFDA Number: 81.041, State Energy Program pp. 26. 4/14/2009.

Task 2.2 Renewable Integration into Power Grid---Wind Forecasting

Five Minutes to Four-Hours Ahead Forecast using PJM Wind Farm

Tulane Energy Institute

August 10, 2012

1 Introduction

2 Notations

$t = 1, 2, 3, \ldots$	5 min time intervals
p_t	observed power at time t
$\hat{p}_t$	forecasted power for time t
$\Delta p_t = p_t - p_{t-1}$	first difference
$\Delta\Delta p_t = \Delta p_t - \Delta p_{t-1}$	second difference
$TV_t = \sum_{k=0}^{(n\_regime-1)} \lvert\Delta p_{t-k}\rvert$	total variation of p_t in $[t - n\_regime, t]$
n_regime	positive integer
$RTV_t = \frac{TV_t}{\max \lvert p_t - p_\tau \rvert}$	relative total variation of p_t in $[t - n\_regime, t]$
$RMSE = \sqrt{\frac{1}{N}\sum_{t=1}^{N}\left(\frac{\hat{p}_t - p_t}{P}\right)^2}$	root mean square error

3 Correlations between p_t, p_{t-1}, Δp_t, Δp_{t-1}, TV_{t-1}, RTV_{t-1}

Our first task was to conduct a review of the power production times series p_t, its Fourier transform, and correlations between power production p_t at time t and previously observed power productions. We performed some of the transformations in our proposed decomposition method. We checked a few of the wind farms provided, but show only the preliminary results from *F022_act* wind farm, *11_GenMW.m05.ipl.act* data set.

We applied the Fourier transform which is the first step of the decomposition methods developed on the California ISO data, but observed no periodic daily component in the PJM power

production data. The Fourier Transform plots are shown in Fig. 3.1. As one can see, the data are quite "noisy", with no oscillations. Thus we found little opportunity to extract a periodic component from the time series of power production at these farms. We believe that location plays a significant role in periodic behavior of wind speed. Since the wind power plants associated with CAISO are located near the ocean, the wind speed there experiences daily oscillations while wind power at PJM' wind farms does not.

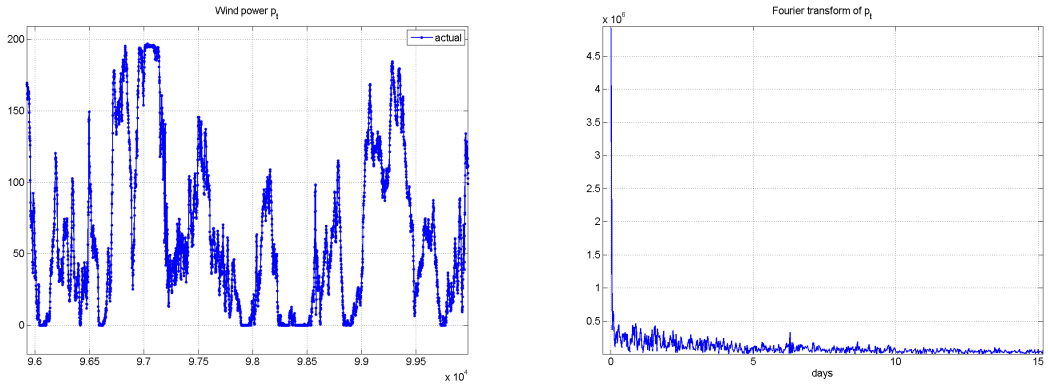

Figure 3.1: Power production p_t (left plot) and its Fourier Transform (right) shows no periodic component.

Next we performed an Autocorrelation Function (ACF) and Partial Autocorrelation Function (PACF) plots. The ACF and PACF, shown in Fig. 3.2, suggest that the time series can be modeled as AR(2) process, second order Markov Chain (MC), or hidden MC. It is worth mentioning that the CAISO wind power production model involves AR(10) process which seems to be in agreement with AR(2) model for the PJM's wind farms since CAISO data are 1 min data. Performance of these models, mentioned above, will be reviewed in details in the following sections.

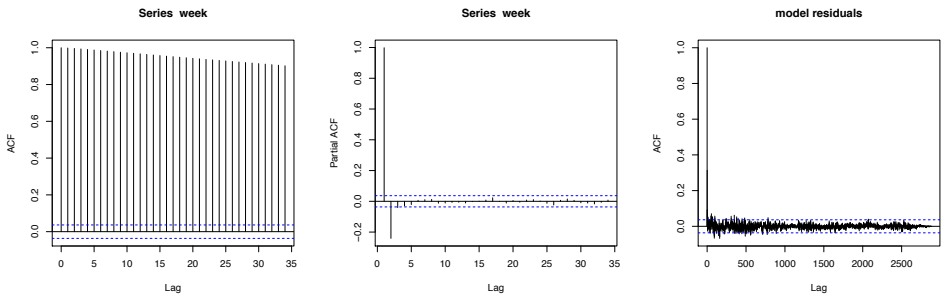

Figure 3.2: ACF of p_t (left plot), PACF of p_t (middle), and AR(2) model residuals (right).

In Fig. 3.3 (left) we note that there are relatively strong correlations between Δp_t and Δp_{t-1}. These correlations allow us to model the power series as a 1st order MC based on Δp_t.

In contrast, simply using the 1st order MC model for p_t, does not model the process well. This result is in agreement with the scatterplot shown in Fig. 3.4, right plot. Thus, we have found that the dynamics of the system is rather defined by Δp_{t-1}, but not by the power production p_{t-1} itself. Correlation between Δp_t and p_t happen to be insignificant, see Fig. 3.4, left scatterplot.

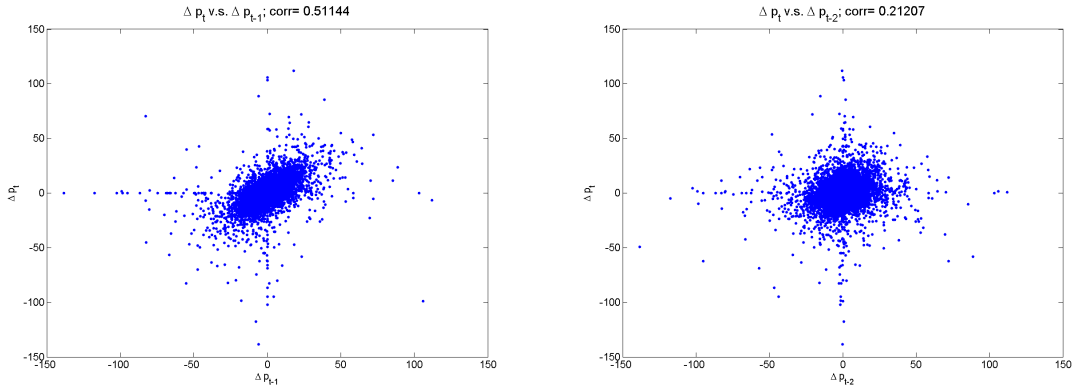

Figure 3.3: Correlations between Δp_t and Δp_{t-1}, Δp_{t-2}.

2nd order MC based on p_t will surely improve the model but it rather equivalent to 1st order MC based on Δp_t in this case. We would prefer lower order MC whenever possible since the number of states significantly impacts the computational complexity.

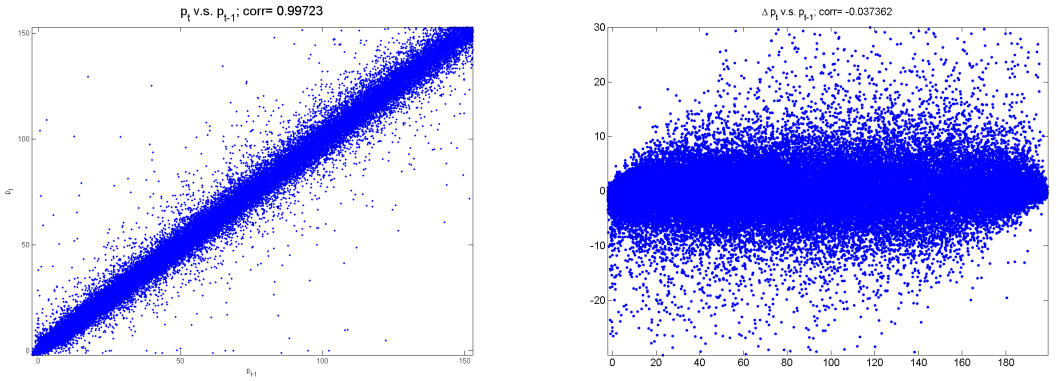

Figure 3.4: Correlations between p_t and p_{t-1} (left scatterplot) and correlations between Δp_t and p_{t-1} (right scatterplot).

In order to improve the model based on Δp_t we will have to go for the 2nd order MC or a sort of hidden MC. Important correlations are shown in Fig. 3.5. Based on these correlations we can try to improve the 1st order MC based Δp_t by introducing hidden states. We observe that the variance of Δp_t depends on the relative total variation defined as follows

$$RTV_t = \begin{cases} \frac{\sum_{k=0}^{(n\_regime-1)} |\Delta p_{t-k}|}{\max |p_t - p_\tau|} & \text{if } \max |p_t - p_\tau| > 0 \\ 0 & \text{if } \max |p_t - p_\tau| = 0 \end{cases} \tag{3.1}$$

where n_regime is a fixed positive integer. We choose 4–10 in the tests. RTV_t describes a stability of the wind power at time t, i.e. counts a number of "oscillations" over the interval $[t - n\_regime, t]$.

4 Persistence Forecasting

From the correlations shown in Fig 3.4, left scatterplot, one can expect that persistent forecasting, i.e. prediction based on the assumption that wind power would stay constant for the next few minutes and even hours

$$\hat{p}_{t+1} = p_t, \tag{4.1}$$

could be a relatively accurate model for few hours ahead horizons. It definitely cannot be beaten by a global model such as Numerical Weather Prediction (NWP) model but can be improved by statistical forecasting which is based on the past wind power observations. Results for the persistence forecasting are shown in grey in the Figures. In the following sections we will try to improve on this simplistic model.

5 Autoregressive Moving Average Model

In this section we construct an Autoregressive Moving Average (ARMA) and Generalized Autoregressive Conditional Heteroskedasticity (GARCH) models for the wind power time series.

Based on ACF and PACF plots (see Fig. 3.2) we choose AR(p) with $p = 2$. The order p and number of days into past used to estimate the model parameters can be empirically optimized in a rigorous way. It, however, will probably not decrease the error significantly but needs to be done in case we decide to work within this particular class of models. We can see that the AR model improves the persistence forecast, the plots are shown in Fig. 5.1. Actual power is plotted in blue, forecasted power is plotted in red.

The performance is evaluated based on Root Mean Square Error (RMSE), defined as

$$RMSE = \sqrt{\frac{1}{N} \sum_{t=1}^{N} \left(\frac{\hat{p}_t - p_t}{P} \right)^2}, \tag{5.1}$$

where P denotes the total capacity of the system; we use historical maximum. N is the total number of wind power observations. RMSE for the AR(2) model is found to be 10.17–10.36% (see Talbe 11.1). The residuals of the AR model are independent, see Fig. 3.2 (right plot), however, they do not seem to be normally distributed. In order to adequately model variance, we construct GARCH model. Results for AR(2)-GARCH(1,1) model are shown in Fig. 5.2, the RMSE is found to be 10.37% (Talbe 11.1), i.e. the model does not improve AR(2). These values can be improved by appropriate adjustments of the model parameters such as order of the model, traning period, appropriate transormations, but one probably cannot expect further significant decrease of the error based on this class of models.

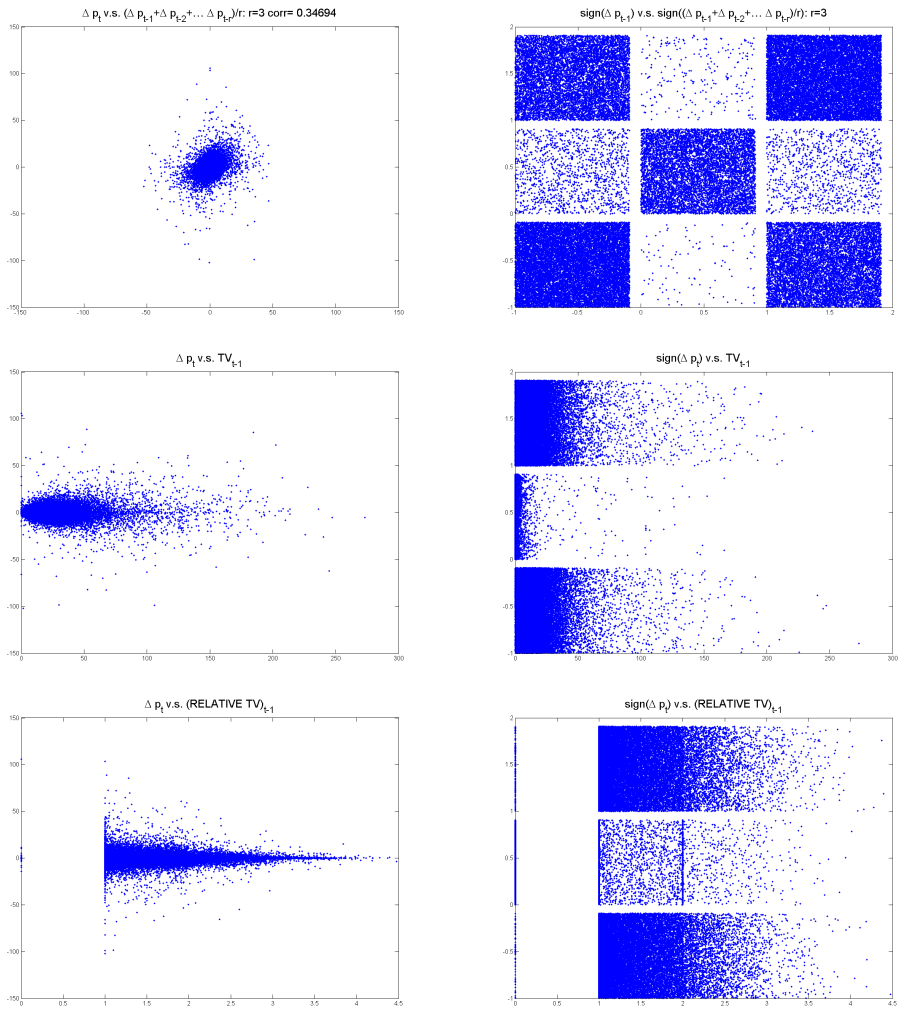

Figure 3.5: Correlations between Δp_t and $(\Delta p_{t-1}+\Delta p_{t-2}+\Delta p_{t-3})/3$, TV_{t-1}, RTV_{t-1} and correlations between the corresponding signs.

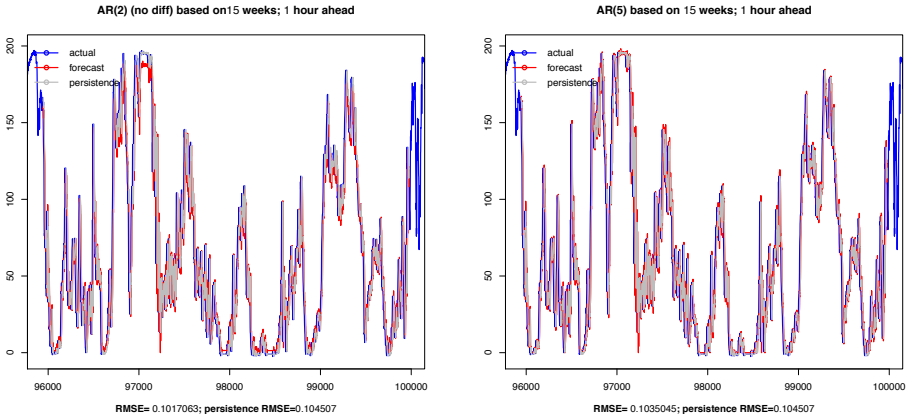

Figure 5.1: AR(2) based on p_t (left plot) and AR(2) based on Δp_t (right plot), i.e. differenced time series. 15 weeks of training period is used. Actual power is plotted in blue, forecasted power is plotted in red.

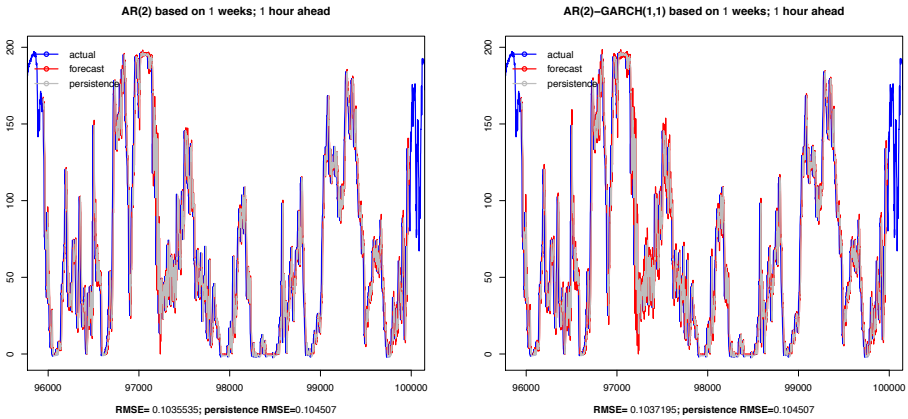

Figure 5.2: AR(2) (left plot) and GARCH (right plot) based on Δp_t. Training period is 1 week. Actual power is plotted in blue, forecasted power is plotted in red.

6 Mycielski Algorithm

Here we consider Mycielski Algorithm for forecasting wind power. The algorithm is sort of naive but quite popular in certain areas, in particularly, it has been applied to wind speed forecasting according to literature. The algorithm searches for the longest repeating sequence in the past, then the observed value in the past, right after the repeating sequence, is assigned as the forecasted value of wind power. The result is shown in Fig. 6.1. RMSE is 16.66% which is significanly larger than for other models. The algorithm does not beat the persistence forecast. The reason is that we are experiencing a problem of overfitting here and do not capture stochastical behavour of time series, similarly as higher order Markov Chain would not be able to adequately represent statistical properties.

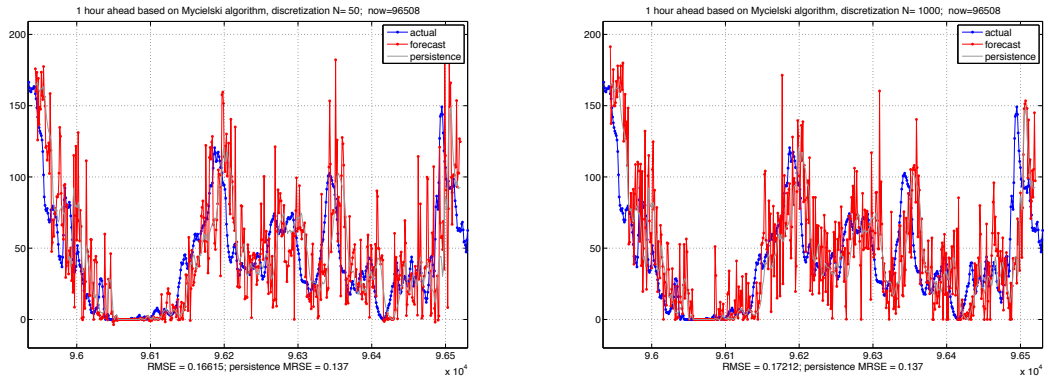

Figure 6.1: Mycielski Algorithm based on p_t discretization $N = 50$ and 1000. Observed power is plotted in blue, forecasted power is plotted in red.

7 1st Order Markov Chain

Markov Chain (MC), especially of second order, seems to perform quite reasonably. 1st order MC constructed for p_t, however, does not model the process well. It is not surprising since, as it can be seen in Fig. 3.4 (right scatterplot), there is almost no correlation between change of power $\Delta p_{t+1} = p_{t+1} - p_t$ and observed power p_t on the previous step. The results for 1st order MC based on p_t are shown in Fig. 7.1 (left plot). The model does not "know" what is going to happen next based on current state p_t only.

However, 1st order MC applied to differenced time series, i.e. to Δp_t, performs much better (see Fig. 7.1, right plot). This result is expected due to the correlations between p_{t+1} and p_t, which are shown in Fig. 3.3. In addition, we have found that nonuniform discretization in accordance with distribution of Δp_t helps improve the result. All results, presented below for the 1st, 2nd order and Hidden MC, are performed on nonuniform grid. Results, based on 1st order MC with nonuniform discretization for 1 step ahead (5 min ahead) forecast are shown in Fig. 7.2. Actual power production is shown in blue, forecst is shown in red.

8

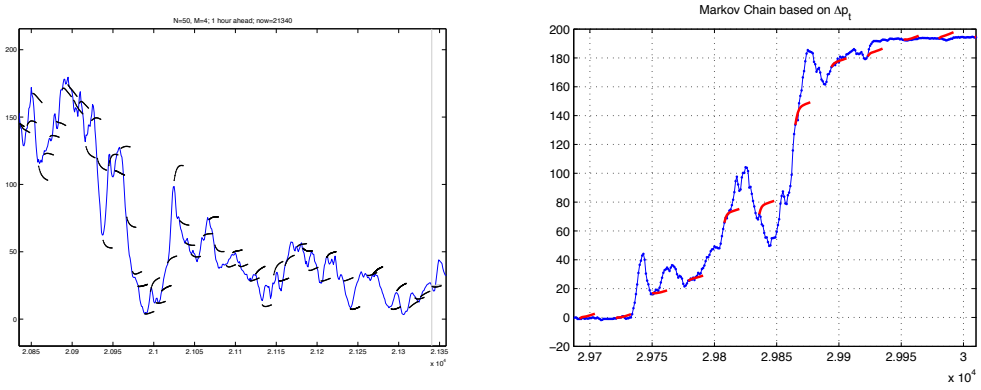

Figure 7.1: 1st order MC based on p_t (left plot) and MC based n Δp_t (right plot); up to 1 hour ahead forecasts.

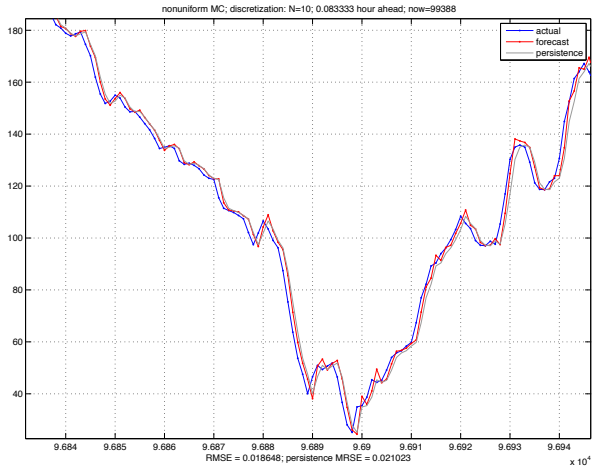

Figure 7.2: 1st order MC based on Δp_t with nonuniform discretization, 5 min ahead forecasts. Observed power is shown in blue, forecast is shown in red.

8 2nd Order Markov Chain

In this section we present results based on 2nd order MC. In the the 2nd order MC the state is characterized with two previous observations Δp_{t-1} and Δp_{t-2}. This model performs quite well, but it is more computationally expensive. If the number of discretization of Δp_t is N, then the transition matrix for the 2nd order becomes N^2 by N^2.

The results for the 2nd order MC are shown in Fig. 8.1. Observed power is shown in blue, forecst is shown in red. Discretization is nonuniform, number of nodes for Δp_{t-1} is $N = 100$ and for Δp_{t-1} is $M = 10$. We have found that accuracy of discretization on the previous step $t - 1$ is more significant for the overall performance. The error RMSE is found to be 10.297% for the 2nd order MC. Also see Table 11.1.

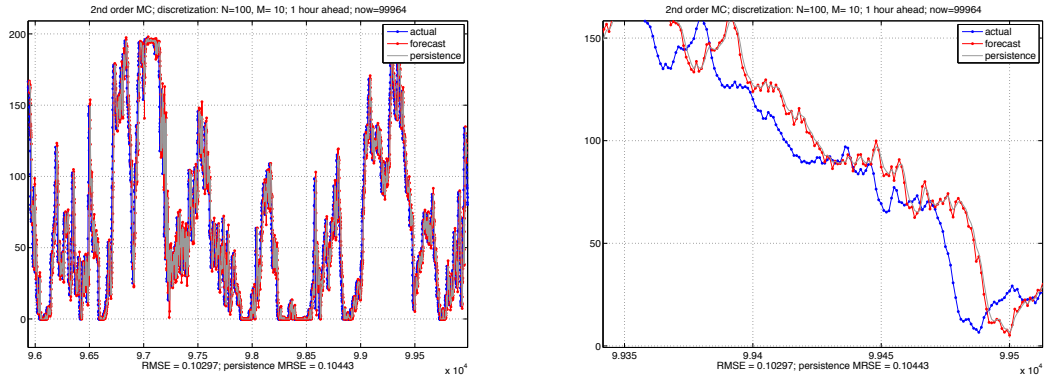

Figure 8.1: 2nd order MC based on Δp_t; 1 hour ahead forecasts, discretization $N = 100$ and $M = 10$. Observed power is shown in blue, forecast is shown in red.

9 Hidden Markov Chain

In order to improve the model, hopefully without going for the 2nd order MC, we have to find some other characteristics which may effect the correlations. First of all, we have modeled the process as nonhomogeneous MC with periodic transition matrix. This model does not improve the performance. This result is, however, expected since there is no daily component observed for wind farms affiliated with PJM, see Fourier Transform in Fig. 3.1 (right plot).

Another hidden harachteristic, which can be implemented in the modeling, is Total Variation and also Relative Total Variation, RTV_t, defined in (3.1). We see in Fig. 3.5 (fifth plot) that variance of Δp_t depends on relative total variation RTV_{t-1} at the previous stage. The relative total variation in this context describes stability of the wind flow. In the case when the wind flow is stable we may predict wind power production with less uncertainty. The results are shown in Fig. 10.1. Hidden MC forecast is plotted in red, actual wind power plotted in blue, black curves correspond to the forecasts used by PJM. The RMSE for blind tests with 14 scan period based on Hidden MC found to be 10.313%, see Table 11.1.

10 Hidden Markov Chain v.s. PJM's forecasts

In this section we briefly compare Hidden MC with the forecasts used by PJM. The 5 min–320 min forecasts, that are based on Hidden MC, are shown in Fig. 10.1 (plotted in red). Black curves correspond to the PJM's forecasts, blue curves are the actual observations. It can be seen that the Hidden MC model is preered up to 3–4 hours ahead, while PJM's forecasting results are better starting form approximetely 6–7 hours horizons. Thsese results are expected since statististical models perform well only for the short term prediction. The results of MRSE for the blind test for the sample of 14 days scan, similar to the Fig. 10.1, are summarized in the Table 10.1.

Table 10.1: Comparison of RMSE of Hidden MC and PJM's current forecasts for 5–350 min horizons.

	5 min	10 min	20 min	40 min	80 min	160 min	240 min	320 min	350 min
PJM Current	21.41%	21.61%	21.97%	22.54%	23.30%	23.84%	24.09%	24.46%	24.59%
Hidden MC	1.77%	3.34%	5.57%	8.31%	12.21%	17.18%	20.49%	24.10%	25.39%

11 Summary

In this section we summarize the results to date. The 1 hour ahead forecasting results, based on Persistence forecasting, AR and GARCH models, Mycielski algorithm, 1st and 2nd order MC, Hidden MC, and PJM's forecasting results are presented in the Table 11.1.

We can see from the table that best models are AR(2) based on 15 weeks of training period ($MRSE \approx 10.17\%$), 2nd order MC based on Δp_t, Δp_{t-1} ($MRSE \approx 10.30\%$), and finally Hidden MC based on ($MRSE \approx 10.31\%$) and hidden states associated with stability of wind, RTV_{t-1}, with discretization $N = 100$, $M = 6$, $n\_regime = 6$. Let's point out that Hidden MC is one of the most attractive models here since the sample space is $N \cdot M = 600$ dimensional only, thus the model peforms very fast and there seems to be an opportunity to futher improve on this model by introducing additional hidden states or even using the hidden 2nd order MC.

The next step would be to empiricaly find an optimal conditions (within each class of models), such as optimal model order, training period, discretization parameters, possible transformations which help improve the model performance, and then an optimal forecasting algorithm can be chosen. At this point, we expect that the optimal model will provide 1 hour forecasts with MRSE equal to approximately 10.1%–10.3%, which is roughly twice smaller than RMSE of the model currenly used by PJM. Stochastic model for very short term prediction, such as 5 min – 40 min ahead, provides even more significant improvement (see Table 10.1).

12 Appendix

12.1 Correlations, Matlab code

```
clear;
%folder='C:\test';
folder='C:\pjm_data';
```

Task 2.3. Renewable Integration into Power Grid---Capacity Modeling

Summary

One of the greatest challenges to integrating renewable energy resources into power operations is the variability in electricity output from these resources. The electricity system works essentially as a supply chain with a nearly zero tolerance for delay and storage resources that remain very limited despite rapid growth. Yet, because no consistent methodology exists to quantify the capacity contribution and system impact of variable generating resources such as wind and solar, these resources have yet to be effectively evaluated, managed, or compensated. To enable analysis of both renewable and traditional energy sources within the system, we adapt an envelope-based modeling method that is inspired by Network Calculus (NetCal) for deterministic queuing systems from the field of telecommunications engineering. The variability of electricity supply and demand can be described by upper and lower envelopes and their corresponding Legendre conjugates, which not only quantify variability across different time scales, but also characterize the tradeoff between any assigned capacity value and its corresponding Quality-of-Service (QoS) measures of performance. In particular, the QoS measure leads to an intuitive interpretation through storage resources. Envelope modeling leads to the definition of two QoS-based capacity metrics--Guaranteed Capacity and Best-Effort Capacity -- whose conceptual and numerical properties we analyze and compare against existing capacity metrics. For illustration, the proposed methods are applied to data from the California Independent System Operator (CAISO). We also explicitly quantify the capacity contribution (via the notion of Best-Effort Capacity) of wind during peak hours and its negative system impact at night. The same envelope characterization further demonstrates the capacity value of storage resources.

We gratefully acknowledge support from the California Independent System Operator and PJM.

Compared with conventional fossil-fuel-based generators, renewable energy resources represent a potentially lower emissions alternative for electricity generation. Over the last decade, the share of electricity produced from these resources has steadily increased worldwide, largely as a result of government policies promoting their advancement. However, the increased penetration of renewable energy creates unprecedented challenges for system operators and utility companies, mainly because of the intermittent nature of the major renewable resources such as wind and solar. In the absence of subsidies, the costs and engineering concerns associated with these technologies could prevent their deployment.

Unlike conventional sources of electricity, the supply from intermittent renewable resources is highly variable (undependable), inflexible (non-dispatchable), and uncertain (difficult to predict). These undesirable features bring engineering and economic challenges to existing systems. For instance, as a system faces increasing production variability, the overall system baseload drops and the average production cost increases. Further, because renewable suppliers receive subsidies, they can find it profitable to produce even at certain times when negative locational marginal prices indicate that additional power is undesirable.

To deal with these issues of integration, a variety of rules have been formulated across utility systems, ranging from wind curtailment in favor of hydroelectric production to the charging of renewable power producers for extra operating reserves to be maintained on the utility system. However, these rules can appear to be arbitrary and potentially conflicting. The industry lacks a standardized method to assess and manage the impact of intermittent resources on the electric grid. At the core of this problem is the difficulty of properly evaluating the capacity contribution of an intermittent power resource and compensating its producers adequately and fairly. Intermittent renewables are well accepted as valuable energy resources, but their performance as a capacity source has not been convincing.

From an operations research perspective, the electricity systems can be viewed as special supply chain with nearly zero tolerance for delay, negligible storage to buffer supply and demand mismatch, inelastic demand, and extremely high standards for reliability. These special characteristics explain the current emphasis on power (generation and consumption in megawatts, MW) instead of energy (cumulative flows in megawatt-hours, MWh) in the analysis of resource adequacy and system reliability. However, progress in technology, in market design and in operation is making the pattern of power supply and demand over time, thus, energy-oriented characterizations more relevant. Indeed, technological improvement and growing investment in storage, demand response, and smart-grid technologies suggest that storage capability and elasticity in demand are

increasing; that information collection and sharing are growing richer and faster; that control is increasingly effective; and that market actions and reactions are gaining efficiency. In such a context, a comprehensive characterization of electricity supply and demand beyond the power domain is becoming more critical. In particular, to rely on single-valued capacity metrics discards valuable information that can help both market formation and system operation.

In this paper, we develop a new way to model variability and capacity based on the concept of Quality-of-Service (QoS) performance guarantees. Essentially, our modeling methodology is to characterize each type of generating resource in terms of both \textbf{quantity} and \textbf{quality}. The quantity attribute is evaluated based on the amount of power the generating facility can produce. The quality attribute refers to a resource's quality of service (QoS). It describes the match/mismatch pattern between power demand and supply, which is profoundly affected by the variability of a generating resource and by the availability and utilization of supplementary resources including storage and demand response. The notion of QoS reflects a view of capacity as a metric of service rather than of equipment.

Our goal is to contribute to the literature on two fronts. First, on the electricity front, the lack of proper analytical tools to quantify and manage the growing variability in the system has been widely recognized in academia and in industry (observations and conversations during visits to the Federal Energy Regulatory Commission (FERC), National Renewable Energy Laboratory (NREL), Electric Reliability Council of Texas (ERCOT), the California Independent System Operator (CAISO), PJM, and the Sacramento Municipal Utility District (SMUD)). The following two features of the proposed envelope method show the sign of promise in closing this analytical gap: (i) in its very nature, the envelope method represents a worst-case analysis perspective, which works very well with the ultra-high reliability standards in the electricity system; (ii) the envelope method can cover constant (e.g. geothermal) and variable generating resources (e.g. wind), load, and supplementary resources including storage and demand response in a unified way, which enables a systematic treatment of renewable integration. In particular, through envelope modeling, variability is captured at every time scale and reveals the trade-off between capacity and QoS performance. The latter directly links variability modeling to capacity evaluation. To our knowledge, this approach has not before appeared in electricity literature.

Second, on the Operations front, we present envelope method here also as generic modeling tool of variability that may potentially be applied to area beyond electricity. To enhance its relevance, we extend Network Calculus (NetCal) for queuing modeling by untangling the key concepts of upper and lower envelopes from their respective NetCal

application-specific counterparts, arrival and service curves, and applying Legendre transforms to convert variability characterization from the time domain to the conjugate domain. As an immediate benefit of this conversion, non-monotonic flows that are excluded by NetCal are naturally included in the Envelope Modeling framework without extra technical efforts.

The remainder of the report is available at http://ssrn.com/abstract=2271177.

Chapter 3
University Of Louisiana at Lafayette

Task 3: Production of Biofuels from Renewables and Wastes

Summary

As indicated by Professor Boopathy, a large amount of agricultural and forestry residues, as well as municipal waste includes carbohydrates that can be converted into renewable fuels to meet needs of transportation sector. In the USA alone, annual consumption of transportation fuels amounts to around 160 billion gallons of gasoline, 60 billion gallons of diesel, and about 60 billion gallons of aviation fuel. In the USA alone, the US Department of Energy estimates that over 1 billion tons of renewable biomass is available for production of biofuels and it can be used to produce 35-45 billion gallons of lipids. In order to make the production of microbial lipids from carbohydrates commercial, several technological advances need to be made and these include (a) reducing the cost of macro- and micronutrients used in the fermentation media, (b) increasing the lipid yield from carbohydrates to as close as possible to the theoretical maximum of 0.32 g lipids per g glucose equivalent, (c) cultivating the cells to high cell density in order to reduce the cell harvesting costs, (d) enhancing the volumetric productivity of lipids, (e) optimizing recovery of lipids from cells. The goal of biofuels research in this project at the University of Louisiana at Lafayette was to address the first three items listed above. The costs of micronutrients were minimized by identifying the costliest micronutrient and replacing it with low-cost vitamins and those of macronutrients were minimized both by optimizing their levels in shake flasks and by identifying their cellular requirements in high-density cultivations. Lipid yields were enhanced by manipulating the C/N ratios in batch and fed-batch cultivations and high density cultivations were conducted by repeated feeding of nutrients and C-sources in the fermentors. As a result, significant cost reductions could be forecasted for the microbial lipids formed by oleaginous yeast *Lipomyces starkeyi*.

Introduction

For the transportation sector, finding substitutes for petroleum fuels (gasoline, diesel, aviation fuel) using natural and renewable resources is turning out to be quite difficult. This difficulty stems from the high energy density of petroleum fuels and the vast amounts of their consumption. In the USA alone, 60 billion gallons of diesel oil, 138 billion gallons of gasoline, and 24 billion gallons of jet fuel were consumed in 2008 (USEIA 2010). Although several groups have been focusing on ethanol as a substitute or additive in gasoline, we are focusing on lipids as raw materials for the production of diesel and aviation fuel additives / substitutes. Lipids are produced by several microorganisms (Subramaniam *et al.* 2010), but the UL Lafayette researchers have focused on microbial lipids from the oleaginous yeast *Lipomyces starkeyi* NRRL Y-11557. This yeast strain (also available from several culture collections around the world and identified as NRRL Y-11557, ATCC 58680, CBS 1807, CCRC 21522, DSM 70295,

IFO 1289, JCM 5995, NRRL Y-1388, Starkey strain 74) possesses not only an ability to accumulate >65% intracellular lipids, but also has slower rate of re-metabolization of accumulated lipids compared to other cell lines [Holdsworth *et al*. 1988].

Materials and Methods

Lipomyces starkeyi NRRLY-11557 was obtained from National Center for Agricultural Utilization Research, United States Department of Agriculture Laboratory, Agricultural Research Service (USDA, ARS), Peoria, IL, USA. Colonies of *Lipomyces starkeyi* were grown on agar slants at 30°C. The slants were prepared with 3 g/L of malt extract, 2.5 g/L of yeast extract, and 2% agar in deionized water (Uzuka *et al.* 1975). The agar slants were stored in the refrigerator and propagated monthly. Inocula for experiments were prepared by incubating the refrigerated cells on fresh agar slants for 48h at 30°C, followed by two successive cell propagations in liquid media at 30°C, once for 48 h and the second time for 30h.

The composition of the fermentation medium (n(C):n(N) = 61.2) containing glucose was: 30 g/L of glucose, 1 g/L of $(NH_4)_2SO_4$, 1.5 g/L of yeast extract, 2.5 g/L of $Na_2HPO_4 \cdot 7H_2O$, 7 g/L of KH_2PO_4, 0.15 g/L of $MgSO_4 \cdot 7H_2O$, 0.1 g/L of $CaCl_2 \cdot 2H_2O$, 8.2 mg/L of $FeSO_4$, 10 mg/L of $ZnSO_4 \cdot H_2O$, 7 mg/L of $MnSO_4 \cdot H_2O$, 9.41 mg/L of $CoCl_2 \cdot 6H_2O$ and 10 mg/L of $CuSO_4$. In starch medium, 30g/L of glucose were replaced with 27.3 g/L of starch (equivalent to 30g/L of glucose). Different C:N molar ratios were achieved by varying the amount of ammonium sulfate.

Shake flask experiments were carried out in 500-mL baffled flasks containing 125 mL of media. Inoculum level was 4% (by volume). Incubations were done at 30°C and 140 rpm in an orbital shaker. Cultivations were carried out in a controlled-pH 1-litre working volume Multigen Convertible Bench-Top Culture Apparatus Model F-1000 (New Brunswick Scientific Co, Edison, NJ, USA). Aeration rate was 1 vvm. Agitation rate in the bioreactor was 1000 rpm. pH was controlled at 5.5 by the addition of 1 M NaOH solution. High density cultivations were conducted in a discretely-fed New Brunswick Scientific BioFlo 2000 fermentor with working volumes from 3-5 L. During the fed-batch fermentation, complete medium as defined above was added only in the beginning and subsequent feeding involved only the sugar solutions with or without $CaCl_2$. In other words, no other nutrient was added to the system except at time zero.

The cell density was measured as dry mass. Glucose, sucrose and maltose concentrations were measured using HPLC. Starch was analyzed using iodine staining (Bader *et al.* 2006). The lipids were extracted from the centrifuged cells using a modified Bligh and Dyer method (Folch *et al.* 1957), and from the freeze-dried cells using Accelerated Solvent Extractor (ASE300 from Dionex, Sunnyvale CA, USA). In both cases, C13:0 fatty acid was added before extraction as an internal standard. Bligh and Dyer extraction involved chloroform-methanol solvent system. The conditions used for ASE extraction were as follows: volume of extraction cell – 40 mL; solvent system – either hexane or chloroform-methanol mixture; sample size – 2 g of freeze-dried microbial cells with

hexane and 1 g of freeze-dried microbial cells with chloroform-methanol; operating pressure –103.4 bar; oven temperature – 125°C for hexane and 40°C for chloroform-methanol system; cycles – two, each consisting of filling the extraction cell with a solvent, oven heat up time of 6 min, static time of 5 min, purging with nitrogen at 10.34 bar for 60 s, flushing with solvent (60% of cell volumes) followed by nitrogen purge for 60 s. Lipid content in the cells was analyzed by gravimetric analysis following the extraction. Fatty acid content in the lipids was determined by formation and analysis of methyl esters of extracted lipids in a GC-MS. The details of experimental and analytical procedures were reported by Wild *et al.* (2010). Lipid content in the cells was measured also using a fluorescent dye whose interaction with lipids results in shifts in wavelength at which the dye fluoresces.

Results and Discussion

Replacement of yeast extract with biotin, calcium pantothenate, and inositol:

Based on the results of shake-flask experiments, medium costs were calculated to produce one gallon of microbial lipids. These calculations showed that yeast extract and phosphates were the two costliest medium components. Response surface methodology (RSM), a collection of mathematical and statistical techniques useful for developing, improving and optimizing processes, was used to evaluate the relative significance of several factors even in the presence of complex interactions. The main objective of RSM is to determine the optimum operational conditions for the system or to determine a region that satisfies the operating specifications. The RSM technique was utilized here to optimize the lipid production medium to reduce the cost of lipids.

Yeast extract is a complex mixture of vitamins, growth factors, and even nitrogen. Considering the compositions of different yeast extracts, it was decided to focus on biotin, calcium pantothenate, and inositol as yeast extract components to substitute yeast extract in the medium. The Center Composite Design (CCD) procedure was used to design experiments for optimizing the variables. A 2^3 full factorial center composite design was chosen to optimize the components. This design had six star (α) points, six replicates at the center point and eight cube points. According to this design, twenty experiments were performed. The value of α was 1.682, which depends upon the number of variables to be optimized. The experimental results of volumetric lipid content in batch fermentation broths for the above design are listed in Table 1. For each combination of the components, triplicate flasks were used; as control, medium containing yeast extract was used.

A model developed from these data is given in Eq.1. The analysis of variance (ANOVA) for the model revealed that the model is significant, as shown by the F and P values, except for the interaction terms (Table 2).

Table 1. Experimental values of lipid production by response surface central composite design

Biotin (µg/L)	Inositol (µg/L)	Ca Pantothenate	g/L of lipid
1	3000	400	2.04
3	3000	400	2.75
3	1000	400	2.94
3	3000	600	2.50
1	3000	600	2.85
1	1000	600	2.77
2	2000	63.6	2.44
2	318.2	400	2.03
3.68	2000	400	2.51
1	1000	200	2.51
2	2000	400	1.37
2	3682	400	2.46
3	1000	600	2.02
0.32	2000	400	1.95
2	2000	736.4	1.97
2	2000	400	1.37
2	2000	400	1.37
2	2000	400	1.37
2	2000	400	1.37
2	2000	400	1.37

$$\text{Lipid concentration} = 4.936 - 0.804\,X_1 - 0.0023\,X_2 - 0.0033\,X_3 + 0.421X_1^2 - 0.00001\,X_3^2 + 0.00020\,X_1X_2 - 0.0025\,X_1X_3 \quad (1)$$

where X_1 = Biotin (µg/L), X_2 = Inositol (µg/L), X_3 = Calcium Pantothenate (µg/L).

Table 2. ANOVA table of the model parameters of response surface center composite design

Source	DF	Seq SS	Adj SS	Adj MS	F	P
Regression	9	6.175	6.175	0.686	3.07	0.048
Linear	3	0.484	2.131	0.710	3.18	0.072
Square	3	4.617	4.736	1.579	7.06	0.008
Interaction	3	1.074	1.074	0.358	1.6	0.25
Residual Error	10	2.235	2.235	0.223		
Lack-of-Fit	5	2.235	2.235	0.447		
Pure Error	5	0	0	0		
Total	19	8.409				

Response surface plots were created using two variables at a time, maintaining the third variable at fixed levels. Such plots are very helpful in understanding both the main and the interaction effects of the two variables. The maximum predicted yield is indicated by the surface confined in the response surface diagram. The relative effect of biotin and calcium pantothenate with inositol at the center point was plotted and shown in Figure 1.

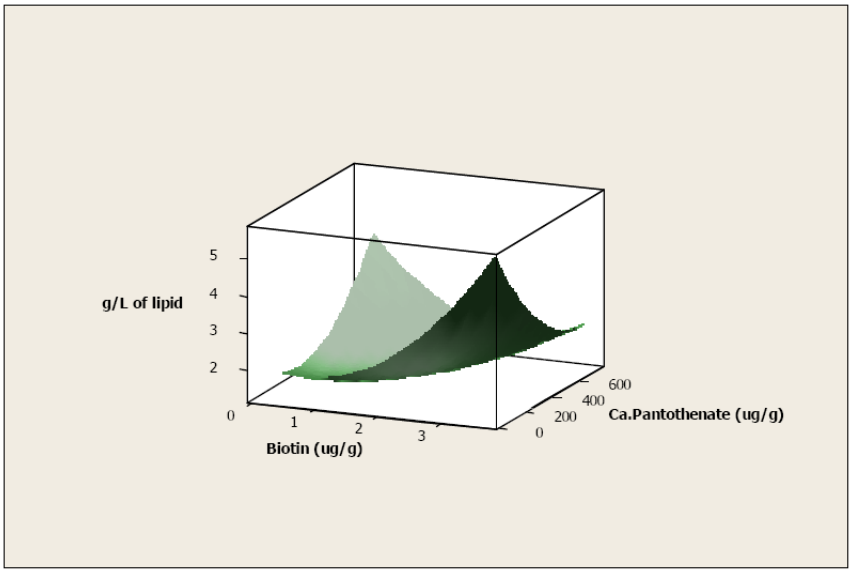

Figure 1.

Similar plot for another combination is shown in Figure 2.

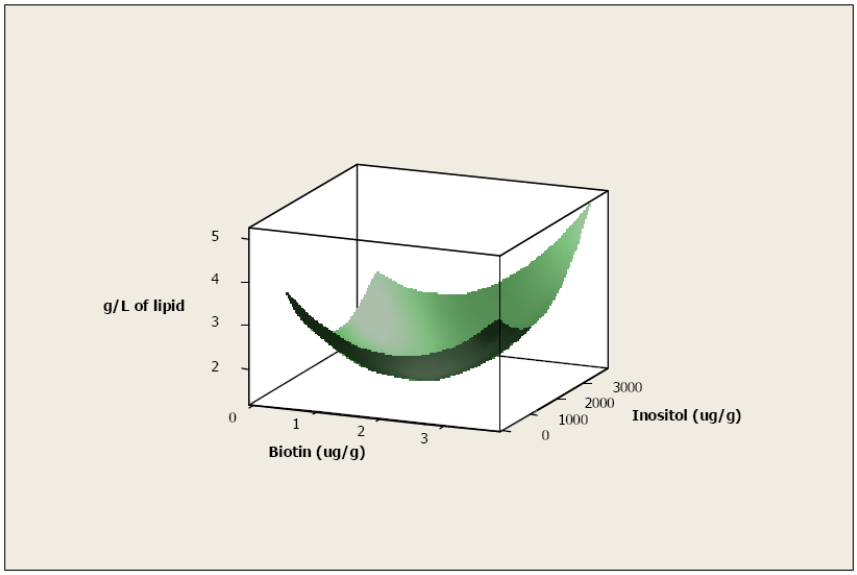

Figure 2

The model (Eq.1) was used to determine optimum concentrations of biotin, inositol, and calcium pantothenate for maximum lipid production, and the optimum values were obtained to be biotin 3.68 µg/L, inositol 3182 µg/L and calciu pantothenate 63.64 µg/L. The predicted maximal lipid production was 6.5 g/L.

Shake flask experiments with the optimized concentrations of biotin, inositol, and calcium pantothenate (in place of yeast extract) were done and the lipid production was observed to be 4.34 g/l. Although this was not as high as the predicted maximum, it was clear that the production could be enhanced by optimizing the medium components. Moreover, this amounts of the three growth factors was same as their amounts in 1.5 g/L yeast extract. Hence, no further optimizations were carried out in shake flasks.

Experiments were then conducted with the optimized values of vitamins as well as with yeast extract in a 5 Liter fermentor (4-L working volume) with controlled pH, temperature and agitation before moving into high density cultivation. The experimentally observed values with yeast extract and with vitamins are given in the Table 3 below. pH in both the cases was controlled at 5.5 by automatic addition of 1N NaOH by a peristaltic pump connected to a pH controller. The temperature in both was controlled at 30^{o}C. In the case of experiment involving yeast extract, the speed of agitation was 400 rpm, where as it was 500 rpm with vitamins. Aeration rate in both the cases was 0.25 vvm. As a result of the low vvm and differences in the rpm, dissolved oxygen concentration in the yeast extract run dipped down to 3-4% after the first 24 hours. This may have been the cause for reduced lipid production (2.93 g/L) in this case. In the experiment with vitamins, the least dissolved oxygen concentration was 66%. In this case, 4.71 g/L lipid production was obtained.

Table 3: Time course of fermentor experiments with yeast extract /or vitamins

	With 1.5 g/L Yeast Extract				With Vitamins			
Sl.No	Time (hr)	Biomass (g/L)	Glucose (g/L)	Lipid (g/L)	Time (hr)	Biomass (g/L)	Glucose (g/L)	Lipid (g/L)
1	0	0.52	29.35	0.00	0	0.24	31.38	0.06
2	8	0.52	30.25	0.02	6	0.08	30.76	0.09
3	14	1.8	33.26	0.02	13	0.26	30.98	0.07
4	19	2.18	29.73	0.05	18	0.42	30.56	0.08
5	24	2.34	31.41	0.14	24	1.14	29.41	0.19
6	30	3.82	27.23	0.27	30	2.62	27.83	0.90
7	36	5.06	22.32	0.47	38	3.36	24.51	1.03
8	42	6.46	15.45	1.73	42	3.76	22.20	0.96
9	48	8.86	6.89	2.76	48	4.82	17.61	1.87
10	49	9.02	6.89	2.93	54	5.98	12.79	2.27
11	56	10.84	3.71	1.60	60	7.08	9.08	3.48
12	60	10.5	3.25	1.21	66	8.04	4.81	4.71
13					72	8.64	3.36	4.01

14		78	8.98	3.28	2.80

DW
Lipids

Optimization of phosphate concentration in broth:

Although phosphate was supplied in the medium in the form of a mixture of KH_2PO_4 and Na_2HPO_4, it was decided to treat total phosphate concentration as a lumped variable and the ratio of KH_2PO_4 and Na_2HPO_4 was kept same as in the original medium. Working in this fashion, the optimization was a single variable optimization and triplicate shake flask experiments were conducted with different phosphate concentrations ranging from 1X (concentration same as in the medium reported under Materials and Methods) to 1/50X. Experiments were done in 500-mL baffled flask with reduced phosphate concentrations (0.1X, 0.067X, 0.05X, 0.033X, 0.025X, and 0.02X of control) to optimize the phosphate concentration. The cell density produced with different concentrations was given in Table 4. The cell mass concentrations did not change much when the phosphate concentration was reduced even by a factor of 50 from its original concentration. All these experiments have been conducted in triplicate and multiple times. Considering the durations of fermentations, it was decided to keep phosphate concentrations at 1/20X.

Table 4. Phosphate optimization

Experiment	Phosphate Concentration (fraction of control)	Cell density (g/L)
Control (1X)	1.0	10.42
1	0.1	9.46
2	0.067	9.80
3	0.050	9.72
4	0.033	9.68
5	0.025	9.49
6	0.020	9.76

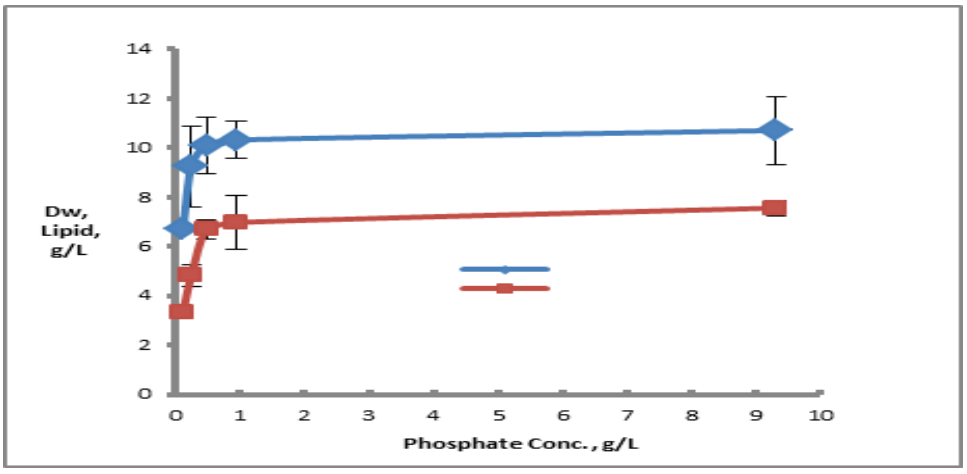

Figure 3

Cultivation of Lipomyces starkeyi in 5-L fermenter with different concentrations of starch:

These experiments were based on the results of RSM optimization ofvitamins to replace the yeast extract from the medium. The experiments were conducted in a 5 Liter fermentor (4-L working volume) with controlled pH, temperature and agitation with the goal of high density cultivation. The results of experiment with 27.3 g/L starch are presented in Figure 4. During these experiments, lipid content in the cells was measured by use of fluorescence dye. The fluorescence measurements were converted into lipid content with the help of calibration curves that were prepared from the samples at the end of the experiments, in which the lipids were extracted from cells using an ACE extractor (methanol/chloroform solvent). Serial dilutions of the end samples were subjected to fluorescence measurements to prepare the calibration curves.

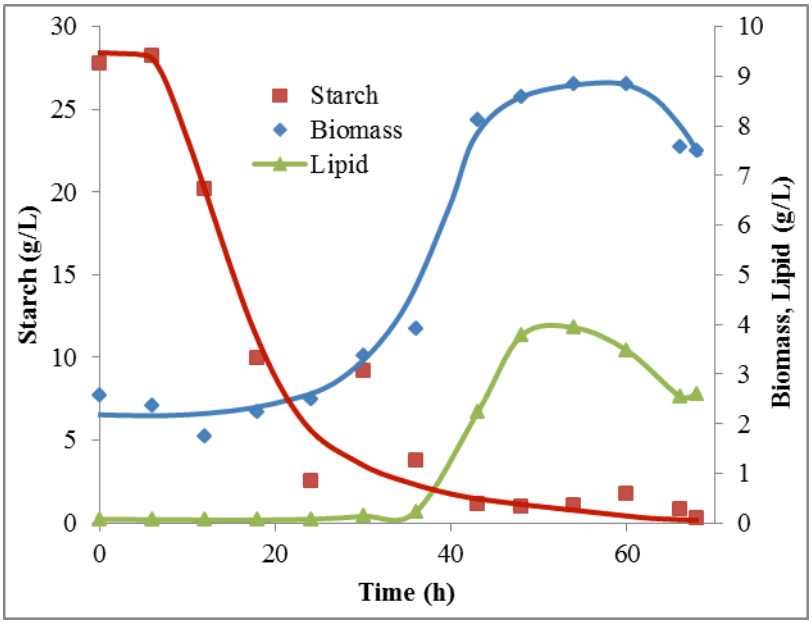

Figure 4: Lipomyces starkeyi growth and lipid production on potato starch (27.3 g/L) in a fermentor (C:N ratio 61.3).

These results show the trends similar to those observed in shake flasks. The maximum lipid content in the cells was 44% at 48-54 hours and then it decreased with the passage of time.

Further experiments were conducted in which starch concentration was increased to enhance the production of cells and, therefore, the production of lipids. Two strategies have been followed in this regard. The first involved increasing all the concentrations in the batch fermentations to provide more nutrients for cell growth and lipid production. The second involved increasing only the concentration of carbon sources while keeping all the other concentrations exactly as before. The rationale for these experiments was (1) to check if the nutrient balance in the broth is optimal for cell growth and lipid production, and (2) to prepare groundwork for fed-batch operation for truly high density fermentations.

Results of an experiment in which starch content was doubled (from 27.27 g/L to 54.54 g/) while retaining the rest of the medium composition are presented in Figure 5. The increase in starch concentration without changing the nutrient levels caused doubling of C:N ratio in broth. The dissolved oxygen concentration remained above 90% saturation during the whole experiment. The total fermentation time increased from 66 hours to 110 hours, but the cell concentration increased to 20 g/L. Lipid concentration on volumetric basis also increased to 14.8 g/L at 90 hours. Lipid was apparently consumed after achieving this peak and reduced to 13 g/L at 110 hours. This experiment demonstrated that N and other nutrients (including biotin, inositol, and Ca-pantathonate) were not limiting the growth of cells even at this high concentration of starch. No starch was analyzable in the broth by iodine measurement method after 40-hours even though major growth and lipid production took place after this time. Apparently, the breakdown products of starch were able to support the cell growth and lipid production. Total carbohydrate content is the broth was not monitored (it will be planned in future experiments).

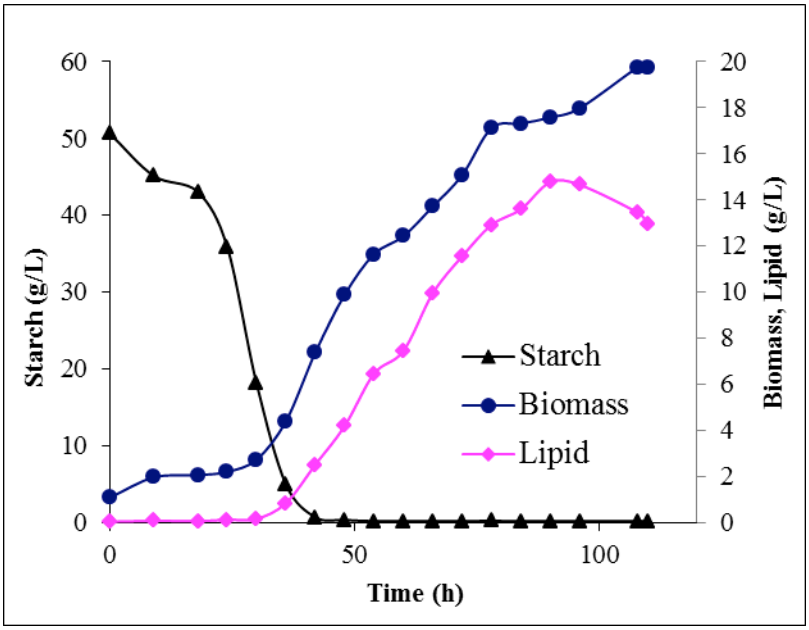

Figure 5: Batch fermentation in a medium with 54.5 g/L starch and C:N ratio of 122.6.

Further increase in starch content to 81.8 g/L without any change in nutrient levels resulted in even further increase in cell and lipid content. The experimental data from this experiment are presented in Figure 6.

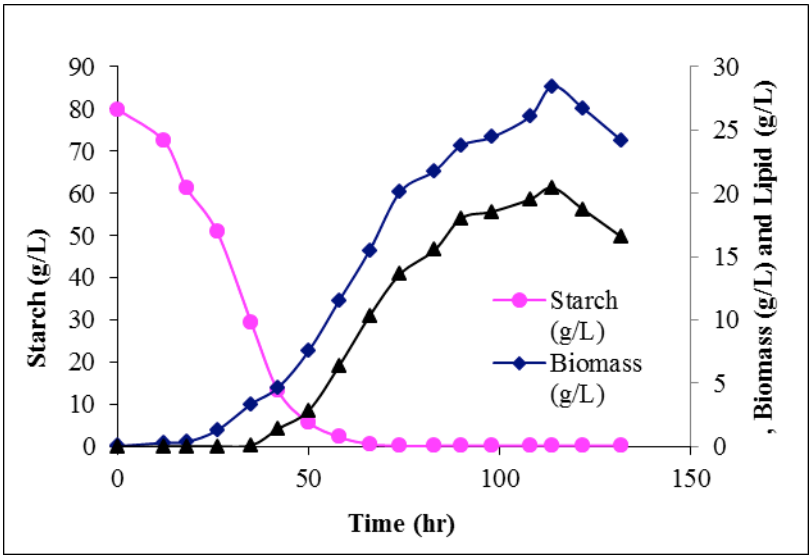

Figure 6: Batch fermentation in a medium with 81.8 g/L starch and C:N ratio of 185.

This increase in starch concentration resulted further increase in cell growth (to 28.5 g/L at 114 h) and lipid production (to 20.4 g/L at 114 h). Both the cell concentration as well as lipid concentration decreased after 114 h. The dissolved oxygen concentration in broth remained above 70% during the experiment. But this experiment was different from the one reported in Figure 4 in many respects. First, the lipid fraction in the cells was not as high as with C:N ratio of 122.6 (74% vs 82%). Secondly, both the cell concentration as well as the lipid content decreased whereas only the lipid content had registered decrease with C:N ratio of 122.6. It appears that the ratio of starch to nutrients was optimal in this case. But more experiments need to be conducted to confirm this. Thirdly, centrifugation to separate the cells from broth became quite ineffective for quite some time during this fermentation. In this case, centrifugation resulted in a second layer over the cell pellet. This second layer was soluble in hot water which was done to wash the cells before cell dry weight measurement.

Both of these experiments were repeated to ensure reproducibility. Several other experiments in which starch and nutrient concentration both were increased showed that nutrients in the 1X concentration broth are sufficient to support high cell concentrations and lipid production.

Further experiments were planned to increase the lipid production in which starch concentration was increased in discrete mode. To start with, the experiment was started with only doubling the concentration of starch and $CaCl_2$ (54.54 g/L of starch and 0.2 g/L $CaCl_2$; the concentration of starch and $CaCl_2$ in the original medium was 27.27 g/L and 0.1g/L) while retaining the rest of the medium composition as same as the original medium. All the starch was utilized by the yeast cells by the 54th hour. At this time, 81.8g starch along with 0.3 g $CaCl_2$ were added as solution in 500mL DI water. This starch was rapidly consumed (within 12 hours). At this point, 218.16 g starch and 0,8 g $CaCl_2$ were again added to the broth as solution in 1-L DI water. No

more starch was added beyond this point. Samples were regularly collected and analyzed for concentration of starch, dry weight of cells and lipids in cells. The experimental data are shown in Figure 7. The cells continued to grow even after starch was consumed from the broth and it is expected that the products of starch hydrolysis were consumed during this process. Total carbohydrates were not measured, but this is planned for future experiments.

The increase in starch concentration without changing the nutrient levels resulted in increase of C:N ratio in broth. The dissolved oxygen concentration remained above 74% saturation during the whole experiment. The maximum concentration of cells as well lipids was observed at 210 hours of the experiment; beyond this time the concentrations decreased. The highest cell concentration was 44.95 g/L and lipid concentration at this time on volumetric basis was 33.5 g/L. Lipid was apparently consumed after 210 h and it reduced to 27.04 g/L at 276 hours. Compared to a previous experiment when 81.8 g/L starch was fed at the start of the experiment, this experiment lasted much longer presumably due to the higher C:N ratio.

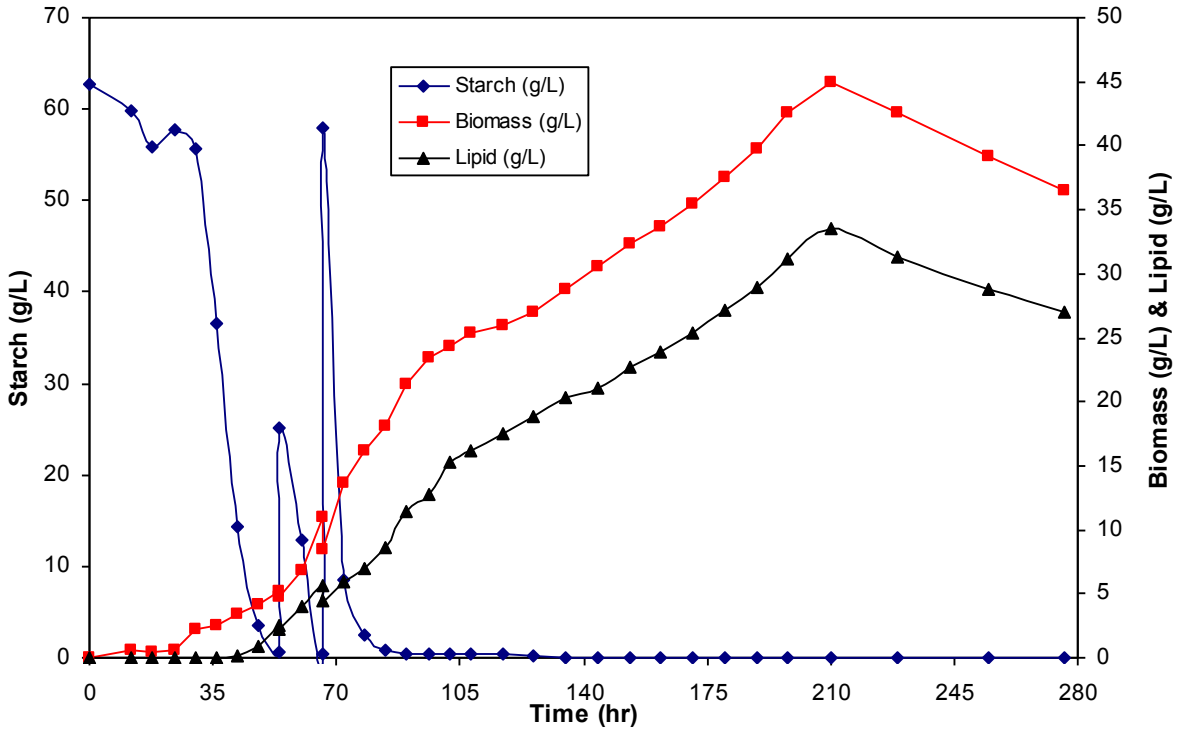

Figure 7: Cultivation of *Lipomyces starkeyi* with 5X starch concentration

Results of this experiment have been confirmed in several repeated experiments and the cells have been used for the extraction studies.

Solvent feed

Fermentation Centrifuge to get cell mass from the broth Drying Extraction

Water utilized medium components Solvent to reuse

Lipids Solvent Recovery Centrifuge to remove cell debris

Medium costs before and after optimization:

Medium component costs in high density fermentations are presented in Table 5 below.

Table 5: Medium costs before and after YE replacement

Medium Components	5X – Carbon 1X – PO4, YE $/ gal Lipid	5X – Carbon 1X – PO4, Vitamins $/ gal Lipid	5X – Carbon 1/20X – PO4, Vitamins $/ gal Lipid
Starch			
$CaCl_2$	0.003	0.003	0.003
$(NH_4)_2SO_4$	0.010	0.010	0.01
KH_2PO_4	0.872	0.872	0.21
$Na_2HPO_4 \cdot 7 H_2O$	0.285	0.285	0.07
$MgSO_4 \cdot 7 H_2O$	0.015	0.015	0.01
$FeSO_4$	0.0003	0.0003	0.0003
$ZnSO_4 \cdot H_2O$	0.0005	0.0005	0.0005
Vitamins	0.50	0.10	0.10
Trace elements	0.0006	0.0006	0.0006
	$1,68	**$ 1.28**	**$ 0.40**

In the whole, the medium costs for production of a gallon of lipids could be reduced by 75%.

Aspen plus simulation and economics of biodiesel production from microbial lipids:

Production of lipid from *Lypomyces starkeyi* with soluble sweet potato starch was simulated in Aspen Plus. The economics were analyzed based upon the sweet potato starch waste availability in Louisiana State as well as in the total United States. Results obtained from the high density cultivation experiments were utilized for this simulation. This simulation consists of 4 steps such as (i) Fermentation, (ii) Separation of cell mass from broth (iii) Extraction and Solvent recovery, and (iv) Transesterification of lipid for biodiesel production. Aspen plus NRTL property method was used throughout this simulation. NREL in-house database developed by NREL laboratory was used to estimate the properties of yeast cell.

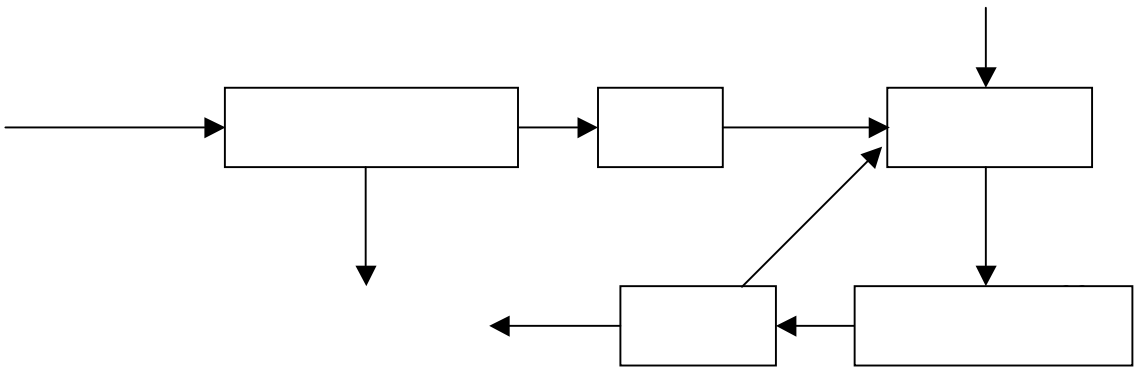

Fermentation:
Fermentation step consists of sterilizing the medium at 121 °C, cooling it down to 30 °C, followed by cell growth and lipid production in an aerated and agitated bioreactor. For the simulation of bioreactor in Aspen Plus, a yield reactor was used. Yield was calculated from the experimental values obtained in the high density cultivation experiments.

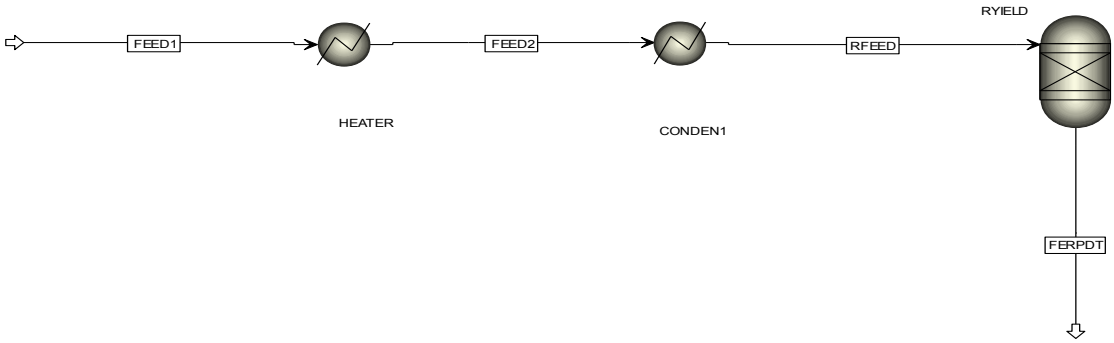

Separation of cell mass from broth:
This step involves simulation of centrifuge and drying operation. Fermentation broth obtained from the fermenter was fed in to centrifuge and supernatant was discarded. The cake from the centrifuge was fed to dryer. For the drying operation the heat duty was calculated based on the heat duty requirements to evaporate the water content present in the wet cells.

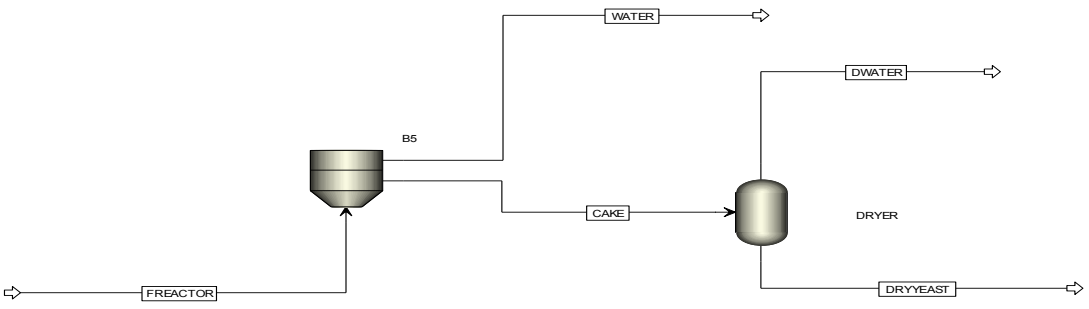

Extraction and Solvent Recovery

This part of simulation consisted of lipid extraction, centrifugation and distillation. 99% of feed solvent was recoverable for recycle. Hexane – isopropanol solvent system was used for extraction. More information and detailed results about this part of simulation were submitted already in the last quarterly report.

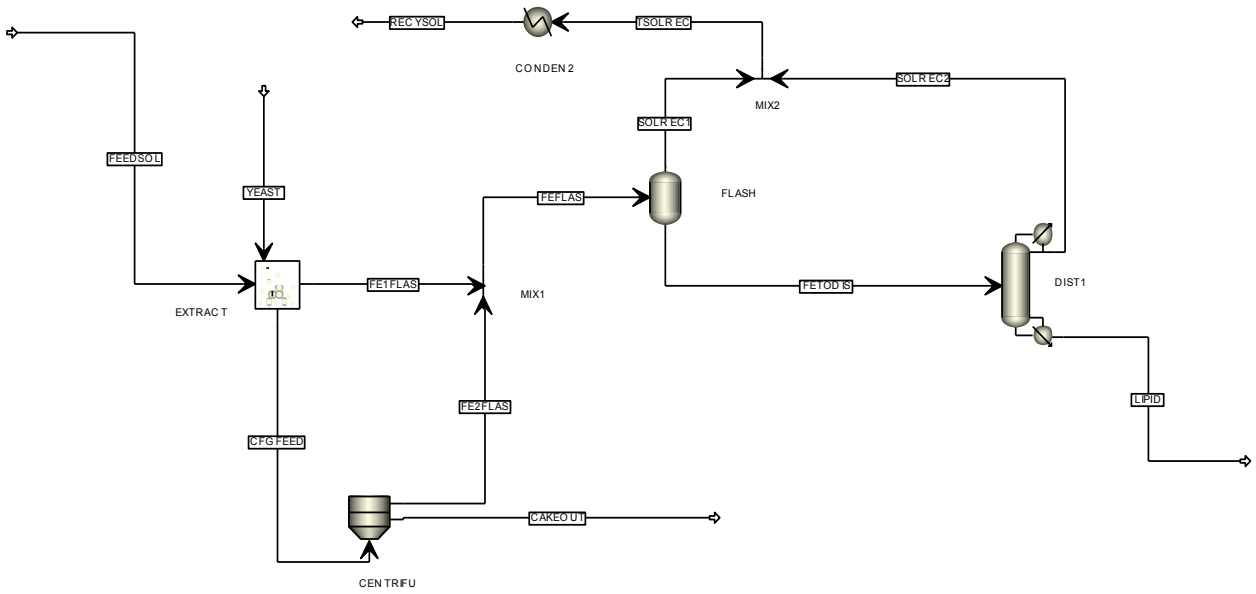

Transesterification

Simulation of transesterification step involves simulation of base catalytic transesterification reaction and methanol separation. Triolein was used to simulate the behavior of lipids. The molar ratio of methanol to lipid (triolein) of 6 was used in the reaction. 99% of residual methanol was recoverable for recycle.

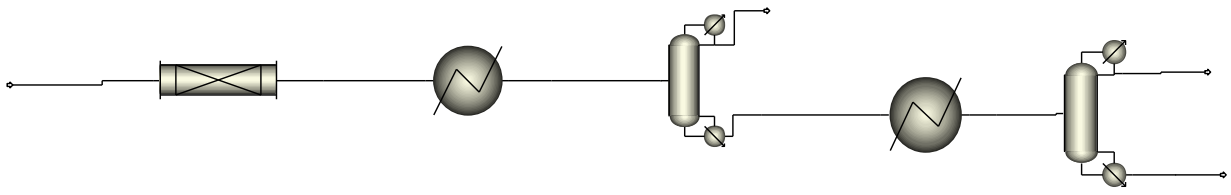

Economics of biodiesel production from the sweet potato starch waste.

Production cost of biodiesel from *Lipomyces starkeyi* with sweet potato starch waste was simulated by using the simulation developed above and based up on the availability of starch waste in the Louisiana State as well as in the United States. According to the sweet potato production statistics of 2010, production of sweet potato in Louisiana was 2.5 x 10^6 cwt while the total United States' production was about 24 x 10^6 cwt. Sweet potato waste takes various forms such as culled potatoes, peelings, and screen waste. Based on the information available from Louisiana Farm

Bureau, 20 % of the crop is culled in the field itself due to size and aesthetic considerations. Another 40% of total production of sweet potato is processed by the food canning industry. During the canning process, 20% of the sweet potato being processed ends up in waste streams. Based on this background information and availability of carbohydrate rich sweet potato waste, it was estimated that 0.54M gal biodiesel/year can be produced from sweet potato waste in Louisiana and about 5.34M gal biodiesel/year from the available waste in the United States. The economic scenarios for two plants (a small one and another large one) based on the availability data presented above are listed in tables 6 and 7.

Table 6. Economics of biodiesel production from sweet potato starch waste in a small plant.

Capacity = 0.543 M gal/year	
Capital cost	$9.5M
Operating cost	$4.9M
Production Cost $/ gal lipid	
Medium Cost	0.22
Operating cost	8.93
Solvent cost	0.5
Total	**9.64**

Table 7. Economics of biodiesel production from sweet potato starch waste in a large plant.

Capacity = 5.34 M gal/year	
Capital cost	$12M
Operating cost	$20M
production Cost $/ gal lipid	
Medium Cost	0.22
Operating cost	3.68
Solvent cost	0.5
Total	**4.39**

As a result, it can be argued that combining locally available starchy wastes to increase production in a single plant is desirable. The present analysis, does not account for transportation costs associated with such centralized production facilities. These can be minimized using localized drying operations followed by transportation

of dried wastes. These costs can be offset by the savings in disposal/treatment costs. These simulations also point to high costs of operation of the plants which include media costs that could be significant for the current medium composition being employed for microbial oil production. Our efforts to reduce these costs have successfully eliminated a large fraction of medium costs.

Extraction of lipids from oleaginous microorganisms

Lipids were extracted from the yeast cells and analyzed by gas chromatography. The relative fatty acid content is shown in Table 8. It is clear that Lipomyces *Starkeyi* is composed mainly of long-chain fatty acids with 16 and 18 carbon atoms. These data show that the distribution of fatty acids, C16:0 (palmitic acid), C16:1 (palmitoleic acid), C18:0 (Stearic acid), C18:1n9c (Oleic acid) and C18:2n6c (Linoleic acid) were almost constant in fermentations with different C:N ratios.

Table 8. Fatty acids composition

Compound Name	Mole %
Palmitic AME (C16:0)	42.97%
Palmitoleic AME (C16:1)	3.15%
Stearic AME (C18:0)	5.84%
Oleic AME (C18:1n9c)	43.72%
Linoleic AME (C18:2n6c)	4.32%

% of Sample Identified (Area Basis)	% Saturated	% Mono Sat.	% Polyunsat.
104.137	48.808	46.873	4.319

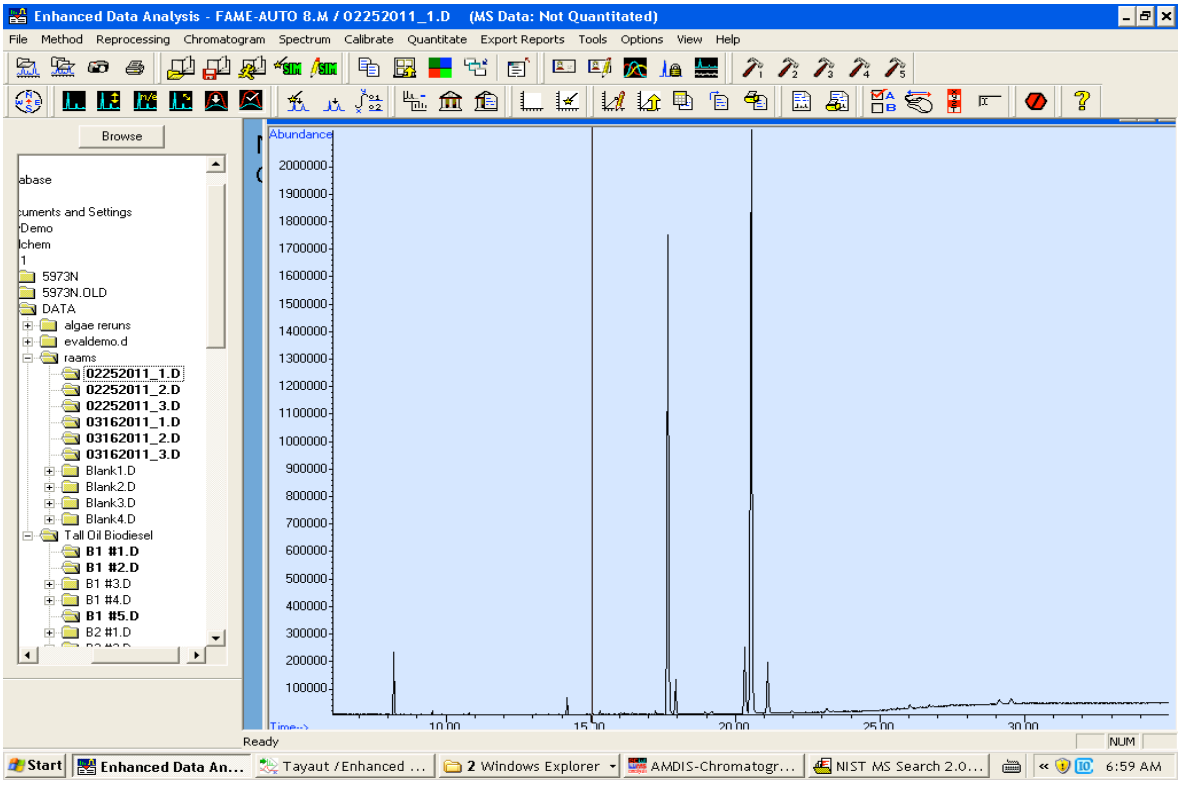

Conclusions

4. *Lipomyces starkeyi* is a producer of a very large fraction of its dry weight as lipids and this can be achieved by appropriate selection of C:N ratio.
5. Medium components and their composition must be carefully selected, otherwise the medium itself can make the production uneconomical. In this case, yeast extract and phosphates were identified as the high cost components in the medium. Yeast extract could be substituted with biotin, calcium pantothenate, and inositol, and phosphate concentrated could be reduced to 25% of the original. Phosphate costs can also be reduced to about 25% of the original.
6. Fed-batch fermentation could be used to achieve cell densities up to 44 g DW/L with intracellular lipid fraction of 75%.

References

Bader J, *et al.* 2006. 'a-amylase production in fed-batch cultivation of Bacillus caldolyticus: An interpretation of fermentation course using 2-D gel electrophoresis'. **Chem. Biochem. Eng. Q. 20**:413–420.

Folch J, *et al.* 1957. 'A simple method for the isolation and purification of total lipids from animal tissues', **J. Biol. Chem. 226**:497–509.

Holdsworth JE, *et al*. 1988. 'Enzyme activities in oleaginous yeasts accumulating and utilizing exogenous or endogenous lipids'. **J. Gen. Microbiol. 134**:2907-2915.

Subramaniam, R, *et al.* 2010. 'Microbial lipids from renewable resources: production and characterization'. **J. Ind. Microbiol. Biotechnol. 37**(12):1271-1287.
US Energy Information Administration (USEIA 2010) Oil: Crude and Petroleum Products Explained – Use of Oil, Washington DC, USA. (http://tonto.eia.doe.gov/energyexplained/index.cfm?page=oil_use).
Uzuka Y *et al.* 1975. 'Isolation and chemical composition of intracellular oil glo-bules from the yeast *Lipomyces starkeyi*'. **J. Gen. Appl. Microbiol. 21**:157–168.
Wild R, *et al.* 2010. 'Lipids from *Lipomyces starkeyi*'. **Food Technol. Biotechnol. 48**(3):329-335.

Patents: None.

Publications / Presentations:

Peer Reviewed Journals

Publications / Presentations:

Wild R, *et al.* 2010. 'Lipids from *Lipomyces starkeyi*'. **Food Technol. Biotechnol. 48**(3):329-335.
Subramaniam, R, *et al.* 2010. 'Microbial lipids from renewable resources: production and characterization'. **J. Ind. Microbiol. Biotechnol. 37**(12):1271-1287.

Cunwen Wang, Lu Chen, Rakesh Bajpai, Yuanhong Quin, Renliang LV, "Technologies for Extracting lipids from Oleaginous Microorganisms for Biodiesel Production". **Front. Energy.** 6(3):266-274 (2012).
S. Dufreche, M. Zappi, R. Bajpai, B. Benson, J. Guillory. "Today's Lipids to Renewable Diesel Fuel Market". **Int. J. Adv. Sci. Technol.** 39:49-65 (2012).
Ayalasomayajula, Srividya, Subramaniam, Rmalingam, Gallo, August, Dufreche, Stephen; Zappi, Mark; and Bajpai, Rakesh. "Potential of Alligator Fat as Source of Lipids for Biodiesel Production". **I&EC Research.** 51:2166-2169 (2012).

Conference Presentations:

Sweet Potato Starch to Lipids Using Oleaginous Yeasts. 2013. Ramalingam Subramaniam, Sharif M. Rahman, Stephen Dufreche, Rakesh Bajpai and Mark E. Zappi MAESC 2013 Technical Program, Oxford, MS 2013. Also, Annual AIChE meeting, San Francisco, CA, November 2013.
Growth, Harvesting, and Modeling of Lipomyces Starkeyi Lipids On Waste Sweet Potatoes. 2013. Melissa Mason, Stephen Dufreche, Mark E. Zappi, Ramalingam Subramaniam and Rakesh Bajpai (2013) AICHE Annual Meeting, San Francisco, CA
Microbial Lipids Production From the Mixture of Glucose and Xylose Using Lipomyces Starkeyi. 2013. Philipp Arbter, Ramalingam Subramaniam, Sharif M. Rahman, Stephen Dufreche, Mark E. Zappi and Rakesh Bajpai (2013) AICHE Annual Meeting, San Francisco, CA

Production of oil from microorganisms (2012) Subramaniam, R. Stephen Dufreche, Rakesh Bajpai and Mark Zappi VerTech 2012 Conference Lafayette, LA

Strategy development for cost effective lipid production from starchy waste (2012) Ramalingam Subramaniam, Stephen Dufreche, Rakesh Bajpai and Mark Zappi AICHE Annual Meeting, Pittsburgh, PA

Anaerobic digestion of waste materials for the production of biogas (2012). Ramalingam Subramaniam, Stephen Dufreche, Rakesh Bajpai, and Mark E. Zappi AICHE Annual Meeting, Pittsburgh, PA

Phosphate optimization for economical lipid production from *Lipomyces starkeyi* grown on starch (2012) Sharif M. Rahman, Ramalingam Subramaniam, Stephen Dufreche, Mark Zappi and Rakesh Bajpai AICHE Annual Meeting, Pittsburgh, PA

Reducing the Cost of Microbial Lipid Production from Carbohydrate Rich Waste Streams. (2012) Subramaniam, R., Rahman, SM., Dufreche, S., Bajpai, R., and Zappi, M. IETC 2012 34TH Industrial Energy Technology Conference, New Orleans, Louisiana

Simulation and Economics of Biodiesel Production From Microbial Lipids, Ramalingam Subramaniam, Spephen Dufreche, Mark Zappi, and Rakesh Bajpai, Paper presented at the 2011 Annual AIChE Meeting, October 16-21, 2011 in Minneapolis, MN.

Extraction and Economics of Lipid Production from *Lipomyces starkeyi* Grown on Starch. R. Subramaniam, S. M. Rahman, S. Dufreche, M. Zappi, R. Bajpai. Paper presented at the 2011 Annual AIChE Meeting, October 16-21, 2011 in Minneapolis, MN.

Effect of Nutrients and production of lipids by *Lipomyces starkeyi* and its economics. M. Popovic, R. Subramaniam, S. Dufreche, M. Zappi, and R. Bajpai. European Conference for Applied biotechnology, Berlin Sep 25- 30, 2011.

Production and Economics of Biofuels from Microbial Lipids, (Oral Presentation by Rakesh Bajpai), 2011 Society of Industrial Microbiology Annual Meeting and Exhibition, New Orleans, LA, July 24-28, 2011.

Progress in Making Microbial Lipid Production Economical. R. Subramaniam, S. M. Rahman, Y. Madueke, S. Dufreche, M. Zappi, and R. Bajpai. Clean Power and Energy Research Consortium (CPERC) Annual Meeting, New Orleans, LA, May 18, 2011.

High Density Cultivation of *Lipomyces starkeyi* on Starch, (Oral Presentation by Ramalingam Subramaniam), 3rd Annual Bioprocessing Symposium of LA, April 12, 2011.

Evaluation and Modification of the Dredging Elutriate Test, (Oral Presentation by Kiran Kumar Salkuti), 3rd Annual Bioprocessing Symposium of LA, April 12, 2011.

Optimization of Geotextile Bag Loading Process, (Oral Presentation by Godson Babu Gummadi), 3rd Annual Bioprocessing Symposium of LA, April 12, 2011.

Anaerobic Digestion – Waste to Fuel, (Oral Presentation by Kelsi Andrus), 3rd Annual Bioprocessing Symposium of LA, April 12, 2011.

Catalytic Conversion of Tall Oil to Renewable Diesel and Biodiesel, (Oral Presentaton by Kiran Pathapati), 3rd Annual Bioprocessing Symposium of LA, April 12, 2011.

Lipids from *Lipomyces starkeyi*. R. Wild, S. Patil, M. Popovic, M. Zappi, S. Dufreche, and R, Bajpai. Food Technol. Biotechnol. 48(3):329-335 (2010).

Microbial Lipids from Renewable Resources - Production and Characterization. R. Subramaniam, S. Dufreche, M. Zappi, R. Bajpai. J. Ind. Microbiol. Biotechnol. 37(12):1271-1287 (2010).

Impact of Nutrients on the Cost of Lipid production by the Oleaginous Yeast. Patil, S., Subramaniam, R., Wang, C., Zappi, M., Bajpai, R., and Dufreche, S. Poser Presentation at the 2010 AIChE Annual Meeting, Salt Lake City, November 7-12, 2010.

Optimization of Medium by response Surface Methodology for Reducing Ethanol Production Cost. Adewusi, A., Subramaniam, R., Wang, C., Zappi, M., Dufreche, S., and Bajpai, R. Oral Presentation at the 2010 AIChE Annual Meeting, Salt Lake City, November 7-12, 2010.

Cost of Butanol Separation from ABE Broth. Subramaniam, R., Wang, C., Zappi, M., Dufreche, S., and Bajpai, R. Oral Presentation at the 2010 AIChE Annual Meeting, Salt Lake City, November 7-12, 2010.

Economic Evaluation of Lipid Production from Sweet Potato Waste. Patil. S., Subramaniam, R., Wang, C., Zappi, M., Dufreche, S., and Bajpai, R. Poster Presentation at the 2010 AIChE Annual Meeting, Salt Lake City, November 7-12, 2010.

Experimental Studies and Reaction Kinetics of Lipid Synthesis from Lipomyces starkeyi. Patil. S., Subramaniam, R., Wang, C., Zappi, M., Dufreche, S., and Bajpai, R. Oral Presentation at the 2010 AIChE Annual Meeting, Salt Lake City, November 7-12, 2010.

Algal Bioreactors – Light Sources/Dymanics. B. Benson, S. Dufreche, M. Zappi, H. Daultani, R. Bajpai. Presentation at the US, China, Japan, Singapore Joint Meeting on Environment, held at Shinghua University Shenzhen Campus, China, May 22, 2010.

Economic Evaluation of Lipid production from Sweet Potato Waste. S. Patil, R. Subramanium, M. Zappi, S. Dufreche, R. Bajpai. Presentation at the Second Annual Bioprocessing Symposium, held at Lafayette, LA, May 01, 2010.

Catalytic Conversion of Tall Oil to Renewable Diesel and Biodiesel. K. Pathapati, S. Dufreche, R. Bajpai, M. Zappi. Presentation at the Second Annual Bioprocessing Symposium, held at Lafayette, LA, May 01, 2010.

Quantification of Lipids and Biodiesel Quality from Louisiana Alligator Fat. S. Ayalasomayajula, A. Gallo, R. Bajpai, M. Zappi. Presentation at the Second Annual Bioprocessing Symposium, held at Lafayette, LA, May 01, 2010.

Light Dynamics in Algal Culture. B. Benson, H. Daultani, M. Zappi, R. Bajpai. Presentation at the Second Annual Bioprocessing Symposium, held at Lafayette, LA, May 01, 2010.

Light Dynamics of Light Emitting Diodes (LED) in a Microalgae Culture. Daultani, H., Benson, B., Zappi, M., Bajpai, R. Oral Presentation at the 2009 Annual AIChE Meeting, Nashville, TN, November 8-13, 2009.

Lipids from Alligator Fat and Production of Biodiesel. Ayalasomayajula, S., Gallo, A., Dufreche, S., Zappi, M., Bajpai, R. Poster Presentation at the 2009 Annual AIChE Meeting, Nashville, TN, November 8-13, 2009.

Production and characterization of lipids using *Lipomyces starkeyi* utilizing starch. Bajpai, R., Patil, S., Dufreche, S., Zappi, M. 2009 Annual Meeting of South Central

Branch of American Society of Microbiology, Nicholls State University, Thibodeaux, LA, November 5-6, 2009.

Biofuels from Algae – Bioreactor Perspectives, Patil, S., Dufreche, S., Zappi, M. , Bajpai, R. 2009 Annual Meeting of South Central Branch of American Society of Microbiology, Nicholls State University, Thibodeaux, LA, November 5-6, 2009.

An Assessment of Algae to biofuels and Secondary Products Using Open Pond Systems. Zappi, M., Dufreche, S., Bajpai, R., Oral Presentation and Proceedings of the 3rd Louisiana Natural Resources Symposium, Baton Rouge, July 16-17, 2009.

Bio-based Vehicular Fuels: An Assessment of a Promising, yet Dynamic Industry. Zappi, M., Dufreche, S., Bajpai, R., Oral Presentation at the 3rd Louisiana Natural Resources Symposium, Baton Rouge, July 16-17, 2009.

Reactor Perspectives in Indoor Cultivation of Phototrophic Algae at Large Scale. Bajpai, R., Benson, B., and Zappi, M. E. Poster paper at the 31st Symposium on Biotechnology for Fuels and Chemicals, San Francisco, CA, May 3-6, 2009.

CHAPTER FOUR
UNO
COAL AND BIOMASS COGASIFICATION

Technical Contact: Professor Ting Wang, (504) 280-7183, twang@uno.edu
Business Contact: Carol Mitton, 504-280-5546, cmitton@uno.edu; orsp@uno.edu
University of New Orleans (UNO)

SUMMARY

Gasification is an efficient method of producing clean synthetic gas (syngas) from hydro-carbon feedstock such as coal, biomass, petroleum coke, refinery residues, and municipal wastes. The produced synthesis gas (syngas) consists primarily of CO, H_2 and some minor CH_4. Syngas and/or syngas-derived **hydrogen** can be used as a fuel for electric generation (through turbines or fuel cells) or as feedstocks for petrochemical and chemical industries. Syngas-derived hydrogen is typically produced through the water-gas-shift reaction with the CO_2 as a companion end product, which can be captured and sequestered. Integrating gasification technology with the combined cycle power generation technology has made IGCC (Integrated Gasification Combined Cycle) an attractive technology to provide clean energy using fossil fuels, especially coals, with the potential of capturing CO_2 more economically than any other means. Typically larger IGCC plants will be more cost effective to build (i.e. lower capital cost) and achieve higher plant efficiency (i,e, lower cost of electricity).

Using biomass **waste** to produce energy is carbon neutral, beneficial to rural economic development, and acts as a hedge against volatility of fossil fuels costs. Nonetheless, there are several challenges facing the effective utilization of biomass wastes: (a) supply is limited and varies with the seasons, (b) limited supplies renders biomass power plants usually small (less than 50 MW) and less efficient, (c) density is low and expensive for long-distance transportation, and (d) there is tar and oil formation in raw syngas. Considering these challenges, **it is more economically attractive and less technically challenging to co-gasify biomass wastes with coal.**

The major **objective** of University of New Orleans' task is to focus on investigating issues dealing with feedstock feeding, gasification process, and control of syngas output quality. The specific goals are:

(a) Improve performance and reliability of gasifiers
(b) Conduct parametric and techno-economic study of IGCC implemented with biomass/coal gasification to investigate various design considerations and cause-effect of implementing carbon capture and sequestration (CCS) schemes.

If the gasifer is large and long enough, the reaction will eventually reach equilibrium results. However, due to some slow reaction rates, it has become economically unsound to use too long or large gasifiers. Therefore, most of the entrained-flow type gasifiers have been usually designed with a residence time of less than 4 seconds. Different flow control schemes and feed-stock feeding schemes have been developed to improve gasifier performance to achieve both gasification efficiency and thermal efficiency by increasing the residence time, augmenting mixing to achieve better uniformity, and using multistage feeding to more effectively control the gasification process. To help improve understanding of how gasfication process interacts with the thermal-flow behavior, the Energy Coversion & Conservation Center (ECCC) of University of New Orleans has developed a 3-D gasification code by incorporating user defined functions into the commercial CFD code, FLUENT. Numerical simulations of the oxygen-blown coal gasification process inside a generic entrained-flow gasifier were carried out. The Navier-Stokes equations and seven species transport equations were solved with three heterogeneous global reactions and two homogeneous reactions.

A coal gasification simulation model involves many sub-models and each of the sub-models needs to be investigated and verified. The following summarizes the results:

Four different devolatilization submodels are employed and compared. The Kobayashi model produces slower devolatilization rate than the other models. The constant rate model produces the fastest devolatilization rate. The single rate model and the chemical percolation model produce moderate and consistent devolatilization rate. Slower devolatilization rate produces higher exit gas temperature, H_2, and CO_2, but lower CO and heating value, and hence, lower gasification efficiency. Combustion of volatiles is modeled with two-stage global reactions with an intermediate stage via benzene.

Turbulence models significantly affect the simulated results. Among five turbulence models tested, the standard k-ε and the RSM models give consistent results. The time scale for employing stochastic time tracking of particles also affects simulated result. Caution has to be exerted to select the appropriate time constant value. Smaller particles have a higher surface/volume ratio and react faster than larger particles. However, large particles possessing higher inertia could impinge on the opposing jet and change the thermal-flow filed and the reaction rates.

Three different gasification reaction models: *instantaneous gasification, global equilibrium, and finite-rate models are compared.* The goal is to determine if the simplified instantaneous gasification model can be used to quickly capture acceptable approximations of thermal-flow and reaction behaviors that can be used as a preliminary screening tool of new design ideas for improving gasifiers' performance. In the

instantaneous gasification model, the interphase exchange rates of mass, momentum and energy are assumed to be infinitely fast. Also, the dispersed phase can be simplified as the gas phase, and the complex two-phase flow is then treated as a single-phase flow. Two water shift rates are used. The fast rate is used with the presence of catalyst, while the slow rate is used without catalyst as in a typical entrained-flow gasifier. The results show that reactions in the instantaneous gasification model occur fast and finish quickly; whereas, the reaction in the finite-rate model, which involves gas-solid reactions, occurs slowly. Varying the coal particle size of the finite-rate model shows that the syngas heating value of the smaller particle size is closer to the instantaneous gasification model. The water shift rate plays a very important role on affecting the accurate prediction of the syngas composition. The syngas composition of using fast water shift rate is very close to that calculated from the global equilibrium method. The overall result reveals that the instantaneous gasification approach can provide an overall evaluation of relative changes of gasifier performance in terms of temperature, heating value, and gasification efficiency corresponding to parametric variations, but not adequately capture the local gasification process predicted by the finite rate model in most part of the gasifier.

Once the fundamental computational model and sub-models are validated. The effects of **different operation parameters** on the gasification process are studied, *including coal mixture (dry vs. slurry), oxidant (oxygen-blown vs. air-blown), and different coal distribution between two stages.* In the two-stage coal-slurry feed operation, the dominant reactions are intense char combustion in the first stage and enhanced gasification reactions in the second stage. The gas temperature in the first stage for the dry-fed case is about 800 K higher than the slurry-fed case. This calls for attention of additional refractory maintenance in the dry-fed case. One-stage operation yields higher H_2, CO and CH_4 combined than if a two-stage operation is used, but with a lower syngas heating value. High heating value (HHV) of syngas for the one-stage operation is 7.68 MJ/kg, compared to 8.24 MJ/kg for two-stage operation with 72%-25% fuel distribution and 9.03 MJ/kg for two-stage operation with 50%-50% fuel distribution. Carbon conversion efficiency of the air-blown case is 77.3%, which is much lower than that of the oxygen-blown case (99.4%). The syngas heating value for the air-blown case is 4.40 MJ/kg, which is almost half of the heating value of the oxygen-blown case (8.24 MJ/kg).

In an entrained-flow gasifer, the non-participating effect of coal particles, soot, ashes, and reactive gases could significantly affect the temperature distribution in the gasifier and hence affects the local reaction rate and life expectancy of wall materials. For slagging type gasifiers, radiation further affects the forming process of corrosive slag on the wall which can expedite degradation of the refractory lining in the gasifier. Applications of **five different radiation models** to coal gasification process are investigated, i*ncluding Discrete Transfer Radiation Model (DTRM), P-1 Radiation*

Model, Rosseland Radiation Model, Surface-to-Surface (S2S) Radiation Model, and Discrete Ordinates (DO) Radiation Model. The result reveals that the various radiation models yield uncomfortably large uncertainties in predicting syngas composition, syngas temperature, and wall temperature. The Rosseland model does not yield reasonable and realistic results for gasification process. The DTRM model predicts very high syngas and wall temperatures in the dry coal feed case. In the one-stage coal slurry case, DTRM result is close to the S2S result. The P1 method seems to behave stably and is robust in predicting the syngas temperature and composition; it yields the result most close to the mean, but it seems to underpredict the gasifier's inner wall temperature.

In recent years, Integrated Gasification Combined Cycle (IGCC) technology has been gaining steady popularity for use in clean coal power operations with Carbon Capture and Sequestration (CCS). This study investigates two approaches to improve efficiency and further reduce the greenhouse gas (GHG) emissions. *First, replace the traditional subcritical Rankine steam cycle portion of the overall plant with a supercritical steam cycle. Second, add different amounts of biomass as feedstock to reduce emissions.* Using the commercial software, Thermoflow®, this study analyzes the baseline plants around 235MW and 267 MW for the subcritical and supercritical designs, respectively. **Both post-combustion and pre-combustion CCS conditions are considered.** The results clearly show that utilizing a certain type of biomass with low-rank coals up to 50% (wt.) can, in most cases, not only improve the efficiency and reduce overall emissions, but may be economically advantageous, as well. Beyond a 10% Biomass Ratio, however, the efficiency begins to drop due to the rising pretreatment costs, but the system itself still remains more efficient than from using coal alone (between 0.2-0.3 points on average). The CO_2 emissions decrease by about 7,000 tons/MW-year compared to the baseline (no biomass), making the plant carbon-negative with only 10% biomass in the feedstock. In addition, implementing a *supercritical steam cycle* raises the efficiency (1.6 percentage points) and lowers the capital costs ($300/kW), regardless of plant layout. Implementing *post-combustion CCS* consistently causes a drop in efficiency (at least 7-8 points) from the baseline, and increases the costs by $3,000-$4,000/kW and $0.06-$0.07/kW-hr. The SO_x emissions also decrease by about 190 tons/year (7.6×10^{-6} tons/MW-year). Finally, the CCS cost is around $65-$72 per ton of CO_2.

For *pre-combustion CCS,* sour-shift appears to be superior both economically and thermally to sweet-shift in the current study. Sour-shift is always cheaper, (by a difference of about $600/kW and $0.02-$0.03/kW-hr), easier to implement, and also 2-3 percentage points more efficient. The economic difference is fairly marginal, but the trend is inversely proportional to the efficiency, with CoE decreasing by 0.5 cents/kW-hr from 0%-10% BMR and rising 2.5 cents/kW-hr from 10%-50% BMR. Pre-combustion CCS plants are smaller than post-combustion ones, and usually require 25% less energy

for CCS due to their compact size for processing fuel flow only under higher pressure (450 psi), versus processing the combusted gases at near-atmospheric pressure. Finally, the CO_2 removal cost for sour-shift is around $20/ton, whereas sweet-shift's cost is around $30/ton, which is much cheaper than that of post-combustion CCS: about $60-$70/ton.

4.1 WORK STATEMENT

Gasification is an efficient method of producing clean synthetic gas (syngas) from hydro-carbon feedstock such as coal, biomass, petroleum coke, refinery residues, and municipal wastes. The produced synthesis gas (syngas) consists primarily of CO, H_2 and some minor CH_4. Syngas can be used as a fuel for electric generation or as the chemical building block for petrochemical and chemical industries. Integrating gasification technology with the combined cycle power generation technology has made IGCC (Integrated Gasification Combined Cycle) an attractive technology to provide clean energy using fossil fuels, especially coals. Typically larger IGCC plants will be more cost effective to build (i.e. lower capital cost) and achieve higher plant efficiency (i,e, lower cost of electricity).

Louisiana is a major producer of sugarcane, sweet potatoes, rice, sorghum, and pecans. Using biomass **waste** to produce energy is carbon neutral, beneficial to rural economic development, and acts as a hedge against rising energy costs derived from fossil fuels. Nonetheless, there are several challenges facing the effective utilization of biomass wastes: (a) supply is limited and varies with the seasons, (b) limited supplies renders biomass power plants usually small (less than 50 MW) and less efficient, (b) density is low and expensive for long-distance transportation, and (c) there is tar and oil formation in raw syngas. Considering these challenges, it is more economically attractive and less technically challenging to co-gasify biomass wastes with coal.

Therefore, the **objective** of this task will focus on investigating issues dealing with feedstock feeding, gasification characteristics, and control of syngas output quality. This project was conducted in three phases.

First phase 10/1/2008 -9/30/2009

Task 4 Hydrogen Production: Improved Performance and Reliability of Gasifiers

Subtask 4.1	Improve existing gasification computational model:
Subtask 4.2	Investigate various gasification operating conditions in a two-stage entrained-flow gasifier:
Subtask 4.3	Construct a two-stage gasifier to experimentally investigate the effect of fuel injection scheme on flow pattern and residence time

Second Phase: 10/1/2009 -12/31/2010

Task 5 Hydrogen Production: Improved Performance and Reliability of Gasifiers

- Subtask 5.1 Improve existing gasification computational model:
- Subtask 5.2 Investigate various gasification operating conditions in a two-stage entrained-flow gasifier:
- Subtask 5.3 Construct a two-stage gasifier to experimentally investigate the effect of fuel injection scheme on flow pattern and residence time

Task 6 Parametric Study of IGCC System Design with Carbon Capture

- Subtask 6.1 Establish a robust tool to simulate IGCC system with CCS.
- Subtask 6.2 Conduct parametric study to investigate various design considerations and cause-effect of implementing CCS schemes.

Third Phase 1/1/2011-9/30/2013

Task 5 Investigation of Co-gasification of Coal and Biomass

- Subtask 5.1 Improve existing coal gasification computational model by incorporating biomass as a co-feedstock
- Subtask 5.2 Investigate various methods for pretreatment of biomass for co-gasification operating conditions.
- Subtask 5.3 Establish a robust tool to simulate coal-biomass cogasification IGCC system with Carbon Capture.

4.2 INTRODUCTION

Gasification is the process of converting various carbon-based feedstocks to clean synthetic gas (syngas), which is primarily a mixture of hydrogen (H_2) and carbon-monoxide (CO), through an incomplete combustion. Feedstock is partially combusted with oxygen and steam at high temperature and pressure with only less than 30% of the required oxygen for complete combustion being provided. After cleaning, the syngas produced can be used as a fuel, usually as a fuel for boilers or gas turbines to generate electricity, or can be used to make a synthetic natural gas, **hydrogen** gas, methanol, or other chemical products. The gasification technology is applicable to any type of carbon-based feedstock, such as coal, heavy refinery residues, petroleum coke, biomass, and municipal wastes.

The hydrogen derived from syngas is typically generated through the water-gas-shift reaction under catalytic condition by converting the carbon monoxide composition in the

syngas to hydrogen and hydrocarbon ($CO + H_2O \Leftrightarrow H_2 + CO_2$). Hydrogen and carbon dioxide is then separated to two independent streams. The CO_2 stream can be captured and sequestered (CCS). The hydrogen can be used as a fuel to feed fuel cells or like syngas to be burned in gas turbines to generate electricity or used as feedstock to produce other chemicals.

When the cleaned syngas or hydrogen to be burned in the gas turbines, it usually takes advantage of the highly efficient combined cycle by employing the Integrated Gasification Combined Cycle (IGCC) technology. The gas is burned with compressed air in the combustor of the gas turbine. The high pressure and hot gases produced in the combustor then expand through the gas turbine to drive the air compressor and an electric generator. The hot exhaust gases from the gas turbine are sent to a heat recovery steam generator (HRSG) to produce steam that expands through a steam turbine to drive another electric generator. IGCC plants can achieve efficiencies of about 55% and low emissions, compared to 43-45% efficiencies and relatively higher emissions for regular or critical pulverized coal combustion power plants. Gasification integrated in IGCC is considered a clean and efficient alternative to coal combustion for power generation. The high-pressure and high-temperature syngas from the gasifier can especially take advantage of the new generation of advanced turbine systems, which require high compression ratio and high turbine inlet temperature to produce up to 60% combined cycle efficiency.

Employing biomass as a feedstock to generate fuels or power has the advantage of being carbon neutral or even carbon negative, if carbon is captured and sequestrated. However, there are challenges facing the effective utilization of biomass wastes: (a) biomass supply is limited and varies with the seasons, (b) biomass density is low and expensive for long-distance transportation, and (c) due to a limited supply of feedstock, biomass plants are usually small, which results in higher capital and production costs. Considering these challenges, it is more economically attractive and less technically challenging to co-combust or co-gasify biomass wastes with coal.

Using IGCC technology results in lower emissions and more energy efficiency than a standard pulverized coal (PC) plant. In addition, IGCC allows implementation of pre-combustion carbon capture and storage (CCS), which is typically much cheaper than post CCS for a PC plant. Furthermore, as this paper aims to demonstrate, using biomass in an existing coal IGCC plant will only further increase these benefits, albeit at a slight drop in gross power output. To avoid some of the added costs of bio-fuels, biomass waste products, bagasse in this instance, can be used for lower costs than biomass crops; and, in some cases, these costs can be turned into profits for removing materials that were going to be incinerated or thrown away to begin with.

In addition, from a biomass perspective, it is more economically feasible to co-gasify biomass with coal than to continue using biomass by itself. Because biomass is seasonal, cannot be transported over long distances ecomomically, and has low energy density, biomass itself is basically limited to smaller scale applications due to limited supply. Thus, by mixing biomass with coal feedstocks, biomass can be used in much larger

plants, allowing it to make use of the same economy and efficiency of scale that coal is. Also, seasonality would no longer be an issue because the larger plants could still function on coal alone for the seasons in which biomass availability is limited or nonexistant.

During the period of this project, comprehensive research has been conducted. The results and achievements are reported in two major categories:

(A) Improve performance and reliability of gasifiers through computational simulation and cold flow experiments.

Topic 1: Investigation of Effects of Turbulence and Devolatilization Models on Gasification Simulation

Topic 2: Investigation of Coal Gasification Process under Various Operating Conditions Inside A Two-Stage Entrained Flow Gasifier

Topic 3: Water-Gas Shift Modeling in Coal Gasification

Topic 4: Effect of Radiation Models on Coal Gasification Simulation

Topic 5: Low-Rank Coal versus High-Rank Coal Gasification

Topic 6: Experimental Study of Cold Particle Flow in an Entrained Flow Gasifier

(B) Investigation of co-gasification of coal and biomass application for IGCC with various design considerations and cause-effect of implementing CCS schemes.

Topic 7: Integrate biomass pretreatment process and coal/biomass cogasification into IGCC plant design

Topic 8: Conduct Techno-Economic Analysis of Biomass/Coal Co-Gasification IGCC Systems with Supercritical Steam Bottom Cycle and Carbon Capture

Topic 9: Investigate both Pre-Combustion and Post-Combustion Carbon Capture Processes with Coal-Biomass Cogasification IGCC

Ultimately, the goal of this study is to demonstrate the effectiveness of biomass and coal being gasified together; so that co-gasification can be developed into a cost-effective and environmentally friendly source of electrical power, partly alleviating the effects of the energy-dependency on foreign oils/gas, increasing the process efficiency, and easing environmental concerns at the same time.

(A) IMPROVING PERFORMANCE AND RELIABILITY OF GASIFIERS THROUGH COMPUTATIONAL SIMULATION AND COLD FLOW EXPERIMENTS

4.3 Computational Model

One of the major goals of the gasification research at the University of New Orleans is to develop a trustworthy computational tool that can be used to help improve gasifier designs to achieve better performance, efficiency, and reliability. It is also desired to reduce the size of gasifiers, which will lead to reduction of their capital and operational costs. A good understanding of the gasification process inside a gasifier is needed to help achieve these goals. The desired product of a gasifier can mostly be obtained if the gasifier is big enough so the residence time is sufficiently long to achieve chemical equilibrium status. However, the corresponding gasifier will be large and expensive and the product yield will be low due to the lengthy residence time. To reduce the gasifier size while augmenting product yield, it is believed that performance of a high-efficiency gasifier is closely related to and affected by the thermal-flow behavior inside the gasifier. CFD simulation is an economic and effective tool to help achieve this goal.

During the period of this project, UNO has successfully developed a 3-D gasification code by incorporating user defined functions into the commercial CFD code, FLUENT. Numerical simulations of the coal gasification process inside generic entrained-flow gasifiers were carried out.

The gasification of coal particles involves three major steps as shown in Fig. 4.1: (a) thermal decomposition (pyrolysis and devolatilization), (b) thermal cracking of the volatiles, and (c) char gasification. Coal particles undergo pyrolysis when they enter the hot combustion environment. Moisture within the coal boils and when the particle temperature reaches the boiling point, it leaves the coal's core structure. The volatiles are then released as the particle temperature continues to increase. This volatile-releasing process is called devolatilization. The long hydrocarbon chains are then thermally cracked into lighter volatile gases such as H_2, CO, C_2H_2, C_6H_6, CH_4, etc. These lighter gases can react with O_2, releasing more heat, which is needed to continue the pyrolysis reaction.

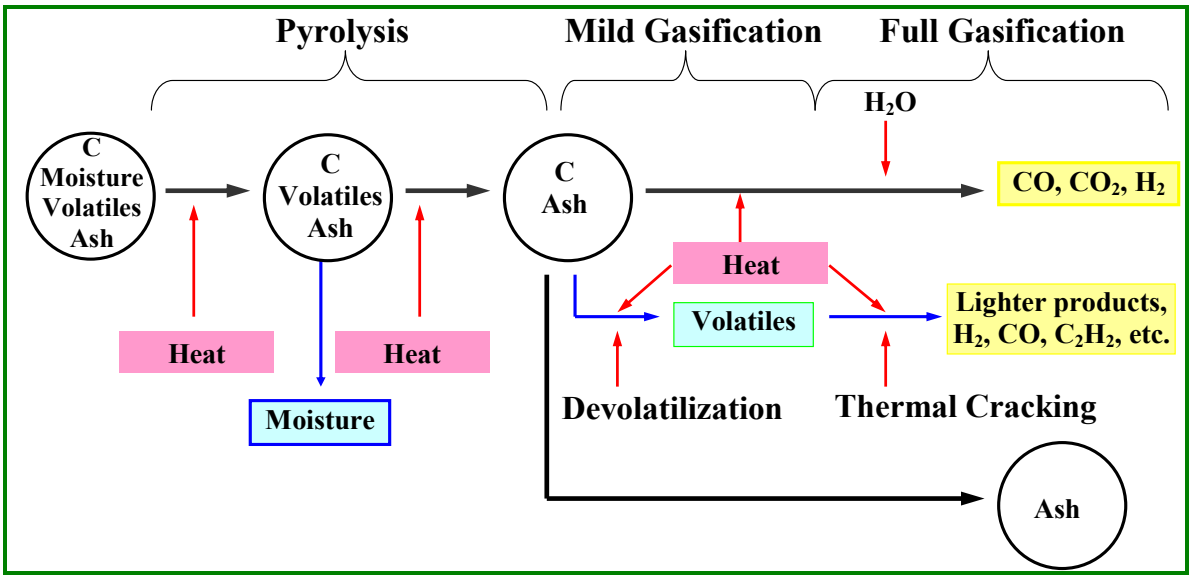

Fig. 4.1 Simplified global gasification processes of coal particles (sulfur and other minerals are not included in this figure).

With only char and ash left, the char particles undergo gasification with CO_2 or steam to produce CO and H_2, leaving only ash. The heat required for the pyrolysis and devolatilization processes can be provided externally or internally by burning the char and/or volatiles.

Devolatilization is a decomposition process that occurs when, under heating, volatiles are driven out from a hydrocarbon material (like coal). The rate of devolatilization is influenced by temperature, pressure, residence time, particle size, and coal type. The heating causes chemical bonds to rupture and both the organic and inorganic compounds to decompose. In a typical fixed bed reactor, the process starts at a temperature of around 100°C (212°F) with desorption of gases, such as water vapor, CO_2, CH_4, and N_2, which are stored in the coal pores. When the temperature reaches above 300°C (572°F), the released liquid hydrocarbon called tar becomes important. Gaseous compounds, such as CO, CO_2, and steam are also released. When the temperature is above 500°C (932°F), the fuel particles are in a plastic state where they undergo drastic changes in size and shape. The coal particles then harden again and become char when the temperature reaches around 550°C (1022°F). As heating continues, H_2 and CO are released through gasification.

The pyrolysis conditions affect the physical properties of the char. It is reported that the heat transfer coefficient decreases by a factor of 10 during the fast heating of the coal particles mixed with a hot solid heat carrier. This reduced heat transfer rate to the particle

surface results in a temperature plateau on the level of about 400°C (752°F) and lasts throughout the devolatilization process.

In general, the larger the particle size the smaller the volatiles yield because in larger particles more volatiles may crack, condense, or polymerize with some carbon deposition occurring during their migration from inside the particle to the particle surface. At high pressures, volatiles yields of bituminous coals decrease due to the low vapor pressure of tar. In contrast, low rank coals do not show decreased volatiles yields with increased pressure since these coals do not have as much tar. The computational model built up in this project uses the following global reactions of gasification process.

Heterogeneous (solid and gas) phase:

$C(s) + ½\ O_2 \rightarrow CO,\ \Delta H°_R = -110.5$ MJ/kmol (R1)

$C(s) + CO_2 \rightarrow 2CO,\ \Delta H°_R = +172.0$ MJ/kmol (Gasification, Boudouard reaction (R2)

$C(s) + H_2O_{(g)} \rightarrow CO + H_2,\ \Delta H°_R = +131.4$ MJ/kmol (Gasification) (R3)

$C + 2H_2 \rightarrow CH_4,\ \Delta H^o_R = -87.4$ MJ/kmol (Direct methanation) (R4)

Homogenous gas phase:

$CO + ½\ O_2 \rightarrow CO_2,\ \Delta H°_R = -283.1$ MJ/kmol (R5)

$CO + H_2O_{(g)} \rightarrow CO_2 + H_2,\ \Delta H°_R = -41.0$ MJ/kmol (Water-shift) (R6)

$CO + 3H_2 \leftrightarrow CH_4 + H_2O,\ \Delta H°_R = -205.7$ MJ/kmol (Methanation) (R7)

$H_2 + ½\ O_2 \rightarrow H_2O,\ \Delta H°_R = -242$ MJ/kmol (R8)

Two-step volatiles gasification models for mild-gasification

$CH_{1.952}O_{0.9278} \rightarrow 0.9278CO + 0.9399H_2 + 0.01203C_6H_6,$ (R9)

(Volatiles cracking via mild-gasification)

$C_6H_6 + 3O_2 \rightarrow 6CO + 3H_2$ Volatiles gasification via C_6H_6 (R10)

Two-step volatiles gasification models for high or low rank coals

$CH_{2.761}O_{0.264} \rightarrow 0.264CO + 0.5085H_2 + 0.336CH_4 + 0.2C_2H_2,\ \Delta H°_R = 6.263$ MJ/kmol (R11)

(Volatiles Cracking for high-rank coals, e.g., Illinois No.6 bituminous)

$CH_{2.694}O_{0.5581} \rightarrow 0.5581CO + 0.7632H_2 + 0.2419CH_4 + 0.1C_2H_2,\ \Delta H°_R = 68.575$ MJ/kmol (R12)

(Volatiles cracking for low-rank coals, e.g., South Hallsville Texas Lignite)

$CH_4 + ½O_2 \rightarrow CO+2H_2,\ \Delta H°_R = -35.71$ MJ/kmol (Volatiles gasification via CH_4) (R13)

$C_2H_2 + O_2 \rightarrow 2CO + H_2,\ \Delta H°_R = -447.83$ MJ/kmol (Volatiles gasification via C_2H_2) (R14)

Note: (a) All $\Delta H°_R$ at 298K and 1 atm. (b) "+" = Endothermic (absorbing heat), "-" = Exothermic (releasing heat)

4.3.1 Background of Coal Gasification Computational Methods

Chen et al. [2000] developed a comprehensive three-dimensional simulation model for entrained coal gasifiers which applied an extended coal gas mixture fraction model with the Multi Solids Progress Variables (MSPV) method to simulate the gasification reaction and reactant mixing process. The model employed four mixture fractions separately track the variable coal off-gas from the coal devolatilization, char-O_2, char-CO_2, and char-H_2O reactions. Chen et al. performed a series of numerical simulations for a 200 ton per day (tpd) two-stage air blown entrained flow gasifier developed for an IGCC process under various operation conditions (heterogeneous reaction rate, coal type, particle size, and air/coal partitioning to the two stages).

Chen et al.'s model predicted that coal devolatilization and char oxidation were responsible for most of the carbon conversion (up to 80%) in the two-stage air blown entrained flow gasifier. It was found that carbon conversion was independent of devolatilization rate, sensitive to the chemical kinetics of heterogeneous reactions on the char surface, and less sensitive to a change in coal particle size. They found that increasing air ratio (or reducing equivalence ratio) leads to increased CO_2 and decreased CO and H_2 concentrations.

Chen et. al. [2000] also predicted that increasing the average coal particle size decreases the carbon conversion, which results in an increase in the exit gas temperature and lower heating value. They also predicted that dry feed yields more CO mole fraction than wet feed does due to injecting less moisture into the system. Chen et. al. model shows that an increase in the system pressure increases the average residence time due to the reduced average gas velocity that further results in increased particle residence time and increased carbon conversion.

Bockelie et al. [2002(a)] of Reaction Engineering International (REI) developed a CFD modeling capability for entrained flow gasifiers that focus on two gasifier configurations: single-stage down fired system and two-stage with multiple feed inlets. The model was constructed using GLACIER, an REI in-house comprehensive coal combustion and gasification tool. The basic combustion flow field was established by employing full equilibrium chemistry. Gas properties were determined through local mixing calculations and are assumed to fluctuate randomly according to a statistical probability density function (PDF) which is characteristic of turbulence. Gas-phase reactions were assumed to be limited by mixing rates for major species as opposed to chemical kinetic rates. Gaseous reactions were calculated assuming local instantaneous equilibrium. The particle reaction processes include coal devolatilization, char oxidation, particle energy, particle liquid vaporization and gas-particle interchange. The model also includes a flowing slag sub-model.

Silaen and Wang [2005] conducted numerical simulations of the coal gasification process inside a generic two-stage entrained-flow gasifier using the commercial CFD solver FLUENT. The 3-D Navier-Stokes equations and seven species transport equations are solved with eddy-dissipation combustion model. They investigated the effects of

several parameters on gasification performance including coal mixture (slurry or dry powder), oxidant (oxygen-blown or air-blown), wall cooling, and various coal distributions between the two stages. The simulation results provide the temperature and species distributions inside the gasifier. The results indicate that coal-slurry feed is preferred over coal-powder feed to produce hydrogen. On the other hand, coal-powder feed is preferred over coal-slurry feed to produce carbon monoxide. The air-blown operation yields poor fuel conversion efficiency and the lowest syngas heating value due to air dilution. The effect of wall cooling has been shown insignificant on the exit gas composition and heating value. The fuel conversion efficiency of the case with coal distribution with 75% (first stage) vs. 25% (second stage) is better than the case with 50% vs. 50% coal distribution. They stated that a two-stage design has an advantage of the flexibility to adjust parameters to achieve desired performance.

In the continuation of that study, Silaen and Wang [2006] carried out a study that focuses on the effect of flow injection directions on the gasification performance using the same generic two-stage entrained flow gasifier. Horizontal injection direction was compared to downward and upward direction. The results reveal that the horizontal injection direction gives the best gasifier performance. Changing the direction of the first-stage injectors downward results in a carbon fuel conversion reduction, but produces more H_2. Changing the direction of the second-stage injectors, however, does little affect the overall flow patterns due to the smaller-quantity of coal injection (25%) and hence the gasifier performance is essentially insignificantly affected.

This study is the continuous work of Silaen and Wang [2005, 2006] and focuses on the effects of different parameters on gasification performance including turbulence models, devolatilization models, finite reaction rates, and solid coal sizes.

In the previous studies by Silaen and Wang [2005, 2006], the instantaneous gasification model of solid coal particles was used, which would result in solid-gas reaction faster than the actual process. In this study, the particle combustion model using the finite rate is incorporated. Since the char particle surface reaction is involved. The transports of CO concentration and heat from the surface layer to the surrounding gases will depend on the thermal-flow behavior. Therefore, turbulence modeling and stochastic tracking of fluctuating particles will affect the simulated results. In addition, the different coal particle size will affect coal surface/volume ratio and result in different gasification performance. To shed some light on the effect of above variables, the objective of this study is to investigate the effects of different turbulence models, devolatilization models, coal particle diameters, reaction heat, and stochastic tracking time constant on the outcome of the simulation.

4.3.2 Computational Model

This research studies an entrained flow coal gasifier. The geometry and computational meshes of the 3-D gasifier is shown in Fig. 4.2. Two opposing injectors are located near the bottom of the gasifier. In the simulations, the buoyancy force is considered, varying fluid properties are calculated for each species and the gas mixture, and the walls are assumed impermeable and adiabatic. The flow is steady and no-slip condition (zero velocity) is imposed on wall surfaces.

Computational Setup

The meshed 3-D computational domains are given in Fig. 4.2 (a) and (b), respectively. A grid sensitivity study is conducted with three different grids, including the coarse grid (148k cells), medium grid (969k cells) and fine grid (1,684k cells). The results in Fig. 4.3 show that the temperature distributions of the medium and fine grids are almost identical. To save computational time, the medium grid of 969k cells is chosen. The near-wall y+ of the 3-D grid is 190.

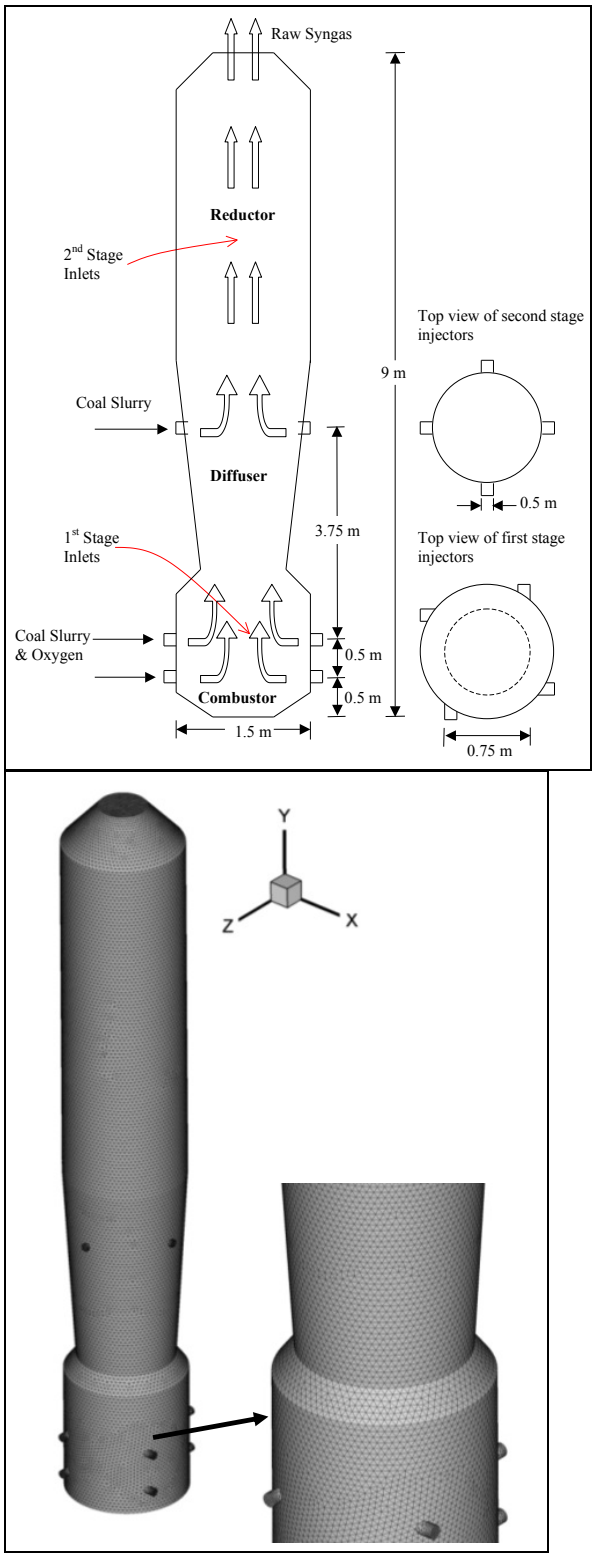

(a) (b)

Fig. 4.2 (a) Schematics of 3-D one-stage entrained flow gasifier configuration studied, and (b) its meshed computational domain.

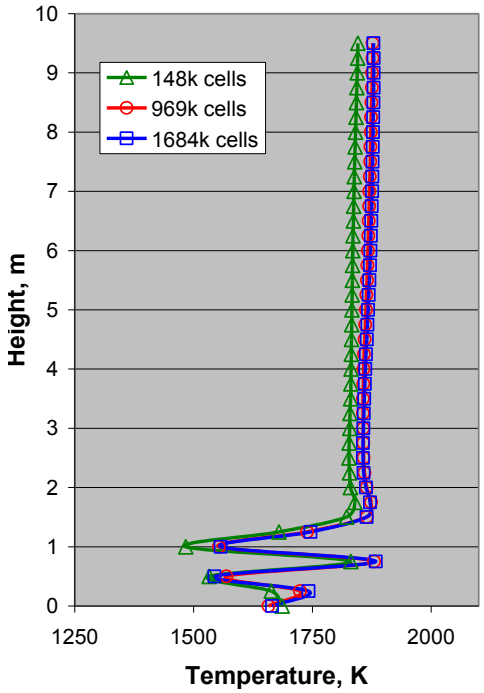

Fig. 4.3 Grid sensitivity study

4.3.3 Governing Equations for Continuous Phase

As mentioned earlier, the Eulerian-Lagrangian method is adopted for this study. In the Eulerian method for the continuous phase, the 3-D time-averaged steady-state Navier-Stokes equations as well as the mass and energy conservation equations are solved. The governing equations for the conservations of mass, momentum and energy are given as:

$$\frac{\partial}{\partial x_i}\left(\rho u_{ij}\right) = S_m \tag{4.1}$$

$$\frac{\partial}{\partial x_i}\left(\rho u_i u_j\right) = \rho \bar{g}_j - \frac{\partial P}{\partial x_j} + \frac{\partial}{\partial x_i}\left(\tau_{ij} - \rho\overline{u_i' u_j'}\right) + S_f \tag{4.2}$$

$$\frac{\partial}{\partial x_i}\left(\rho c_p u_i T\right) = \frac{\partial}{\partial x_i}\left(\lambda \frac{\partial T}{\partial x_i} - \rho c_p \overline{u_i' T'}\right) + \mu\Phi + S_h. \tag{4.3}$$

The symmetric stress tensor, τ_{ij}, is given by

$$\tau_{ij} = \mu\left(\frac{\partial u_j}{\partial x_i} + \frac{\partial u_i}{\partial x_j} - \frac{2}{3}\delta_{ij}\frac{\partial u_k}{\partial x_k}\right). \tag{4.4}$$

Species transport model is used to model the mixing and transport of the chemical species. The equation for species transport is

$$\frac{\partial}{\partial x_i}\left(\rho u_i C_j\right) = \frac{\partial}{\partial x_i}\left(\rho D_i \frac{\partial C_j}{\partial x_i} - \rho\overline{u_i' C_j'}\right) + S_j. \tag{4.5}$$

S_j in Eq. 4.5 is the source term to accept increased or decreased chemical species resulted from the chemical reactions.

4.3.4 Turbulence Models

The velocity field in turbulent flows always fluctuates. As a result, the transported quantities such as momentum, energy, and species concentration fluctuate as well. The fluctuations can be small scale and high frequency, which is computationally expensive to be directly simulated. To overcome this, a modified set of equations that are computationally less expensive to solve can be obtained by replacing the instantaneous governing equations with their time-averaged, ensemble-averaged, or otherwise manipulated to remove the small time scales. However, the modifications of the instantaneous governing equations introduce new unknown variables. Many turbulence models have been developed to determine these newρ unknown variables (such as Reynolds stresses or higher order terms) in terms of known variables. Two of the turbulence models are explained below.

Standard k-ε Model

The standard k-ε model defines the Reynolds stresses as

$$-\rho\overline{u_i' u_j'} = \mu_t\left(\frac{\partial u_i}{\partial x_j}+\frac{\partial u_j}{\partial x_i}\right)-\frac{2}{3}\rho k\delta_{ij} \tag{4.6}$$

where k is the turbulence kinetic energy, and μ_t is the turbulence viscosity given by

$$\mu_t = \rho C_\mu k^2 / \varepsilon \tag{4.7}$$

where C_μ is a constant and ε is the turbulence dissipation rate. The equations for the turbulence kinetic energy (k) and dissipation rate (ε) are

$$\frac{\partial}{\partial x_i}(\rho u_i k)=\frac{\partial}{\partial x_i}\left[\left(\mu+\frac{\mu_t}{\sigma_k}\right)\frac{\partial k}{\partial x_i}\right]+G_k-\rho\varepsilon \tag{4.8}$$

$$\frac{\partial}{\partial x_i}(\rho u_i \varepsilon)=\frac{\partial}{\partial x_i}\left[\left(\mu+\frac{\mu_t}{\sigma_\varepsilon}\right)\frac{\partial \varepsilon}{\partial x_i}\right]+C_{1\varepsilon}G_k\frac{\varepsilon}{k}-C_{2\varepsilon}G_k\rho\frac{\varepsilon^2}{k}. \tag{4.9}$$

G_k is the generation of turbulence kinetic energy due to the mean velocity gradients. The turbulent heat flux and mass flux can be modeled with the turbulent heat conductivity (λ_t) and the turbulent diffusion coefficient (D_t), respectively.

$$\rho c_p\overline{u_i' T'} = -\lambda_t\frac{\partial T}{\partial x_i}=-c_p\frac{\mu_t}{Pr_t}\frac{\partial T}{\partial x_i}. \tag{4.10}$$

$$\rho\overline{u_i' C'} = -\rho D_t\frac{\partial C}{\partial x_i}=-\frac{\mu_t}{Sc_t}\frac{\partial C}{\partial x_i}. \tag{4.11}$$

The constants $C_{1\varepsilon}$, $C_{2\varepsilon}$, C_{μ}, σ_k, and σ_{ε} used are: $C_{1\varepsilon} = 1.92$, $C_{2\varepsilon} = 0.09$, $C_{\mu} = 1.0$, $\sigma_k = 1.3$ (Launder and Spalding, 1972). The turbulence Prandtl number, Pr_t, is set to 0.85, and the turbulence Schmidt number, Sc_t, is set to 0.7.

The turbulence models are valid for the turbulent core flows, i.e. the flow in the regions somewhat far from walls. The flow very near the walls is affected by the presence of the walls. Viscous damping reduces the tangential velocity fluctuations and the kinematic blocking reduces the normal fluctuations. The solution in the near-wall region can be very important because the solution variables have large gradients in this region.

However, the solution in the boundary layer is not important in this study. Therefore, the viscous sublayer, where the solution variables change most rapidly, does not need to be solved. Instead, the wall functions, which are a collection of semi-empirical formulas and functions, are employed to connect the viscosity-affected region between the wall and the fully-turbulent region. The wall functions consist of:

- the laws-of-the-wall for mean velocity and temperature (or other scalars)
- the formulas for near-wall turbulent quantities.

There are three types of wall function: (a) standard wall function, (b) non-equilibrium wall function, and (c) enhanced wall function.

Standard Wall Function – The momentum is expressed as

$$U^+ = \frac{1}{\kappa}\ln\left(Ey^+\right) \tag{4.12}$$

where

$$U^+ \equiv \frac{U_P C_\mu^{1/4} k_P^{1/2}}{\tau_w/\rho} \tag{4.13}$$

$$y^+ \equiv \frac{\rho C_\mu^{1/4} k_P^{1/2} y_P}{\mu} \tag{4.14}$$

and

κ = von Karman constant (= 0.42)
E = empirical constant (= 9.793)
U_P = mean velocity of fluid at point P
k_P = turbulence kinetic energy at point P
y_P = distance from point P to the wall
μ = dynamic viscosity of the fluid.

The wall function for the temperature is given as

$$T^+ \equiv \frac{(T_w - T_P)\rho c_p C_\mu^{1/4} k_P^{1/2}}{\dot{q}} = \begin{cases} Pry^+, y^+ < y_T^+ \\ Pr_t\left[\frac{1}{\kappa}\ln(Ey^+) + P\right], y^+ > y_T^+ \end{cases} \quad (4.15)$$

where P is given as

$$P = 9.24\left[\left(\frac{Pr}{Pr_T}\right)^{3/4} - 1\right]\left[1 + 0.28e^{-.007Pr/Pr_T}\right] \quad (4.16)$$

and

r = density of the fluid

c_p = specific heat of fluid

q = wall heat flux

T_P = temperature at cell adjacent to the wall

T_W = temperature at the wall

Pr = molecular Prandtl number

Pr_t = turbulent Prandtl number (0.85 at the wall)

A = 26 (Van Driest constant)

κ = 0.4187 (von Karman constant)

E = 9.793 (wall function constant)

U_c = mean velocity magnitude at $y^+ = y^+_T$

y^+_T = non-dimensional thermal sublayer thickness.

The species transport is assumed to behave analogously to the heat transfer. The equation is expressed as

$$Y^+ \equiv \frac{(Y_{i,w} - Y_i)\rho c_p C_\mu^{1/4} k_P^{1/2}}{J_{i,w}} = \begin{cases} Scy^+, y^+ < y_c^+ \\ Sc_t\left[\frac{1}{\kappa}\ln(Ey^+) + P_c\right], y^+ > y_c^+ \end{cases} \quad (4.17)$$

where Y_i is the local mass fraction of species i, Sc and Sc_t are the molecular and turbulence Schmidt numbers respectively, and $J_{i,w}$ is the diffusion flux of species i at the wall. The molecular Schmidt number, Sc, is given as $\mu/\rho D$, where μ is the viscosity and D is the diffusivity. The P_c and y^+_c are calculated in a similar way as P and y^+_T, with the difference being that the Prandtl numbers are replaced by the corresponding Schmidt numbers.

In the k-ε model, the k-equation is solved in the whole domain, including the wall-adjacent cells. The boundary condition for k imposed at the wall is

$$\frac{\partial k}{\partial n} = 0 \quad (4.18)$$

where n is the local coordinate normal to the wall. The production of kinetic energy, G_k, and its dissipation rate, ε, at the wall-adjacent cells, which are the source terms in the k-equation, are computed on the basis of equilibrium hypothesis with the assumption that

the production of k and its dissipation rate assumed to be equal in the wall-adjacent control volume. The production s of k and ε are computed as

$$G_k \approx \tau_w \frac{\partial U}{\partial y} = \tau_w \frac{\tau_w}{\kappa \rho C_\mu^{1/4} k_p^{1/4} y_P} \tag{4.19}$$

and

$$\varepsilon_P = \tau_w \frac{C_\mu^{3/4} k_p^{3/2}}{k y_P}. \tag{4.20}$$

Notice that in the wall-adjacent control volume when the equilibrium hypothesis is employed, the k-transport Eq. 4.8 is solved, while the ε-transport Eq. 4.9 is not solved but is replaced by Eq. 4.20.

Enhanced Wall Function – The k-ε model is mainly valid for high Reynolds number fully turbulent flow. A special treatment is needed in the region close to the wall. The enhanced wall function is one of several methods that model the near-wall flow. In the enhanced wall treatment, the two-layer model is combined with the wall functions. The whole domain is separated into a viscosity-affected region and a fully turbulent region by defining a turbulent Reynolds number, Re_y,

$$Re_y = y k^{1/2} / \nu \tag{4.21}$$

where k is the turbulence kinetic energy and y is the distance from the wall. The standard k-e model is used in the fully turbulent region where $Re_y > 200$, and the one-equation model of Wolfstein (1969) is used in the viscosity-affected region with $Re_y < 200$. The turbulent viscosities calculated from these two regions are blended with a blending function (θ) to smoothen the transition.

$$\mu_{t,enhanced} = \theta \mu_t + (1-\theta)\mu_{t,l} \tag{4.22}$$

where μ_t is the turbulence viscosity from the k-ε model of high Reynolds number, and $\mu_{t,l}$ is the viscosity from the near-wall one-equation model. The blending function is defined so it is equal to 0 at the wall and 1 in the fully turbulent region. The linear (laminar) and logarithmic (turbulent) laws of the wall are also blended to make the wall functions applicable throughout the entire near-wall region. A similar thermal wall function equation is employed for the temperature calculation.

Reynolds Stress Model

The Reynolds stress model (RSM), a second-moment closure, is considered in this study. The Reynolds stress transport equation can be given as

$$\frac{\partial}{\partial x_k}\left(\rho u_k \overline{u'_i u'_j}\right) = -\frac{\partial}{\partial x_k}\left[\rho u_k \overline{u'_i u'_j u'_k} + \overline{P(\delta_{kj}u'_i + \delta_{ik}u'_j)} + \mu \frac{\partial}{\partial x_k}\left(\overline{u'_i u'_j}\right)\right]$$
$$-\rho\left(\overline{u'_i u'_k}\frac{\partial u_j}{\partial x_k} + \overline{u'_j u'_k}\frac{\partial u_i}{\partial x_k}\right) + \overline{P\left(\frac{\partial u'_i}{\partial x_j} + \frac{\partial u'_j}{\partial x_i}\right)} - 2\mu\overline{\frac{\partial u'_i}{\partial x_k}\frac{\partial u'_j}{\partial x_k}} \tag{4.23}$$

The diffusive term on the right-hand side can be modeled as

$$-\frac{\partial}{\partial x_k}\left[\rho u_k \overline{u'_i u'_j u'_k} + \overline{P(\delta_{kj}u'_i + \delta_{ik}u'_j)} + \mu \frac{\partial}{\partial x_k}\left(\overline{u'_i u'_j}\right)\right] = \frac{\partial}{\partial x_k}\left(\frac{\mu_t}{\sigma_k}\frac{\partial}{\partial x_k}\left(\overline{u'_i u'_j}\right)\right) \tag{4.24}$$

The second term on the right-hand side of Eq. 4.23 is the production term, and it is notated as G_{ij}

$$G_{ij} = -\rho\left(\overline{u'_i u'_k}\frac{\partial u_j}{\partial x_k} + \overline{u'_j u'_k}\frac{\partial u_i}{\partial x_k}\right) \tag{4.25}$$

The third term is the pressure-strain term, which can be modeled as

$$\overline{P\left(\frac{\partial u'_i}{\partial x_j} + \frac{\partial u'_j}{\partial x_i}\right)} = C_1\rho\frac{\varepsilon}{k}\left(\overline{u'_i u'_j} - \frac{2}{3}\delta_{ij}k\right) - C_2\left[A_{ij} - \frac{1}{3}\delta_{ij}A_{kk}\right] \tag{2.26}$$

where $A_{ij} = G_{ij} - \frac{\partial}{\partial x_k}\left(\rho u_k \overline{u'_i u'_j}\right)$. The constants C_1 and C_2 are 1.8 and 0.6, respectively. The last term in Eq. 4.23 can be approximated by

$$2\mu\overline{\frac{\partial u'_i}{\partial x_k}\frac{\partial u'_j}{\partial x_k}} = \frac{2}{3}\delta_{ij}\rho\varepsilon \tag{2.27}$$

with the assumption that the dissipation is isotropic.

Modeling of the turbulent heat flux and mass flux are similar as in the k-ε model. The turbulent kinetic energy and its dissipation rate can be calculated from the Reynolds stresses.

Other Turbulence Models

Ignoring details here, the turbulent models adopted in this study also include the RNG k-ε model, k-ω model, and the shear-stress transport (SST) k-ω model. RNG k-ε model was derived using renormalization group theory (Choudhury, 1993). It has an additional term in the ε-equation to improve the accuracy for rapidly strained flows. It uses the effective viscosity to account for the low-Reynolds-number effects. Theoretically, this model is more accurate and reliable than the standard k-ε model. The standard k-ε model

is an empirical model based on transport equations for the turbulence kinetic energy (k) and the specific dissipation rate (ε), which can also be considered as the ratio of ε to k (Wilcox, 1998). The low-Reynolds-number effect is accounted for in the k-ω model. The SST model is a mixture of the k-ω model and the k-ε model: close to the wall it becomes the k-ω model while in the far field the k-ε model is applied (Menter, 1993).

4.3.5 Radiation Model

Five different radiation models to coal gasification process have been investigated in this study, including Discrete Transfer Radiation Model (DTRM), P-1 Radiation Model, Rosseland Radiation Model, Surface-to-Surface (S2S) Radiation Model, and Discrete Ordinates (DO) Radiation Model. The P-1 radiation model is used to calculate the flux of the radiation at the inside walls of the gasifier in this study. The general descriptions of P-1 model are stated as below.

The P-1 radiation model is the simplest case of the more general P-N radiation model that is based on the expansion of the radiation intensity I. The P-1 model requires only a little CPU demand and can easily be applied to various complicated geometries. It is suitable for applications where the optical thickness **a**L is large where "**a**" is the absorption coefficient and L is the length scale of the domain.

The heat sources or sinks due to radiation is calculated using the equation

$$-\nabla.q_r = \mathbf{a}G - 4\mathbf{a}sT^4 \tag{4.28}$$

where

$$q_r = -\frac{1}{3(a+\sigma_s)-C\sigma_s}\nabla G \tag{4.29}$$

and q_r is the radiation heat flux, **a** is the absorption coefficient, s_s is the scattering coefficient, G is the incident radiation, C is the linear-anisotropic phase function coefficient, and s is the Stefan-Boltzmann constant. The gases are assumed to be the participating media. However, when the effect of particles is included in the radiation model, the heat sources or sinks due to radiation become,

$$-\nabla\cdot q_r = -4\pi\left(a\frac{\sigma T^4}{\pi}+\varepsilon_p\right)+(a+a_p)\nabla G \tag{4.30}$$

where e_p and a_p are the equivalent emissivity and equivalent absorption of the particle, respectively.

The flux of the radiation, $q_{r,w}$, at walls caused by incident radiation G_w is given as

$$q_{r,w} = -\frac{4\pi\varepsilon_w\frac{\sigma T_w^4}{\pi}-(1-\rho_w)G_w}{2(1+\rho_w)} \tag{4.31}$$

where e_w is the emissivity and is defined as

$$e_w = 1 - r_w \tag{4.32}$$

and r_w is the wall reflectivity.

4.3.6 Discrete Phases (Solid Particles or Liquid Particles)

Discrete phases include coal particles and liquid particles. The Lagrangian method to track each particle is adopted in this study. The discrete phase is justified in entrained-flow gasification process because the particle concentration is lower than 10%. Particles in the airflow can encounter inertia and hydrodynamic drags. Because of the forces experienced by the particles in a flow field, the particles can be either accelerated or decelerated. The velocity change is determined by the force balance of the particle, which can be formulated by

$$m_p dv_p/dt = F_d + F_g + F_o \tag{4.33}$$

where F_d is the drag force of the fluid on the particle and F_g is the gravity. F_o represents the other body forces, typically include the "virtual mass" force, thermophoretic force, Brownian force, Saffman's lift force, etc. In this study, Saffman's lift force reaches about 30% of Fg, so it is included in this study.

The drag force, F_d, is calculated as

$$F_D = \frac{18\mu}{\rho_p d_p^2}\frac{C_D Re}{24}\left(v - v_p\right)m_p \tag{4.34}$$

and the gravity force, F_g, is calculated using the following equation

$$F_g = \frac{g\left(\rho_p - \rho\right)}{\rho_p} m_p \tag{4.35}$$

where m_p is particle mass, d_p is particle diameter, v is the fluid phase velocity, v_p is the particle velocity, r is the fluid phase density, r_p is the particle density, g is gravity, m is the fluid phase molecular viscosity, and C_D is the drag coefficient. The relative Reynolds number, Re, is defined as

$$Re = \frac{\rho d_p \left|v_p - v\right|}{\mu} \tag{4.36}$$

4.3.7 Coal particles Devolatilization Models

Gasification or combustion of coal particles undergoes the following global processes: (i) evaporation of moisture, (ii) devolatilization, (iii) gasification to CO and (iv) combustion of volatiles, CO, and char.

After all the moisture contained in the coal particle has evaporated, the particle undergoes devolatilization. Four different devolatilization models widely used are the Kobayashi model, single rate model, constant rate model, and CPD (Chemical Percolation Devolatilization) model.

(a) Kobayashi model --- The Kobayashi model (Kobayashi, 1976) with two-competing devolatilization rates are expressed as a weighted function of two competing rates, R_1 and R_2, as shown below,

$$\frac{m_v(t)}{(1-f_{w,0})m_{p,0}-m_a} = \int_0^t (\alpha_1 R_1 + \alpha_2 R_2)\exp\left(-\int_0^t (R_1+R_2)dt\right)dt \quad (4.37)$$

where a_1 and a_2 are yield factors, f_w is mass fraction of moisture, m_p is mass of particle, m_a is mass of ash, and R_1 and R_2 are given as,

$$R_1 = A_1 e^{-(E_1/RT_p)} \quad (4.38)$$

and,

$$R_2 = A_2 e^{-(E_2/RT_p)}. \quad (4.39)$$

The value of the constants are $A_1 = 2x10^5$, $A_2 = 1.3x10^7$, $E_1 = 1.046x10^8$ J/kmol, and $E_2 = 1.67x10^8$ J/kmol.

(b) Single rate model --- The devolatilization rate is dependent on the amount of volatiles remaining in the particle (Badzioch and Hawsley, 1970). The devolatilization kinetic rate is defined in Arrhenius form below

$$k = Ae^{-(E/RT)} \quad (4.40)$$

where the pre-exponential factor, A, used in this study is $4.92x10^5$ and the activation energy, E, is $7.4x10^7$ J/kgmol.

(c) Constant rate model --- This model assumes that volatiles are released at a constant rate (Baum and Street, 1971). The rate used in this study is 12/s (Pillai, 1981).

(d) Chemical Percolation Devolatilization (CPD) model --- The CPD model considers the chemical transformation of the coal structure during devolatilization. It models the coal structure transformation as a transformation of chemical bridge network which result in release of light gas, char, and tar (Fletcher and Kerstein (1992), Fletcher et al. (1990), and Grant et al. (1989)). The initial fraction of the bridges in the coal lattice is 1, and the initial fraction of char is 0. The lattice coordination number is 5. The cluster molecular weight is 400 and the side chain molecular weight is 50.

Volatiles released by coal particles contain a large amount of various lighter gases. When simulating coal gasification, decision has to be made as to what lighter gases are released during the devolatilization.

Silaen and Wang (2010) compared the effect of these four different devolatilization models on the gasification process respectively. The analysis concluded that the rate calculated by the Kobayashi two-competing rates devolatilization model [H. Kobayashi et al. (1976)] is very slow, while that of the CPD model gives a more reasonable result. Therefore, the Chemical Percolation Devolatilization (CPD) model was chosen for this study.

The study by Chen et al. (2000) modeled that hydrogen, oxygen, nitrogen, and sulfur in the coal particles to be released as a volatile species. The volatile species then reacts with oxygen according to Eq. 4.41 below for oxygen-rich conditions and Eq. 4.42 for oxygen-lean conditions.

For oxygen-rich conditions,

$$C_{m1}H_{m2}O_{m3}N_{m4}S_{m5}mois_{m6} + \left(m_1 + \frac{m_2}{4} - \frac{m_3}{2} + m_5\right)O_2 \rightarrow m_1CO_2 + \left(m_7 + \frac{m_2}{4}\right)H_2O + m_5SO_2 + \frac{m_4}{2}N_2 \quad (4.41)$$

For oxygen-lean conditions $\left(\varphi < \left(m_1 + \frac{m_2}{4} - \frac{m_3}{2} + m_5\right)\right)$,

$$C_{m1}H_{m2}O_{m3}N_{m4}S_{m5} + \varphi O_2 \rightarrow \alpha_1 CO_2 + \alpha_2 CO + m_1(1-\alpha_1-\alpha_2)CO_2 + \left[\frac{(1-\alpha_1)}{2}(m_2 - 2m_5) - 2(1-\alpha_1-\alpha_2)\right]H_2 + \frac{\alpha_1(m_2-2m_5)}{2}H_2O + \frac{\alpha_1(m_2-2m_5)}{2}H_2O + m_5H_2S + \frac{m_4}{2}N_2 \quad (4.42)$$

The values of m_1 through m_6, which determine the composition of the volatile, in Eqs. 4.41 and 4.42 above are calculated from the proximate and ultimate analyses of the coal. The coefficient φ is the criteria for which the condition is considered oxygen-lean.

Kumar et al. (2009) modeled that volatiles are broken up as follow,

$$\text{Volatiles} \rightarrow \alpha_1\ CO + \alpha_2\ H_2O + \alpha_3\ CO_2 + \alpha_4\ H_2 + \alpha_5\ CH_x + \alpha_6\ N_2 \quad (4.43)$$

where the stoichiometric coefficients α_i's and value of x in CH_x are determined by the proximate and ultimate analyses of the coal. In this study, the volatile matters contained in the coal are assumed to be composed of CO, H_2, N_2, CH_4, and C_6H_6 (Tomeczek, 1994) or C_2H_2. However, the devolatilization model used can only model the release of one volatile gas. Thus, the devolatilization model is divided into two steps:

(i) Release of a volatile gas modeled using the devolatilization model. All of the volatile matters are lumped into one intermediate gas species ($C_xH_yO_z$), whose release rate is given by the devolatilization model.

(ii) Thermal cracking of the volatile gas into several different gases. Once this intermediate is released, it is decomposed into the volatile gases – CO, H_2, and CH_4 – through chemical reaction: $C_xH_yO_z \rightarrow aCO + bH_2 + cCH_4$

To model part (i), the chemical formula of the intermediate gas species ($C_xH_yO_z$) has to be known. However, coal composition does not provide the volatiles' chemical formula. Thus, the chemical formula needs to be found out. Based on the proximate and ultimate analyses, the elemental composition of the volatiles is calculated. The enthalpy of the volatiles is calculated from the coal heating value.

4.3.8 Liquid droplets

Theoretically, evaporation occurs at two stages: (a) when temperature is higher than the saturation temperature (based on local water vapor concentration), water evaporates from the particle's surface, and the evaporation is controlled by the water vapor partial pressure until 100% relative humidity is achieved; (b) when the boiling temperature (determined by the air-water mixture pressure) is reached, water continues to evaporate even though the relative humidity reaches 100%. After the moisture is evaporated due to either high temperature or low moisture partial pressure, the vapor diffuses into the main

flow and is transported away. The rate of vaporization is governed by concentration difference between surface and gas stream, and the corresponding mass change rate of the particle can be given by,

$$\frac{dm_p}{dt} = \pi d^2 k_c (C_s - C_\infty) \tag{4.44}$$

where k_c is the mass transfer coefficient and C_s is the concentration of the vapor at the particle's surface, which is evaluated by assuming that the flow over the surface is saturated. C_∞ is the vapor concentration of the bulk flow, obtained by solving the transport equations. The values of k_c can be calculated from empirical correlations by (Ranz and Marshall, 1955):

$$Sh_d = \frac{k_c d}{D} = 2.0 + 0.6 Re_d^{0.5} Sc^{0.33}. \tag{4.45}$$

where Sh is the Sherwood number, Sc is the Schmidt number (defined as n/D), D is the diffusion coefficient of vapor in the bulk flow. Re_d is the particle slip Reynolds number, defined as un/d, where u is the particle slip velocity relative to the gas flow.

When the droplet temperature reaches the boiling point, the following equation can be used to evaluate its evaporation rate (Kuo, 1986):

$$\frac{dm_p}{dt} = \pi d^2 \left(\frac{\lambda}{d}\right)(2.0 + 0.46 Re_d^{0.5}) \ln\left(1 + c_p (T_\infty - T)/h_{fg}\right)/c_p \tag{4.46}$$

where l is the heat conductivity of the gas/air, h_{fg} is the droplet latent heat, and c_p is the specific heat of the bulk flow.

The droplet temperature can also be changed due to heat transfer between droplets and the continuous phase. The droplet's sensible heat change of the droplet is shown in the following equation

$$m_p c_p \frac{dT}{dt} = A_p h (T_\infty - T) + \frac{dm_p}{dt} h_{fg} + f_h \frac{dm_p}{dt} H_{reac} + A_p \varepsilon_p \sigma \left(\theta_R{}^4 - T^4\right) \tag{4.47}$$

where q_R is the radiation temperature. The convective heat transfer coefficient (h) can be obtained with a similar empirical correlation to equation (4.35):

$$Nu_d = \frac{hd}{\lambda} = 2.0 + 0.6 Re_d^{0.5} Pr^{0.33} \tag{4.48}$$

where Nu is the Nusselt number, and Pr is the Prandtl number.

4.3.9 Stochastic Tracking

The various turbulence models are based on the time-averaged equations. Using this flow velocity to trace the droplet will result in an averaged trajectory. In the real flow, the instantaneous velocity fluctuation would make the droplet dance around this average track. However, the instantaneous velocity is not calculated in the current approach as the time averaged Navier-Stokes equations are solved. One way to simulate the effect of instantaneous turbulence on droplets dispersion is to use the stochastic tracking scheme (Fluent, 2012). Basically, the droplet trajectories are calculated by using the

instantaneous flow velocity ($\bar{u} + u'$) rather than the average velocity ($\bar{u}$). The velocity fluctuation is then given as:

$$u' = \zeta\left(\overline{u'^2}\right)^{0.5} = \zeta(2k/3)^{0.5} \tag{4.49}$$

where ζ is a normally distributed random number. This velocity will apply during a characteristic lifetime of the eddy (t_e), given from the turbulence kinetic energy and dissipation rate. After this time period, the instantaneous velocity will be updated with a new ζ value until a full trajectory is obtained. When the stochastic tracking is applied, the basic interaction between droplets and continuous phase keeps the same, accounted by the source terms in the conservation equations. The source terms are not directly but rather indirectly affected by the stochastic method. For example, the drag force between droplets and the airflow depends on the slip velocity calculated by the averaged Navier-Stokes equations if without the stochastic tracking. With the stochastic tracking a random velocity fluctuation is imposed at an instant of time, and the drag force and additional convective heat transfer will be calculated based on this instantaneous slip velocity. The source terms associated with this instantaneous drag force and convective heat transfer enter the momentum and energy equations without any additional formulation. For a steady-state calculation, the "instant of time" means "each iteration step." Therefore, the averaged momentum equation will not be affected by the stochastic tracking scheme; rather the trajectory of the droplet will reflect the effect of the imposed instantaneous perturbation.

4.3.10 Reaction Models

Particle Reactions

The reaction of particle occurs after the devolatilization process has finished. The rate of depletion of solid due to a surface reaction is expressed as (Smith, 1982),

$$\bar{R} = A\eta Y R \tag{4.50}$$

$$R = k\left(p_n - \frac{R}{D}\right)^N \tag{4.51}$$

where

$\bar{R}$ = rate of particle surface species depletion (kg/s)
A = particle surface area (m^2)
Y = mass fraction of surface the solid species in the particle
h = effectiveness factor (dimensionless)
R = rate of particle surface species reaction per unit area (kg/m^2-s)
p_n = bulk concentration of the gas phase species (kg/m^3)

D = diffusion rate coefficient for reaction
k = kinetic reaction rate constant (units vary)
N = apparent order of reaction.
The kinetic rate of reaction is usually defined in an Arrhenius form as

$$k = AT^{n}e^{-(E/RT)} . \tag{4.52}$$

For reaction order N = 1, the rate of particle surface species depletion is given by

$$\overline{R} = A\eta Y p_{n} \frac{kD}{D+k} . \tag{4.53}$$

For reaction order N = 0,

$$\overline{R} = A\eta Y k . \tag{4.54}$$

For reaction order N = 0, the unit for the kinetic reaction rate constant, k, is kg/m^2-s.

The reaction order of the particle reaction is assigned 0. Thus, Eq. 4.50 is used to calculate rate of depletion of the solid, $\overline{R}$ (kg/s). The kinetic reaction rate constant, k (kg/m^2-s), is to be supplied by the user.

The kinetic reaction rate constants, k, for the solid-gas char reactions are determined by kinetic reaction rate constants adopted from published literatures as presented in Table 4.1. These rate constants are taken from Chen et al. (2000(a)). These kinetic reaction rate constants have to be carefully checked and adjusted if necessary so that their units are consistent with the unit of k (kg/m^2-s) in Eq. 4.54. The sources of these kinetic reaction rate constants are introduced and discussed below.

Table 4.1 Kinetic reaction rate constants for solid-gas reactions. (Chen et al., 2000)

Reaction	***Rate Constant***	***Parameters***
C(s) + ½O_2 → CO (Combustion)	k = AT^n exp(-E/RT) (kg/m^2-s-Pa$^{0.5}$)	n = 0 A = 0.052 kg/m^2-s-Pa$^{0.5}$ E = 6.1x10^7 J/kmol
C(s) + CO_2 → 2CO (Gasification, Boudouard reaction)	k = AT^n exp(-E/RT) (kg/m^2-s-Pa$^{0.5}$)	n = 0 A = 0.0732 kg/m^2-s-Pa$^{0.5}$ E = 1.125x10^8 J/kmol
C(s) + H_2O(g) → CO + H_2 (Gasification)	k = AT^n exp(-E/RT) (kg/m^2-s-Pa$^{0.5}$)	n = 0 A = 0.0782 kg/m^2-s-Pa$^{0.5}$ E = 1.15x10^8 J/kmol

4.3.11 Gas Phase (Homogeneous) Reactions

Three approaches are adopted to solve homogenenous gas- phase reactions: (a) eddy-dissipation model, (b) global equilibrium model, and (c) finite-rate kinetic model.

(a) Eddy-dissipation model takes into account the turbulent mixing of the gases. It assumes that the chemical reaction is faster than the time scale of the turbulence eddies. Thus, the reaction rate is determined by the turbulence mixing of the species. The net rate of production of species i due to reaction r, $R_{i,r}$ is given by the smaller of the two expression below:

$$R_{i,r} = \nu'_{i,r} M_{w,i} A \rho \frac{\varepsilon}{k} \min_R \left(\frac{Y_R}{\nu'_{R,r} M_{w,R}} \right) \quad (4.55)$$

$$R_{i,r} = \nu'_{i,r} M_{w,i} A B \rho \frac{\varepsilon}{k} \left(\frac{\sum_P Y_P}{\sum_j^N \nu''_{j,r} M_{w,j}} \right) \quad (4.56)$$

where $\nu'_{i,r}$ is the stoichiometric coefficient of the reactant i in reaction r, and $\nu''_{j,r}$ is the stoichiometric coefficient of the product j in reaction r. Y_P is the mass fraction of any product species P, and Y_R is the mass fraction of a particular reactant R. A is an empirical constant equal to 4.0, and B is an empirical constant equal to 0.5. The smaller of the two expressions is used because it is the limiting value that determines the reaction rate.

(b) Global equilibrium model.

(c) The finite-rate kinetic model calculates the reaction rate using an expression that takes into account temperature, but does not take into account the turbulent mixing of the species. For non-reversible reaction, the net source of chemical species i due to reaction is computed as the sum of the Arrhenius reaction sources over N_R reactions that the species participate in:

$$R_i = M_{w,i} \sum_{r=1}^{N_R} \Gamma (\nu''_{i,r} - \nu'_{i,r}) \left(k_{f,r} \prod_{j=1}^{N} \left[C_{j,r} \right]^{\left(\eta'_{j,r} + \eta''_{j,r} \right)} \right) \quad (4.57)$$

where,

$M_{w,i}$ = molecular weight of species i (kg/kmol)

$\nu'_{i,r}$ = stoichiometric coefficient of reactant i in reaction r

$\nu''_{i,r}$ = stoichiometric coefficient of product i in reaction r

$k_{f,r}$ = forward kinetic reaction rate constant for reaction r (s^{-1})

$[C_{j,r}]$ = molar concentration of species j in reaction r ($kmol/m^3$)

$\eta'_{j,r}$ = rate exponent of reactant species j in reaction r

$\eta''_{j,r}$= rate exponent of product species j in reaction r

Reaction rate constant, k, is usually expressed in an Arrhenius form, $k = AT^n \exp(-E/RT)$. The unit of k is s^{-1}. (Note that this is different from the unit in Eq. 4.54 because it

is the reaction rate constant for homogenous gas phase reaction while the k in Eq. 4.54 is based on surface rate for the heterogeneous gas-solid reaction)

For each gas-phase homogeneous reaction in this study, the reaction rates based on both the eddy-dissipation and finite-rate kinetic rate are calculated. The smaller of the two is used as the reaction rate. The summary of the kinetic reaction rate constants for the gas-phase homogeneous reactions are presented in Table 4.2. The reaction rate constant for the reaction $CO + ½\ O_2 \rightarrow CO_2$ is taken from Westbrook and Dryer (1981). The reaction rate constant for the water-gas-shift (WGS)reaction ($CO + H_2O_{(g)} \rightarrow CO_2 + H_2$) listed in the table has been reduced from the original value by Jones and Lindstedt (1988). Jones and Lindstedt obtained the reaction rate constant through experiment where catalyst was used. Since catalyst is not used in this study, the reaction rate constant would not be correct. The original reaction rate constant by Jones and Lindstedt was used in the preliminary study. It was found that the syngas contained no H_2O with very low CO and very high H_2 and CO_2. This indicates that the water-shift reaction was dominant. The reaction rate constant for the water-shift was then purposely slowed down to make the syngas composition consistent with that in the actual similar commercial entrained-flow gasifier with coal-slurry feed from bottom operated by Wabash River Energy Ltd. (Wabash River Energy Ltd., 2000).

Table 4.2 Kinetic reaction rate constants for finite-rate gas phase reactions.

Reaction	**Rate Constant**	**Parameters**
$CO + ½\ O_2 \rightarrow CO_2$	$k = AT^n \exp(-E/RT)$ (s^{-1})	$n = 0$ $A = 2.2 \times 10^{12}$ $E = 1.67 \times 10^8$ J/kmol
$CO + H_2O(g) \rightarrow CO_2 + H_2$ (Watershift)	$k = AT^n \exp(-E/RT)$ (s^{-1})	$n = 0$ $A = 2.75 \times 10^2$ $E = 8.38 \times 10^7$ J/kmol
$C_2H_2 + O_2 \rightarrow 2CO + H_2$	Eddy-dissipation only	

4.4 Topic 1: Investigation of Effects of Turbulence and Devolatilization Models on Gasification Simulation

(See Silaen and Wang (2010) in International Journal of Heat and Mass Transfer for details.)

4.4.1 Boundary and Inlet Conditions

Indonesian coal is used as feedstock in this study. Its composition is given in Table 4.3 and the feed rates used are given in Table 4.4. The coal/water weight ratio of the coal slurry is 60%-40%. The oxidant used is 95% O_2 and 5% N_2. Oxidant/coal slurry feed rate used in Table 4 gives O/C (fixed carbon) value of 0.3. The temperatures of the slurry coal and the oxidant are 300K and 420K, respectively. Figure 2 presents the boundary conditions used in this study. The outlet is set as a constant pressure condition at 24 atm. The operating pressure inside the gasifier is at 24 atm.

The oxidant is considered as a continuous flow and coal slurry is considered as a discrete flow. The discrete phase only includes the fixed carbon and water which comes from the moisture content of the coal and from the water added to make the slurry. In other words, in the computational model, the slurry particle basically consists of a coal particle inside a water droplet. Other components of the coal, such as N, H, S, O, and ash, are injected as gas, together with the oxidant in the continuous flow. N is treated as N_2, H as H_2, and O as O_2. Reactions of S and ash are not simulated and they are lumped with N_2 as inert gases. The coal slurry size is uniformly given as 100, 200, 300 μm respectively for three different cases

Table 4.3 Composition of Indonesia Coal

	Weight %
Volatile	38.31%
H_2O	8.25%
ash	3.90%
C	37.95%
H	2.68%
N	0.69%
S	0.31%
O	7.91%
Total, wt %	100.00%
HHV, kcal/kg	5690

Table 4.4 Feed rates used in the study

	Feed rate (kg/s)
Coal slurry	18.58
Oxidant	3.56

The walls are assigned as adiabatic with internal emissivity of 0.8. The boundary condition of the discrete phase at walls is assigned as “reflect”, which means the discrete phase elastically rebound off once reaching the wall. At the outlet, the discrete phase simply escapes/exits the computational domain.

4.4.2 Results and Discussions of Submodels of Turbulence, Devolatilations, Stochastic Time Scale, and Particle Sizes

Effects of Time Scale in the Stochastic Particle Tracking

Stochastic particle tracking employs the concept of integral time scale, which defines the time spent in turbulent motion along the particle path. The integral time scale can be calculated using the empirical formula $T = T_C\, k/\varepsilon$, where T_C is the time constant, k is the turbulence kinetic energy and ε is the turbulence dissipation rate. The suggested value of T_C is 0.15. However, since this value of 0.15 was empirically obtained for a specific flow, it is not clear whether this value is adequate for the present thermal-flow field in a gasifier. Hence, a sensitivity study is conducted by comparing the results of using various T_C values with the reference case without stochastic tracking (i.e. $T_C = 0$). The result in Fig. 4.4 shows that the mass-weighted temperature and various species distribution curves move closer to the reference curve when the T_C value is decreased from 0.15 to 0.0015 but move away from the reference curve when the T_C value is further decreased to 0.00015. By examining the hystereses effect of T_C's influence, it seems the value 0.15 overcounts the random fluctuating effect of discrete particles. The result for T_C = 0.00015 is seen close to that of T_C = 0.015 and provides a comfortable upper and lower bounds of T_C values which give consistent and similar results. Therefore, 0.015 is chosen instead of 0.00015 in this study as the value of T_C to save calculation time because a larger T_C value requires less integration during the stochastic tracking calculation.

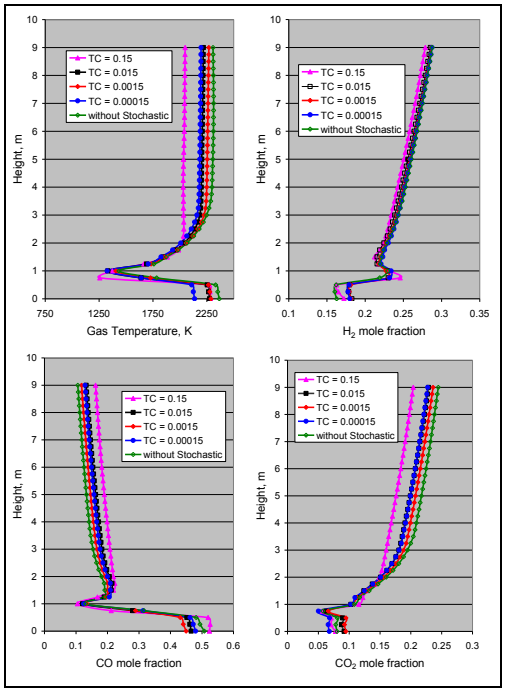

Fig. 4.4 Mass-weighted average temperature and species using standard k-ε model with different stochastic tracking T_C (time scale) constants.

Effects of Turbulence Models

The effects of turbulence models are shown in Fig. 4.5 in terms of mass-weighted averages of temperature and species distribution along the height of the gasifier. The comparison shows that standard k-ε, RSM, and k-ω SST models give consistent and similar results while the results from the k-ω and k-ε RNG models deviate from the consistent trend. Further examination shows although standard k-ε, RSM, and k-ω SST give similar results above the fuel injection location, the results below the injection location show the k-ω SST model deviates from the standard k-ε and the RSM models. The similar results from the standard k-ε and the RSM models provide the advantage of using the standard k-ε model to conduct parametric studies to significantly save the computational time while the high-order RSM model is used to "verify" the relatively simpler standard k-ε model.

Regarding the k-ω SST model, although it is more complicated than the standard k-ε model by incorporating the low-Reynolds number effect and near-wall dissipation rate, it does not model the anisotropic Reynolds stresses as in the RSM model. Since the k-ω SST model does also confirm the consistency of the results of the standard k-ε model above the injection location, all the parametric studies are then conducted by the standard k-ε model to significantly save the computational time.

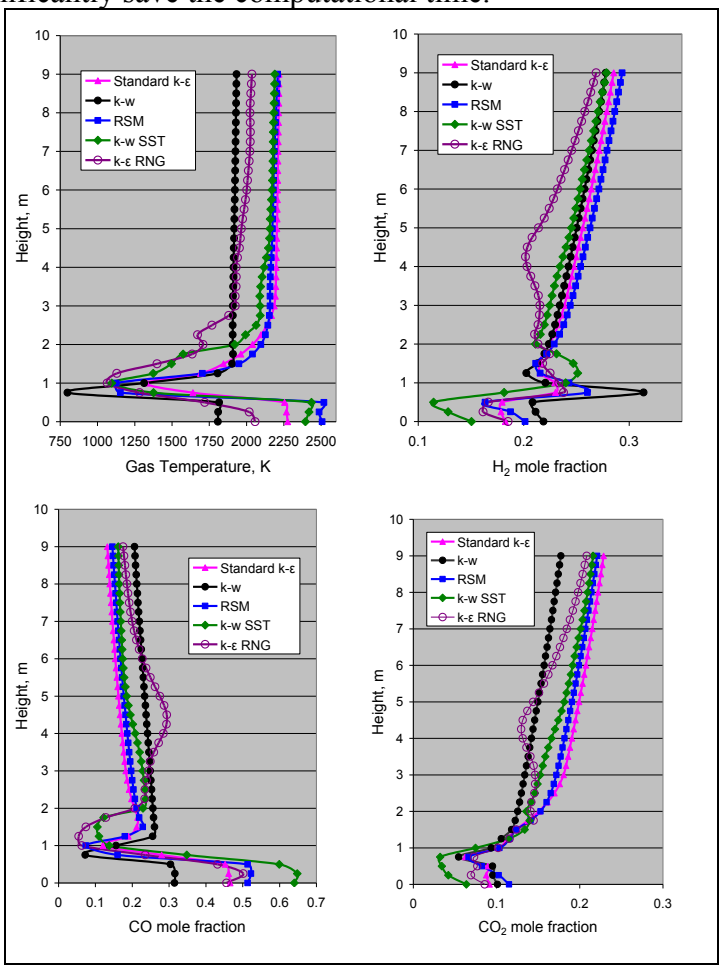

Fig. 4.5 Mass-weighted average temperature and species with different turbulence models.

Effect of Devolatilization Models

Particle tracks for cases with different devolatilization rates are presented in Fig. 4.6. The overall tracks look very similar, except that the tracks for the Kobayashi model are a little bit longer. This means that the particle reaction (oxidation and gasification in Eq. R1, R2, and R3) finishes later than that of the other models. The VM concentration contour plot in Fig. 4.6 also confirms that the devolatilization process using the Kobayashi model seems to starts later compared to other models with a smaller high-concentration core. Thus, it appears that the Kobayashi devolatilization model, which utilizes two weighted competing rates, is slower than the other models. Since particle reaction occurs after most of the moisture and volatiles have been released from the particle, as a result of the relatively slow devolatilization rate, the particle reaction starts and finishes much later compared to the other models.

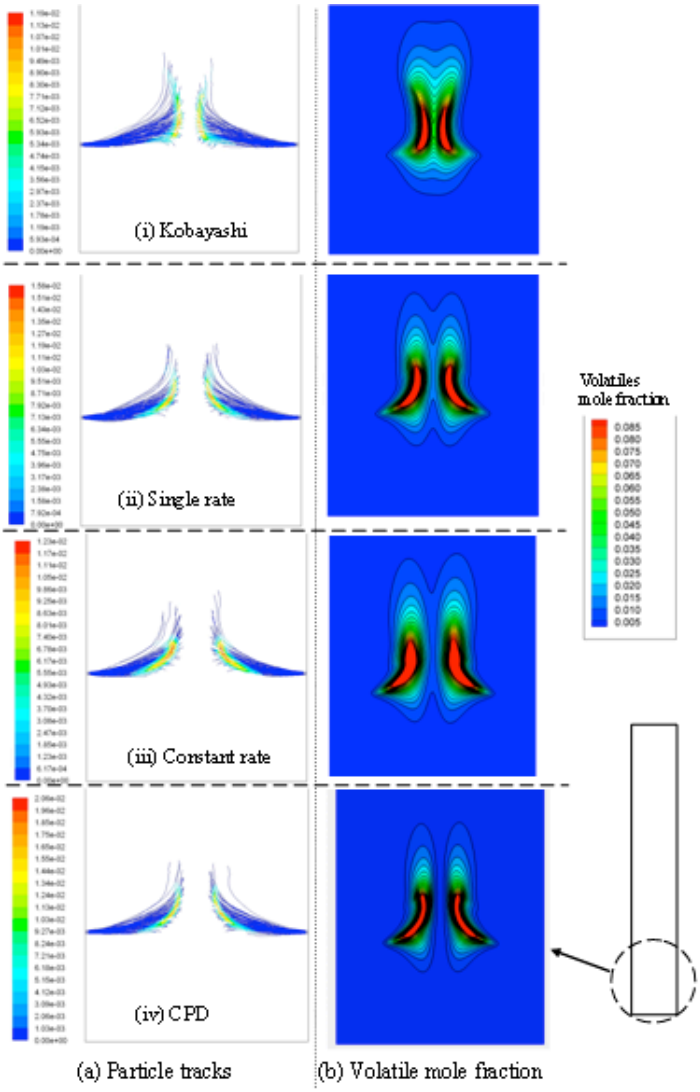

Fig. 4.6 Effect of four devolatilization models of 200-μm particle: (a) particle tracks colored by devolatilization rate (kg/s) and (b) volatiles mole fraction.

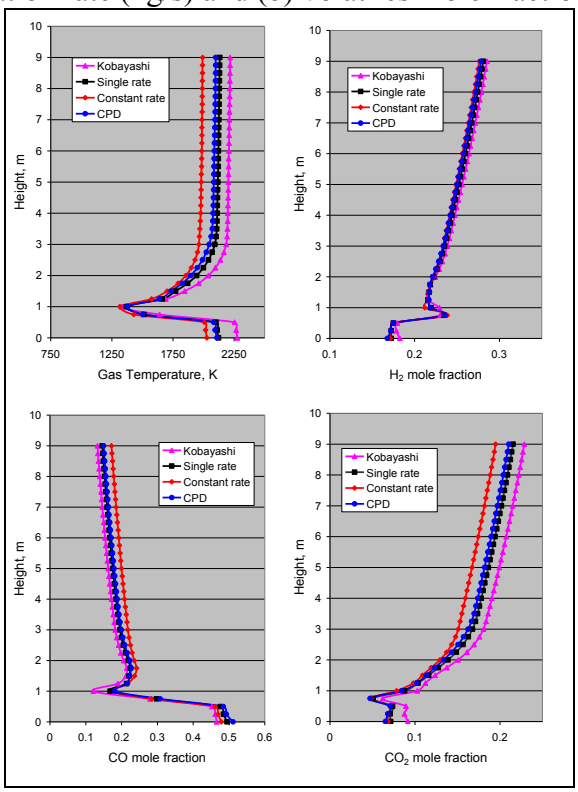

Fig. 4.7 Mass-weighted average temperature and species for standard k-ε model with different devolatilization models.

The particle tracks of the constant rate model and single rate model cases are very similar. The temperature and species distributions for both cases shown in Fig. 4.7 as well as the exit syngas composition listed in Table 4.5 are also similar. In summary, Kobayashi models predicts lower CO, but higher exit gas temperature, H_2, and CO_2, and hence lower gasification efficiency and lower heating value. CPD and single rate models produce more consistent results.

Effect of Particle Size

The coal slurry particles are assumed to be spherical. The coal slurry particle of 200 μm is assigned to the baseline case. Two other different coal slurry particle diameters, 100 μm and 300 μm, are also simulated for comparison. It is understood that the particle distribution in the real operation is not uniformly distributed. However, uniform particle size is assigned in each case to allow a more convenient way to track the change of particle size during the gasification process as well as to provide a clear comparison of the effect of particle sizes. The particle tracks presented in Fig. 4.7 show that 100-μm particles require more time to completely react than the 200-μm particles, which seems to be counterintuitive because the surface/volume ratio of smaller particle is larger than the

larger particles and they should react more quickly. To look for explanation to this phenomenon, the focus is moved towards examining the relative motion between the particles and gases. Figure 4.8 presents side by side the particle tracks (discrete phase) and the streamlines of the continuous phase (gas). It can be seen that the tracks of the 100 μm particles follow the streamlines of the continuous flow; whereas the 200-μm particles deviate from the continuous flow streamlines. It seems that the deviation of the 200-μm particles from the streamlines increases the slip velocity which results in enhanced convective transports of heat and species concentrations. In the meantime, the mixing of the particles also augments particle reactions. Thus the 200-μm particles require less time to completely react than the 100-μm particles. When the particle diameter is increased to 300μm, the residence time for reaction increases. Other than the factor of reduced surface/volume ratio, it can be seen that the particles actually have much more inertia after fuel injection and are able to impinge on the opposite jet and split the particle streams in both above and below the injection location. Strong recirculation zones contribute to trapping particles and lengthen the residence time.

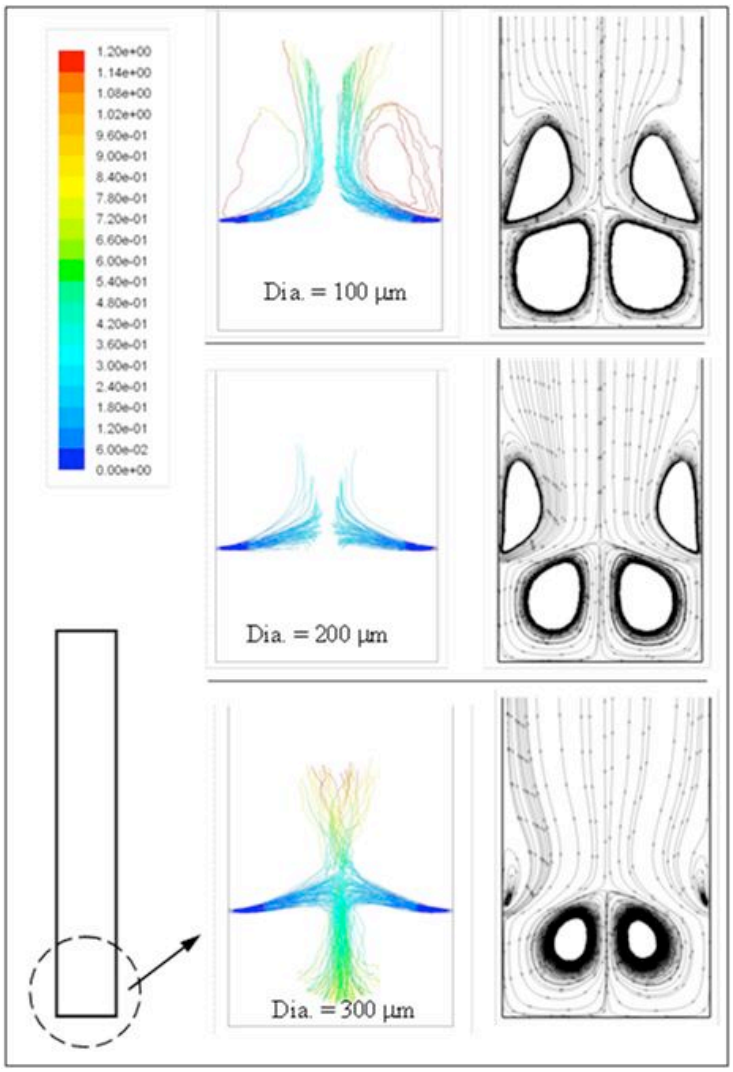

Fig. 4.8 Particle tracks and gas streamlines show effect of different coal slurry particle sizes. The particle tracks are colored by residence time (s). Kobayashi devolatilization model is used.

Mass-weighted temperature and species distribution curves in Fig. 4.9 show that there is a large exit temperature difference about 420K (1839 K vs. 2252K) between using smaller and larger particles (100 μm vs. 300 μm). The temperature near the gasifier bottom for the 300-μm case is much higher than those of the 100-μm and 200-μm cases. This is because the particles that impinge at the center and then go downward eventually burn out near the gasifier bottom. The exit syngas composition listed in Table 4.6 shows that the smallest particles give the highest syngas heating value. Generally speaking, larger particles produce more H_2, less CO, higher exit gas temperature, and more CO_2, and hence less efficient. Figure 4.10 shows particle tracks colored by particle temperature in the combustor section.

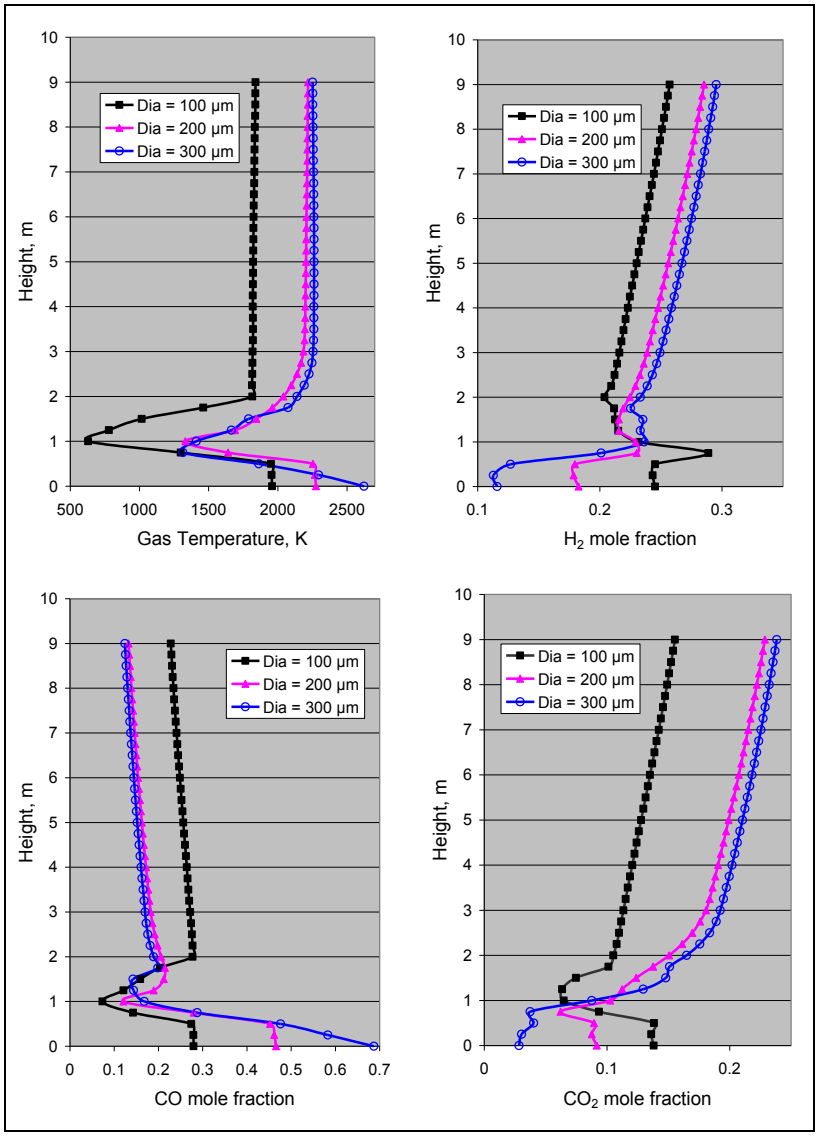

Fig. 4.9 Mass-weighted average temperature and species distributions for standard k-ε model with different coal slurry particle sizes.

Table 4.5 Exit gas temperature and compositions for the 2D case with different devolatilization models

Parameters	*Kobayashi*		*Single rate*		*Constant rate*		*CPD*	
Exit temperature, K	2218		2133		1992		2100	
Components at exit:								
	Mole fraction	Mole no. (mole)	Mole fraction	Mole no. (mole)	Mole fraction	Mole no. (mole)	Mole fraction	Mole no. (mole)
CO	14.0%	72.86	15.4%	80.73	18.1%	95.80	15.8%	83.00
H_2	28.9%	150.41	28.5%	149.41	28.1%	148.72	28.2%	148.14
CO_2	22.9%	119.19	21.5%	112.71	19.5%	103.21	21.0%	110.31
VM	0.0%	0.00	0.0%	0.00	0.0%	0.00	0.0%	0.00
H_2O	33.3%	173.31	33.6%	176.14	33.4%	176.77	34.0%	178.60
C_6H_6	0.0%	0.00	0.0%	0.00	0.0%	0.00	0.0%	0.00
N_2	0.9%	4.68	1.0%	5.24	0.9%	4.76	1.0%	5.25
C	0.0%	0.00	0.0%	0.00	0.0%	0.00	0.0%	0.00
Heating value (MJ/kg)	5.9		6.1		6.5		6.1	

Table 4.6 Exit gas temperature and compositions for the 2-D case with different coal slurry sizes

Parameters	*100 μm*		*200 μm*		*300 μm*	
Exit temperature, K	1839		2218		2252	
Components at exit:						
	Mole fraction	Mole no. (mole)	Mole fraction	Mole no. (mole)	Mole fraction	Mole no. (mole)
CO	24.0%	128.04	14.0%	72.86	12.9%	67.20
H_2	26.3%	140.31	28.9%	150.41	29.8%	155.25
CO_2	15.5%	84.13	22.9%	119.19	23.8%	123.99
VM	0.0%	0.00	0.0%	0.00	0.0%	0.00
H_2O	33.3%	180.75	33.3%	175.03	32.6%	171.03
N_2	0.9%	4.89	0.9%	4.73	0.9%	4.72
C	0.0%	0.00	0.0%	0.00	0.0%	0.00
Heating value (MJ/kg)	7.1		5.9		5.9	

Particle tracks from one injector given in Fig. 4.10 show that particle temperatures do not reach above 1000 K until the particles nearly reach the area of the next injector downstream at higher elevation. The hottest region in the combustor section occurs in the region near the wall as pictured in Fig. 4.11. The O_2 distribution, also pictured in Fig. 4.11, shows that O_2 does not travel far from the injectors before it is fully depleted. During that time, water evaporates and devolatilization follows. Once the particles have passed the downstream second-level injectors, they react with the O_2 injected through the second-level injectors. The top view shows that some high-temperature particles burn out near the wall and contributes to the high-temperature region near the combustor wall.

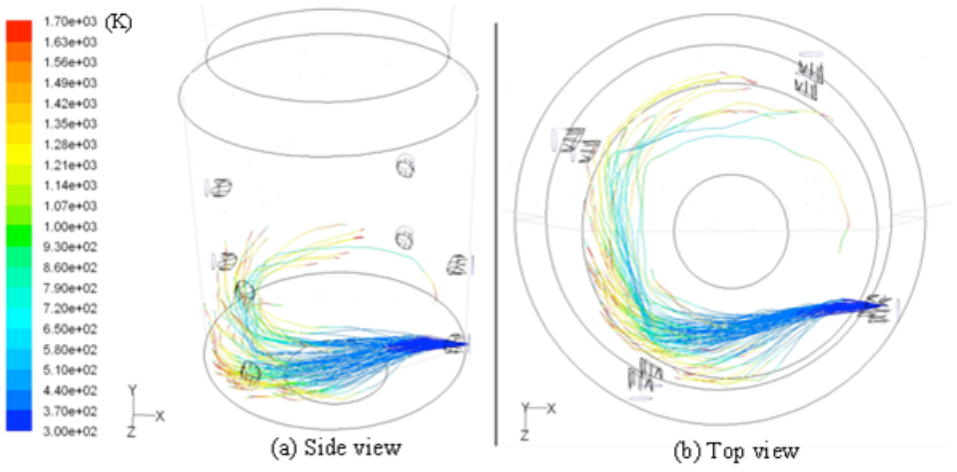

Fig. 4.10 Particle tracks colored by particle temperature in the combustor section. For clarity, only one injection is shown.

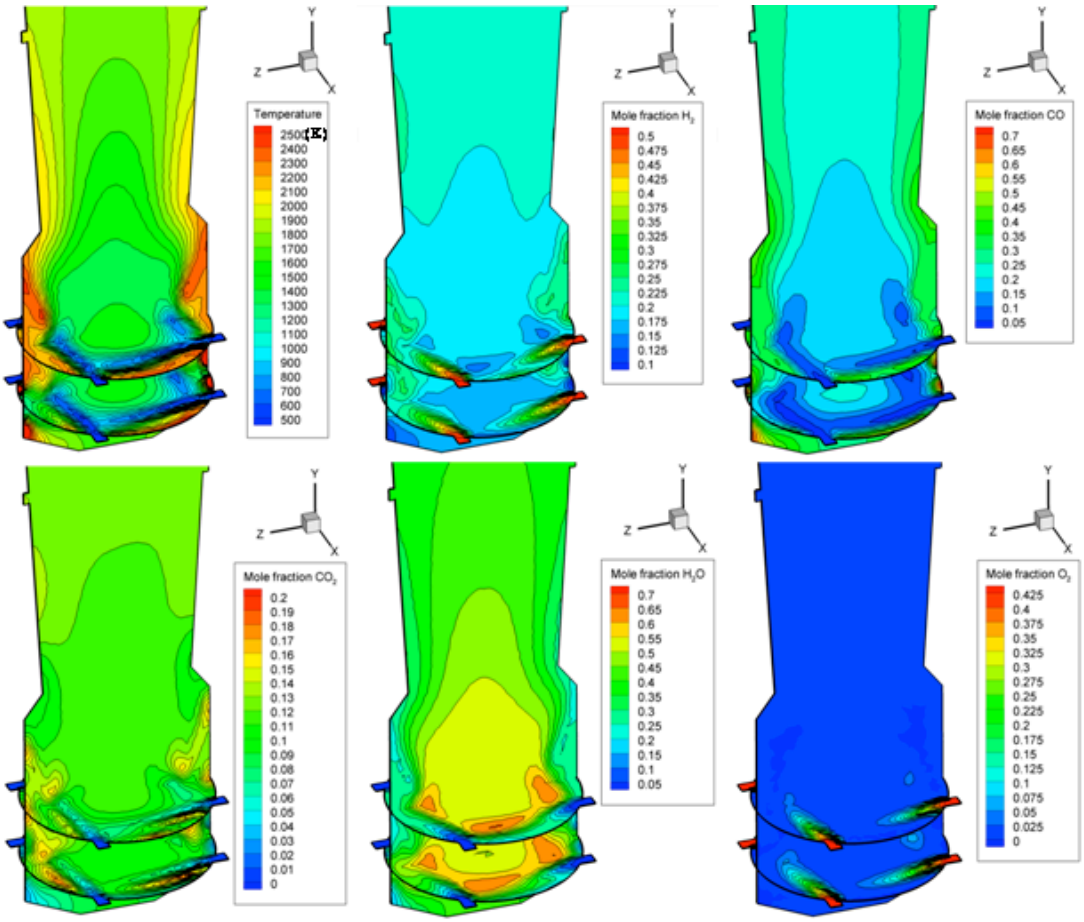

Fig. 4.11 Temperature and species distributions in the combustor section of a 3-D gasifier

4.4.3 Conclusions of Submodels of Turbulence, Devolatilations, Stochastic Time Scale, and Particle Sizes

Turbulence models significantly affect the simulated results. Among five turbulence models tested, the standard k-μ and the RSM models give consistent results.

The time scale for employing stochastic time tracking of particles affects simulated result. Caution has to be exerted to select the appropriate time constant value. In this study, the time constant value of 0.015 and 0.00015 produce consistent results.

Among four devolatilization models, the Kobayashi model produces slower devolatilization rate than the other models. The constant rate model produces the fastest devolatilization rate. The single rate model and the chemical percolation model produces moderate and consistent devolatilization rate. Slower devolatilization rate produces lower CO, but higher exit gas temperature, H_2, and CO_2, and hence both the heating value and gasification efficiency are lower.

Usually smaller particles have larger surface/volume ratio and react more quickly than larger particles. However, it is discovered that larger particles possess higher inertia after injection. Higher inertia produce higher slip velocity which increases higher convective transport and hence higher reaction rate. High inertia can also propel the particles cross the gas streamlines and increase particle-gas mixing which results in enhanced reaction rate. When the inertia continue increases as particle size increases, the injection jet impinges on the opposite jet and results in strong recirculation zones which can trap the particles and increase the residence time.

4.5 Topic 2: Investigation of Coal Gasification Process under Various Operating Conditions Inside A Two-Stage Entrained Flow Gasifier

(See Silaen and Wang (2012) in ASME Journal of Thermal Science and Engineering Applications for details.)

4.5.1 Boundary and Inlet Conditions

Indonesian sub-bituminous coal is used as feedstock in this study; its composition is given in Table 4.3. Boundary conditions for the baseline case are shown in Fig. 4.12. The summary of the studied cases are listed in Table 4.7. In the baseline (Case 1) of this study, coal-slurry-fed and two-stage configuration is used with fuel distribution of 75%-25% between the first and the second stages. Total mass flow rates of the coal slurry and the oxidant are 21.9 kg/s and 9.92 kg/s, respectively. The total mass flow rate of the dry coal powder case (Case 2) is 12.90 kg/s. The difference in fuel mass flow rates is caused by water added for slurry. The moisture in the coal is included in both slurry and dry feed cases. The coal/water weight ratio of the coal slurry is 60%-40%. Oxidant/coal slurry feed rate gives O_2/coal equivalence ratio of 0.4. The equivalence ratio is defined as the percentage of oxidant provided over the stoichiometric amount for complete combustion.

The oxidant is considered as a continuous flow and coal slurry is considered as a discrete flow. The discrete phase only includes the fixed carbon and water from the moisture content of coal (8.25% wt) and water added to make the slurry. The slurry coal is treated as particles containing both coal and liquid water. Other components of the coal, such as N, H, S, O, and ash, are injected as gas, together with the oxidant in the continuous flow. N is treated as N_2, H as H_2, and O as O_2. S and ash are not modeled and their masses are lumped into N_2. The coal slurry size is uniformly given as 50 μm for the purpose of conveniently tracking the particle size reducing rate. Investigation of effects of coal particle size on gasification performance has been performed by Silaen and Wang (2009 and 2010) and is not repeated here.

The walls are assigned as adiabatic with internal emissivity of 0.8. The boundary condition of the discrete phase at walls is assigned as “reflect”, which means the discrete

phase elastically rebound off once reaching the wall. At the outlet, the discrete phase simply escapes/exits the computational domain. The gasifier is operating at 24 atm.

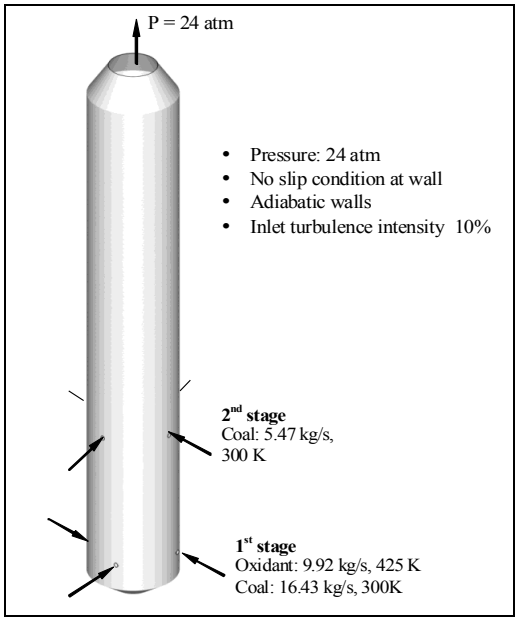

Fig. 4.12 Boundary conditions of the baseline case of the two-stage entrained-flow gasifier.

4.5.2 Results and Discussions of Various Operating Conditions

The following five cases are studied:

Case 1: Baseline case, oxygen-blown, coal slurry, 75%-25% distribution in 2 stages

Case 2: Oxygen-blown, dry coal, 75%-25% distribution in 2 stages.

Case 3: Oxygen-blown, coal slurry, 50%-50% distribution in 2 stages.

Case 4: Oxygen-blown, coal slurry, 100% distribution in the 1st stage.

Case 5: Air-blown, coal slurry, 75%-25% distribution in 2 stages

4.5.2.1 Baseline Case (Case 1)

The baseline case (Case 1) is the two-stage oxygen-blown operation with coal slurry distribution of 75%-25% between the first and the second stages. Gas temperature and species mole fraction distributions on the horizontal and center vertical planes in the gasifier are shown in Fig. 4.13. The gas temperature is seen higher in the region between the first stage and second stage injection locations than in the region above the second stage injection location. Maximum gas temperature in the first stage reaches 2400K (3860°F). The dominant reaction in the first stage is the intense char combustion ($C + ½ O_2 \rightarrow CO$ and $CO + ½ O_2 \rightarrow CO_2$) in the first stage and gasification reactions (mainly char-CO_2 gasification, $C + ½ CO_2 \rightarrow CO$) in the second stage. Oxygen is completely depleted through the char combustion in the first stage. Char gasification is enhanced in the second stage with the injection of the remaining coal without oxygen. Char is

gasified with CO_2 produced in the first stage through reaction $C + CO_2 \rightarrow CO$ and with H_2O through reaction $C + H_2O \rightarrow CO + H_2$.

Table 4.7 Parameter and operating conditions of the studied cases. The changed parameters are highlighted.

Parameters	*Case 1*			*Case 2*			*Case 3*			*Case 4*			*Case 5*		
Type															
Fuel	Slurry			**Dry**			Slurry			Slurry			Slurry		
Oxidant	Oxygen			Oxygen			Oxygen			Oxygen			**Air**		
Stage	*1*	*2*	*Total*	*1*	*2*	*Total*	*1*	*2*	*Total*	*1*	*2*	*Total*	*1*	*2*	*Total*
Distribution															
Fuel	75%	25%		75%	25%		**50%**	**50%**		**100%**	**0%**		75%	25%	
Oxidant	100%	0%		100%	0%		100%	0%		100%	0%		100%	0%	
Mass flow rate															
Fuel (kg/s)	16.43	5.47	21.9	9.47	3.16	12.90	10.95	10.95	21.90	21.90	0.00	21.90	8.12	2.70	10.82
Oxidant (kg/s)	9.92	0.00	9.92	9.92	0.00	9.92	9.92	0.00	9.92	9.92	0.00	9.92	21.00	0.00	21.00

*** Oxidant for Case 5 is air (78% N_2, 22% O_2).**

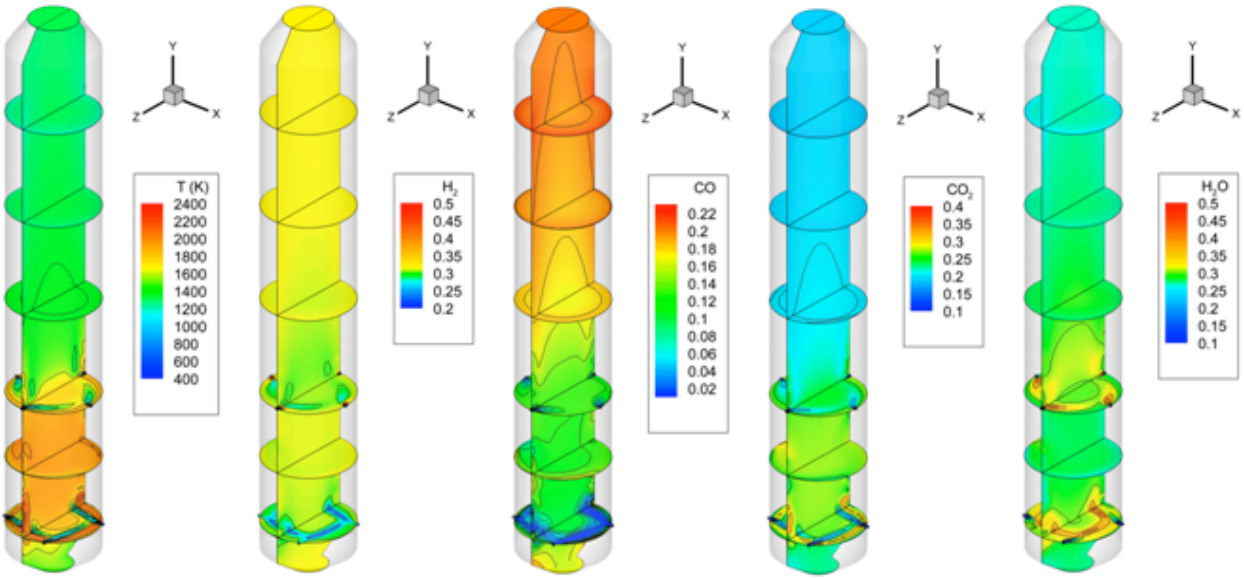

Fig. 4.13 Gas temperature and species mole fraction distributions for Case 1 (2-stage, 75%-25%, coal slurry, oxygen-blown).

Mass-weighted averages of gas temperature and species mole fractions along the gasifier height for Case 1 are shown in Fig. 4.14. The dips in the graphs occur at the injector elevations at heights of 0.75 m for the first stage and 3 m for the second stage. The CO_2 mole fraction and the gas temperature decrease from roughly 27% to roughly 19% as the gas flows from the first stage to the second stage. On the other hand, CO mole fraction increases from 12% to 20%, due to the endothermic char-CO_2 (R1.2) gasification mentioned above. Meanwhile, the increase in the average mole fraction of H_2 in the second stage is negligible. This may indicate that char-CO_2 gasification is more dominant than char-H_2O gasification in the second stage.

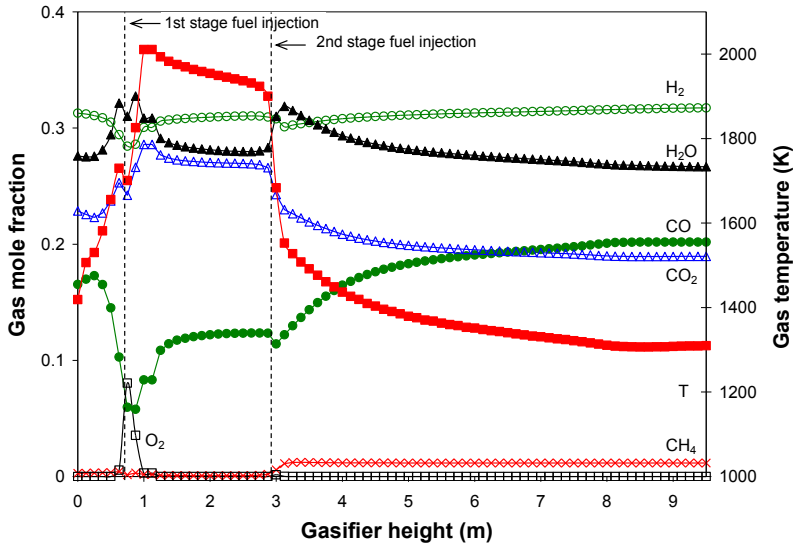

Fig. 4.14 Mass-weighted averages of gas temperature and species mole fraction distributions along gasifier height for Case 1 (2-stage, 75%-25%, coal slurry, oxygen-blown)

At the gasifier height of 8.5 m, the graphs for the average gas temperature and gas mole fractions flatten out. This indicates that the rates of reactions are slowing down. Making the gasifier longer or higher would probably not make significant change in the syngas temperature and compositions. The significant temperature drop from roughly 1900K (2960°F) to 1500K (2240°F) across the second stage clearly indicates the advantage of injecting only coal at the second stage to protect the refractory liner and reduce the maintenance cost.

Fig. 4.15(a) shows helical flow pathlines inside the gasifier; the helical pattern lengthens the flow residence time to allow more time for the reactions to take place. Velocity vectors on vertical midplane and horizontal injection levels are presented in Fig. 4.16. Due to the vortex generated by the tangential fuel injections in the first stage, strong upward flow occurs near the wall, and weak downward flow occurs in the center. The central core near the second stage exhibits an almost stagnant region due to the opposing fuel injections at the second stage. The flow below the first stage injection level is weak, which could result in some gas being trapped. The momentum of each jet in the second stage is not strong enough to reach the center, and hence the jets are swept upward by the strong main flow from the first stage. Figure 4.15(b) shows the coal particle distribution. The particles injected in the first stage are depleted fairly quickly, while those injected in the second stage are depleted at a slow rate.

Exit syngas temperature and mole fraction compositions are listed in Table 4.8. Carbon conversion efficiency is 99.4%, which is the comparison of the total mass of

carbon injected into the gasifier to the total mass of carbon at the gasifier exit. The high heating value (HHV) of the exit syngas is 8.24 MJ/kg.

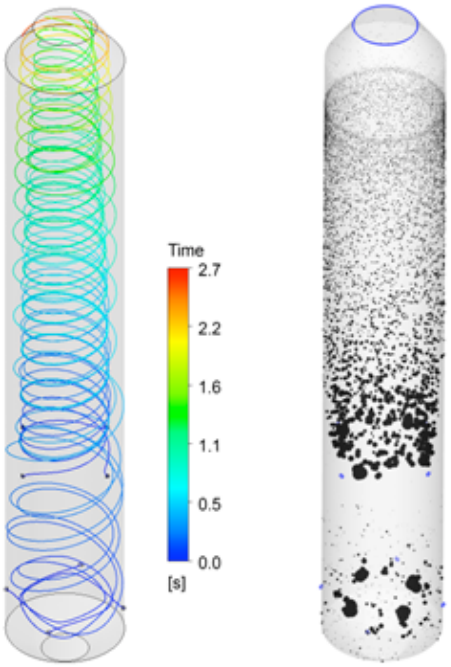

(a) (b)

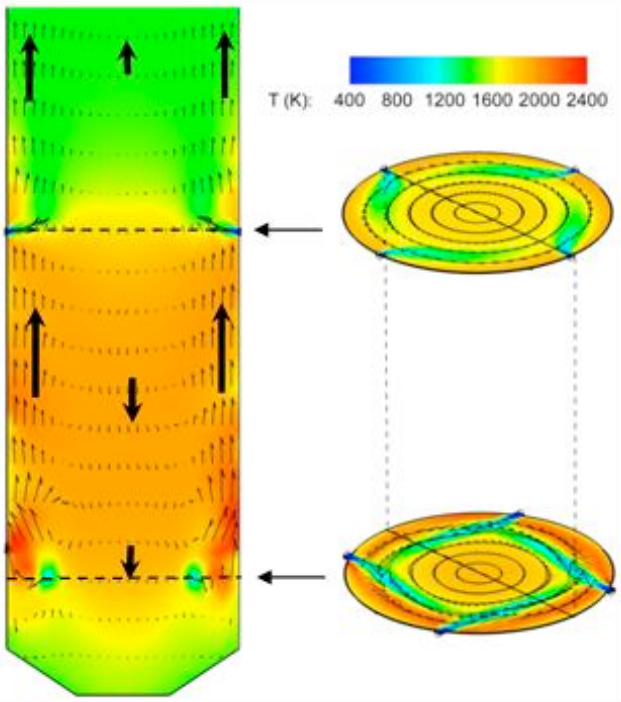

ig. 4.16 Velocity vectors and temperature
idance time temperature and (b) particle
ield on the center vertical plane and injection
tribution for Case 1
planes for Case 1

Table 4.8 Exit syngas temperatures and compositions

	Case 1	***Case 2***	***Case 3***	***Case 4***	***Case 5***
Fuel distribution	2-stage (75%-25%)	2-stage (75%-25%)	2-stage (50%-50%)	1-stage	2-stage (75%-25%)
Oxidant	oxygen	oxygen	oxygen	oxygen	air
Fuel type	slurry	dry	slurry	slurry	slurry
Exit syngas:					
T (K)	1310	1882	1250	1407	1143
T (°F)	1898	2928	1790	2073	1598
Mole fraction:					
H_2	31.7%	33.8%	31.1%	32.2%	19.0%
CO	20.2%	31.4%	19.7%	21.5%	7.6%
CO_2	18.9%	19.0%	19.2%	18.0%	12.5%
CH_4	1.2%	1.7%	1.3%	0.7%	0.4%
H_2O	26.7%	0.8%	27.4%	26.3%	16.4%
N_2	1.3%	13.3%	1.3%	1.3%	44.1%
O_2	0.0%	0.0%	0.0%	0.0%	0.0%
Carbon conversion efficiency	99.4%	100.0%	98.3%	94.8%	77.3%
HHV at 25°C (MJ/kg)	8.24	9.45	9.03	7.68	4.40

4.5.2.2 Effects of Coal Mixture (Slurry vs. Dry)

Case 2 is conducted to investigate the effects of using dry coal as the fuel. Coal and oxidant feed rates are kept the same as for Case 1. Nitrogen is used as the transport gas for the coal powder. The amount of N_2 transport gas used is 0.3 times the mass of coal powder. The same fuel and oxidant distributions as in Case 1 are used, which is two-stage operation with 75%-25% fuel distribution between the first and second stages and 100% oxidant injected into the first stage with no oxidant injection at the second stage.

The distribution of gas temperature presented in Fig. 4.17 shows that the local highest temperature in the first stage is approximately 3200 K (5300°F), which is 800 K (1440°F) higher than the coal slurry case (Case 1). Unlike the coal slurry case, the dry coal case does not have a lot of H_2O to absorb the heat released by the char combustion, nor does much water react with char through the char-H_2O gasification. H_2O presented

in Case 2 comes from the moisture contained in the coal, while H_2O in Case 1 comes from both the moisture contained in the coal and water added to the coal to make the slurry. This higher gas temperature means that the fuel injectors and refractory liner in the first stage will experience more severe thermal loading and maintenance issues than in the coal slurry operation.

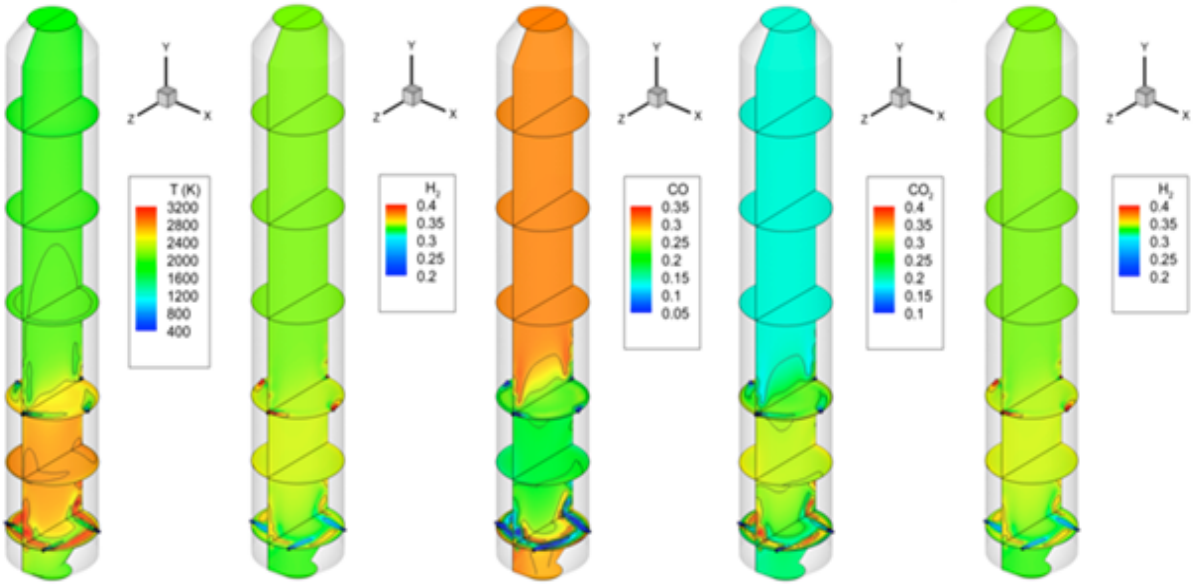

Fig. 4.17 Gas temperature and species mole fraction distributions for Case 2 (2-stage, 75%-25%, dry coal, oxygen-blown).

As seen in Fig. 4.18, the average CO mole fraction in the first stage is slightly higher than in the coal slurry case (Case 1), approximately 19% versus 12%. The same is observed for the average CO_2 and H_2 mole fractions, 30% for CO_2 and 34% for H_2 in the dry coal case compared to 27% for CO_2 and 31% for H_2 in the coal slurry case.

Similar to the coal slurry operation in Case 1, char gasification is enhanced in the second stage by injecting the remaining fresh coal. But because the coal injected is dry coal, char gasification that occurs is mainly char-CO_2 gasification.

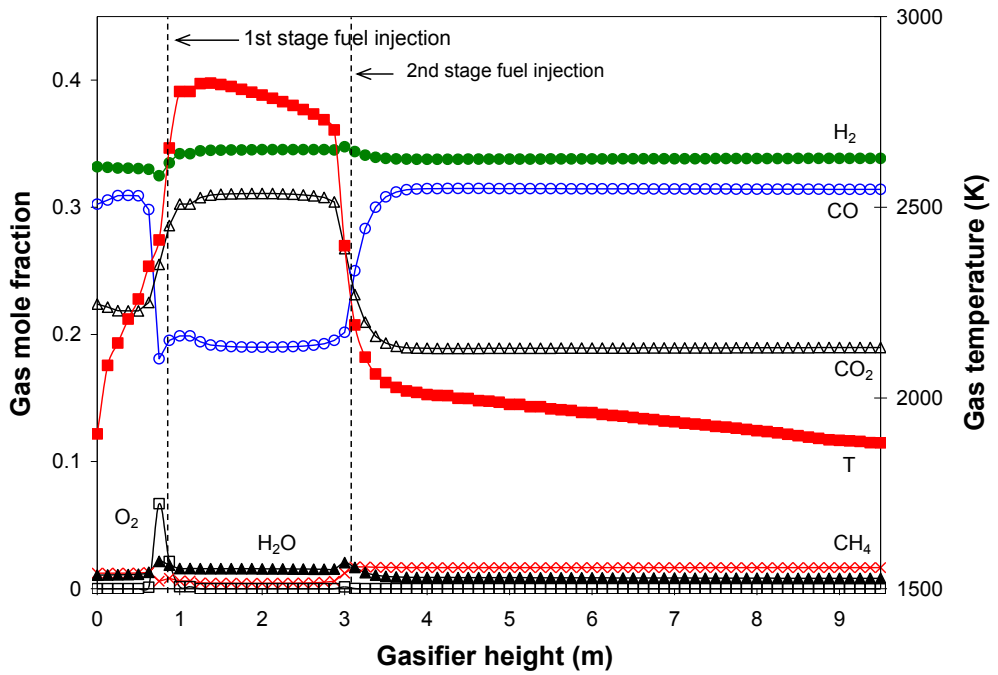

Fig. 4.18 Mass-weighted averages of gas temperature and species mole fraction distributions along gasifier height for Case 2 (2-stage, 75%-25%, dry coal, oxygen-blown).

Both Figs. 4.17 and 4.18 show a significant increase in CO (from approximately 19% to 31%) and decrease in CO_2 (from approximately 30% to 19%) in the second stage, due to the char-CO_2 gasification. Minor char-H_2O reaction also occurs in the second stage. The small decrease in H_2 in the second stage is due to dilution by the additional coal.

The average temperature of the exit syngas listed in Table 4.8 is 1882 K (2928°F), which is 572 K (1030°F) higher than the syngas for the coal slurry case (Case 1), due to lack of steam in the dry coal operation. Compared to the coal slurry case, there is less H_2O to absorb the heat from the char combustion and less H_2O to react with C through the endothermic char-H_2O reaction.

H_2 and CO_2 contents of the syngas are higher than those of the coal slurry case, 33.8% and 31.4% versus 31.7% and 20.2%, respectively. The syngas HHV of the dry coal case is also higher than the coal slurry case, 9.45 MJ/kg versus 8.24 MJ/kg. Of course, a higher heating value is better. However, in addition to potential increased maintenance issue related to fuel injectors and refractory liner, the higher syngas temperature of the dry coal case means that thermal efficiency will reduce when the syngas temperature is cooled down to the acceptable level for operating the downstream gas clean-up system. Although syngas cooler can transfer the thermal energy of the high raw syngas temperature to high-pressure steam, degradation of the energy quality will inevitably affect the overall plant thermal efficiency.

4.5.2.3 Effects of Fuel Distribution

In the baseline case (Case 1), fuel is distributed by 75%-25% between the first and the second stages. Cases 3 & 4 are conducted to study the effects of different fuel distributions. In Case 3, the fuel is evenly distributed between the first and the second stages, i.e. 50%-50%. In Case 4, all (100%) of the fuel is injected in the first stage. In other words, Case 4 simulates the one-stage operation of the gasifier. The same total feed rate of coal slurry and oxidant in Case 1 is used in Cases 3 & 4. As in Case 1, all of the oxidant is injected in the first stage.

Figure 4.19 presents the comparison of average gas temperature and species mole fractions for Cases 1, 3, and 4. Higher mass-weighted average gas temperature 2500 K (4040°F) occurs in the first stage for Case 3 (50%-50%) compared to 1900 K (2960°F) of Case 1 (75%-25%) and is due to the higher O_2/char ratio in the first stage for Case 3. Higher O_2/char causes more char to burn, resulting in a higher average gas temperature. However, counter-intuitively, lower O_2/char ratio in Case 4 (100%-0%) in the 1st stage also produces higher average gas temperature than Case 1. A plausible explanation would be that the higher temperature in Case 3 is not actually caused by rich combustion as first thought, but it is caused by less water presence, and hence, less heat capacity to absorb heat generated by combustion. This explanation can be supported by the high oxygen and CO_2 concentrations but low CO and H_2 concentration in the first stage of Case 3 shown in Fig. 4.19. This means combustion in the 1st stage in Case 3 is complete (i.e. high CO_2) but the gasification process is less productive (i.e. low CO and H_2). On the other hand, in Case 4 when 100% coal is injected in the 1st stage, oxygen is quickly consumed (i.e. low O_2) to produce CO with high temperature. The relatively lower average gas temperature in the injector area for Case 1 (75%-25%) has the benefit of helping prolong the life of fuel injectors and refractory liners.

The graph of O_2 mole fraction for Case 3 shows that a little amount of O_2 still exists when the gas reaches the second stage injection level. This means that char has a good opportunity to react with the abundant O_2 at the first stage. Meanwhile, for Case 1 (75%-25%) and Case 4 (100%-0%), O_2 is quickly completely depleted in the first stage. The comparison of CO and CO_2 mole fractions for all three cases confirms that char combustion is more intense in Case 3. Case 3 has the highest CO_2 mole fraction and the lowest CO mole fraction in the first stage. It implies that a large amount of char in the first stage goes through complete combustion. Case 4 (100%-0%), which has the lowest O_2/char ratio in the first stage, has the lowest CO_2 mole fraction and the highest CO mole fraction.

The exit syngas composition listed in Table 4.8 indicates that among the three cases, Case 4 (100%-0%) yields the highest H_2 production – 32.2% compared to 31.7% for Case 1 (75%-25%) and 31.1% for Case 3 (50%-50%). Case 4 also has the highest CO production – 21.5% compared to 20.2% for Case 1 and 19.7% for Case 3. However,

Case 4 has the highest exit syngas temperature at 1407 K. Syngas temperature for Cases 1 and 3 are 1310 K and 1250 K, respectively.

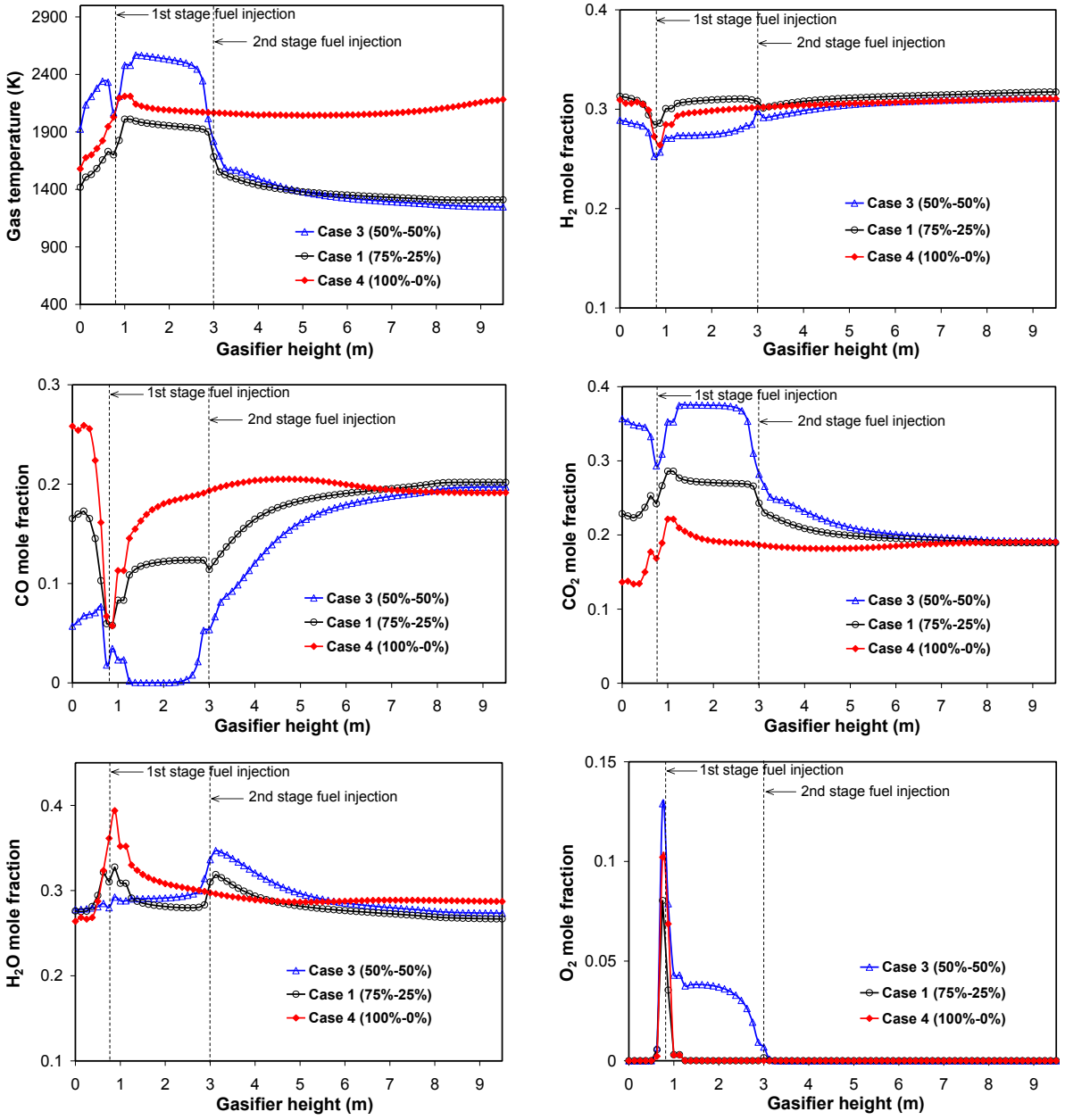

Fig. 4.19 Mass-weighted averages of gas temperature and species mole fraction distributions along gasifier height for Cases 1, 3 and 4.

Even though Case 4 has the highest H_2, CO and CH_4 combined, its syngas high heating value is the lowest among three cases. Case 4's HHV is 7.68 MJ/kg, compared to 8.24 MJ/kg for Case 1 and 9.03 MJ/kg for Case 3. This is due to the lower carbon conversion efficiency of Case 4 (94.8%) compared to the other two cases (99.4% for

Case 1 and 98.3% for Case 3). The exit syngas of Case 4 contains the most unreacted char. Thus, combined with its high temperature, it has the lowest HHV. Note that when the syngas exit temperature is high more chemical energy has been converted to the sensible heat of the syngas and less chemical energy is reserved in the syngas. This sensible heat could be effectively used in the gas turbine combustor if the syngas could be fed directly into the gas turbine combustor without going through the gas cleanup. In reality, the sensible heat will be used to produce steam to produce power through the steam turbine because the syngas temperature needs to be reduced for cleaning and desulfurization.

Based on the syngas temperature and composition, the 50%-50% fuel distribution (Case 3) gives the best result. It has the highest syngas HHV (9.03 MJ/kg) even though its carbon conversion efficiency (98.3%) is slightly lower than that of the 75%-25% case (Case 1 with carbon conversion efficiency of 99.4%). Besides the highest syngas HHV, Case 3 has the lowest syngas temperature (1250 K, 1790°F). This lowest syngas temperature compared to the other cases means that there will be less energy loss during the syngas clean-up process. However, its mass-weighted average of gas temperature (2500 K, 4040°F) in the first stage is highest compared to those of the other cases, 1900 K (2960°F) for Case 1 and 1500 K (2240°F) for Case 4. This high gas temperature will put the gasifier's fuel injectors and wall refractory bricks in a higher thermal loading; consequently, they will be more prone to failure and require more maintenance.

Velocity vectors on vertical midplane and horizontal injection levels for Case 3 are presented in Fig. 4.20. With 50% of the fuel injected in the second stage, the fuel jests are stronger than in Case 1 (Fig. 4.16) and are able to penetrate deeper to the center crossing the upcoming flow from the first stage.

4.5.2.4 Effects of Oxidant (Oxygen-Blown vs. Air-Blown)

Case 5 simulates the air-blown two-stage operation of the gasifier. Air with composition of 22% O_2 and 78% N_2 by weight is used as the oxidant. The O_2/C mole ratio is maintained the same as in Case 1 (oxygen-blown) which is 0.4. Total feed rate of coal and oxidant combined is the same as for Case 1. Similar to Case 1, the fuel is distributed 75% and 25% between the first and the second stages.

As expected, the mass-weighted average of gas temperature in the first stage shown in Fig. 4.21 is lower than in Case 1 (oxygen-blown) due to the abundance of N_2 as a diluent in the air-blown case. The maximum cross-sectional mass weighted average gas temperature is approximately 1450 K (2150°F), while the maximum average gas temperature in the oxygen-blown case is 2000 K (3140°F).

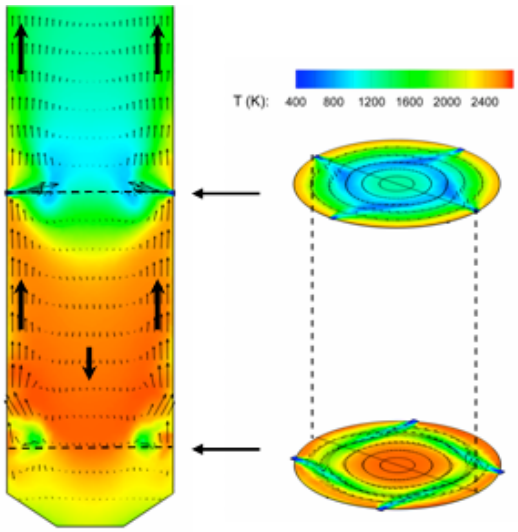

Fig. 4.20 Velocity vectors and temperature field on the center vertical plane and injection planes for Case 3 (50%-50%)

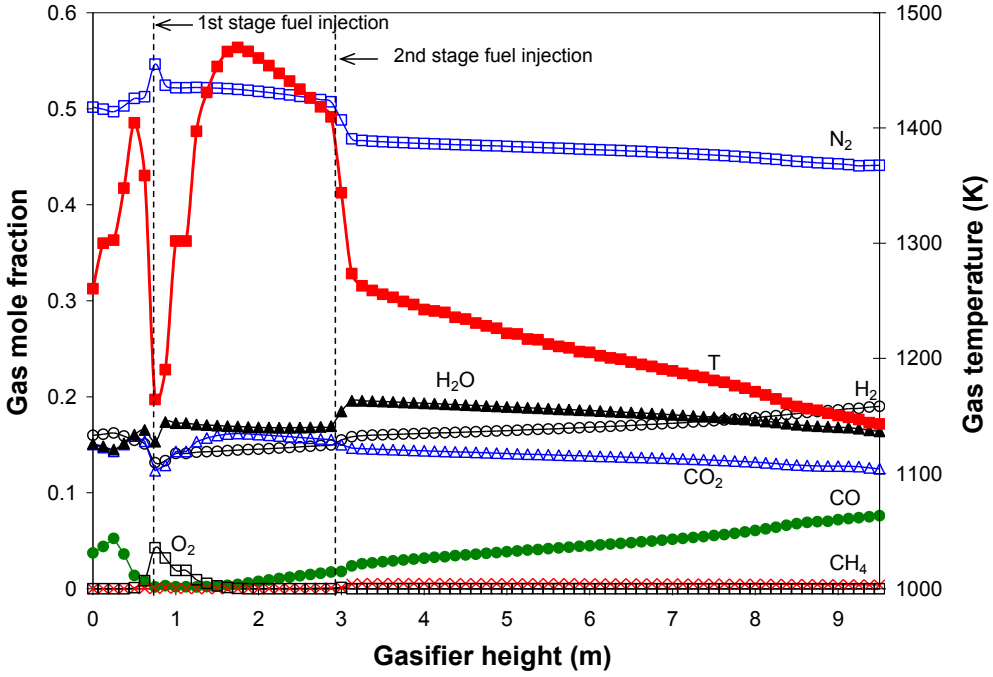

Fig. 4.21 Mass-weighted averages of gas temperature and species mole fraction distributions along gasifier height for Case 5 (2-stage, 75%-25%, coal slurry, air-blown)

The syngas composition listed in Table 4.8 shows that the mole fraction ratio of CO/H_2 is 0.4 for the air-blown case (Case 5), which is much lower than those of the oxygen-blown case (Case 1). The syngas HHV for Case 5 is approximately only half of Case 1, 4.40 MJ/kg vs. 8.24 MJ/kg. The syngas of Case 5 is diluted with N_2, which causes this low heating value. However, its low carbon conversion efficiency at 77.3% also contributes to this low syngas heating value. Low carbon conversion efficiency is

due to the lower overall gas temperature inside the gasifier, where less energy is available to drive the endothermic gasification reactions.

To give a fair comparison between the syngas in Cases 1 and 5, syngas compositions and heating values for both cases are recalculated after the N_2 contained in the syngas are removed. The recalculated compositions are compared in Table 4.9. The mole fraction of H_2 (34.0%) for the air-blown case (Case 5) becomes slightly higher than the oxygen-blown (Case 1, 32.1%), but the CO mole fraction for the air-blown (13.6%) is 6.5 percentage points lower than the oxygen-blown case. As expected, the heating value of the syngas increases from 4.40 MJ/kg to 7.26 MJ/kg after N_2 is removed. Nonetheless, this recalculated syngas heating value is still lower by roughly 1 MJ/kg than that of the oxygen-blown case (8.25 MJ/kg) even after N_2 is removed.

Table 4.9 Comparison of exit syngas temperature and composition between Cases 1 and 5 after N_2 is removed from the syngas.

	Case 1	***Case 5***
Fuel distribution	2-stage (75%-25%)	2-stage (75%-25%)
Oxidant	oxygen	air
Fuel type	slurry	slurry
Exit syngas:		
T (K)	1310	1143
Mole fraction:		
H_2	32.1%	34.0%
CO	20.5%	13.6%
CO_2	19.1%	22.4%
CH_4	1.2%	0.7%
H_2O	27.1%	29.3%
O_2	0.0%	0.0%
Carbon conversion efficiency	99.4%	77.3%
HHV at 25°C (MJ/kg)	8.25	7.26

4.5.3 Conclusions for Various Operating Conditions

Effects of Coal Mixture (Slurry vs. Dry)

The temperature in the first stage for the dry-fed case is approximately 2800 K (4580°F), which is 400 K (720°F) higher than the slurry-fed case. Unlike the slurry-fed case, the dry-fed case does not have a lot of H_2O to absorb the heat released by the char

combustion, nor does much steam react with char through the char-H_2O gasification. This higher gas temperature means that the fuel injectors and refractory walls in the first stage will experience higher thermal loading than in the coal slurry operation. The syngas HHV of the dry coal case is also higher than the coal slurry case -- 9.45 MJ/kg vs. 8.24 MJ/kg. However, the higher syngas temperature of the dry coal case would result in a lower plant thermal efficiency because it needs to be cooled before it goes through the gas clean-up system downstream of the gasifier. Consequently, a lot of energy will be downgraded (i.e. loss of exergy) via waste heat exchanger even though part of the energy can be recovered to produce superheated steam to generate electricity through the steam turbine.

Effects of Fuel Distribution between Two Stages

Due to less water to absorb heat, reducing the fuel feed in the first stage does result in higher gas temperatures in the first stage. One-stage operation yields higher H_2, CO and CH_4 combined than if a two-stage operation is used but with a lower syngas heating value. The 50%-50% fuel distribution case yields the highest syngas HHV and lowest syngas exit temperature among the studied cases. The exit syngas of one-stage operation contains the most unreacted char, combined with its high exit temperature, results in the lowest heating value.

Effects of Oxidant (Oxygen-Blown vs. Air-Blown)

Gas temperature inside the gasifier for the air-blown case is lower than in the oxygen-blown gasifier due to the abundant presence of N_2. Lower than the oxygen-blown case (99.4%), the carbon conversion efficiency of the air-blown case is 77.3%. The syngas heating value for the air-blown case is 4.40 MJ/kg, which is almost half of the heating value of the oxygen-blown case (8.24 MJ/kg). Even when N_2 is removed for comparison, the HHV of the air-blown case is still about 1 MJ/kg less than the oxygen-blown case.

4.6 Topic 3: Water-Gas Shift Modeling in Coal Gasification

(See Lu and Wang (2013) in FUEL for details.)

Gasification is an incomplete oxidation process of converting various carbon-based feedstocks into clean synthetic gas (syngas), which is primarily a mixture of hydrogen (H_2) and carbon monoxide (CO), with minor amounts of methane (CH_4) and inert nitrogen gas (N_2). Syngas coming out of a gasifier is usually very hot. Cooling is necessary to allow this syngas to be transported without damaging downstream piping or equipment. Furthermore, the existing cold syngas cleaning technology also requires that the syngas temperature to be reduced below 600^{o}F. The syngas cooling process would significantly reduce the thermal efficiency of the system if care is not taken to employ the energy cascading scheme to properly maintain the grade (or quality) of the energy during the heat transfer process by applying cooling at different temperature ranges with an optimum pinch point for each cooling stage in a sequentially descending order. Radiant syngas coolers have been usually employed to achieve the highest thermal efficiency. However, a radiant syngas cooler is large, bulky, and expensive, so the direct syngas quenching process has also been adopted for the benefits of reduced space, cost, and maintenance, although it is accompanied by reduced thermal efficiency. A rule of thumb is that a gasification system using a radiant syngas cooler will have approximately 2-3 percentage points higher thermal efficiency than a unit employing the quenching scheme.

Recently, as carbon capture and sequestration (CCS) has become an important approach to curb global warming, the syngas quenching approach has become more popular in the gasification process because CCS typically employs the water-shift process (WGS) ($CO + H_2O \Leftrightarrow CO_2 + H_2$) to convert steam and CO to CO_2 and H_2, and, in this process, relatively low-temperature steam (below 600^{o}C, see Table 4.10) is required to allow the reaction to move in forward direction towards products. Since a large amount of relatively low-temperature steam is required, it might as well just directly employ quench cooling. This will allow preliminary water-shifting to occur and also provides the possibility of utilizing the quench chamber to serve as the first-stage shift reactor, thus removing the cost of installing an actual first-stage shift reactor. In addition to providing cooling and driving the WGS reaction, a water quench can also help clean out ash and other particulate matter. These additional benefits unfortunately are accompanied with another disadvantage: the unburned chars can also be washed away, causing a downgrade in the carbon conversion efficiency.

Table 4.10 Water-gas shift (WGS) reaction equilibrium balance constant

T(^{o}C)	600	800	1000	1200	1400

$\log K_p$	1.396	0.553	0.076	-0.222	-0.424

The WGS reaction rate has been discovered to play an important role in affecting the accurate prediction of the syngas composition during simulations of the gasification process. The earliest data recording the WGS reaction dates back to 1888, and its prominence came with the Haber ammonia synthesis process and catalyst development by Bosch and Wilde in 1912. Most of the reaction rates for the WGS reaction were obtained from experiments with specific catalysts under laboratory conditions of relatively narrow ranges of pressure and temperature. A few of the reaction rates without using catalysts were obtained under various supercritical (water) conditions because a large excess of water solvent could possibly drive the reaction to produce hydrogen without a catalyst. However, the pressure under a supercritical condition is much higher than that in an operating gasifier. In either case, it is not clear how the published reaction rates can be trustfully used to predict the actual WGS reaction rate in a gasifier without the presence of catalysts and under different temperature and pressure conditions than those used in the laboratory. Due to the unavailability of appropriate WGS reaction rates for broad operating conditions in actual gasifiers, the objective of this study is to obtain an appropriate representative WGS global reaction rate under non-catalytic conditions by calibrating the WGS rate against the experimental data from water quench section of an experimental gaisifer, then apply the calibrated WGS reaction rate to CFD simulation of fully gasification process.

4.6.1 Review of WGS Reaction Rates

WGS Catalytic Reactions

Chen et al. (2008) investigated the characteristics of carbon monoxide conversion and hydrogen generation from the WGS reaction experimentally using a high-temperature catalyst and a low-temperature catalyst. The important parameters, including the catalyst type, residence time of the reactants in the catalyst bed, reaction temperature, and CO/steam ratio, were addressed as the influential factors that affected the performance of the WGS reaction. The experimental results showed that when the residence time was as long as 0.09s, the WGS developed well no matter which catalyst was used. It also revealed that the WGS reactions with the high-temperature catalyst and the low-temperature catalyst were governed by chemical kinetics and thermodynamic equilibrium.

It is difficult to narrow down the expression for the WGS reaction with a catalyst because the rate of the reaction is dependent on various parameters, including the composition of the catalyst, the active surface area and structure of the catalyst, the size of the catalyst, age of the catalyst, the operating temperature and pressure, and the composition of the gases. Smith, et al. (2010) made a comprehensive review of research

on the WGS reaction rate and the developments in modeling approaches for designing WGS reactors. They consolidated a listing of the various important kinetic expressions published for both the high temperature and the low temperature water-gas shift reactions along with the details of the make-up of the catalysts and the operating conditions at which the kinetics were obtained. Selected studies from Smith et al.'s review are shown in Tables 4.11-13.

Table 4.11 WGS Reaction Rate with Noble Metal Catalysts (Smith et al., 2010)

Catalyst	Opertating Conditions	Arrhenius Parameters		Reference
		A	E (kJ/mol)	
Ru	300°C-1000°C 0.008 to 0.05 contact time Coated on alumina support 5wt% loading	1.6×10^7 (1/s)	80	Wheeler et al. (2004)
Ru/Ceria		5.0×10^7 (1/s)	80	
Ni		8.0×10^7 (1/s)	85	
Ni/Ceria		1.7×10^8(1/s)	85	
Pd		4.0×10^6(1/s)	100	
Pd/Ceria		4.0×10^7(1/s)	100	
Pt		1.0×10^6(1/s)	80	
Pt/Ceria		2.5×10^7(1/s)	80	
Rh/SiO_2	350°C	3.23×10^6 (molecules/s/site)	22.8±2.5 (kcal/mole)	Grenoble et al. (1981)
Pt/Al_2O_3	270°C	1.9×10^6 (molecules/s/site)	19.6±2.5 (kcal/mole)	
Pt/SiO_2	340°C	1.9×10^6 (molecules/s/site)	19.1±0.8 (kcal/mole)	
Pt/C	340°C	3.84×10^6 (molecules/s/site)	25.5±1.4 (kcal/mole)	
$CuO.1CeO.8O_{2-y}$ (Cu ceria)	200°C - 350°C	1.8×10^3 (1/s)	61	Kusar et al. (2006)
$CuO.1CeO.8O_{2-y}$ (Cu ceria)	300°C - 350°C	4.0×10^3 (1/s)	78	

Table 4.12 WGS Reaction Rate with High-Temperature Catalysts (310°C-450°C) (Smith et al., 2010)

Catalyst	Operating Conditions	Arrhenius Parameters		Reference
		A	E (kJ/mol)	
Power plant data	1/4" × 3/8",2.20g/cm^3	9.4 × 10^7 (1/s)	21.4(kCal/gmol)	Rase (1977)
Fe_3O_4/Cr_2O_3	3-5bar, 573°C-633°C	ln A = 26.1	95	Keiski et al.(1996)
Fe_3O_4/Cr_2O_3 8wt% Cr_2O_3	1atm, 350°C-440°C	ln A = 11.5	112	Rhodes et al. (2003)
Fe_3O_4/Cr_2O_3	1bar, 380°C-450°C	ln A = 10.1±0.2	118±1	
Fe_3O_4/Cr_2O_3	6bar, 380°C-450°C	ln A = 12.0±0.2	124±1	
Fe_3O_4/Cr_2O_3	27bar, 350°C-450°C	ln A = 7.4±0.1	111±1	
80-95% Fe_3O_4, 5-10% Cr_2O_3, 1-5%CuO	1atm, 450°C	$10^{0.659}$(mol/gcat-s)	88	San et al. (2009)

Table 4.13 WGS Reaction Rate with Low-Temperature Catalysts (200°C-250°C) (Smith et al., 2010)

Catalyst	Opertating Conditions	Arrhenius Parameters		Reference
		A	E (kJ/mol)	
ICI 52-1 (Copper based catalyst) density=5.83g/cm^3	1atm, 200°C	K = 5.37 × 10^{-7} (mol/m^{2}s)/atm^{1+m}		Salmi et al. (1989)
Cu-ZnO-Al_2O_3 (EX-2248)Sud Chemie	200-250µm, 120-250°C	lnA = 12.6	47.4	Choi et al. (2003)
42% CuO-ZnO-Al_2O_3	123°C-175°C CO/H_2O=1/3	4.9 × 10^6 (S^{-1})	71	Henrik et al. (2006)

$CuO-ZnO-Al_2O_3$	1atm, 200°C	-	79	Koryabkina et al. (2003)

WGS non-catalytic reactions

The above studies reviewed by Smith, et al. (2010) are all involved with catalysts, whereas those studies without using catalysts were all conducted under supercritical (water) conditions. Watanabe et al. (2001) did the research on the partial oxidation of *n*-hexadecane at 673K in supercritical water and found that when a carbon to oxygen ratio of 3:1 was used, the CO concentration in the products could reach almost 40%. So, it is possible to use partial oxidation of hydrocarbons to produce CO via the WGS reaction. In other words, it is possible to develop a non-catalytic way of reforming hydrocarbons without using high temperatures (1073-1273K).

Hirth and Franck (1993) reported the equilibrium constant K_a of WGS reaction at 773-873K and 40MPa. It is also mentioned that K_a is largely different from that in the ideal gas state and the equilibrium shifted to the reactants' side with increasing pressure. Holgate et al. (1992) proposed a global rate expression of the WGS reaction by conducting experiments in non-catalytic, supercritical conditions at 712-866K at 24.6MPa, $R_{WGS} = 10^{2.6\pm1.2} \exp[(-67\pm11)/RT](CO)^{0.81\pm0.19}$.

Sato et al. (2004) studied the kinetics of the WGS reaction under non-catalytic, supercritical conditions (653-713K and 10-30MPa) with an initial CO/H_2O ratio of 0.03 in a flow-type reactor. By analyzing the rate constants obtained by their study and those reported previously, a global reaction model for the WGS reaction under supercritical conditions was proposed as $k = 10^{5.58\pm1.38} \exp(-1.16 \pm 0.19 \times 10^5/RT)$ /s at 10-59.6 MPa and 653-866K. Wade et al. (2008) conducted experiments on the WGS reaction non-catalytically in the temperature range of 770 to 1050 K with an operating pressure of 24 MPa. They obtained the rate constants of $A = 2.512 \times 10^5$ and $E = 1.325 \times 10^5$ J/mol.

NETL (2004) evaluated the reverse WGS reaction rate in an empty quartz reactor at elevated-temperature (1148-1198K), low-pressure (0.1MPa) conditions in the absence of a diluent gas. The rate they proposed is $A = 1.09 \times 10^7$ $L^{0.5}mole^{-0.5}s^{-1}$ and E = 222 kJ/mol. Meanwhile, experiment at high temperature, high pressure conditions (up to 1.6 MPa) was also conducted in a pressure-equilibrated quartz reactor, the results yielded $A = 5.99 \times 10^8$ $L^{0.5}mole^{-0.5}s^{-1}$ and E = 218kJ/mol. For forward WGS reaction rate, NETL (2005) studied under conditions of high temperature (1070-1134K) and both low (0.1MPa) and high pressure (1.6MPa). The forward rate they got is $A = 4.7 \times 10^8$ $L^{0.5}mole^{-0.5}s^{-1}$ and E = 288.3 kJ/mol. Further, they also proposed that the effect of the high pressure condition on the forward reaction rate was negligible.

Siemens (2011) experimental investigated thermodynamic equilibrium of WGS reaction under water quench process. They proposed that thermodynamic equilibrium of the WGS reaction cannot be achieved for realistic residence times due to kinetic limitations for temperature below 1223K. Nevertheless, catalytic effects caused by gasification ash or slag may enhance CO conversion within water quench section under the condition of atmospheric pressure and the temperature between 773 and 1273K.

4.6.2 WGS Reaction Rates Used in CFD Modeling

Usually, there are two approaches to modeling the WGS reaction rate in CFD. The first approach is to use the detailed kinetics with both forward and backward elementary reactions. In this approach, the rates of the elementary reactions are usually too many to be calculated in the CFD model, so the reaction rates are calculated separately in another software package, like Chemkin, at each iteration as the local temperature and pressure change. The advantage of this approach is that it provides the most appropriate vehicle to model the correct kinetics for the reaction rates, while the disadvantages are that the elementary kinetics may not be adequately known and that it could be difficult to achieve convergence in CFD computation. The second approach is to use Global Reaction Rates that are obtained by experiments. Since the rates are global, the rates usually reflect the net rate between the difference of the forward and backward rates. The advantages are that the global rates simplify the complex CFD modeling and conserve the computational power, while the disadvantages are that (a) the experimental data are usually obtained in relatively narrow temperature and pressure ranges, (b) the rates are usually obtained when the products are lean and the presence of other species commonly in a gasifier is nonexistent, and (c) there is still a lack of sufficient data covering the entire span of the temperature range for the gasification process.

Watanabe and Otaka (2006) performed a numerical simulation with the coal gasification model on the Japanese 2 tons/day, research scale coal gasifier supported by the Central Research Institute of Electric Power Industry (CRIEPI). The rate constants of the WGS reaction that they used is $A = 2.75 \times 10^{10}$ and $E = 8.37 \times 10^{7}$ J/kmol for the forward reaction rate and $A = 2.65 \times 10^{-2}$ and $E = 3.96 \times 10^{3}$ J/kmol for the backward reaction rate. The influence of the air ratio on gasification performance, gas temperature distribution, and product gas composition were presented and discussed in their paper. The numerically simulated results were compared favorably with the experimental data, and most features of the gasification process were claimed to have been captured adequately. Ajilkumar et al. (2008) used the same WGS finite rate constant as employed by Watanabe and Otaka to simulate the same coal gasification process in the CRIEPI gasifier, but their computational domain was a small section of a simplified, axisymmetric cylinder (i.e. this was essentially a 2-D computation.) It was not clear how

the inlet conditions and fuel injection were scaled down from 3D to 2D; however, they claimed that the predicted results showed good agreement with the experimental data of the CRIEPI gasifier. If Ajikumar et al.'s claim were correct, it implies that the gasfier's geometry and injection locations would not be critical for designing a gasifier. Further studies are needed to verify this implication.

Silaen and Wang (2011) used Jones and Lindstedt's rate (1998, abbreviated as Jones's rate later) and compared their CFD-simulated syngas results with that from the actual production of a commercial, slurry-fed, entrained-flow coal gasifier fed from the bottom. Perhaps due to the fact that Jones's rate was obtained under catalytic conditions, they found that Jones's rate was too fast and they had to purposely reduce the reaction rate constant to A= 2.75 x 10^2 to match the operating data. In this study, in addition to the modified Jones rate, the other two WGS reaction rates (Sato's and Wade's rates) obtained under non-catalytic conditions are to be employed for comparison as shown in Table 4.14.

Table 4.14 WGS Reaction Rates used in this study

Sources of the WGS rate	Catalyst	$k = AT^n \exp(-E/RT)$ with n=0
Jones and Lindstedt, 1998	Yes	$A = 2.75 \times 10^{10}$ s^{-1}, $E = 8.38 \times 10^7$ J/kmol
Wade et al., 2008	No	$A = 2.512 \times 10^5$ s^{-1}, $E = 1.325 \times 10^5$ J/mol
Sato, et al. 2004	No	$A = 10^{5.58 \pm 1.38}$ s^{-1}, $E = 1.16 \times 10^5$ J/mol

4.6.3 The Strategy for Generating Experimental Data for WGS Reaction Rate Calibration

For any calibration process, a set of clean experimental data is of the utmost importance. Unfortunately, a clean set of data needed for this study is not available in public domains. The syngas data typically published are usually taken after the gas clean-up process (scrubbing and desulfurization) with very different syngas compositions (H_2, CO, CO_2, and H_2O) from the raw syngas right at the exit of a gasifier. Fortunately, we were able to collaborate with the Industrial Technology Research Institute (ITRI) in Taiwan to obtain a relatively clean data set by specifically measuring the raw syngas information before and after the quench section. Since the reaction in the quench section is mainly WGS without involving other complex reactions and since the experiment was conducted in an industrial environment instead of in a lab test cell, this data set is thought to be very valuable and unique for the intended calibration process. A description of the ITRI's gasifier and quench section follows below.

The Industrial Technology Research Institute (ITRI) has installed and operated a small, experimental, oxygen-blown, entrained-flow coal gasifier in Taiwan for six years. In previous operations, dry, pulverized coal was pneumatically transported via nitrogen to the gasifier and injected from the bottom of the gasifier. This gasifier has been modified

with a new design which requires that the feedstock be mixed with water to form coal slurry and be injected with oxygen from top of the gasifier, while the syngas exits near bottom of the gasifier (see Fig. 4.22(a)). The syngas is usually very hot (1400-1700K or 2200-2600^{o}F for oxygen-blown gasification) and needs to be cooled for two purposes: (a) so that it may be transported without damaging downstream piping materials or other equipment and (b) to satisfy the lower-temperature requirement of the desulfurization and other cleaning processes. Direct water quench scheme is used for ITRI gaisifer. The schematic of the quench section is presented in Fig. 4.22(b). The syngas flow enters the main chamber in the center of the quench section, impinges on the water bath surface, and deflects radially outward through eight openings to an annular outflow peripheral section that surrounds the main central chamber and is separated from the main chamber by a wall. The flow then moves upward and leaves the quench section through two outlets. The temperature and pressure of the incoming flow are 954 K and 3 atm, respectively. There are two injection locations: the primary one is located near the entrance of the quench section in the main flow chamber and another set of eight injectors serve as the secondary sprays. The primary injection provides the main water spray cooling with two pairs of opposing jets, separated 90^{o} apart. The secondary sprays are located in the annular duct and spray water downward against the up-flowing gas. This set of secondary injectors is used to aid in fine-tuning the temperature and syngas composition. The syngas composition is taken immediately before it enters and exits the quench section. Hence, the computational domain simulation is conducted by only taking the quench section of the gasifier.

The experiment data taken in the gasifier before the syngas cooling section is very limited, typically no information on the water vapor concentration is available. Lack of adequate "raw data" has made calibration of the gasification model and the WGS reaction rate uncertain and difficult. For example, the data of syngas composition published from the Wabash River Coal Gasification Repowering Project (2000) didn't show the mole fraction of water vapor at the exit of the gasifier, although the water vapor information was shown for syngas composition after desulfurization. The experimental data provided by the Tampa Electric Polk Power Station IGCC Project (2002) was the cleaned syngas composition, which was taken after the syngas cooler and gas cleanup processes. Hughes et al. (2010) provided the syngas data from a two-tonne per day (slurry feed rate) pilot-scale gasifier, and, similarly, no water vapor mole fraction was given. Wained and Whitty (2010) performed tests in a 1 ton/day pressurized, slurry-fed, oxygen-blown, entrained-flow coal gasifier. The experimental data also lacked information for the water vapor content at the exit. So far, to the authors' knowledge, the only published experimental syngas data obtained before syngas cooling with water vapor content information is from the CRIEPI research scale coal gasifier presented in the paper by Watanabe and Otaka (2006). Therefore, the CRIEPI data is used for calibrating the WGS reaction rate in fully gasification process in this study.

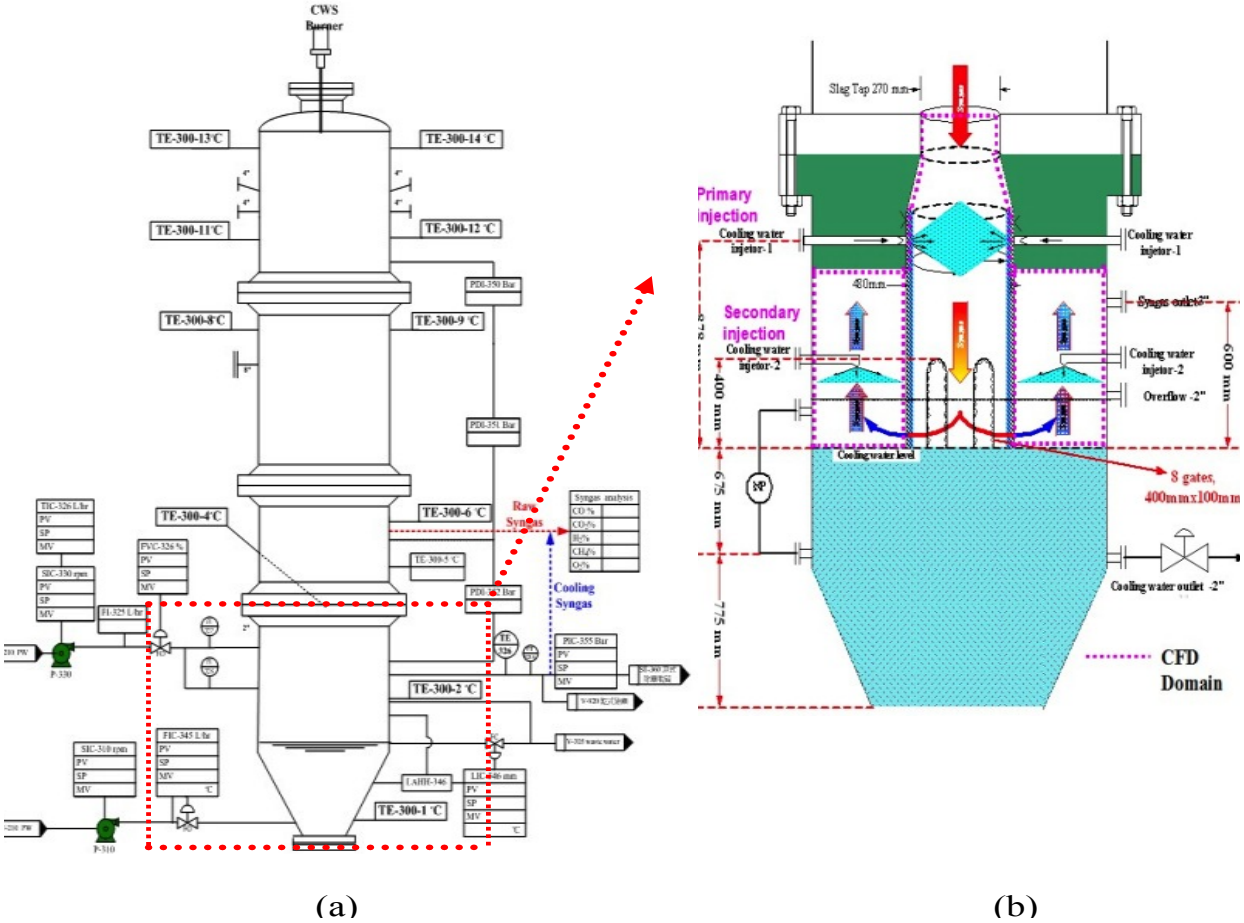

Fig. 4.22 (a) Schematic diagram of ITRI downdraft coal slurry-fed gasifier (b) gasifier's quench section showing locations of water injections: primary at the inlet and secondary in the outer annular

The coal used in this study is Japanese Black Coal, whose compositions are given in Table 4.15. The compositions of volatiles are derived from the coal's heating value, proximate analysis, and ultimate analysis. The oxidant is considered to be a continuous flow and the coal particles are considered to be discrete. The discrete phase only includes the fixed carbon and liquid water droplets from the moisture content of coal (5.3% wt). Other components of the coal, such as N, H, S, O, and ash, are injected as gas, together with the oxidant in the continuous flow. N is treated as N_2, H as H_2, and O as O_2. S and ash are not modeled and their masses are lumped into N_2.

Table 4.15 Compositions of Japanese Black Coal

Proximate Analysis (MF), wt%		Ultimate Analysis (MF), wt%	
Volatile	46.8	C	68.2
Fixed Carbon	35.8	H	5.71
Moisture	5.3	O	12.26
Ash	12.1	N	0.99
	100	S	0.19
HHV (kJ/kg)	2.74×10^4	Ash	12.65
			100.00

4.6.4 Boundary and Inlet Conditions

Boundary and Inlet Conditions for the ITRI Water Quench Simulation

The computational domain of the quench section of the ITRI gasifier is shown in Fig. 4.23. The computational domain contains roughly 300,000 elements. FLUENT 12.0.16 is used as the CFD solver. The simulation uses the segregated solver, which employs an implicit pressure-correction scheme and decouples the momentum and energy equations. The SIMPLE algorithm is used to couple the pressure and velocity. The second-order upwind scheme is selected for spatial discretization of the convective terms and species. The computation is conducted for the continuous phase first. After obtaining an approximate, converged flow field of the syngas the droplet trajectories are calculated. At the same time, the drag, heat transfer, and mass transfer between the droplets and the syngas are calculated.

Based on the experimental data, the mass flow rate of 0.04 kg/s for raw syngas is assigned as the inlet conditions at the top of the quench section. The entrance of the quench section connects to the bottom of the gasifer (Fig. 4.22). The temperature and pressure of the incoming flow are 954 K and 3 atm, respectively. The locations of the primary and secondary injectors are shown in Fig. 4.24.

The walls are all set as adiabatic and with no slip (ie. velocity is zero), but the thermal boundary condition of the shell wall of the main chamber (i.e., the wall between the primary injection and secondary injection) is set as "coupled," which means the heat fluxes on both sides of the wall will be calculated and matched to obtain the heat flux through the wall. The particles are assigned to reflect if they hit any wall. The operating pressure inside the gasifier is set at 3 atm. The outlet is set as a constant pressure condition at 1 atm. The syngas is considered to be a continuous flow, and the water from the spray is considered to be a discrete particle flow. The water droplets are all considered to be perfectly spherical with a uniform, arithmetic diameter of 10 μm. Although the actual size distribution of the atomized water droplets will be non-uniform,

simulation using a uniform droplet size distribution provides a more convenient way to track the droplet evaporation process than a non-uniform droplet size distribution.

Water droplets are injected from the center of each primary injectors and secondary injectors. Stochastic tracking method is used to simulate the effect of instantaneous turbulence on water droplets dispersion. Each injector has ten different tracks, the time scale constant is set as 0.015. The number of continuous phase iterations per dispersed phase iteration is set as 10, which means 10 iterations are down in the continuous phases before it is switched to the discrete phase. Converged results are obtained after the residuals satisfy a mass residual of 10^{-4}, an energy residual of 10^{-6}, and momentum and turbulence kinetic energy residuals of 10^{-5}. These residuals are the summation of the imbalance for each cell, scaled by a representative of the flow rate. Also, the simulations are proceeded until the mass fractions of various species are stabilized. A typical number of iterations of about 3000 is required for reaching the steady state.

Grid sensitivity study is conducted by comparing the results syngas temperature and composition from the models with 0.3, 0.6 and 0.9 million mesh size. The difference between the results of each case is within 2%. The model with 0.3 million mesh size is chosen in this study in order to save computational time.

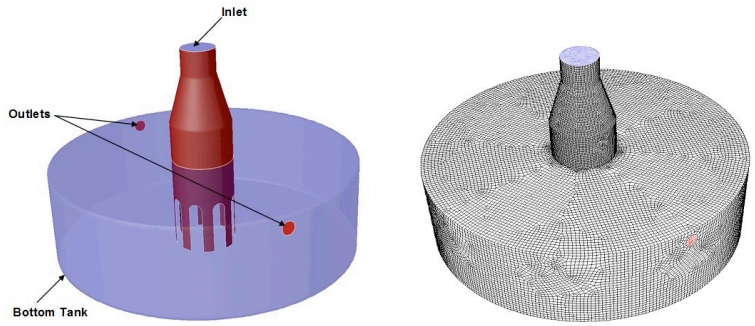

Fig. 4.23 Geometry, boundary conditions and meshed computational domain of the quench section of the ITRI Gasifier

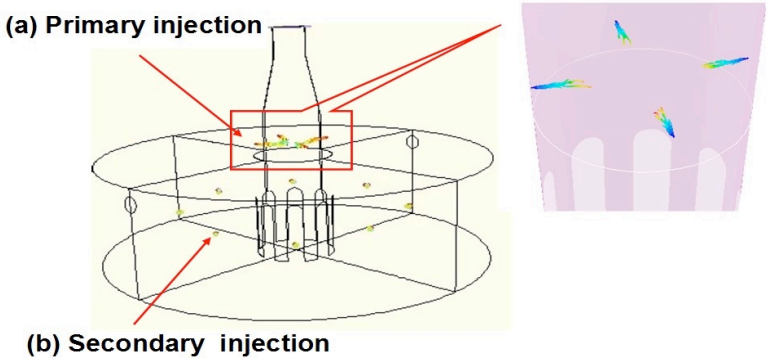

Fig. 4.24 Locations of water injections: (a) the primary injection consisting of two pairs of opposing jets and (b) the secondary injection consisting of eight injectors spraying downward against the up moving flow.

Boundary and Inlet Conditions for the Simulation of Gasification in the Japanese CRIEPI Gasifier

The geometry of the CRIEPI gasifier described by Watanabe and Otaka (2006) is shown in Fig 4.25. A simplified geometry shown in Figure 4.26 is employed in this present study without including the contraction section connecting the oxidation and reduction sections. The coal (fuel) injection design follows that of CRIEPI, consisting of a two-stage injection method with four tangential injections at the first stage and two opposite injections at the second stage. The residence time is around 3-4 seconds. The recycled char is injected from two opposite char injection locations at the first stage in the CFD model. The grid consists of 1,106,588 unstructured tetrahedral cells. In the simulations, the buoyancy force is considered, varying fluid properties are calculated for each species and the gas mixture, and the walls are assumed impermeable and adiabatic.

Japanese Black coal is used as the feedstock in this study; its composition is given in Table 4.15. The CRIEPI gasifier is an air-blown, dry-fed gasifier and is operated at 20 atm. The inlet, boundary, and operating conditions for the baseline case are shown in Figure 4.26. At the first stage, coal is injected tangentially with a mass flow rate of 0.00695 kg/s at each injection location. The recycled char is injected oppositely with a mass flow rate of 0.0045 kg/s at each injector. The total mass flow rate of air is distributed into four injectors equally at 0.095 kg/s. At the second stage, coal is injected through a pair of opposite injectors with a mass flow rate 0.00725 kg/s at each injection location. The total mass flow rate of air is 0.0172 kg/s. All of the parameters stated above are the same as the experiment data.

The walls are all set to be adiabatic and with the no-slip condition (i.e. zero velocity). The boundary condition of the discrete phase at the walls is assigned as “reflect”, which means the discrete phase elastically rebounds off once reaching the wall. The operating pressure inside the gasifier is set at 2MPa. The outlet is set at a constant pressure of 1 bar. The syngas is considered to be a continuous flow, and the coal and char from the injection locations are considered to be discrete particles. The particle size is uniformly given as spherical droplets with a uniform arithmetic diameter of 40 μm. Although the actual size distribution of the coal particles will be non-uniform, a simulation using uniform particle size provides a more convenient way to track the devolatilization process of coal particles than a non-uniform size distribution.

Same as the simulation of ITRI water quench process, the simulation of the Japanese CRIEPI gasification process is steady-state and uses the pressure-based solver, which employs an implicit pressure-correction scheme and decouples the momentum and energy equations. SIMPLE algorithm is used to couple the pressure and velocity. The second-order upwind scheme is selected for spatial discretization of the convective terms. For the finite rate model, where the Eulerian-Lagrangian approach is used, the iterations are conducted by alternating between the continuous and the discrete phases. Initially, one iteration in the continuous phase is conducted followed by one iteration in the discrete phase to avoid having the flame die out. The iteration number in the continuous phase gradually increases as the flame becomes more stable. Once the flame is stably established, fifteen iterations are performed in the continuous phase followed by one iteration in the discrete phase. The drag, particle surface reaction, and mass transfer between the discrete and the continuous phases are calculated. Based on the discrete phase calculation results, the continuous phase is updated in the next iteration, and the process is repeated. Converged results are obtained when the residuals satisfy a mass residual of 10^{-3}, an energy residual of 10^{-5}, and momentum and turbulence kinetic energy/dissipation residuals of 10^{-4}. These residuals are the summation of the imbalance in each cell, scaled by a representative for the flow rate.

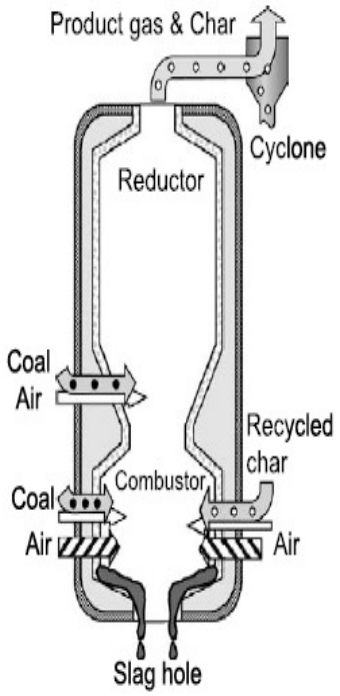

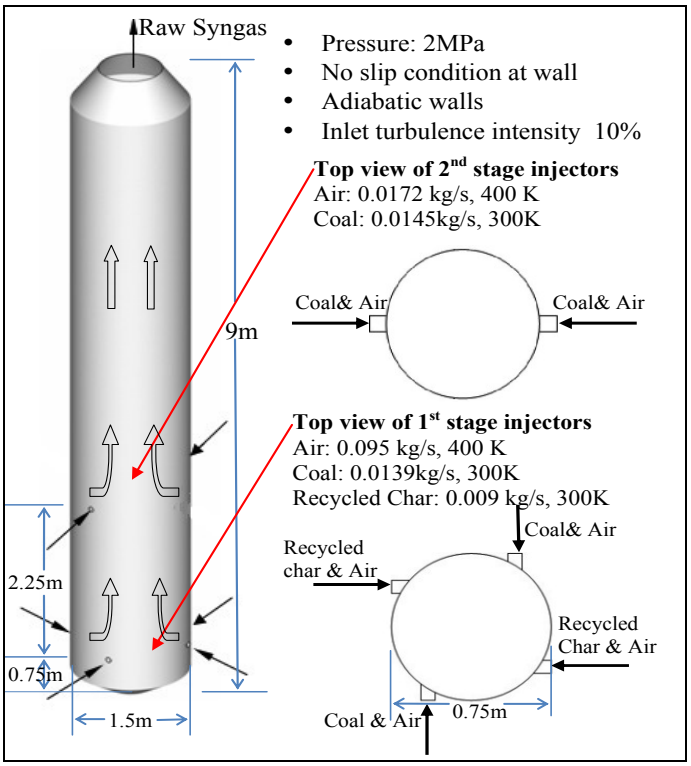

Fig. 4.25 CRIEPI research coal gasifier Fig. 4.26 Boundary conditions of the simulated gasifier

4.6.5 Results and Discussions for ITRI Water Quench Process

In this study, investigation of syngas as the inlet flow is carried out with a syngas mass flow rate of 0.04 kg/s, a temperature of 954 K, and a pressure of 3 atm. The syngas compositions and inlet conditions are taken from the ITRI experimental data and shown in Table 4.16.

Table 4.16 Syngas inlet composition

	Mole fraction
CO	0.31
H_2	0.24
CO_2	0.19
H_2O	0.25
CH_4	0.01
Temp (K)	954

Calibration of WGS Rates with Experimental Data of ITRI Water Quench Experiment

As mentioned before, most of the reaction rates for the water-gas shift (WGS) reaction were obtained from experiments under simplified laboratory conditions with specific catalysts. A few of the reaction rates without using catalysts were obtained under supercritical (water) conditions, with the pressure much higher than those in a typical gasifier. In either case, it is not clear how the published reaction rates can be trustfully used to predict the actual WGS reaction rate in a gasifier without the presence of a catalyst and under different temperature and pressure conditions than those in the laboratory. This study focuses first on reviewing the published WGS reaction rates with and without the presence of catalysts, followed by calibrating the WGS reaction rate to match the experimental data taken from Industrial Technology Research Institute (ITRI) gasifier, as well as the CFD thermodynamic equilibrium results.

Due to the uncertainty of the WGS reaction rate, three different reaction rates (Jones's rate under catalytic condition and Wade's and Sato's rates under non-catalytic conditions) are used with water spraying at the primary injection location with a flow rate of 0.0052 kg/s. The result in Table 4.17 shows that all the three reaction rates are too fast because most of CO has been converted to H_2 and CO_2, since the computed mole fractions of H_2 and CO_2 are higher than the experimental data while that of CO is lower. Also, because the reaction rates are too fast, the exit syngas reaches equilibrium and the results of all three rates are essentially identical. The CO conversion rate in Table 4.9 is defined as $(CO_{in} - CO_{out})/CO_{in}$, where CO_{in} is the mass flow rate of CO at inlet and CO_{out} is the mass flow rate of CO at outlet. Furthermore, the exit syngas temperature is approximately 173 K higher than the experimental data, indicating more heat is released from the WGS reaction. These discrepancies could be caused by the fact that this study employs the rates at different operating pressure and temperature ranges than those in the laboratory conditions under which the published rates themselves were derived.

To calibrate the reaction rates, the exponential constant, A, of each reaction rate is then progressively adjusted to lower values until the syngas composition matches the experimental data. An example of this process is shown in Table 4.18 by adjusting the A value of Wade's rate from 2.512×10^{5} to 2.512×10^{-5}. There is a large change of syngas composition from the case with $A = 2.512 \times 10^{5}$ to the case with $A = 2.512 \times 10^{-3}$, but no notable further change is seen after Compared with the experimental data, the result of the CFD simulated case with $A = 2.512 \times 10^{-1}$ fairs best. The progressive change of syngas composition is shown in Fig. 4. 27 which clearly shows that a faster rate produces more H_2 and CO_2, lower CO, and a higher exit temperature. The similar calibration process is applied to both Jones's and Sato's rates and all their results are listed in Table 4.19 for comparison. It appears that all of the original rates can be adjusted to a slower rate that can match the experimental gas composition data well. Without much preference between Sato's and Wade's rate, Wade's rate was chosen for the calibration with $A = 2.512 \times 10^{-1}$ and $E = 1.325 \times 10^{5}$ J/mol under a non-catalytic condition. However, even though the experimental gas composition data have been matched well by the calibrated WGS reaction rate, the computed gas exit temperature is still about 170K higher than the experimental data. This temperature difference could be contributed by two possible reasons: (a) The heat loses through the real wall, which can't be perfectly insulated as assumed in the simulation model; (b) The additional gas cooling due to gas stream penetrating into the water bath is not included in the simulation model either.

Note that the experimental data doesn't have the water vapor composition because a large part of the water vapor has condensed during the transportation of the sampled syngas to the gas analyzer. Therefore, the water vapor amount is not included in the comparison and the syngas composition of the simulated CFD results are renormalized by taking off the water vapor component.

Table 4.17 CFD simulated syngas composition using three original published WGS reaction rates (Note, experimental water vapor data is not available for comparison.)

Primary injection	Experiment data	$A=2.75\times10^{10}$ $E= 8.38\times10^{7}$J/kmol Jones et al. (1998)	$A=10^{5.58}$, $^{1.38}$ $E= 1.16\times10^{5}$J/mol Sato et al. (2004)	$A=2.512\times10^{5}$ $E=1.325\times10^{5}$J/mol Wade et al. (2008)
Syngas composition	Exit Mole Fraction			
H_2	0.36	0.50	0.49	0.49
CO_2	0.29	0.46	0.45	0.45
CO	0.34	0.03	0.05	0.05
CH_4	0.01	0.01	0.01	0.01
CO conversion (%)		88	80	80
Temperature (K)	673	948	944	946

Table 4.18 Effect of WGS rate constants on quenched syngas composition by changing A value of Wade's rate (Note, experimental water vapor data is not available for comparison)

Primary injection	Exper. data	$A=2.512\times10^{5}$ $E=1.325\times10^{5}$ J/mol	$A=2.512\times10^{0}$ $E=1.325\times10^{5}$ J/mol	$A=2.512\times10^{-1}$ $E=1.325\times10^{5}$ J/mol	$A=2.512\times10^{-3}$ $E=1.325\times10^{5}$ J/mol	$A=2.512\times10^{-5}$ $E=1.325\times10^{5}$ J/mol
Syngas composition	Exit mole fraction					
H_2	0.36	0.49	0.46	0.37	0.31	0.31
CO_2	0.29	0.45	0.41	0.30	0.25	0.25
CO	0.34	0.05	0.12	0.32	0.42	0.42
CH_4	0.01	0.01	0.01	0.01	0.02	0.02
CO conversion (%)		80	62	16	2	2
Temperature (K)	673	946	864	875	857	848

Table 4.19 CFD simulated syngas composition using three calibrated WGS reaction rates (Note, experimental water vapor data is not available for comparison)

Primary injection	Experiment data	$A=2.75\times10^{3}$ $E=8.38\times10^{7}$J/kmol	$A=10^{-1}$ $E=1.16\times10^{5}$J/mol	$A=2.512\times10^{-1}$ $E=1.325\times10^{5}$J/mol
Syngas Composition	Exit mole fraction			
H_2	0.36	0.36	0.34	0.37
CO_2	0.29	0.28	0.29	0.30
CO	0.34	0.38	0.36	0.32
CH_4	0.01	0.01	0.01	0.01
CO conversion (%)		8	10	16
Temperature (K)	673	842	864	875

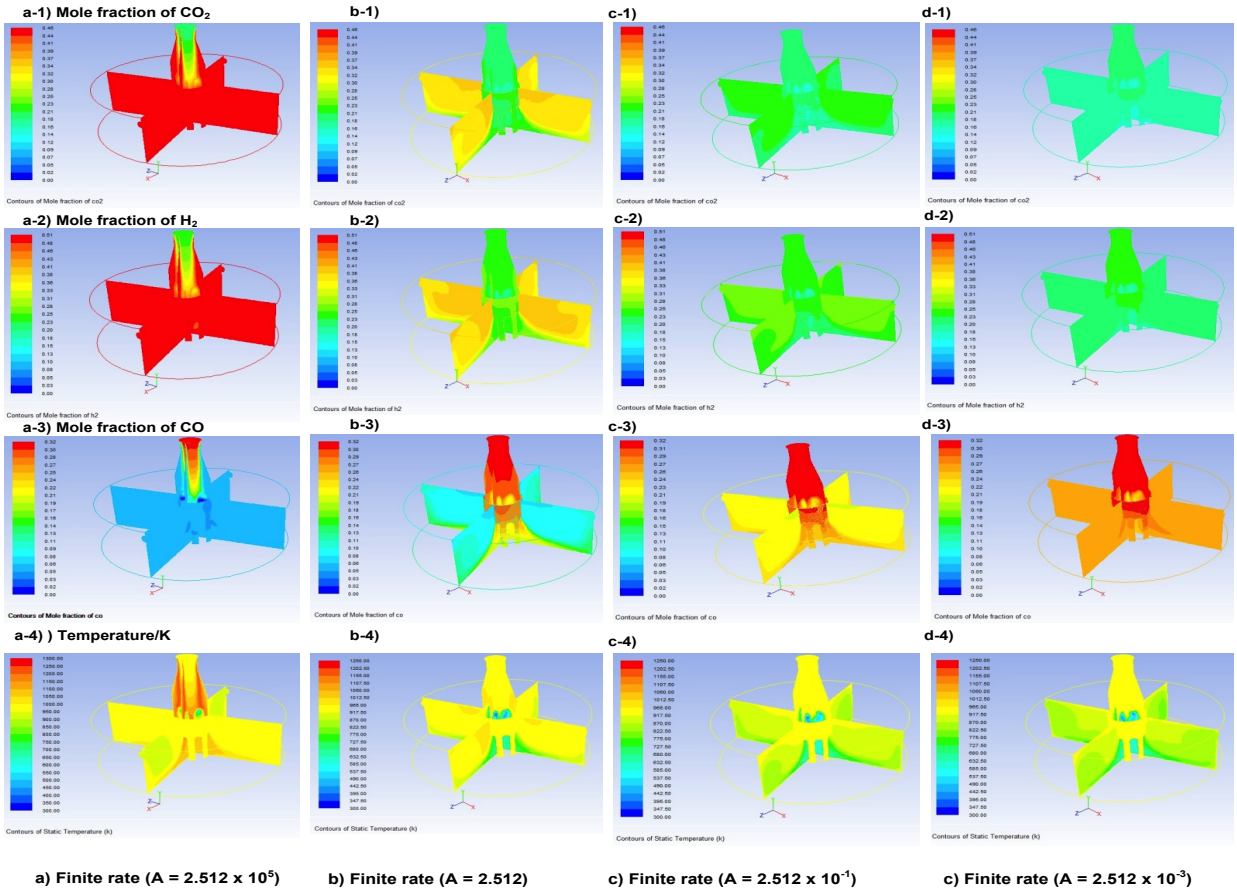

Fig. 4.27 Variation of Temperature and syngas composition by changing the A value of Wade's rate with the primary water injection

Calibration of WGS Rates including backward WGS Reactions

The WGS reaction rates employed so far are the net global rates, which means that they are the net results of forward and backward reactions. In order to see if adding a backward reaction rate would change the results, two different approaches are. The first approach is adding a backward WGS reaction ($CO_2 + H_2 \rightarrow CO + H_2$) as a separate equation with Jones's backward WGS reaction rate (A = 2.65 x 10^{-2} and E = 3.96x 10^3 J/kmol). The result shows that adding this backward WGS reaction equation only increases the computational time for achieving convergence, but it doesn't change the gas composition and temperature at the gasifier exit as the data without adding the backward WGS reaction in Table 4.9 does. The backward WGS reaction equation is, therefore, not added to the rest of the cases.

The WGS forward and backward reaction rates from NETL (2005) are also employed for water quench simulation. The result is very similar to that of Jones' rate: the forward

rate dominates the process (i.e., too fast), and the computed mole fractions of H_2 and CO_2 are higher than the experimental data while that of CO is lower. This exercise further implies that the WGS reaction rates need be carefully calibrated before it is applied to the simulation of water quench process because each WGS rate only works for a specific temperature and pressure range.

The second approach is to calculate the backward reaction rate through *chemical equilibrium*. In this approach, the laminar finite rate model is chosen. The backward rate constant for reaction r, $k_{b,r}$, is computed from the forward rate constant using the following relation:

$$k_{b,r} = \frac{k_{f,r}}{K_r} \tag{4.58}$$

Where $k_{f,r}$ is the forward rate, Kr is the equilibrium constant for the r^{th} reaction, computed from

$$K_r = \exp\left(\frac{\Delta S_r^0}{R} - \frac{\Delta H_r^0}{RT}\right)\left(\frac{p_{atm}}{RT}\right)^{\sum_{i=1}^{N}\left(\nu''_{i,r} - \nu'_{i,r}\right)} \tag{4.59}$$

where p_{atm} denotes atmospheric pressure (101,325 Pa). The term within the exponential function represents the change in Gibbs free energy, and its components are computed as follows:

$$\frac{\Delta S_r^0}{R} = \sum_{i=1}^{N}\left(\nu''_{i,r} - \nu'_{i,r}\right)\frac{S_i^0}{R} \tag{4.60}$$

$$\frac{\Delta H_r^0}{RT} = \sum_{i=1}^{N}\left(\nu''_{i,r} - \nu'_{i,r}\right)\frac{h_i^0}{RT} \tag{4.61}$$

where S_i^0 and h_i^0 are the standard-state entropy and standard-state enthalpy (heat of formation). In this study, $\Delta S°_r$= -41929J/kmol-K, $\Delta H°_r$= -4.12 x10^{-7}J/kmol.

Table 4.20 shows the experimental data, results of original Wade's rate, calibrated Wade's rate, as well as the thermodynamic equilibrium state of Wade's rate. The thermodynamic equilibrium results also consolidate our justification that original Wade's rate is too fast, based on the CO conversion percentage comparison, 80% for Original rate vs 38% for thermodynamic equilibrium. However, thermodynamic equilibrium results show faster forward rate compared to the calibrated rate since CO conversion for

Calibrated rate is only 16%. There are two possible reasons. Firstly, syngas residence time inside of the domain is too short that WGS reaction cannot reach to thermodynamic equilibrium state. Secondly, Wade's rate is experimental taken with an operating pressure of 24 MPa, while the operating condition of ITRI water quench section is only 3 MPa. The huge pressure difference will affect WGS reaction rate drastically as mentioned in the introduction part.

Table 4.20 CFD simulated syngas composition using original Wade's rate, calibrated Wade's rate ($A=2.512x10^{-1}$ $E=1.325x10^{5}$J/mol) and thermodynamic equilibrium method (Note, experimental water vapor data is not available for comparison.)

Primary injection	Experiment data	Original Wade's rate	Calibrated Wade's rate	Thermodynamic equilibrium
Syngas Composition	Exit mole fraction			
H_2	0.36	0.49	0.37	0.40
CO_2	0.29	0.45	0.30	0.34
CO	0.34	0.05	0.32	0.25
CH_4	0.01	0.01	0.01	0.01
CO conversion (%)		80	16	38
Temperature (K)	673	946	875	890

4.6.6 Results and Discussions for Japanese CRIEPI gasification Process

Results of Using Three Original Experimental WGS Reaction Rates

The three original experimental WGS reaction rates shown in Table 4.14 are used first for comparison. In Watanabe and Otaka's paper, the sum of the mole fractions of CO, CO_2, H_2O, and H_2 in the syngas composition is only 45%. The other 55% of the gases are not stated, although the major component is N_2. For the convenience of comparison between the experimental data and the CFD results, the mole fractions of CO, CO_2, H_2O, and H_2 are renormalized to 100% as shown in Table 4.21. The CFD results show that all three of the originally published rates are too fast, as can be seen by the much higher mole fraction of H_2 (product) and much lower mole fraction of remaining CO (reactant). Due to the exothermic character of the WGS reaction, the rapid WGS reaction rate results in the exit temperatures of all three cases being 100 – 130 K higher than the experimental data. This phenomenon further supports the conclusion derived from the results of water quench part—the original rates cannot work well in the simulation of gasification process due to different operating range in temperature and pressure. Since the adopted approach, keeping the activation energy intact and subsequently reducing the pre-exponential constant value (A), has been examined and proved by comparing results with experimental results and thermodynamic equilibrium results of water quench part, the same approach has been used here.

For Jones's rate, which was obtained under a catalytic condition, it could be explained that the WGS reaction rate is low because no catalyst is used in the gasifier.

For Wade's rate and Sato's rate, there are two reasons that might partially contribute to the faster experimental reaction rates: (a) the experiments were conducted in an environment deprived of concentrations of products (H_2 and CO_2) and other gases, so the forward experimental reaction rates could be faster. (b) The experimental pressure and temperature conditions are different from those in the gasifier. In the gasifier, the temperature is higher than in the experimental conditions, thus the WGS reaction rate could be lower in the gasifier than in the experimental test condition. The temperature and species distributions in the gasifier are show in Fig. 4.28.

Table 4.21 Comparison of exit temperature and syngas composition between the experimental data and the simulated cases using the 3 original WGS rates

Mole fraction	Experimental Data	*Jones's Rate* $A=2.75x10^{10}$ $E=8.38x10^{7}$ *J/kmol*	Wade's Rate A=2.512 x 10^5 E=1.325 x10^5J/mol	Sato's Rate A = $10^{5.58 \pm 1.38}$ E=1.16x 10^5 J/mol
T	1250K	1356K	1382K	1378K
H_2	0.20	0.48	0.48	0.48
CO	0.42	0.27	0.26	0.27
CO_2	0.20	0.25	0.26	0.25
H_2O	0.18	< 0.01	< 0.01	< 0.01

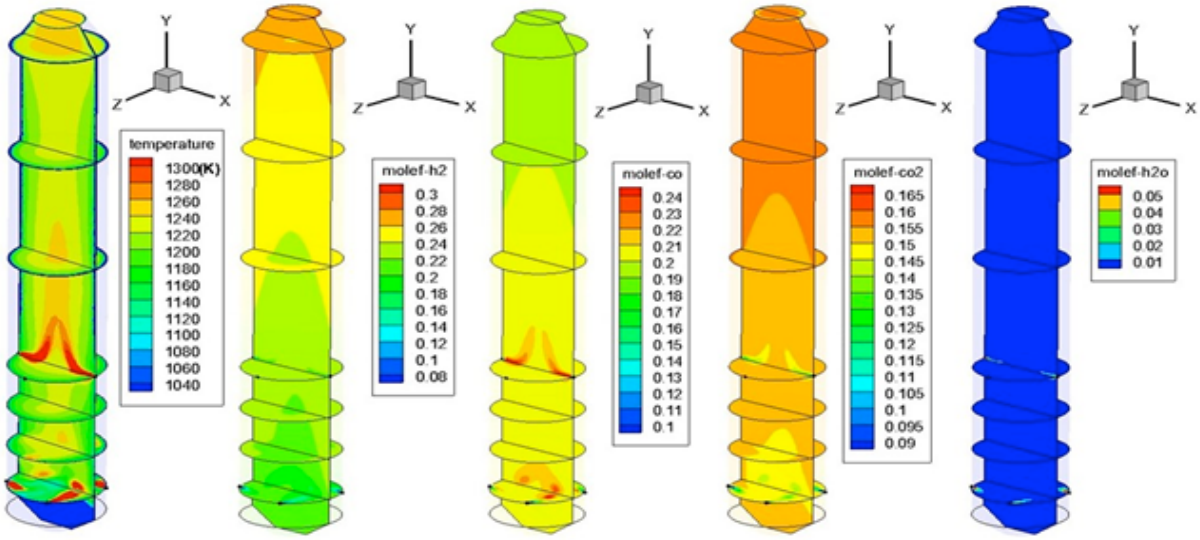

Fig. 4.28 Gas temperature and species mole fraction distributions for using the Jones's rate (A=2.75x10^{10} E=8.38x10^7 J/kmol) (Note: the mole fractions in this figure are based on all gases and are not the same as those shown in Table 4.21)

Calibration of the Catalytic WGS Rates (Jones's) Against the Experimental Data

The purpose of this study is calibrating WGS reaction rate by matching experimental data of real entrained flow gasification process. The approach, adjusting pre-exponential rate constant and keep activation energy value, is discussed and proved above. Therefore, the same calibration approach against the experimental data of Japanese CRIEPI

gasification is performed by consecutively changing the pre-exponential rate constant, A, from 2.75 $x10^{10}$ in Jones's rate to 2.75 x 10^{-2}, while the activation energy is kept the same as the original value (E = 8.38$x10^{7}$ J/kmol). The calibration of non-catalytic WGS rates (Wade's and Sato's) is stated earlier. The CFD results of seven cases are shown in Table 4.22 together with the experimental data. The result clearly shows the gradual change of syngas composition and temperature at the exit when the A value is reduced from 2.75 x 10^{10} to 2.75 x 10^{-2}. There is little change in syngas composition and temperature at the exit when the rate constant A is reduced from 2.75 x 10^{10} to 2.75 x 10^{4} because the water vapor content is almost completely consumed in both cases. It demonstrates that the rate A = 2.75 x 10^{4} is still too fast compared to the experimental data. There is a relatively big change of the gas composition when the rate constant A is reduced from 2.75 x 10^{2} to 2.75. When the A-value is reduced below 2.75, the result appears stabilized and fluctuates slightly. The case with **A=2.75** seems to result in the best match with the experimental data. Figure 4.29 shows the comparison of syngas composition at exit with the experimental data, original Jones' rate, and calibrated Jones' rate. This calibrated pre-exponential rate constant, A=2.75, has one three order of magnitude difference compared to the calibrated rate derived from Part 1, A=2750. This deviation is mainly caused by two different types of experiments. For the WGS rate which calibrated by the water quench experimental data, is only involved WGS reaction, the operating pressure is 3 atm, the temperature range inside of domain is around 700K-1000K. For the real entrained flow gasification process, it is involved nine reactions, include devolatilization, combustion and gasification process. More species and reactions make the case become much more complicated than water quench process. Furthermore, the operating pressure of the gasification process is 20 atm, the temperature range is approximate 1000K-1700K. All these factors could affect the WGS reaction rate in different reaction processes.

Figures 4.30 and 4.31 shows the contours and mass weighted average of gas temperature and species mole fraction distributions for the Case with A=2.75 and E=8.38$x10^{7}$ J/kmol respectively. The gas temperature is higher in the region above the second stage injection location than it is in the region between the first and second stages. The maximum gas temperature in the first stage reaches 1650K near the fuel injection locations, and, in the second stage, it reaches 1570K. This phenomenon is different from the well-known E-gas gasifier in which no oxygen is provided at the second stage, so the temperature after the second-stage injection is much lower than in the first stage because the endothermic Char-CO_2 (R2) and Char-steam (R3) gasification processes are very active after the second stage injection. In this gasifier, it is very interesting to see that the highest production of CO_2 occurs near the first stage injection locations and the lowest production occurs near the second stage. The CO_2 mole fraction is low in most parts of the production until the syngas reaches the top quarter of the gasifier where the CO_2 mole

fraction increases again. This history of the CO_2 mole fraction changes indicates that complete char combustion (R5) occurs near the first-stage injection, but CO_2 is effectively consumed via Char-CO_2 gasification in most parts of the gasifier to produce H_2 and CO, as also is evidenced by increasing H_2 and CO mole fractions. The WGS seems to become more active in the upper quarter of the gasifier as the temperature increases due to the exothermic effect of the WGS process. In this upper quarter region, the active WGS reaction can be evidenced by the increased H_2 and CO_2 and decreased CO.

Furthermore, similar to water quench part, we also employed the WGS forward and backward reaction rates from NETL (2005) for gasification simulation. The result is very similar to that of water quench part: the forward rate dominates the process and the computed mole fraction of H_2 is 2.5 times higher than the experimental data while that of CO is lower. It further supports the necessity of calibrating the WGS reaction rates before it is applied to the simulation of both water quench and gasification process.

Table 4.22 Comparison of the temperature and syngas composition at exit with the experimental data by consecutively reducing the pre-exponential value, A, of the Jones' rate

Exit	Exp. Data	2.75×10^{10}	2.75×10^{4}	2.75×10^{2}	2.75×10^{1}	**2.75**	2.75×10^{-1}	2.75×10^{-2}
T	1250K	1356K	1296K	1282K	1278K	**1267K**	1246K	1236K
H_2	0.20	0.48	0.44	0.41	0.31	**0.27**	0.29	0.27
CO	0.42	0.27	0.31	0.32	0.41	**0.45**	0.44	0.45
CO_2	0.20	0.25	0.25	0.23	0.14	**0.12**	0.12	0.12
H_2O	0.18	< 0.01	< 0.01	0.05	0.14	**0.16**	0.15	0.16

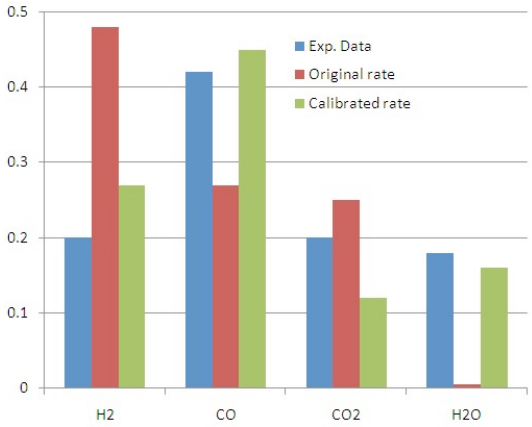

Fig. 4.29 Comparison of syngas composition at exit with the experimental data, original Jones' rate, calibrated Jones' rate (A=2.75 and $E=8.38\times10^{7}$ J/kmol)

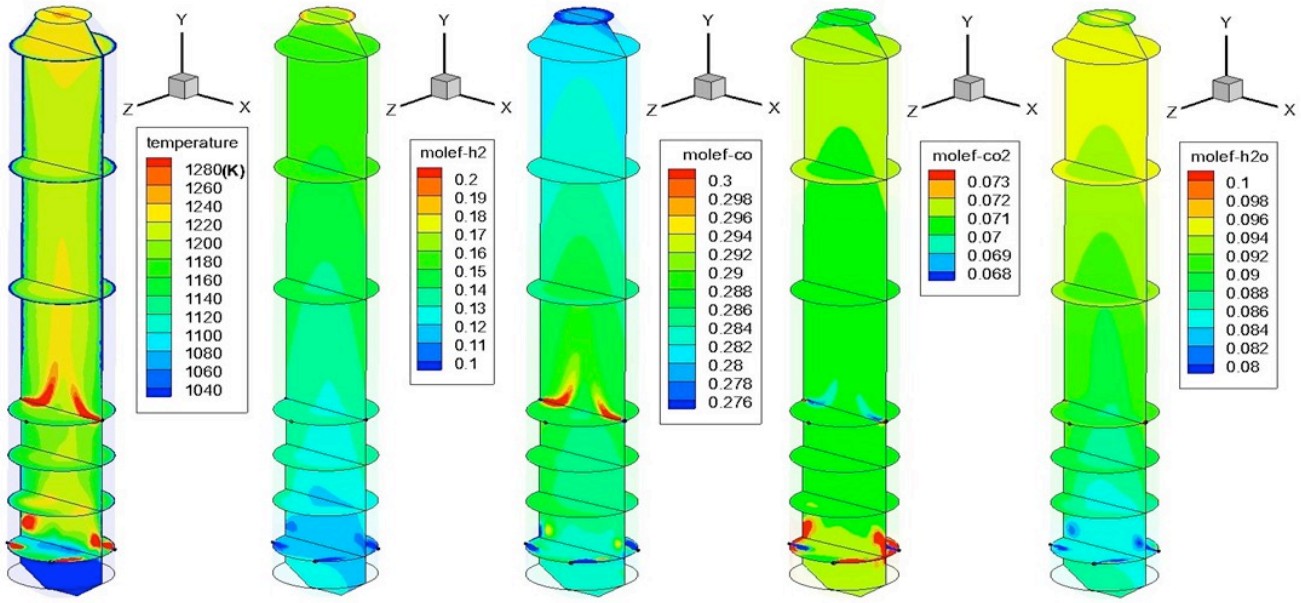

Fig. 4.30 Gas temperature and species mole fraction distributions for the Case with modified Jones's rate (A=2.75 and E=8.38x10^7 J/kmol). (Note: the mole fractions in this figure are based on all gases and are not the same as those shown in Table 4.22)

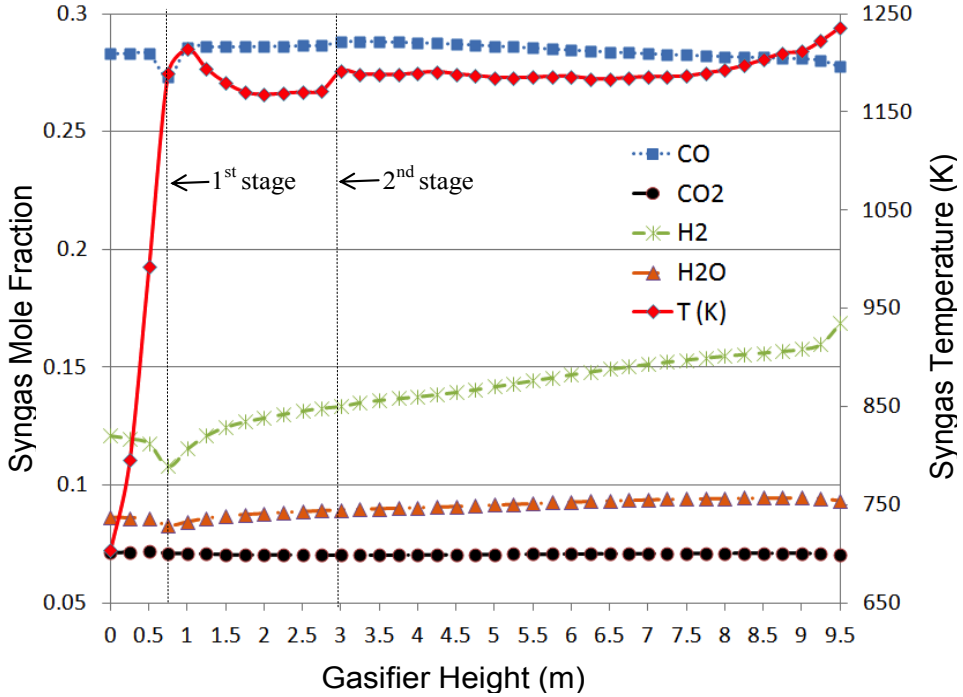

Fig. 4.31 Mass-weighted averages of gas temperature and species mole fraction distributions along gasifier height for the Case with modified Jones's rate (A=2.75 and E=8.38x10^7 J/kmol)

Calibration of the Non-catalytic WGS Rates (Wade's and Sato's) Against the Experimental Data

The same calibration process is performed for Wade's and Sato's rates, which were obtained without using catalysts, but in the supercritical range. Without showing all the incremental cases, only three selected cases are shown in Table 4.23. The results of A = 2.512 x 10^{-3} for Wade's rate and A = 1 x 10^{-3} for Sato's rate show the best matches with the experimental data. Both rates are slower than those obtained from quench-only process.

In summary, all three WGS reaction rates can be modified to match the experimental data reasonably well by reducing the value of the pre-exponential rate constant, A. The exit temperature can be matched within 2% (20K) of the experimental value. The mole fractions of CO and H_2O can be matched fairly well within 4 percentage points (or 10%); however, the simulated H_2 mole fractions are always 7-9 percentage points (or about 40%) higher than the experimental data.

Table 4.23 Temperature and syngas composition at exit for six cases and experiment data based on Wade's rate and Sato's rate

MF		A-value of Wades' Rate (E=1.325x10^5J/mol)			A-value of Sato's Rate (E=1.16x10^5 J/mol)		
(%)	Exp. Data	2.512x10^5	2.512x10^{-1}	**2.512x10^{-3}**	$10^{5.58}_{\pm 1.38}$	1x10^{-1}	**1x10^{-3}**
T	1250K	1382K	1280K	**1273K**	1378K	1276K	**1238K**
H_2	0.20	0.48	0.43	**0.29**	0.48	0.40	**0.28**
CO	0.42	0.26	0.29	**0.43**	0.27	0.33	**0.46**
CO_2	0.20	0.26	0.24	**0.12**	0.25	0.21	**0.11**
H_2O	0.18	0	0.04	**0.16**	0	0.06	**0.15**

4.6.7 Conclusions

The WGS reaction rate has been discovered to affect notably the result of CFD modeling of coal gasification processes in a gasifier. Almost all of the published WGS rates were conducted with catalysts under limited temperature ranges and at a certain fixed pressure condition. Only a few WGS rates were obtained without involving catalysts, but they were performed under supercritical (water) conditions. Therefore, employing any of the published WGS reaction rates to simulate the coal gasification process in a gasifier, which usually doesn't use catalysts and doesn't operate at the same temperature or pressure conditions as in the laboratory conditions, is likely to result in misleading or uncertain results. To help calibrate the global WGS reaction rates, three published WGS reaction rates are used in this study. They are Jones's rate (A =

$2.75x10^{10}$, E = $8.38x10^{7}$ J/kmol,) Wade's rate (A = 2.512 x 10^{5}, E = 1.325 x 10^{5}J/mol,) and Sato's rate (A = 105.58 ±1.38, E = 1.16x 10^{5} J/mol.) The study is focused on both water quench section of ITRI gasifier, which only involves WGS reaction, and fully gasification process in the Japanese CRIEPI gasifier. Calibrated WGS rates are derived from comparing CFD results the experimental data, as well as with thermodynamic equilibrium results. The conclusions are:

(1) All of the originally published rates cannot work well in the simulation of both water quench process and coal gasification process due to different temperature and pressure range. Adding the backward WGS reaction rate (Jones' rate) as a separate reaction equation results in the same gas composition and temperature at the gasifier exit as the case without adding the backward WGS reaction rate.

(2) For water quench part, the result of employing the forward and backward rates from NETL is very similar to that of Jones' rate—the forward rate dominates the process (too fast) and the computed mole fractions of H_2 and CO_2 are higher than the experimental data while that of CO is lower.

(3) Applying the chemical equilibrium approach further verifies that original WGS rates are too fast in applying in the range of water quench operation parameters.

(4) Each of the three rates are slowed down by consecutively reducing the pre-exponential rate constant, A, while the activation energy is kept the same as the original value. The results show that all three WGS reaction rates can match the experimental data well by reducing the value of the pre-exponential rate constant, A. For the results of gasification process, the exit temperature can be matched within 2% (20K). The mole fractions of CO and H_2O can be matched fairly well within 4 percentage points (or 10%); however, the simulated H_2 mole fractions are always 7-9 percentage points (or about 40%) higher than the experimental data.

(5) The calibrated global WGS reaction rates that best match the experimental data of ITRI water quench process are:
- Modified Jones's rate: A = 2.75, E = $8.38x10^{7}$ J/kmol
- Modified Wade's rate: A = 2.512 x 10^{-3}, E = 1.325 x 10^{5}J/mol and
- Modified Sato's rate: A = 1 x 10^{-3}, E = 1.16x 10^{5} J/mol

(6) The calibrated global WGS reaction rates that best match the experimental data of Japanese CRIEPI coal gasification process are:
   - Modified Jones's rate: A = 2.75, E = 8.38×10^7 J/kmol
   - Modified Wade's rate: A = 2.512×10^{-3}, E = 1.325×10^5 J/mol and
   - Modified Sato's rate: A = 1×10^{-3}, E = 1.16×10^5 J/mol

(7) There is a two orders of magnitude difference of the pre-exponential rate constant, A, between the calibrated WGS reaction rates derived from these two different simulations. This deviation is mainly caused by two different types of experiments. For the WGS rate which calibrated by the water quench experimental data, is only involved WGS reaction, the operating pressure is 3atm, the temperature range inside of domain is around 700K-1000K. For the real entrained flow gasification process, it is involved nine reactions, include devolatilization, combustion and gasification process. More species and reactions make the case become much more complicated than water quench process. Furthermore, the operating pressure of the gasification process is 20 atm, the temperature range is approximate 1000K-1700K. All these factors could affect the WGS reaction rate in different reaction processes.

It needs to be emphasized that the modified reaction rates are obtained under air-blown and dry-fed operating conditions. These modified rates may not be applicable to slurry-fed or oxygen-blown gasifiers because the higher water vapor concentration in slurry-fed gasifiers and higher operating temperatures in oxygen-blown gasifiers may affect the global WGS rate. More studies, as well as more adequate experimental data, are needed in the future. The adequate data are those data taken immediately at the end of gasification section but right before the syngas cooling section in the gasifier, and it is important that the water vapor concentration must be included. An alternative approach is to include the kinetics of elementary reactions instead of taking a global data match on the condition that the adequate elementary reactions are known.

4.7 Topic 4: Effect of Radiation Models on Coal Gasification Simulation

(See Lu and Wang (2013) in International Journal of Heat and Mass Transfer for details.)

In the majority of industrial combustion devices, thermal radiation plays a significant role for an important energy transfer. Even though the coal gasification process undergoes a partial combustion process, thermal radiation may still play a very important role in heat and energy transfer between different gas species, coal particles, as well as the wall of gasifier. Furthermore, in order to extend the lifetime of the refractory bricks and to reduce the maintenance cost, keeping the process temperature relatively low, but still effective in performing the gasification process and cracking the volatiles, is one of the important goals for gasification research. Therefore, an accurate and computationally efficient thermal radiation model is needed to predict flame shape and temperature distributions of syngas at the wall of gasifier. In this study, five radiation models are applied into gasification simulation: Discrete Transfer Radiation Model (DTRM), P-1 Radiation Model, Rosseland Radiation Model, Surface-to-Surface (S2S) Radiation Model, and Discrete Ordinates (DO) Radiation Model. The objectives are to identify the pros and cons of each model's applicability to gasification process and determine which radiation model is most suitable for simulating gasification process in entrained-flow gasifiers with a consideration of the gasifier's geometry, radiative properties of participating medium (mainly CO, CO_2, H_2 and water vapor), and coal particles interactions.

4.7.1 Literature Review of Radiation Models Implemented in Gasification Simulation

Chen et al. (2000) developed a three-dimensional simulation model for entrained-flow coal gasifiers, which applied an extended coal-gas mixture fraction model with the Multi Solids Progress Variables (MSPV) method. The model employed four mixture fractions separately track the variable coal off-gases from the coal devolatilization, char-O2, char-CO2, and char-H2O reactions. Chen et al. performed a series of numerical simulations for a 200 ton per day (tpd) two-stage air blown entrained flow gasifier developed for an IGCC process under various operation conditions (heterogeneous reaction rate, coal type, particle size, and air/coal partitioning to the two stages). In these computational models, the discrete transfer method (DTRM) based on the solution of the fundamental radiative transfer equation within discrete solid angles was used.

Bockelie et al. (2002) developed a comprehensive CFD modeling tool (GLACIER) to simulate entrained-flow gasifiers, including a single-stage, down-fired system and a two-stage system with multiple feed inlets. They used DO radiation model which included the

heat transfer for absorbing-emitting, anisotropically scattering, turbulent, and sooting media. The radiative intensity field was solved based on properties of the surfaces and participating media, and the resulting local flux divergence appeared as a source term in the gas phase energy equation.

The U.S. Department of Energy/National Energy Technology Laboratory (NETL) developed a 3D CFD model of two commercial-sized coal gasifiers (Guenther and Zitney, 2005). The commercial CFD software, FLUENT, was used to model the first gasifier, which was a two-stage, entrained-flow, slurry-fed coal gasifier. The Eulerian-Lagrangian method was used in conjunction with the discrete phase model to simulate the entrained-flow gasification process. The second gasifier was a scaled-up design of a transport gasifier. The NETL open source MFIX (Multiphase Flow Interphase Exchanges) Eulerian-Eulerian model was used for this dense multiphase transport gasifier. MFIX is a general-purpose hydrodynamic model that describes chemical reactions and heat transfer in dense or dilute fluid-solids flows, typically occurring in energy conversion and chemical processing reactors. The radiative heat transfer is not considered in this model. NETL has also developed an Advanced Process Engineering Co-Simulator (APECS) that combines CFD models and plant-wide simulation. APECS enables NETL to couple its CFD models with the steady-state process simulator, Aspen Plus.

Chodankar et al. (2009) developed a steady state model to estimate the gas production from Underground Coal Gasification (UCG) Process. This model featured surface reactions of coal char with gasification medium to produce combustible gaseous product, and predicts gas composition, temperature and gross calorific value of product gas across the gasification channel. P1 radiation model was used in their study. Ajilkumar (2009) performed a numerical simulation on a steam-assisted tubular coal gasification process. The syngas temperature, carbon conversion, heating value of the exit gas, and cold gas efficiency were predicted and compared with the experimental data. P1 model was chosen as the radiation model in their simulation model study. Wu et al. (2010) used 3D CFD model for the simulation of an entrained coal slurry gasification process. The effect of particle size on coal conversion, as well as the effect of the coal slurry concentration and molar ratio of oxygen/carbon on the gasifier performance, was investigated. The P1 radiation model was also used in their study. Chen (2010) used a 3-D simulation model to investigate the effect of oxygen/carbon ratio and water/coal ratio on the entrained flow coal gasification process. P1 model was selected as the radiation model in his study.

From 2005 to 2011, Silaen and Wang (2005, 2006, 2011) have conducted a series of study of entrained-flow gasification process using the commercial CFD solver, FLUENT. In these studies, they investigated the effects of several parameters on gasification

performance, including the coal input condition (slurry or dry powder), oxidant (oxygen-blown or air-blown), wall cooling, flow injection angles, and various coal distributions between the two stages. They also investigated the effects of various turbulence models and devolatilization models on the result of gasification simulations (Silaen and Wang, 2010). Furthermore, they compared the effect of instantaneous, equilibrium and finite rate gasification models on the entrained flow coal gasification process (Silaen and Wang, 2009). Lu and Wang (2011) investigated the effect of Water-Gas-Shift (WGS) reaction rate on gasification process. They found that most of the published WGS reaction rates, both under catalytic and non-catalytic conditions, are too fast in gasification simulation process. By adjusting the pre-exponential rate constant value (A) against experimental data, calibrated WGS reaction rate were obtained. In all of the above studies, only the P1 radiation model was used.

In collaboration with the research team of Industrial Technology Research Institute (ITRI), Wang and Silaen effectively employed the CFD gasification model to investigate gasification process under the influences of different part loads, two different injectors, and three different slagging tap sizes (Wang and Silaen, 2006, 2007, 2010). In 2011, Wang, et al. (2011) performed the simulation on the effects of potential fuel injection techniques on gasification performance in order to help design the top-loaded fuel injection arrangement for an entrained-flow gasifier using a coal-water slurry as the input feedstock. Two specific arrangements were investigated: (a) coaxial, dual-jet impingement with the coal slurry in the center jet and oxygen in the outer jet and (b) four-jet impingement with two single coal-slurry jets and two single oxygen jets. Wang and Lu (2011) investigated the performance of a syngas quench cooling design in the ITRI downdraft entrained flow gasifier. Numerical simulation was performed to investigate the effect of different injection stage of cooling water, and water gap level on syngas composition, higher heating value and temperature at exit of gasifier. Again, only the P1 radiation model was used.

Based on the above literature review, only the P1 model has been widely used in gasification simulation. Although Chen et al.(2000) and Bockelie et al. (2002) used DTRM and DO radiation models respectively, to the authors' knowledge, no study has been published in the public domain to compare the results obtained from different radiation models. The lack of information on the uncertainty of simulated results resulting from employment of different radiation models has motivated the investigation conducted in this study.

4.7.2 Review of Radiation Models

Radiation of Participating Media (Gas Phase)

In coal gasification process, CO, H_2, CO_2, and water vapor are produced and participate in radiant heat transfer by the virtue of interaction of infrared radiation with vibrational and rotational modes of energy absorption by gaseous molecules.

Two aspects of radiation heat transfer in participating media need to be modeled: one is the radiant energy transfer in the participating media, described by the radiative transfer equation, the other is the absorption, emission, and scattering of radiation by the participating media itself.

For the first aspect, the transfer equation alone with a number of representative rays could be solved by discrete transfer method described by Lockwood and Shah (1981) as well as by the discrete ordinate method described by Chandrasekhar (1950). The accuracy of the solution is the function of numerical errors that could be reduced to any required level by solving enough number of rays or directions.

For the second aspect, several models for participating media have been introduced in conjunction with the flow field by simultaneously solving the fluid flow equations such as the mixed grey gas models introduced by Hottel and Sarofim (1967). Grosshandler (1980) introduced the total transmittance non-homogeneous model, which is a simplified model, using total transmittance data to predict the radiance emanating from non-isothermal, variable concentration carbon dioxide and water-vapor mixtures. Computational times using this model are two-orders of magnitude less than that required by the Goody statistical narrow-band model with Curtis-Godson approximation, but with a sacrifice in accuracy of less than 10%.

Edwards and Balakrishnan (1973) introduced exponential wide band model and presented the generalized expressions for the calculation of the emissivity, absorptivity, and other relevant radiation properties of molecular gases. Cumber et al. (1998) adapted a spectral version of the exponential-wide band for implementation within a computational fluid dynamic framework. They also showed that the spectral wide band approach is in a reasonable agreement with experimental data and achieves accuracy comparable to that of the narrow band model in total quantities while requiring almost one order of magnitude less of computational time.

Radiation of Combustion Particles (Solid Phase)

During the coal gasification process, radiation of solid particles also plays an important role in heat transfer since the coal particles will go through preheating, devolatilization, ignition, and partial combustion process at the beginning stage of the

gasification process. For the field of radiation heat transfer of solid particles, most of the studies have been carried out in coal combustion system. Sarofim and Hottel (1978) gave a detailed review of the importance of radiative heat transfer in combustion systems. All combustion processes are very complicated. There are intermediate chemical reactions in sequence or parallel, intermittent generation of a variety of intermediate species, generation of soot, agglomeration of soot particles, and partial burning of the soot sequentially. Since thermal radiation contributes greatly to the heat and energy transfer mechanism of combustion, fundamental understanding and appropriate modeling of the processes of radiation of combustion particles need to be addressed and implemented for gasification process, which involves partial combustion and several other reactions.

Coal particles and fly ash dispersions -- To calculate the radiative properties of arbitrary size distributions of coal particles, their complex index of refraction as a function of wavelength and temperature must be investigated. Foster and Howarth (1968) have employed a Fresnel reflectance technique to measure the complex refractive index of coals at different ranks. Brewster and Kunitomo (1984) questioned the validity of the reflectance technique applied to the coal. They measured the absorption index of some Australian coals to be less than 0.05 in the infrared by using a transmission technique for small coal particles.

Viskanta et al. (1981) summarized the representative values for the complex index of refraction in the near infrared for different coals and ashes, such as carbon, anthracite, bituminous, lignite, and fly ash. They also found that variations with particle distribution functions are relatively minor, and the different index of refraction made a difference only for mid-sized particles. Buckius and Hwang (1980) analyzed the extinction and absorption coefficients, as well as the asymmetry factor for polydispersions of absorbing spherical particles. By showing that dimensionless spectral radiation properties are independent of the explicit size distribution of the particle, they indicated the usefulness of the dimensionless and mean properties for defining the optical properties of coal particles which are wavelength dependent.

Char -- In the radiation heat transfer process of coal gasification, optical constants of char are considered to be more important than that of coal since the coal devolatilization time is generally insignificant compared with the char burning and char gasification time. Grosshandler and Monteiro (1982) investigated the absorption and scattering of thermal radiation within a dilute cloud of pulverized coal and char. They proposed an empirical equation of the form $\alpha\lambda = 0.78 + 0.18/\lambda^{1/2}$ for all coals and chars within 5 percent in the spectral region of $\lambda = 1.2–5.3$ μm. They also recommended a single total hemispherical absorptivity of 0.89 for heat transfer calculation in pulverized coal and char clouds, if the particles can be assumed to act as Mie scatters and if the volume fraction of ash and soot

particles is small. Brewster and Kunitomo (1984) determined the extinction efficiency from transmissivity measurements on micron-sized char suspensions by a particle extinction technique using compressed KBr tablets. IM and Ahluwalia (1992) conducted a dispersion analysis of the transmissivity measurement by Brewster and Kunitomo on char particles dispersed in infrared transmissive KBr pellets. They introduced some question as to the uniqueness of the optical constants inferred purely from the extinction measurement. In order to properly resolve the contributions of absorption and scattering to extinction efficiency, they recognized that it is necessary to measure a second independent variable.

Soot -- Soot particles are produced in fuel-rich flames, or fuel-rich parts of flames, as a result of incomplete combustion of hydrocarbon fuels. In coal gasification process, soot production coincides with the stage of volatile matters being driven from the coal. Since soot particles are very small and are generally at the same temperature as the flame, they strongly emit thermal radiation in a continuous spectrum over the infrared region. Experiments have shown that soot emission often is considerably stronger than combustion gases' emission. Foster and Howarth (1968) were first to report experimental measurements for the complex index of refraction of hydrocarbon soot based on various carbon black powders. Lee and Tien (1981) used the dispersion theory applied to a two bound and one free-electron oscillator model to analyze the optical constants of soot. Their results show that the infrared optical properties of soot are relatively independent of the ratio of fuel hydrogen to carbon and the molecular structure of soot. Thus their dispersion constants can be treated as some mean values applicable to many fuels. Since the soot effect on gasification process is very complicated, it is not investigated in the current study.

4.7.3 Radiation Model

Five radiation models which allow you to include radiation into simulation process: Discrete Transfer Radiation Model (DTRM), P-1 Radiation Model, Rosseland Radiation Model, Surface-to-Surface Radiation Model, and Discrete Ordinates (DO) Radiation Model. The theories of these five radiation models are briefly summarized below. The detailed theories can be found in any radiation textbook such as Hottel (1967), Siegel and Howell (1980) and Modest (2003).

Radiative transfer equation

The radiative transfer equation for an absorbing, emitting and scattering medium at position $\vec{r}$ in the direction $\vec{s}$ is

$$\frac{dI(\vec{r},\vec{s})}{ds} + (a+\sigma_s)I(\vec{r},\vec{s}) = an^2\frac{\sigma T^4}{\pi} + \frac{\sigma_S}{4\pi}\int_0^{4\pi} I(\vec{r},\vec{s}')\phi(\vec{s}\cdot\vec{s}')d\Omega' \quad (4.62)$$

where $\vec{r}$ = position vector

$\vec{s}$ = direction vector

$\vec{s}'$ = scattering direction vector

s = path length

a = absorption coefficient

n = refractive index

σ_s = scattering coefficient

σ = Stefan-Boltzmann constant (5.672×10^{-8} W/m^2-K^4)

I = radiative intensity, which depends on position ($\vec{r}$) and direction ($\vec{s}$)

T = local temperature

ϕ = phase function

Ω' = solid angle

The sum of ($\mathbf{a}+\sigma_s$) is the extinction coefficient K. Integration of K along a distance "s" in the participating medium gives the optical thickness or opacity, $\kappa(s) = \int_0^s K(s)ds$. For a uniform gas medium with constant **a** and **σ**, the optical thickness can be simplified as $(a+\sigma_s)\times s$. The refractive index n is important when considering radiation in semi-transparent media. Absorption coefficient "**a**" and scattering coefficient σ_s are functions of local concentrations of H_2O and CO_2, path length, temperature and total pressure. In this study, absorption coefficient and scattering coefficient are calculated by piecewise polynomial approximation.

4.7.3.1 P-1 Radiation Model

For a gray medium (or on a spectral basis) with a known temperature distribution, the general problem of radiative transfer entails determining the radiative intensity from an integro-differential equation in five independent variables, including three space coordinates and two direction coordinates. The method of spherical harmonics provides a vehicle to obtain an approximate solution of arbitrarily high order, by transforming the equation of transfer into a series of simultaneous partial differential equations. To simplify the problem, an approximation is made by truncating the series of equations after very few terms. The highest value N, gives the method its order and its name, *P-N approximation*. It is known from neutron transport theory that approximations of odd order are more accurate than even ones of net highest order, so that P-2 approximation is never used.

The P-1 radiation model is the simplest case of the more general P-N radiation model. The P-1 model requires relatively little CPU demand and can easily be applied to various complicated geometries. This model includes the effect of scattering It is suitable for applications where the optical thickness **a**L is large, where "**a**" is the absorption coefficient and L is the length scale of the domain. In a gasifier, the optical thickness is thick due to the presence of various gases, coal particles, soot, and ashes. There are some limitations for this model. First, P-1 model assumes all surfaces are diffuse, which means the reflection of incident radiation at the surface is isotropic with respect to the solid angle. Second, the implementation of P-1 model assumes gray radiation. Third, when optical thickness is small, P-1 model may loss some accuracy, depending on the complexity of the geometry. Meanwhile, P-1 model tends to overpredict the radiative flux from localized heat sources or sinks. The equations of P-1 were shown in Section 4.3.5 in Eqs. (4.28) – (4.32) and are not repeated here.

When the model includes a dispersed second phase of particles the effect of particles can be included in the P-1 radiation model. Note that when particles are present, scattering in the gas phase is ignored. For a gray, absorbing, emitting, and scattering medium containing absorbing, emitting, and scatting particles, the transport equation for the incident radiation can be written as

$$\nabla \cdot (\Gamma \nabla G) + 4\pi\left(a\frac{\sigma T^4}{\pi} + E_P \right) - \left(a + a_p\right)G = 0 \tag{4.63}$$

where E_p is the equivalent emission of the particles and a_p is the equivalent absorption coefficient. These are defined as follow:

$$E_P = \lim_{V\to 0} \sum_{n=1}^{N} \varepsilon_{pn} A_{pn} \frac{\sigma T_{pn}^4}{\pi V} \tag{4.64}$$

$$a_P = \lim_{V\to 0} \sum_{n=1}^{N} \varepsilon_{pn} \frac{A_{pn}}{V} \tag{4.65}$$

In Equations 4.64 and 4.65, ε_{pn}, A_{pn}, and T_{pn} are the emissivity, projected area, and temperature of particle n. The summation is over N particles in volume V. These quantities are computed during particle tracking.

The projected area A_{pn} of particle n is defined as

$$A_{pn} = \frac{\pi d_{pn}^2}{4} \tag{4.66}$$

where d_{pn} is the diameter of the nth particle.

The quantity Γ in Equation 4.63 is defined as

$$\Gamma = \frac{1}{3(a + a_p + \sigma_{p)}} \quad (4.67)$$

where the equivalent particle scattering factor is defined as

$$\sigma_p = \lim_{V \to 0} \sum_{n=1}^{N} (1 - f_{pn})(1 - \varepsilon_{pn}) \frac{A_{pn}}{V}$$

(4.68)

and is compute during particle tracking. In equation 4.68, f_{pn} is the scattering factor associated with the n-th particle. Heat sources (sinks) due to particle radiation are included in the energy equation as follows:

$$-\nabla \cdot q_r = -4\pi \left(a \frac{\sigma T^4}{\pi} + E_P \right) + (a + a_p) G \quad (4.69)$$

4.7.3.2 Rosseland Radiation Model

The Rosseland model is valid when the medium is optically thick, $((a+\sigma_s)L \gg 1)$. Usually this model can be used when the optical thickness is greater than 3. The Rosseland model can be derived from the P-1 model, with some approximations. The difference between the P-1 model and the Rosseland model is the incident radiation G. Rosseland model assumes the intensity is the blackbody intensity at the gas temperature, while P-1 model calculates a transport equation for incident radiation G. Thus for Rosseland model, $G = 4\sigma n^2 T^4$, where n is the refractive index. The radiation flux is obtained by

$$q_r = -16\sigma\Gamma n^2 T^3 \nabla T$$

(4.70)

where $\Gamma = \frac{1}{(3(a + \sigma_s) - C\sigma_s)}$ and C is the linear-anisotropic phase function coefficient. By simplification, Rosseland model has two advantages over P-1 model. Rosseland model can be calculated faster than P-1 model and requires less memory since it does not solve an extra transport equation for the incident radiation, while P-1 model does.

4.7.3.3 Discrete Transfer Radiation Model (DTRM)

The main assumption of the DTRM model is that the radiation leaving the surface element in a certain range of solid angles can be approximated by a single ray. This "ray tracing" technique could provide a prediction of radiation heat transfer between surfaces without conducting explicit view factor calculations. Thus, the accuracy of this model really depends on the number of rays traced and the computational gird.

The equation for change of radiant intensity, *dI,* along a path, *ds,* can be presented by

$$\frac{dI}{ds} + aI = \frac{a\sigma T^4}{\pi} \quad (4.71)$$

Here, the refractive index is assumed to be unity. DTRM model integrates Equation (4.71) along a series of rays emanating from boundary faces. Thus in DTRM model, I(s) can be represented as

$$I(s) = \frac{\sigma T^4}{\pi}(1 - e^{-as}) + I_0 e^{-as} \quad (4.72)$$

where I_0 is radiant intensity at the start of the incremental path, which is determined by the appropriate boundary condition. The energy source in fluid due to radiation is calculated by summing the change in intensity along the path of each ray that is traced though the fluid control volume.

DTRM model is a relatively simple model, and the accuracy of this model can be increased by increasing the number of rays. Nevertheless, DTRM can be computationally expensive if there are too many surfaces to trace rays from and too many volumes being crossed by rays. There are some limitations for DTRM model. DTRM model assumes gray radiation: all surfaces are diffuse. Meanwhile, the effect of scattering is not included in the DTRM model.

4.7.3.4 Discrete Ordinates (DO) Radiation Model

The DO model solves the radiative transfer equation for a finite number of discrete solid angles, each associated with a vector direction $\vec{s}$ fixed in the global Cartesian system (x, y, z). Different from DTRM model which performs ray tracing, DO model transforms the radiative transfer equation (4.63) into a transport equation for radiation intensity in the spatial coordinates (x, y, z). The DO model solves for as many transport equations as there are directions $\vec{s}$. It can be implemented by two approaches: energy uncoupled or energy coupled. The uncoupled implementation is sequential in nature and uses a conservative variant of DO model called the finite-volume scheme. The equations for the energy and radiation intensities are solved one by one, assuming prevailing values

for other variables in uncoupled implementation. On the contrary, the discrete energy and intensity equations are solved simultaneously in the energy coupled method. The advantage of the coupled approach is that it can speed up applications involving high optical thicknesses and high scattering coefficients. Typically, energy coupled DO model is used when optically thickness is greater than 10. This is typically encountered in glass-melting applications. The energy coupling DO model sometimes will lead to slower convergence when there is weak coupling between energy and directional radiation intensities.

The DO model considers the radiative transfer equation (RTE) in the direction $\vec{s}$ as a field equation. Also, DO model allows the modeling of non-gray radiation by using a gray-band model. Thus, the RTE for the spectral $I_\lambda(\vec{r},\vec{s})$ can be written as:

$$\nabla\cdot(I_\lambda(\vec{r},\vec{s})\vec{s})+(a_\lambda+\sigma_s)I_\lambda(\vec{r},\vec{s})=a_\lambda n^2 I_{b\lambda}+\frac{\sigma_S}{4\pi}\int_0^{4\pi} I_\lambda(\vec{r},\vec{s}')\phi(\vec{s}\cdot\vec{s}')d\Omega' \tag{4.73}$$

Here λ is the wavelength, a_λ is the spectral absorption coefficient, and $I_{b\lambda}$ is the black body intensity given by the Planck function. The scattering coefficient, the scattering phase function, as well as the refractive index n are assumed independent of wavelength. The total intensity $I(\vec{r},\vec{s})$ in each direction $\vec{s}$ at position $\vec{r}$ is computed by

$$I(\vec{r},\vec{s})=\sum_k I_{\lambda_k}(\vec{r},\vec{s})\Delta\lambda_k \tag{4.74}$$

where the summation is over the wavelength bands.

Compared with other radiation models, DO model can fit for the entire range of optical thickness. Moreover, scattering effect, exchange of radiation between gas and particulates, and non-gray radiation have been considered in this model. It also allows considerations of the radiation at a semi-transparent wall, a specular wall, and a partially-specular wall. The disadvantage of DO model is that solving a problem with a fine angular discretization is computationally expensive.

4.7.3.5 Surface-to-Surface (S2S) Radiation Model

The main assumption of the S2S model is that any absorption, emission, or scattering of radiation can be ignored. Therefore, S2S model can be used to account for the radiation exchange in an enclosure of gray-diffuse surfaces. The energy exchange between two surfaces depends only on "view factor."

The energy flux leaving a given surface is composed of directly emitted and reflected energy, which is

$$J_k = \varepsilon_k \sigma T_k^4 + \rho_k \sum_{j=1}^{N} F_{kj} J_j$$

(4.75)

where J_k represents the energy that is given off (or radiosity) of surface k, ρ_k is reflectivity of surface k. The view factor F_{jk} is the fraction of energy leaving surface k that is incident on surface j, which is given by:

$$F_{ij} = \frac{1}{A_i} \int_{A_i} \int_{A_j} \frac{\cos\theta_i \cos\theta_j}{\pi r^2} \delta_{ij} dA_i dA_j$$

(4.76)

where δ_{ij} is determined by visibility of dA_j to dA_i. $\delta_{ij} = 1$ if dA_j is visible to dA_i and 0 otherwise.

S2S model is good for modeling the enclosure radiative heat transfer without participating media. Compared with DTRM and DO models, S2S model has a much faster computation time per iteration, although the view factor calculation itself is CPU-intensive. Since S2S model doesn't include participating media, it serves as a reference case for comparing the effect of participating media on gasification process.

4.7.4 Physical Characteristics of the Model and Assumptions

This study investigates a two-stage entrained flow coal gasifier as shown in Fig. 4.32. The gasifier capacity is around 1700 ton/day for coal input, and the energy output rate is around 190MW. The grid consists of 1,106,588 unstructured tetrahedral cells. In the simulations, the buoyancy force is considered, varying fluid properties are calculated for each species and the gas mixture, and the walls are assumed impermeable and adiabatic. Since each species' properties, such as density, Cp value, thermal conductivity, absorption coefficient, et al. are functions of temperature and pressure, their local values are calculated by using *piecewise polynomial approximation* method. The mixture properties are calculated by mass weighted average method. The flow is steady and no-slip condition (zero velocity) is imposed on the wall surfaces.

For gas phase, each species' properties, such as density, Cp value, thermal conductivity, absorption coefficient, et al. are functions of temperature and pressure. To reflect this relationship, the local value of each property is calculated by using piecewise polynomial approximation method. The absorption coefficient of each species at different temperature and pressure range is based on Hottel chart (1967) and Zhang's chart (2001). For particulate effect, only the P-1 and DO models account for exchange of radiation

between gas and particulates. The particulates' equivalent absorption coefficient a_p and equivalent particle scattering factor σ_p are defined below as:

$$a_p = \lim_{V \to 0} \sum_{n=1}^{N} \varepsilon_{pn} \frac{A_{pn}}{V}$$

(4.77)

$$\sigma_p = \lim_{V \to 0} \sum_{n=1}^{N} (1 - f_{pn})(1 - \varepsilon_{pn}) \frac{A_{pn}}{V}$$

(4.78)

where ε_{pn}, A_{pn}, T_{pn}, f_{pn} are the emissivity, projected area, temperature and scattering factor of particle n. They are computed during the particle tracking.

4.7.5 Boundary and Inlet Conditions

The Indonesian coal shown in Table 4.3 is used in this study. The boundary and inlet conditions are shown in Fig. 4. 32. The total mass flow rates of the coal slurry and the oxidant are 19.86 kg/s and 14.50 kg/s, respectively (Case 1, 3). The total mass flow rate of the dry coal case (Case 2) is 19.86 kg/s. The difference in fuel mass flow rates is caused by water added for making coal slurry. The inherent moisture in the coal is included in both the slurry and the dry feed cases. The coal/water weight ratio of the coal slurry is 60%-40%. Oxidant/coal slurry feed rate gives O_2/C stoichiometric ratio of 0.5. The stoichiometric ratio is defined as the percentage of oxidant provided over the stoichiometric amount for complete combustion of carbon. For the dry coal case, N_2 (25% of total weight of Oxidant) has been injected with O_2 to transport the coal power into the gasifier.

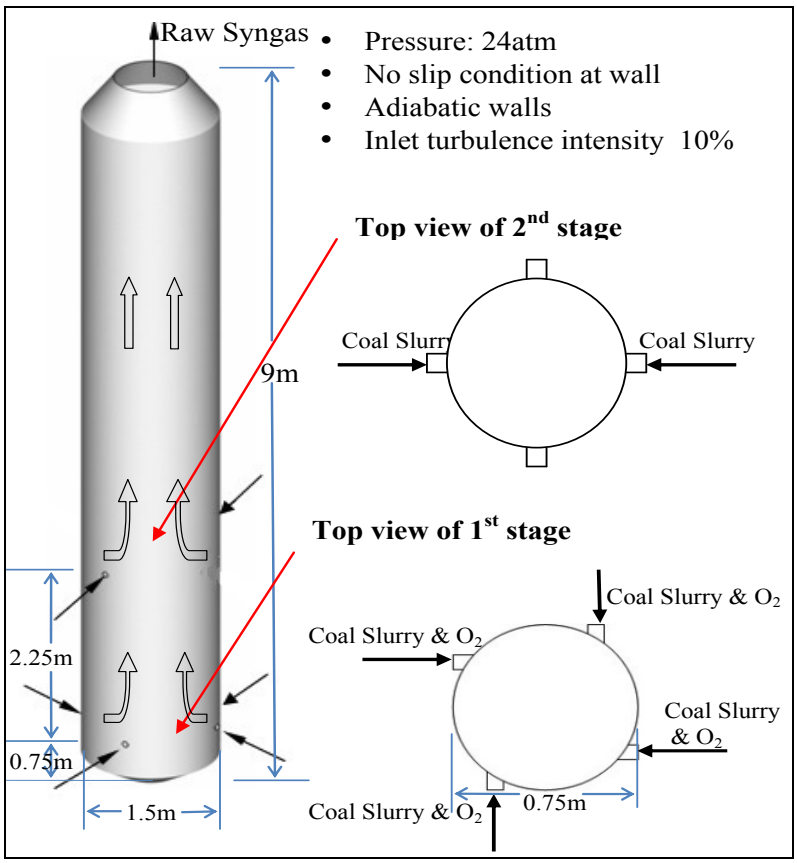

Fig. 4.32 Schematic of the two-stage entrained-flow gasifier

The oxidant is considered as a continuous flow and the coal slurry is considered as a discrete flow. The discrete phase only includes the fixed carbon and water from the inherent moisture content of coal (8.25% wt.) and water added to make the slurry. The slurry coal is treated as particles containing both coal and liquid water. Other components of the coal, such as N, H, S, O, and ash, are injected as gas together with the oxidant in the continuous flow. N is treated as N_2, H as H_2, and O as O_2. S and ash are not modeled, and their masses are lumped into N_2.

The walls are all set to be adiabatic and imposed with the no-slip condition (i.e., zero velocity). The internal emissivity of inlet, exit and wall is set as 0.8. The gasifier's wall is set as opaque and the internal emissivity is also 0.8. The boundary condition of the discrete phase at the walls is assigned as "reflect," which means the discrete phase elastically rebounds off once reaching the wall. The operating pressure inside the gasifier is set at 24 atm. The exit pressure is the same as operating pressure, 24 atm. The syngas is considered to be a continuous flow, and the coal and char from the injection locations are considered to be discrete particles. The particle size is uniformly given as spherical droplets with a uniform arithmetic diameter of 40 μm. Although the actual size distribution of the coal particles is non-uniform, a simulation using uniform particle size

provides a more convenient way to track the devolatilization process of coal particles than a non-uniform size distribution.

The following three cases are studied. Each case is performed without radiation model, with DTRM model, P-1 model, Rosseland Model and DO radiation models, respectively. S2S radiation model is investigated in the baseline case only.

Case 1: Baseline case, oxygen-blown, coal slurry, fuel stream: 100% in 1 stage
Case 2: Oxygen-blown, dry coal, fuel stream: 100% in 1 stage
Case 3: Oxygen-blown, coal slurry, fuel stream: 50%-50% distribution in 2 stages

The summary of the studied cases are listed in Table 4.24 In the baseline (Case 1) of this study, dry-coal-fed and two-stage configuration is used with fuel distribution of 100%-0% between the first and the second stages.

4.7.6 Results and Discussions of Effects of Radiation Models

Baseline Case (Case 1, coal slurry)

The baseline case (Case 1) is the two-stage oxygen-blown operation with coal slurry distribution of 100%-0% between the first and the second stages, which means all the fuel is injected from the first stage. Syngas temperature and species mole fraction distributions at exit for different sub-cases are shown in Table 4.24. It is observed that the syngas compositions at exit for the cases without radiation model, with P1 model, and with DO model have very similar results, while DTRM model, S2S model and Rosseland model yield slightly lower mole fractions of CO_2 and H_2. The reason for this phenomenon is that the Water-Gas-Shift (WGS) reaction $CO+H_2O \leftrightarrow CO_2+H_2$ proceeds in the forward direction and yields more CO_2 and H_2 for the cases of P1 and DO models. The syngas temperature for the cases of P1 and DO models are higher (200K-300K) than the rest of the three models, since an exothermic WGS reaction releases more reaction heat. By comparing the average value and standard deviation, the P1 model has the result most close to the mean.

Based on the energy balance, higher syngas temperature should yield lower syngas Higher Heating Value (HHV) since the "total HHV" of the syngas consists mainly of the sensible heat (evaluated at the gasifier's exit temperature) and the heating value (evaluated at 298K). When the gas temperature is high, it implies that more heating value in the fuel has been converted to the syngas's sensible heat, so the HHV of syngas tends to be low. This is verified as the total HHV (kJ/kg) values (syngas heating value + sensible heat) in Table 4.24 —the total HHV (kJ/kg) value of syngas in each case is

similar. The minor difference may be caused by the different kinetic energy at gasifier exit of each case or by the fact that syngas composition is normalized by excluding the minor species, N_2, CH_4, and $O_{2,}$, resulting in a minor difference in the real syngas molecular weight.

Table 4.24 Syngas composition and temperature at exit for case 1 (1 stage slurry) with different radiation models (Syngas composition is normalized by $CO + H_2O + CO_2 + H_2 = 1$.)

Radiation Model	None	DTRM	P1	Rosseland	DO	S2S	Average	Standard Deviation
CO_2 (Vol)	0.10	0.07	0.09	0.08	0.10	0.08	0.087	0.012
CO (Vol)	0.31	0.33	0.32	0.34	0.31	0.32	0.322	0.012
H_2O (Vol)	0.39	0.42	0.40	0.39	0.39	0.42	0.402	0.015
H_2 (Vol)	0.20	0.18	0.19	0.19	0.20	0.18	0.190	0.009
T_{exit} (K)	1756	1415	1665	1500	1721	1480	1590	142.24
Carbon Conversion Rate (CCR)	99%	97%	98%	99%	98%	98%	98%	0.008
HHV(kJ/kmol)	160,746	161,906	161,123	166,105	160,746	159,076	159,284	6544
Total HHV (kJ/kmol)	215,783	202,507	215,571	210,071	215,153	202,589	207,946	8466
Total HHV (kJ/kg)	10,526	10,005	10,334	10,277	10,495	10,029	10,278	223
Average CPU time per iteration (s)	10.1	21.4	11.3	10.9	20.5	13.4	14.5	5.1

The syngas and inner wall temperature distributions for the different sub-cases are shown in Figs 4.33 (syngas temperature at the mid-plane) and 4.34 (average wall temperature). It is surprising to see the large variations of syngas and wall temperatures predicted by different radiation models. For syngas temperature distribution, it can be observed that the results are separated into two groups with the none radiation model, the P1 model, and the DO model forming the first group producing higher syngas temperature, while the results for cases with the S2S model, the Rosseland model, and the DTRM model form the second group, producing syngas temperatures approximately 300K lower than the first group. This large variation of predicted syngas temperature could be caused by the reason that both the S2S model and DTRM model do not consider exchange of radiation between gas and particulates, nor are the mechanisms of scattering and emissivity considered. Therefore, the syngas temperature at second stage drops more in DTRM model and S2S model because the syngas at the second stage cannot receive

the radiation energy coming from the syngas at the first stage which is at a higher temperature. Nonetheless, the predicted temperatures in the combustion zone (near the first stage injection location) from all the models converge at around 2050K. This indicates that it is more consistent in predicting combustion temperatures with different radiation models, but it is very uncertain and challenging by applying an appropriate radiation model in simulating the gasification process.

The result of the Rosseland model seems unreasonable because it shows that mass-weighted average temperature maintains almost at a constant value along the gasifier. Hence, the Rosseland model is not suitable for radiation modeling of Case 1. This unreasonable result may be caused by the fact that the Rosseland model only works for optically very thick media and that it assumes the intensity to be the black-body intensity at gas temperature. This is different from the P1 model that actually calculates the radiation intensity through solving a transport equation.

For the inner wall temperature shown in Fig. 4.34, the variation span (about 500K near the exit) is wider than the variation of syngas temperature. The non-radiation case has the highest value, whereas the P1 model case has the lowest wall temperature. The difference of wall temperature between these two cases is about 300K-500K. In the second stage, the S2S model gives a relatively uniform inner wall temperature when compared to other models. It appears that, when the radiation effect is included, both the syngas and wall temperatures decrease under the slurry coal gasification condition.

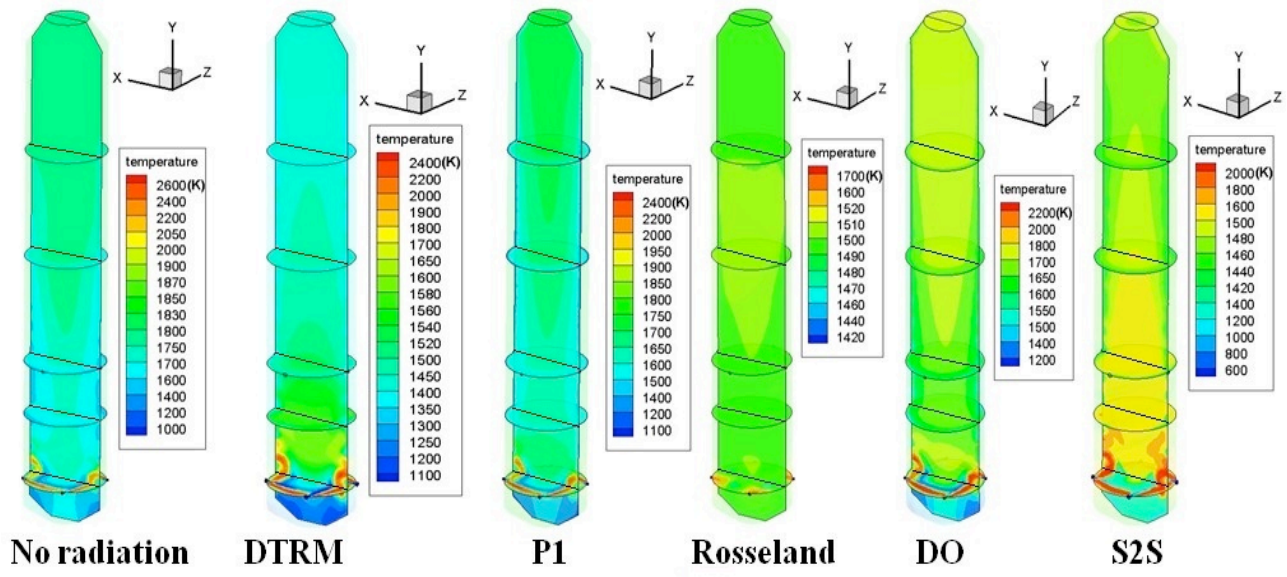

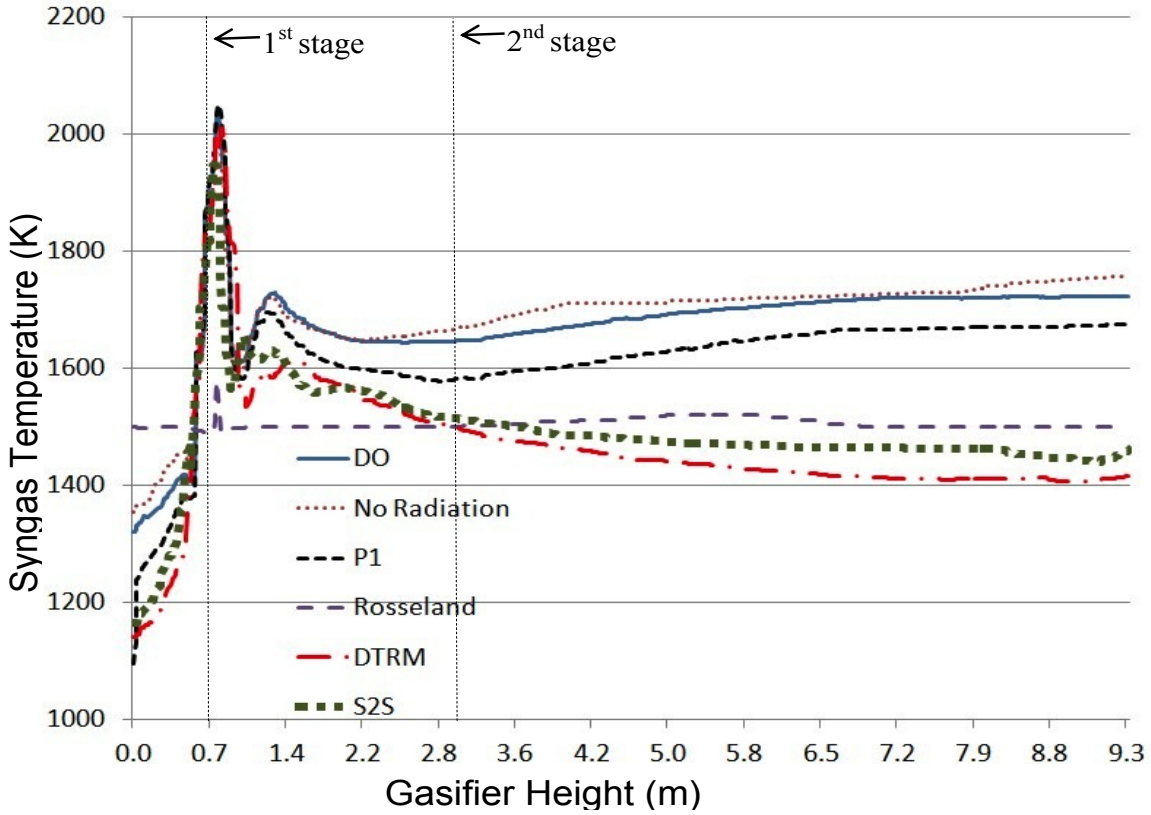

Figure 4.33 **Mid-plane syngas** temperature contour and mass-weighted average of syngas temperature distribution along the gasifier for Cases 1 (coal slurry)

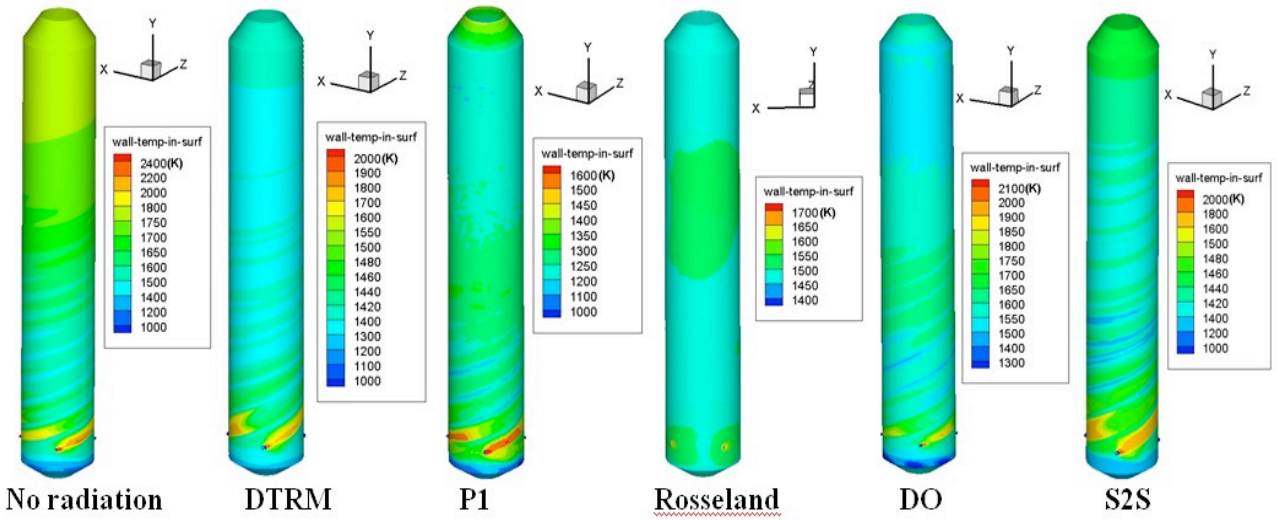

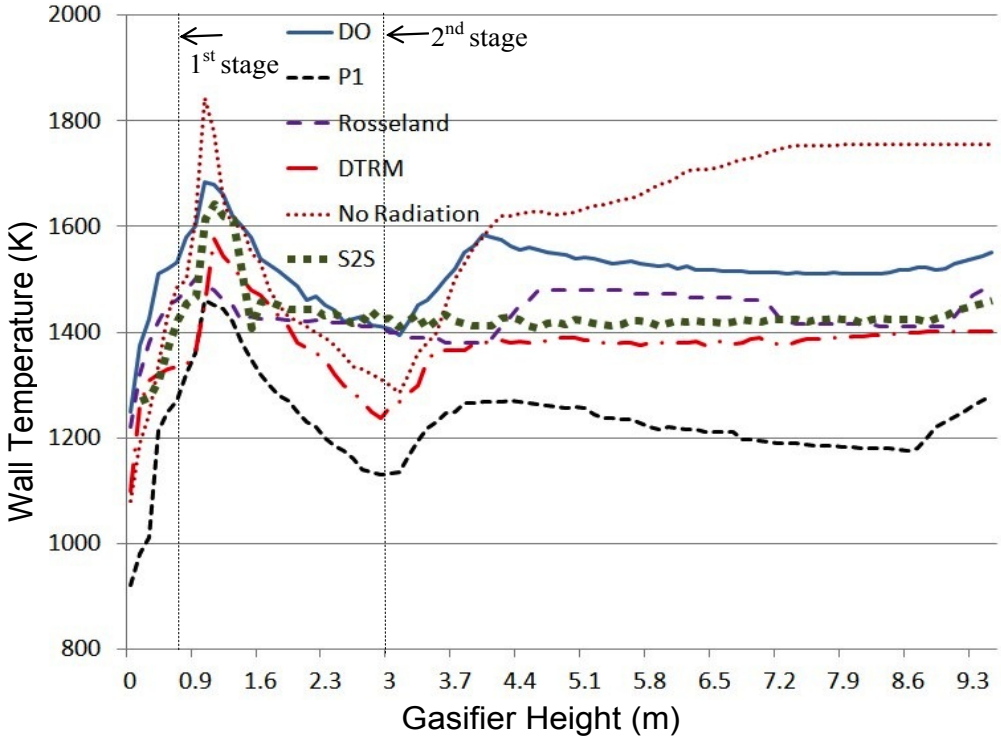

Figure 4.34 **Wall temperature** contour and **circumferential average** of gasfier inner wall temperature distribution along the gasifier for Cases 1 (coal slurry)

Table 4.24 also shows the average CPU time per iteration for each case. It can be clearly seen that DO and DTRM model take about twice more CPU time than other models. Due to an extreme computational time required for using the gray band method, only the total gray radiation approach is employed in this paper. For angular discretization in the DO model, the Theta Divisions and Phi Divisions are both set as 3 to obtain reliable results. The pixelation of 1×1 is used because it is sufficient for modeling gray-diffuse radiation.

Case 2 (dry coal, 100%-0% for two stage injection)

Case 2 is the two-stage oxygen-blown operation with dry coal distribution of 100%-0% between the first and the second stages. Syngas temperature and species mole fraction distributions at exit for different sub-cases are shown in Table 4.25. Similar to Case 1 (1 stage coal slurry), it is shown that the sub-cases with the none radiation, the P1 and the DO models have very similar results of syngas composition and temperature at the exit, while the results of the DTRM model and the Rosseland model yield noticeably different syngas compositions and produce very high exit syngas temperatures (400K-700K higher). Different from Case 1 with coal slurry, in the dry coal study of Case 2, the lower syngas exit temperatures predicted by the DO and P1 model could be caused by the slower forward WGS reaction rate than in the cases with Rosseland and DTRM models. Since water content in dry coal is much less than in the coal slurry, steam has not been sufficiently provided to promote forward WGS reaction to produce more H_2 and CO_2, so

the results of syngas composition for P1 and DO models in Case 2 with more CO and less H_2 are thought to be more reasonable than the sub-cases with DTRM and Rosseland models.

Table 4.25 Syngas composition and temperature at exit for Case 2 (dry coal, 100%-0%) with different radiation models (Syngas composition is normalized by CO + H_2O + CO_2 +H_2 =1.)

Radiation Model	None	DTRM	P1	Rosseland	DO	Average	Standard Deviation
CO_2 (Vol)	0.06	0.10	0.05	0.10	0.07	0.076	0.023
CO (Vol)	0.53	0.51	0.53	0.48	0.52	0.514	0.021
H_2O (Vol)	0.18	0.14	0.17	0.17	0.18	0.168	0.016
H_2 (Vol)	0.23	0.25	0.23	0.26	0.23	0.24	0.014
T_{exit} (K)	1733	2145	1747	2476	1770	1974	328.81
CCR	99%	97%	97%	99%	98%	98%	0.01
HHV(kJ/kmol)	223,042	221,472	222,635	217,060	220,212	220,884	2405
Total HHV(kJ/kmol)	267,605	288,503	270,533	299,184	270,446	279,254	13893

Figures 4.35 and 4.36 provide contour and mass-weighted temperature distributions for both syngas and inner wall temperatures. It is interesting to see that the syngas temperature distributions predicted by none radiation model, the P1 model, and the DO model are very consistent, while the DTRM model gives a higher syngas temperature (about 400K higher at the exit). The result of syngas temperature distribution for the Rosseland model is apparently not reasonable because it yields a very large and unrealistic swing of both syngas and wall temperatures along the gasifier.

For the inner wall temperature, the case with the DO model yields a similar result with the case without employing any radiation model. The wall temperature for P1 model is around 400K lower than it for DO model, while the temperature for DTRM model is about 300K higher than DO model. Note that in both the slurry coal and dry coal cases, P1 model predicts the lowest wall temperature.

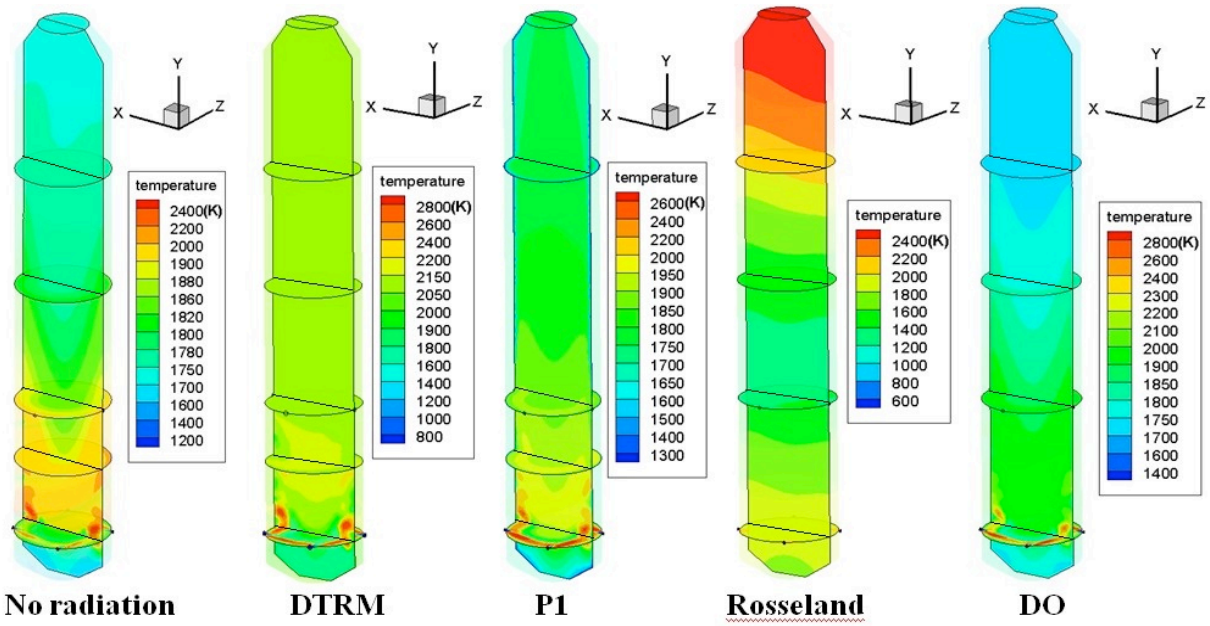

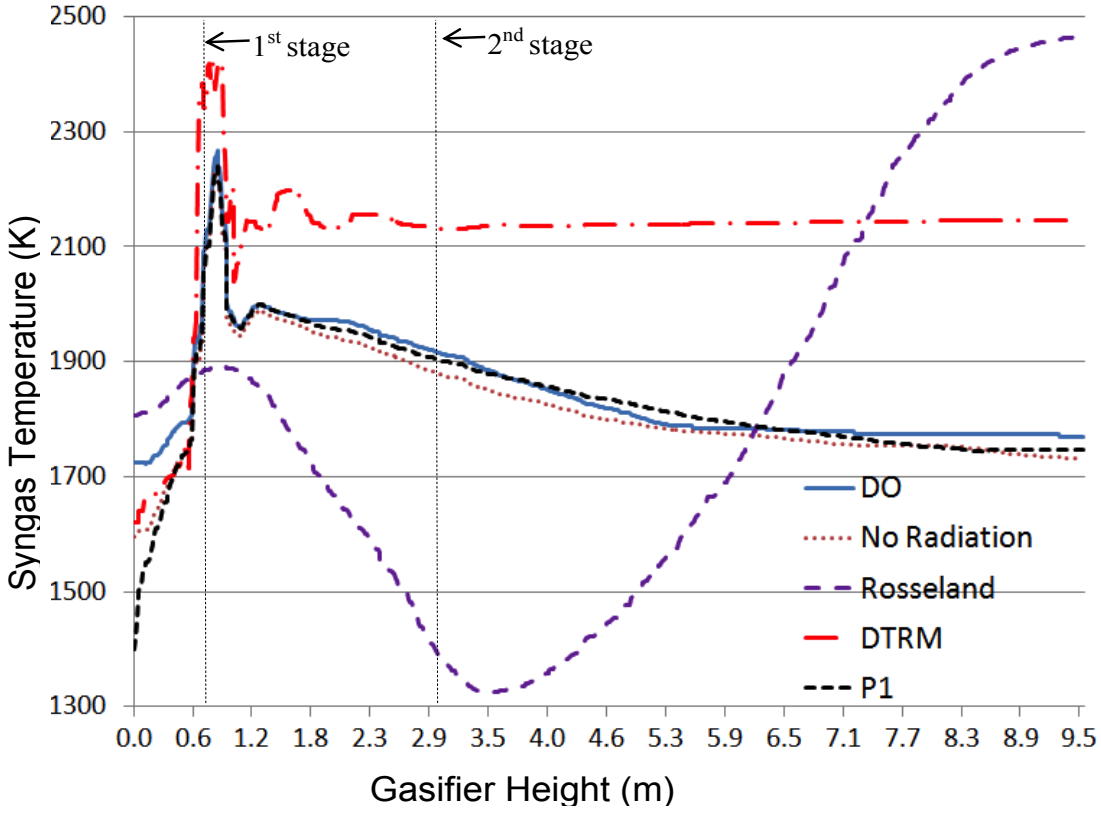

Figure 4.35 **Mid-plane syngas** temperature contour and **mass-weighted average** of syngas temperature distribution along the gasifier for Cases 2 (dry coal)

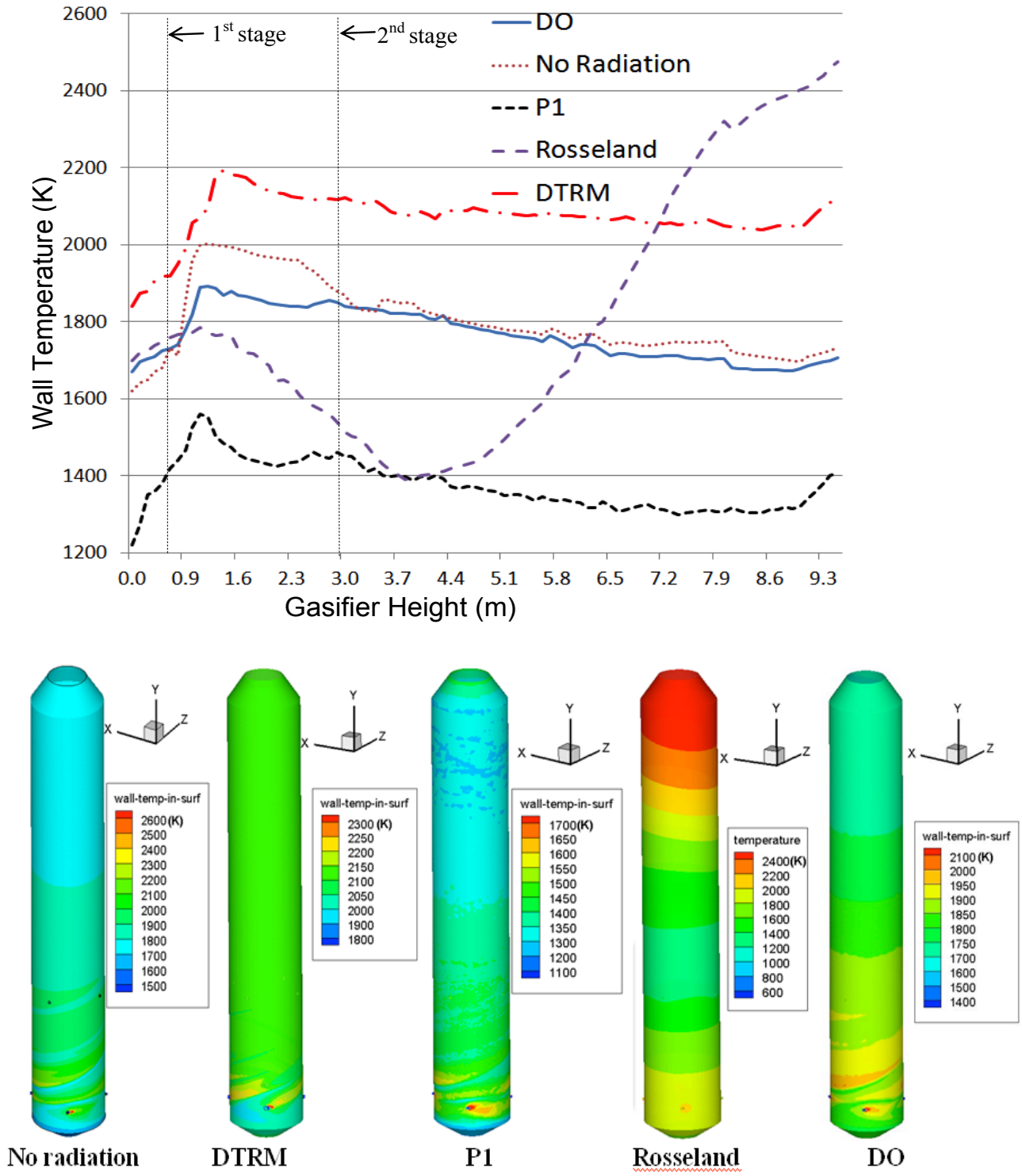

Figure 4.36 **Wall temperature** contour and **circumferential average** of wall temperature distribution along the gasifier for Cases 2 (dry coal)

Case 3 (coal slurry, 50%-50% for two stage injection)

Case 3 is the two-stage oxygen-blown operation with dry coal distribution of 50%-50% between the first and the second stages. Syngas temperature and species mole fraction distributions at exit for different sub-cases are shown in Table 4.26. Syngas temperature and inner wall temperature distribution are shown in Figures 4.37 and 4.38. Similar to Case 1, the Rosseland model gives uniform syngas temperature distribution, so this model does not work for gasification simulation. DO model, P1 model, DTRM model, and none radiation model have the same syngas temperature distribution with different levels. The combustion process is the main reaction at the first stage. The DO model yields the highest syngas temperature, while the P1 model continues to give the lowest syngas temperature; the maximum temperature difference between DO and P1 models is about 1000K between the first and second stage at around 2.5 m. Because 50% coal slurry is injected from second stage injection without oxygen, the gasification process dominates in the second stage; and, consequently, the syngas temperature drops drastically near the second stage injection location, as shown in Figure 4.37. The syngas temperature slightly increases at the second stage all the way to the exit of gasifier. This temperature increase may be caused by the exothermic process from the WGS reaction in the second stage after coal slurry has been consumed completely.

At the second stage, the maximum wall temperature difference between the DO model and P1 model is about 300K. Different from the syngas temperature distribution, the inner wall temperature decreases from the first stage injection location (combustion area) all the way to the exit of gasifier. The case with the DTRM model predicts the highest inner wall temperature, while the P1 model continues to predict the lowest one. The biggest temperature difference between these two models reaches an uncomfortably large value of approximately 1000K.

Table 4.26 Syngas composition and temperature at exit for case 3 (2 stage slurry) with different radiation models (Syngas composition is normalized by $CO + H_2O + CO_2 + H_2 = 1$)

Radiation Model	None	DTRM	P1	Rosseland	DO	Row Average	Standard Deviation
CO_2 (Vol)	0.09	0.08	0.12	0.05	0.12	0.092	0.029
CO (Vol)	0.30	0.32	0.26	0.28	0.28	0.288	0.023
H_2O (Vol)	0.41	0.39	0.44	0.41	0.41	0.412	0.018
H_2 (Vol)	0.20	0.21	0.18	0.26	0.19	0.208	0.031
T_{exit} (K)	1551	1216	1312	1498	1414	1398	136.184

CCR	98%	99%	97%	99%	98%	98.2%	0.008
HHV(kJ/kmol)	158,727	166,440	142,910	170,217	150,209	157,701	11280
Total HHV(kJ/kmol)	205,613	198,642	181,381	208,106	175,493	193,847	14637

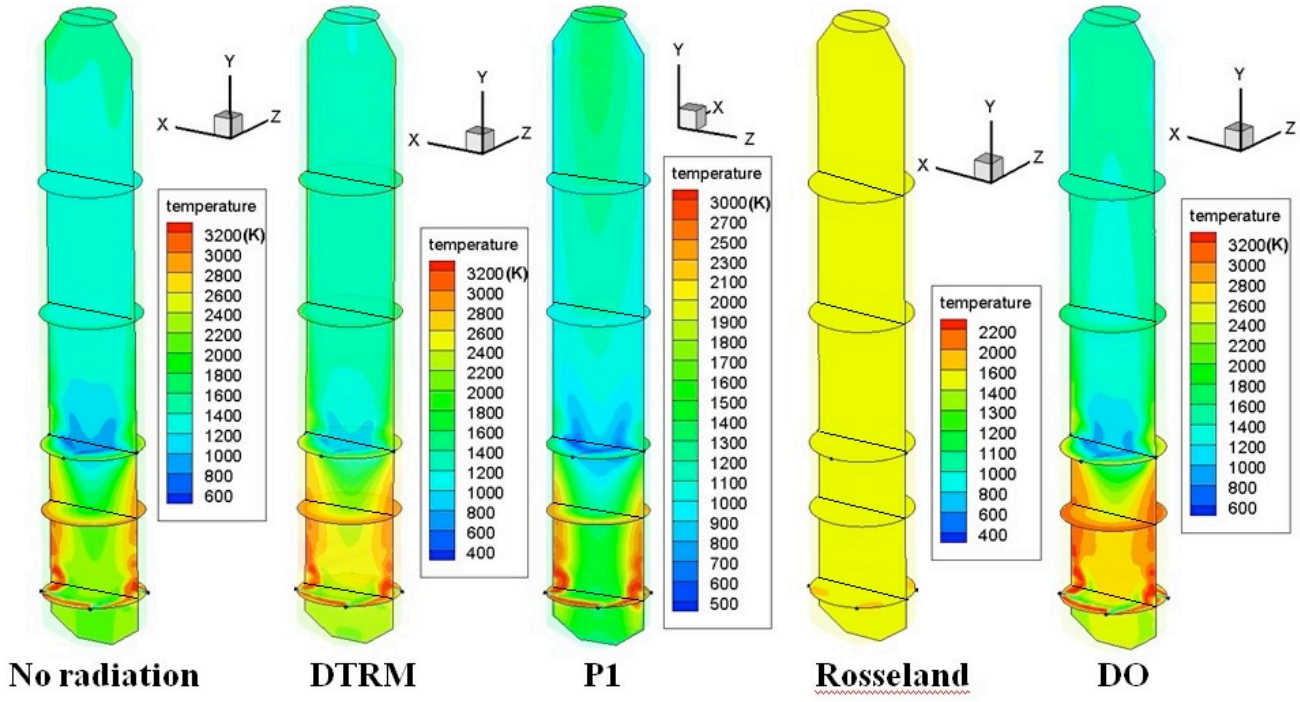

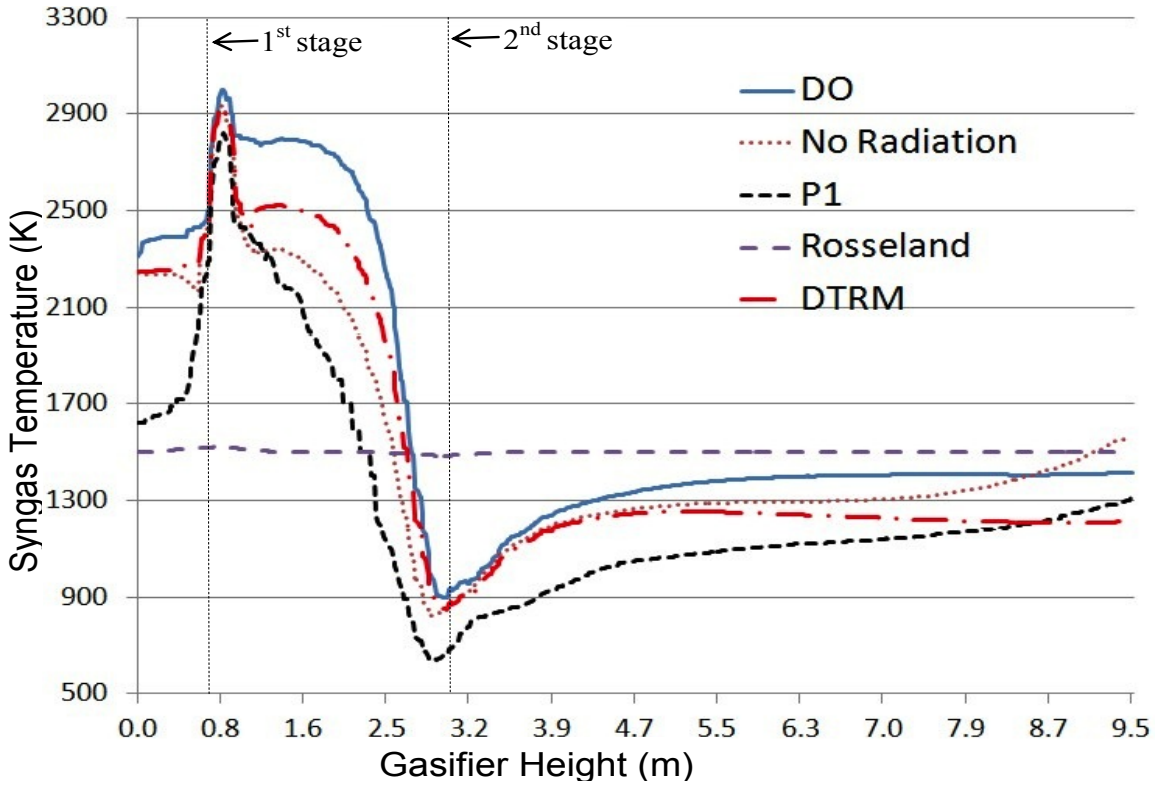

Figure 4.37 Mid-plane **syngas temperature** contour and **mass-weighted average** of syngas temperature along the gasifier for Cases 3 (Coal slurry, 50%-50%)

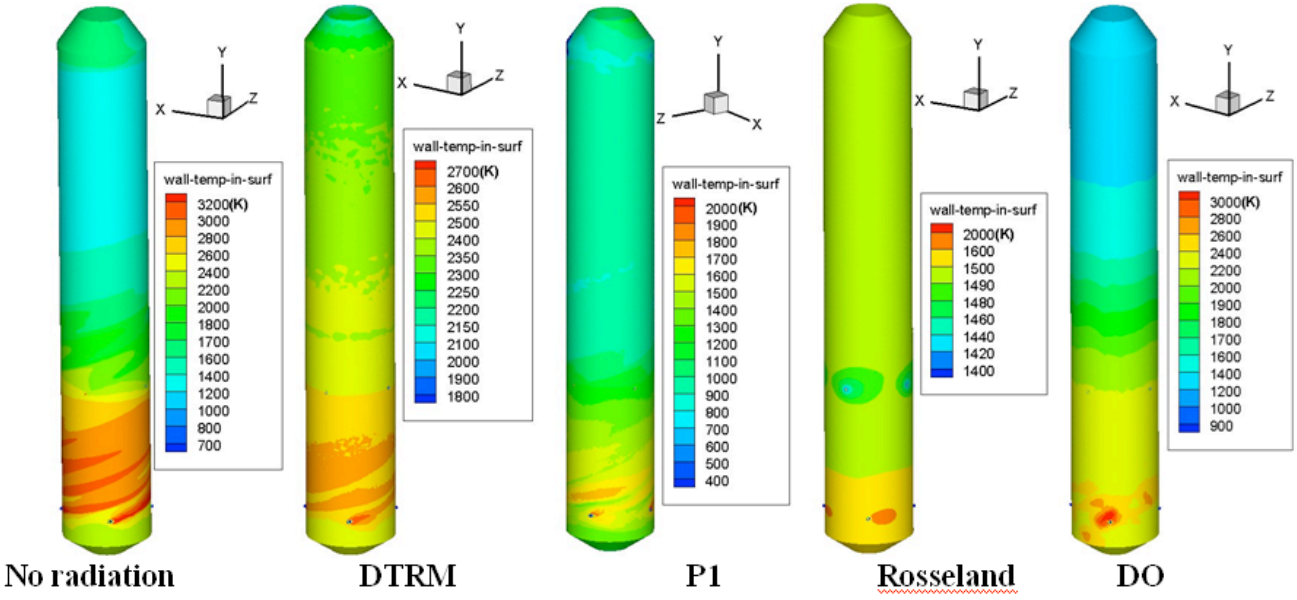

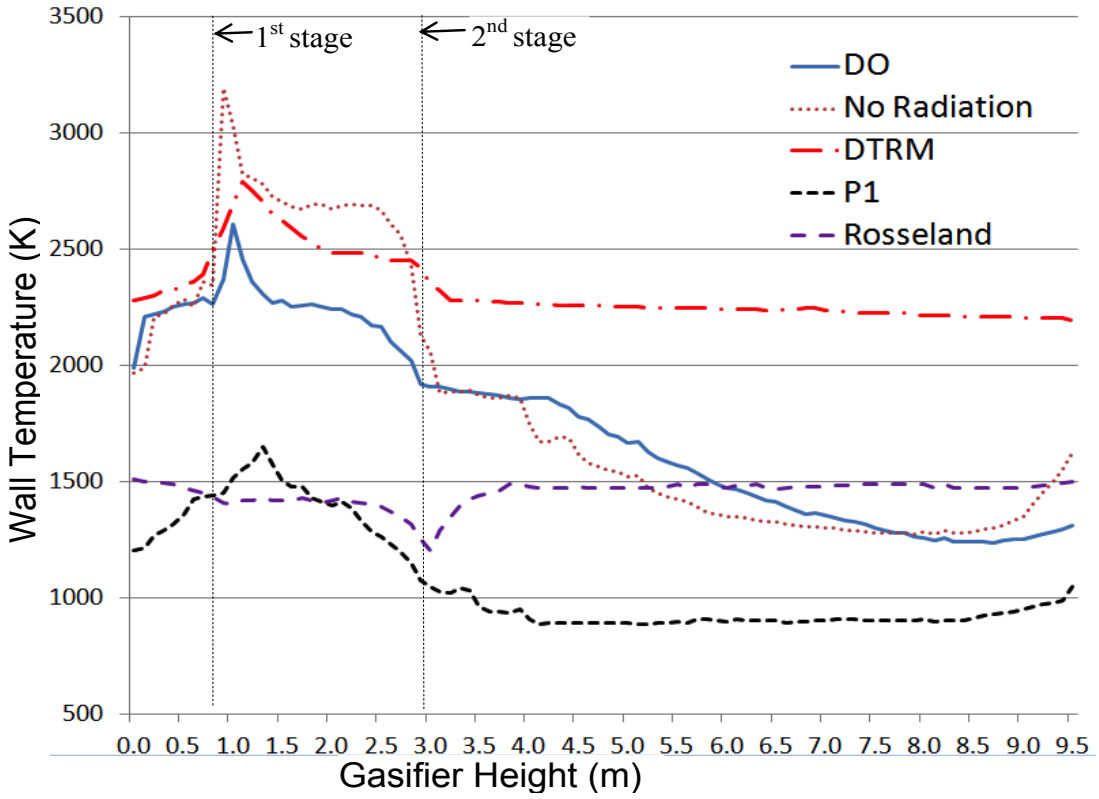

Figure 4.38 **Wall temperature** contour and **circumpherential average** of inner wall temperature distribution along the gasifier for Cases 3 (Coal slurry, 50%-50%)

4.7.7 Conclusions on Effects of Radiation Model

Five different radiation models have been tested through three different operating conditions of gasification process. The results of syngas composition, syngas temperature, as well as the inner wall temperature in each case have been compared. The conclusions are:

a. Rosseland model does not yield reasonable and realistic results for gasification process. It either predicts an uncharacteristic nearly-constant syngas and wall temperature distributions along the gasifer for the slurry coal cases or a unreasonably large swing of temperature from very high to very low and back to very high value along the gasifier for the dry-coal feed case.
b. Inner wall temperature is more uniform in the case of S2S model than any other radiation models, since S2S model only considers the enclosure radiation transfer without including participating media.

c. The effect of radiation is much more significant in predicting the inner wall temperature than syngas temperature distribution.
d. The P1 model always predicts the lowest inner wall temperature in all the cases.
e. The DTRM model predicts very high syngas and wall temperatures in the dry coal feed case. In the one-stage coal slurry case, DTRM result is close to the S2S result.
f. DO and DTRM model take about twice more CPU time than the other models.

In this study, the various radiation models yield uncomfortably large uncertainties in predicting syngas composition (18%), syngas temperatrure (21%), and wall temperature (28%). No solid conclusion can be derived from this study without a comparison with detailed experimental data consisting of local syngas composition and temperature information, as well as of the inner wall temperature distribution of the gasifier. However, it is fair to note that the Rosseland model does not seem to work reasonably well for simulating the gasification process. The P1 method seems to behave stably and is robust in predicting the syngas temperature and composition, but it seems to underpredict the gasifier's inner wall temperature.

4.8 Topic 5: Low-Rank Coal versus High-Rank Coal (Summary only)

(See Lu and Wang (2012) in Proceedings International Pittsburgh Coal Conference for details.)

Low-rank coal contains more volatiles, more inherent moisture, high alkali metals (Na, K, Ca), high oxygen content and low sulfur than high-rank coal. Low-rank coal gasification usually has lower efficiency than high-rank coal, since more energy has been used to drive out the moisture and volatile matters and vaporize them. Nevertheless, Low-rank coal comprises about half of both the current utilization and the reserves in the United States and is the largest energy resource in the United States, so it is worthwhile and important to investigate the low-rank coal gasification process.

Among the existing commercial coal gasifiers, two-stage fuel feeding has been employed only in updraft gasifiers, such as the E-gasifier. In this study, the two-stage fuel feeding scheme is investigated in a downdraft, entrained-flow, and refractory-lined reactor. The two-stage coal feeding gasification process injects all of the oxygen in the first stage and provides a certain amount of coal slurry without oxygen in the second stage. The endothermic gasification process downstream of the second stage could keep the gasifier at a lower temperature; and hence, the life of the refractory bricks can be extended and maintenance costs reduced. However, this benefit gained at the second stage is obtained at the cost of a higher peak combustion temperature in the first stage than a typical one-stage gasifier. Since the combustion temperature of low-rank coal is lower than the high rank coal, it is hypothesized that low-rank coal can help reduce the peak temperature at the first stage. Therefore, hypothetically, it seems that it is more advantageous for utilizing low-rank coals to in a two-stage coal gasification process. This study aims to investigate these hypotheses.

Both high-rank coals and low-rank coals have been used for comparison. Considering that the high-moisture content in the low-rank coal cannot help reduce the amount of water needed for making an appropriate recipe of coal slurry, dry coal feeding seems to be more energy efficient than slurry coal feeding. Hence, both dry coal feeding with and without steam injection are studied, and the results are compared. Considering that the inherent moisture inside of low-rank coals is difficult to be driven out, which is different from abundant surface moisture in the coal slurry, the case of low-rank coals gasification without drying process is also studied by applying simple model, the results are compared.

This study focuses on a low-rank coal gasification study. The South Hallsville Texas (SHT) Lignite was used as the low-rank coal and Illinois No.6 bituminous coal was used as the high-rank coal in this study. Several comparisons have been conducted on the same

operating conditions: 1) low-rank coal vs. high-rank coal; 2) one-stage injection vs. two-stage injection; 3) low-rank coal with pre-drying vs. without pre-drying; and 4) dry coal feeding without steam injection vs. with steam injection at the second stage. Several conclusions are drawn as follows:

a. Syngas produced from lignite has 21% (538 K) lower exit temperature and 18% (30,222 kJ/kmol) greater HHV than syngas produced from Illinois #6 (high-rank coal). Based only on this result of HHV value, it follows that low-rank coal could be a better alternative fuel for coal gasification.

b. The one-stage and two-stage fuel injection schemes have similar syngas compositions and Higher Heating Values at the exit. However, the two-stage fuel feeding scheme results in a lower wall temperature (around 100 K) in the lower half of the gasifier than the single-stage injection scheme. The introduction of the second injection with a pair of opposing jets produces a flattened plane stretching from the hot reaction zone laterally towards the wall, resulting in a peak wall temperature about 0.3 meters downstream of the second injection location.

c. Without pre-drying, the high inherent moisture content in the lignite causes the syngas HHV to decrease by 27% and the mole fractions of both H_2 and CO to decrease by 33%, while the water vapor content increases by 121% (by volume). The low-rank coal, without pre-drying, will take longer to finish the demoisturization and devolatilization processes, resulting in delayed combustion and gasification processes.

d. When the coal slurry with the mass ratio of total water (inherent moisture + surface moisture) to dry coal of 40% - 60%, is injected into the gasifier at the second stage for the pre-dried lignite, the exit syngas temperature decreases by 15% (323 K) compared Case 1. Also compared with Case 1, the syngas HHV in Case 5 also decreases by 39% (77,951 kJ/kmol).

2.

4.9 Topic 6: Experimental Study of Cold Particle Flow in an Entrained Flow Gasifier (Summary Only)

Motivation

Conducting experiments on a full-scale commercial entrained flow gasifiers are expensive and time consuming. In order to help to understand the particle flow behavior in a gasifier, a laboratory scale cold particle flow gasifier system is designed. It is understood that cold particle flow behavior is not exactly the same as the actual reactive particle flows. However, some insights of particle flow characteristics and behaviors, especially particle flow transportation mechanics and injection phenomena, can be obtained from cold particle experiments.

Objective

The objective of this project is to design and install a cold particle flow model gasifier, and then perform experiment to qualitatively analyze the flow behavior of feedstock (simulated with plastic beads) in the gasifier in different injection cases. To achieve the objective of this project, following tasks are performed:

1. Design and manufacture an entrained flow gasifier model
2. Install the gasifier
3. Select plastics beads and flakes to simulate pulverized coal particles
4. Design Feeding System for the Gasifier
5. Install Feeding System for the Gasifier
6. Perform Experiments
7. Analyze Results of the Experiment
8. Derive Conclusions

Approach

In an industrial entrained flow gasifier powdered/pulverized coal is used as fuel or feedstock and oxygen as a gasifying agent. For the purpose of this project, coal particles will be replaced by plastic beads and flakes, and the air will be used instead of oxygen. The name cold flow analysis for this project comes from the fact that heat or chemical reaction (combustion or gasification) will not be used in the experiment. Table 4.27 lists different kinds of plastics beads and residues along with their apparent density that are used as feedstock in the experiment.

Table 4.27 Plastic beads and their properties for simulating coal particles

Material	Black Polypropylene
Apparent Density	578.99 kg/m^3
Physical Appearance	Unsymmetrical, Spherical

Material	Green Acetyl
Apparent Density	840.1 kg/m^3
Physical Appearance	Unsymmetrical, Spherical

Material	Gray Polypropylene
Apparent Density	428.68 kg/m^3
Physical Appearance	Regrind

Material	White Acetyl
Apparent Density	698.43 kg/m^3
Physical Appearance	Regrind

Design of the gasifier

Figure 4.39 shows the main chamber of the gasifier. The air flow is fed in from the injectors subjecting the model to an internal pressure of 1.5 bars (22 psia). The objective is to investigate the particle flow behavior under different flow injection arrangements. Five different interchangeable sections, as shown in Fig. 4.40, are designed for the first

stage (at the bottom of the gasifier) and two interchangeable sections for the second stage. The main section of the gasifer is optical clear for flow visualization. The material and joints are manufactured strong enough to sustain pressure up to 30 psia. The 1" nozzle at the bottom of the gasifier is to be closed in such a way as to facilitate easy removal of dry granular sediment by gravity drain. Fig. 4.41 show some parts for the gasifier. The plastic model was manufactured by SR Innovations Company in South Carolina. The finished plastic parts are shown in Fig. 4.42. The overall flow system for the gasifier is provided in Fig. 4. 43.

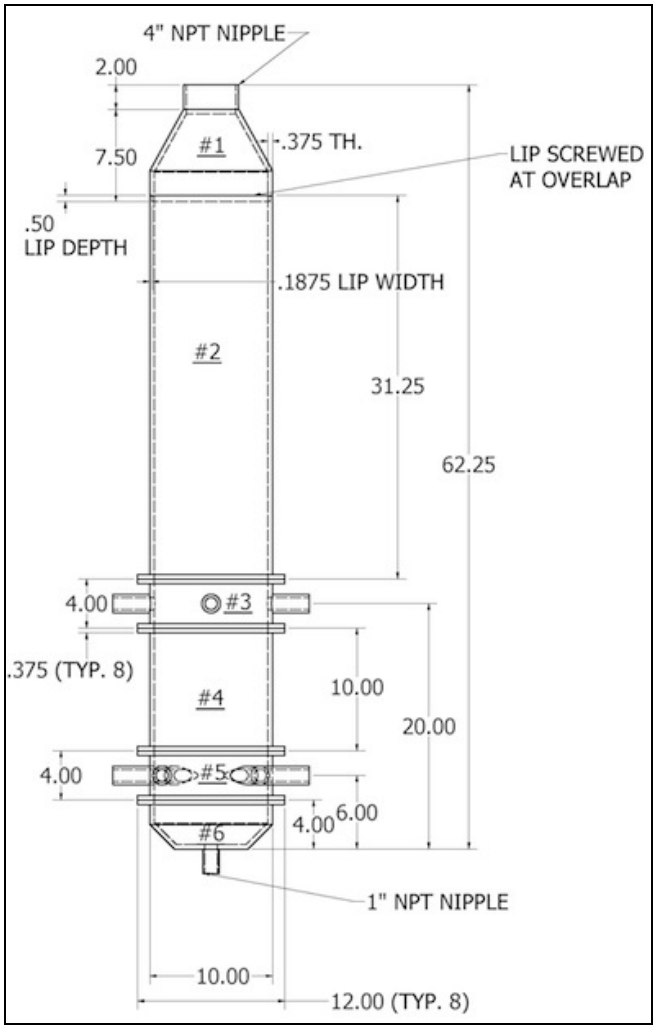

Fig. 4.39 The designed main module of the gasifier

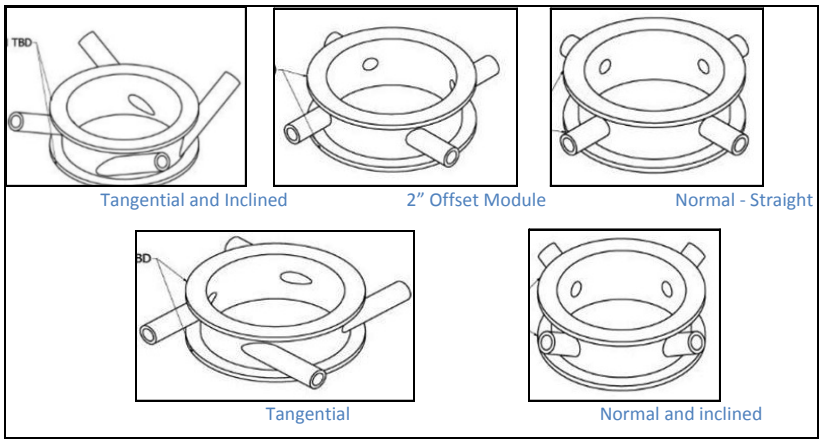

Fig. 4.40 Interchangeable injector sections for the first stage (at the bottom of the gasifier)

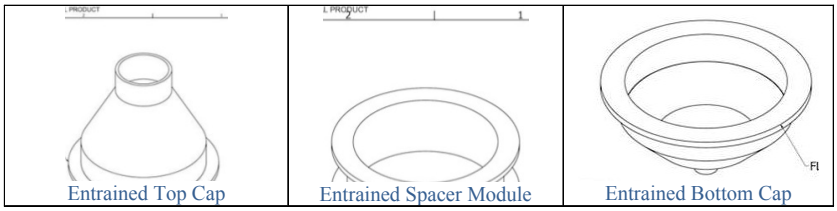

Fig. 4.41 Some parts for the gasifier model

2.3 Manufacturing of Parts

Entrained Bottom Cap

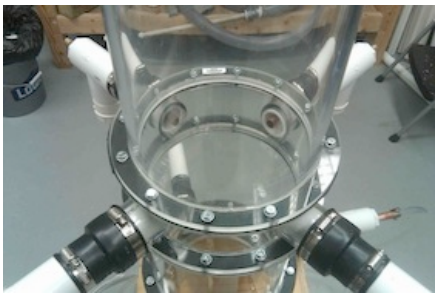

Normal Module

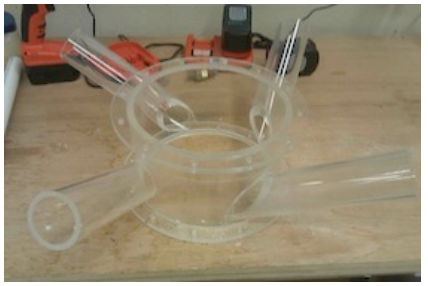

Tangential and Inclined Module

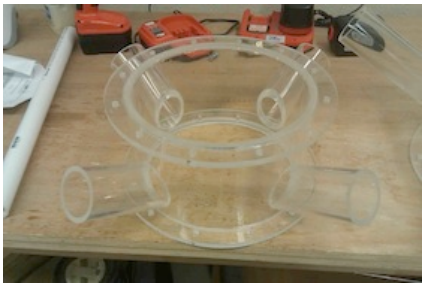

Normal and Inclined Module

Entrained 2" Offset Module

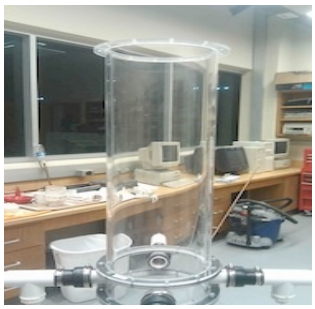

Entrained Gasifier Schematic

Fig. 4.42 Manufactured plastic parts of the gasifier model

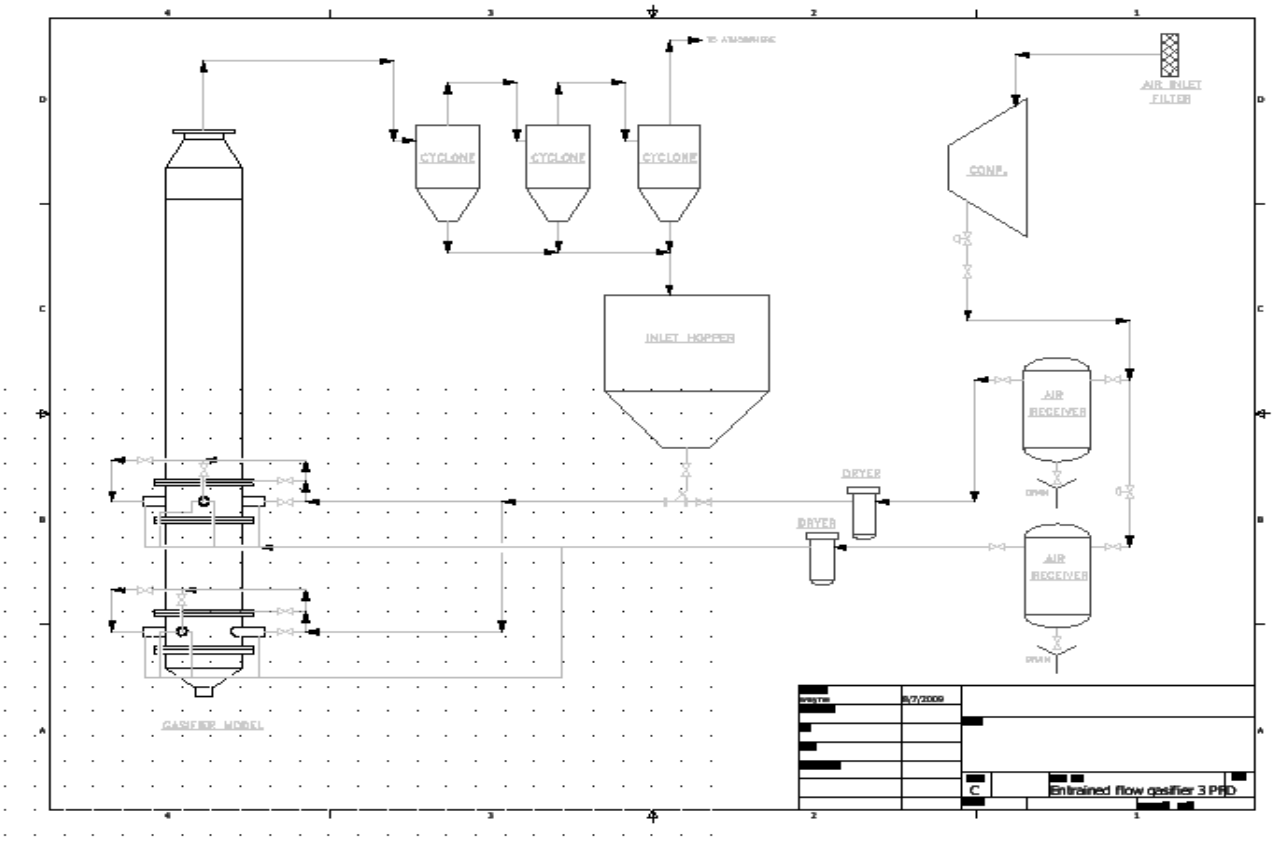

Fig. 4.43 The flow system for the experimental entrained flow gasifier rig

Design of Feeding Systems for the Gasifier

Feedstock transport and fuel injection have been important processes for coal gasification operation. The cold particle flow study is expected to encounter the similar challenges in the laboratory. There are three major feeding practices that need to be handeled. The first one is related to transport the particles along the duct system including the typical elbows and valves the feeding of primary air supply; the second one is the injection of the particle through the injectors into the gasifier; and the third one is related to the adequate supply of oxidant (air or oxygen) to gasifier at an adequate location. Figure 4.45 shows the arrangement of the feedstock feeding system. To provide an adequate locking mechanism under pressurized feeding system, hoppers and pressure distribution manifolds are added as shown in Fig. 4.46. Compressed air is used to pressurize the hoppers and to feed the plastics beads. A 3 hp blow is used to supply the air as the oxidant.

Results and Discussions

Experiments are conducted with different mass flow feeding rates by adjusting the compressed air pressure and the blower's flow rate. The experiments are successful run continuously for about 20 minutes for each batch. However, the return loop of the beads frequently get clogged due to lack of flow pressure. This bead return-loop is for conserving and reusing all the beads; which is not required in a real system. During the

running time of 20 minutes, the flow pattern and particle paths of different injection angles and strategies can be observed and results can be used for validating computational models. The flow visualization could be significantly improved if a high-speed camera were available. This project has successfully established a preliminary cold-flow particle experimental gasifier model that can be continuously improved for future research needs.

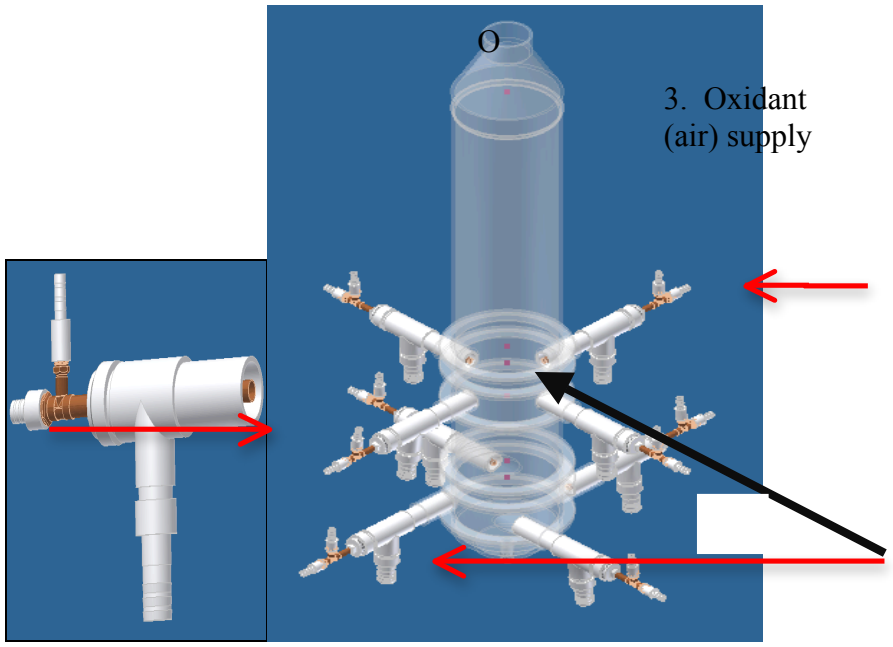

Fig. 4.45 Gasifier Model with feedstock feeding arrangeement

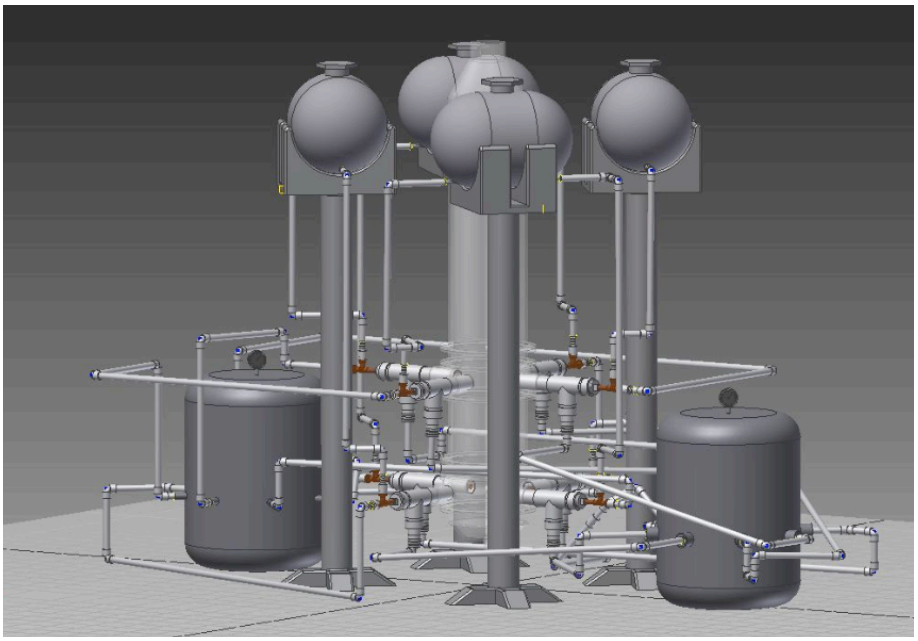

Fig. 4.46 Pressure distribution manifolds and feed stock-feeding hoppers

(B) Investigation of co-gasification of coal and biomass application for IGCC with various design considerations and cause-effect of implementing CCS schemes

4.10 Topics 7, 8, and 9: Techno-Economic Analysis of Biomass/Coal Co-Gasification IGCC Systems with Supercritical Steam Bottom Cycle and Carbon Capture

The primary objective of this study is to improve upon existing IGCC systems by (1) reducing the GHG emissions of such plants, (2) reducing their capital and electricity costs, and (3) increase the efficiency, if possible. A previous study by Long and Wang [2013] was performed with these goals in mind using a baseline IGCC plant and changing the standard Rankine steam cycle to a supercritical steam cycle, where they noticed an improvement in efficiency of more than 1.5 percentage points. In addition, up to 10% biomass could be added for another 0.7 efficiency percentage point increment. This extra efficiency reduced the emissions of the plant by over 600 tons/MW-yr, and the addition of the supercritical cycle also reduced capital costs by about $300/kW. However, in order to achieve the first goal of reducing emissions, the primary, most effective method remains to be utilizing carbon capture and sequestration (CCS) technology. Both post-combustion and pre-combustion CCS systems are studied in this paper. As in the previous study, biomass up to 50% (wt.) will be added to the baseline coal feedstock in order to further reduce the emissions. To achieve the second and third goals of reducing capital costs and raising the efficiency, a supercritical Rankine cycle is implemented to replace the traditional subcritical Rankine cycle as in the baseline. Although supercritical steam systems are more expensive than subcritical ones, the idea is that the extra provided power and efficiency will make up for the increased total cost, reducing the overall capital cost per unit power output.

4.10.1. MOTIVATIONS

Raising the inlet temperature and pressure of the steam turbine in a traditional Rankine cycle is the most direct way to increase the operating efficiency of said cycle. As early as the 1950's, scientists and engineers have been highly focused on this area of potential steam cycle improvement [Retzlaff, 1966]. It was during this period where the maximum inlet pressure and temperature were raised from 2400PSI/1000^{o}F to near 4500PSI/1150^{o}F [Retzlaff, 1966]. This was the onset of the first supercritical steam generation plant. The term "supercritical" comes from the idea that the steam running through the boiler or HRSG is *above* the "critical point" at the top of the vapor dome on a standard temperature-entropy diagram at around 3200PSI [Voss and Gould, 2011]. For reference, the typical efficiency of a standard subcritical Rankine (steam) cycle is around 30-38%, while a supercritical cycle under the same environmental conditions can achieve an efficiency of 42-45% [Hough, 2009]. So far, all of the research and industrial efforts going into supercritical cycle design are meant for standard, pulverized coal (PC) plants.

To the authors' knowledge, there is currently no literature available documenting a supercritical steam bottom system being used in any real-world IGCC system.

The use of biomass in IGCC is not a new idea. The first pure biomass IGCC plant was constructed in Värnamo, Sweden 1993. As a demonstration plant, it provided roughly 6 MW of net electricity to the grid by using a fuel equivalent energy input of approximately 18 MW [Stah, et al., 2004]. Several other biomass plants in the range of 40-100MW have been constructed, such as the Hawaiian biomass gasification experimental plant developed by Siemens-Westinghouse [1999] and the McNeil Station in Burlington, Vermont [Wiltsee, 2000]. In addition, other, more traditional plants have been modified for use with biomass and gasification processes, such as the Chowchilla I in California and the Lahti Co-firing Project in Finland, which both used syngas derived from biomass to run a Rankine cycle [Wiltsee, 2000]. All of these plants, however, have either failed or been removed from the commercial power sector due to not being economically competitive.

Due to the controversies surrounding issues of cultivating energy crops, in this study, only biomass wastes are considered. For convenience, the word "wastes" is dropped from the rest of the paper. The first and greatest challenge with utilizing biomass is associated with its availability, sustainability, and quantity. The supply of most biomass is seasonal and is limited by quantity. In addition, biomass cannot be economically transported over long distances due to its low mass density. A solution to some of these problems is by *co-feeding* biomass alongside coal in a larger plant. This allows biomass to be used whenever it is available and with the same economy of scale that coal has. Doing this also reduces fossil fuel consumption, which is a benefit both for the environment and for energy providers, since most of biomass wastes are either free or bear very low costs. Next, since biomass is cleaner than coal is, co-feeding results in lower emissions than a pure coal plant, and is able to provide much more power than a pure biomass plant. Furthermore, because there is coal mixed in with the biomass, corrosion is less of an issue than it is with plants that use purely biomass.

However, there are still operational problems that biomass can cause to co-fed systems. For one, biomass has very low energy density. Coupled with its low mass density, this means that the required volumetric flow rates for providing the required energy to run the plant are higher than those of coal. [Long and Wang, 2011] Limited biomass supplies and transport issues inhibit profitable operation of larger pure biomass plants, meaning that effectively utilizing pure biomass in any plant bigger than about 50-80MW is uneconomical at best. Secondly, most types of biomass are very fibrous and tough, and tend to get stuck in various types of feeding machinery. Thirdly, biomass tends to contain many corrosive compounds that can damage other internal parts

[Bergman, 2005]. Lastly, biomass has an expiration date: it cannot be stored for any extended length of time due to its tendency to rot and decompose, being rendered almost useless as a fuel in the process.

To overcome this new set of challenges of biomass feeding and long-term storage, one available solution is employing *pretreatment.* Various chemical, thermal, and biological processes are available to transform raw biomass into a form that makes it more suitable for power generation. The type of pretreatment taken into consideration for this study is *torrefaction.* Torrefaction is a thermal process, wherein raw biomass is heated to about 200-300^{o}C and essentially "cooked," removing a large portion of the moisture content, and altering the chemical structure of the biomass in such a way that it loses its tough, fibrous consistency, and "torrefied biomass," a reddish-brown, brittle, solid substance that has calorific properties that greatly approach those of low- to mid-grade coals [Bergman, 2005a]. During torrefaction, the biomass looses roughly 30% of its mass as torrefaction gases, and roughly 10% of its internal energy with them [Bergman, 2005b]. A simple algebraic calculation shows that this would result in a 28% increase in the calorific value per unit mass for the feedstock [Bridgeman, et al., 2007].

In addition, torrefied biomass has a higher mass density than untreated biomass, is less corrosive, has higher grindability, and is much easier to store and transport [Bergman, 2005 and Bridgeman, et al., 2007]. Despite these benefits, using torrefaction at all requires that a separate, torrefaction plant be constructed on-site, which is a significant investment for most plants, especially the smaller ones. In fact, in one 1999 study done on a failed test plant by Siemens-Westinghouse in Maui, Hawaii, the researchers speculated that, while torrefaction itself is very effective at solving virtually all the feeding problems they had been having, investing in one might not be economically viable [Siemens-Westinghouse, 1999]. However, a 2005 study by P.C.A. Bergman of the Netherlands showed that torrefaction when combined with Pelletization (another process that increases the mass density of the biomass) was not only viable in Europe, but perhaps profitable as well, albeit with a high dependency upon the price of the biomass feedstock and other factors [Bergman, 2005].

While some biomass-coal co-feeding studies have been done in the realm of *co-combustion* of biomass with coal [Parameswaran et al., 2009 and Jesionek, et al., 2010] they were mainly based on subcritical PC plant designs. In IGCC plants, the biomass and coal are *co-gasified* instead of co-combusted. For instance, the Polk IGCC plant performed several experiments in which a wood-based eucalyptus biomass feedstock was co-fed into an existing IGCC coal plant, in Tampa, Florida. The results showed that the existing Coal/Petcoke fed IGCC system was feasible to feed biomass, and the emissions of NO_x and SO_x were reduced about 10% [McDaniel, et al., 2002]. The Buggenum IGCC

plant in Netherlands also successfully co-gasified biomass (50% wt.) with coal using 3 major biomass sources: wood, sewer sludge, and manure, using about 300 tons of feedstock per year [Kanaar, 2006]. Biomass has also been used successfully in supplementary firing in a combined cycle plant [Datta, et al., 2008 and Tremel et al., 2012] (that is, using an additional fuel to preheat the gas turbine exhaust before delivering it to the steam cycle), but the challenges for implementing this are very different from co-gasification. In addition, biomass can be used in gasification for the production of substitute natural gas [Tremel, et al., 2012].

This study, like the previous study from Long and Wang [2011], focuses on investigating *co-gasification* of biomass and coal for application in IGCC systems with both subcritical and supercritical bottom Rankine cycle systems, but with the addition of carbon capture plants. Carbon capture is the next logical addition to such a plant given the current political situation: many countries around the world are or are considering implementing a "carbon tax" on industry, meaning there will be government-imposed fines for expelling too much carbon in the form of emissions into the atmosphere. A carbon capture system can drastically reduce such emissions, and potentially help many power companies to save money in the form of avoided tax penalties. In addition, the captured CO_2 may have other uses once captured, such as in advanced oil recovery [Tremel, et al., 2012]. When CCS is combined with biomass, it is possible, assuming biomass is carbon-neutral, for a plant to become *carbon-negative*. This means that, although emissions are produced, there is a net *decrease* in the amount of carbon put into the atmosphere, because plant-based biomass spends a great portion of its lifetime consuming CO_2 through photosynthesis. This is opposed to coal, which contains CO_2 taken from the atmosphere over thousands to millions of years that is released back to atmosphere in a few of hours.

I

In all, the focus of this study is to further investigate the effects of supercritical steam cycles and biomass on IGCC from the previous study, and how these affect systems with carbon capture.

4.10.2 Plant Design

The software used for this study was Thermoflow® program suite's GTPro®. GTPro is a commercial software program that uses a top-down design approach for building gas turbine power plants and combined cycle plants. Figure 1 shows the general layout of the baseline case (No CCS), designed for around 240 MW of net power output. It consists of a single gasifier, based on the GE gasifier, which is slurry-fed and oxygen-blown with quench cooling. The gas cleanup system contains a section for particulate removal (a "scrubber"), a section for COS hydrolysis, a cooling segment, and Acid Gas Removal

(AGR). The power block consists of a single GT, modeled after the Siemens SGT6-4000F turbine, with steam injection in the combustor to reduce NO_x formation, and a single ST, with a fixed steam inlet temperature and pressure.

The plant is designed exclusively for power generation, so no chemicals or energy gases are exported anywhere in the middle of cleanup, and all waste products are assumed to be simply disposed of. The biomass is torrified before entering the gasifier. Seen in Fig. 4.46, the fuel preparation block is where the fuel undergoes all related processes. Around 200kW-hr of energy per ton of biomass is assumed to be required to completely convert the biomass. All condensed water extracted from the raw syngas during cooling is used as makeup water for the steam system (not shown). The deaerator is assumed to be a tray-type, and all process water is returned to it via a series of pipes. The deaerator also provides additional water to auxiliaries wherever more is needed and acts as the de-superheating source for all water streams that require cooler water/steam sources. Lastly, the air separation unit (ASU) is assumed to be a cryogenic system with an operating pressure of 10 atm (147 PSI), and always delivers a stream of 95% pure oxygen at the required pressure to the gasifier.

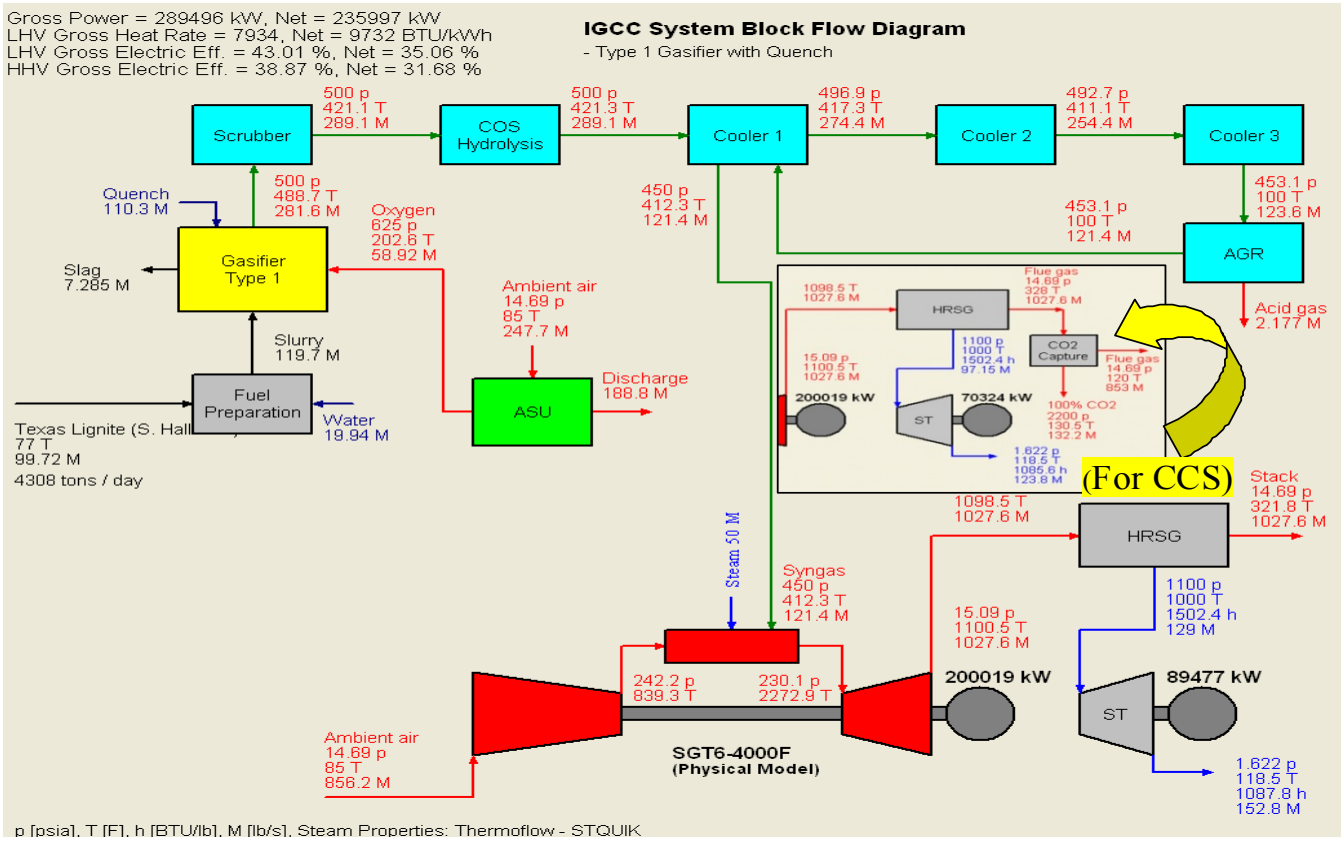

Fig. 4.46. General plant layout without CCS (Subcritical cycle, 0% biomass) with insert showing post-combustion system attachment.

The plant was assumed to be built around New Orleans, Louisiana, at an elevation of 10 feet above sea level. The climate condition was assumed to be an average of 85°F and 90% relative humidity in summer to provide a conservative plant output and thermal efficiency. ISO conditions (59°F and 60% R.H.) were not used as the baseline because those conditions are not common for Louisiana on the whole. It was deemed better to be more conservative with the model prediction by using conditions applicable to a Louisiana late summer/early fall. While both the temperature and humidity given above are highly unlikely to occur at the same time, they are meant to represent more of a weighted average: sometimes it will be 90+ degrees with 70% humidity, and at others, perhaps, 80-90 degrees with 80-95% humidity. As such, the conditions above were chosen to represent an "average" Louisiana summer day.

For coal, Louisiana is situated between two of the largest producers of lignite ore in the entire United States: Texas and Mississippi. In addition, Louisiana shares a very close relationship with both of these states in many areas from business to politics to tourism. For this reason, the coal chosen for the plant was South Hallsville Texas Lignite. In addition to being cheap, lignite is very easy to obtain and is abundant, especially in this region, and lignite from Texas is one of the best energy resources in the Southern United States. As a low-rank coal, lignite's heating value is fairly low due to its high moisture and ash content. However, this is in opposition to its very low cost per unit weight, which means it can be burned more cheaply and in greater quantities than coals of higher rank, especially since higher ranked coals are not as plentiful in the region in which the main plant is assumed to be constructed.

As for biomass, Louisiana is one of the largest producers of sugarcane in the United States, and, out of those producers, Louisiana has the oldest and most historic part played in the sugar production industry [Legendre, et al., 2000 and Day, 2011]. About 16% of all sugar produced in the U.S. comes from Louisiana farms and factories [Legendre, et al., 2000], and around 16 million tons of raw sugarcane is harvested per year [Day, 2011]. Since there is a lot of bagasse left as the waste product of the refinement process, sugarcane bagasse was selected as the feedstock. The fuel data, including ultimate analyses, for both lignite and bagasse can be seen in Table 4.28.

Table 4.28 Fuel Data

Component	S. Hallsville Texas Lignite (wt%)	Torrified Bagasse (wt%)	Raw Sugarcane Bagasse (wt%)
C	41.3	43.59	24.32
H_2	3.053	5.26	2.935

N_2	0.623	0.14	0.078
S	0.7476	0.04	0.0223
O_2	10.09	38.39	21.42
Cl_2	0	0	0
H_2O	37.7	10.39	50
Ash	6.479	2.19	1.222
LHV (Btu/lb)	6398	6714	3282
Price ($/ton)	19.00	65.00	-

From: GTPro® internal fuel library, EIA[2010], & D. Day[2011]

4.10.3 Gasifier & Gas Turbine Block

The gasifier is modeled after the GE/Texaco gasifier. It is slurry-fed (35% water by weight) and oxygen-blown with an ASU pressure of 147 psi (10 bar), and has no coolers at all. The raw syngas is *quenched* with water at 300°F (149°C), up to a relative humidity of 50%. This selection of a quenched gasifier will allow for a more direct comparison when carbon capture is introduced to the design. Figure 4.47 shows the basic gasifier layout, with the numbers shown being representative of the pure coal, subcritical case with no CCS. For both sets of cases (sub and supercritical), the GT used was a Siemens SGT6-4000F with steam injection. For all the cases, the turbine inlet temperature of the GT is fixed and the total mass flow rate through the GT is also fixed.

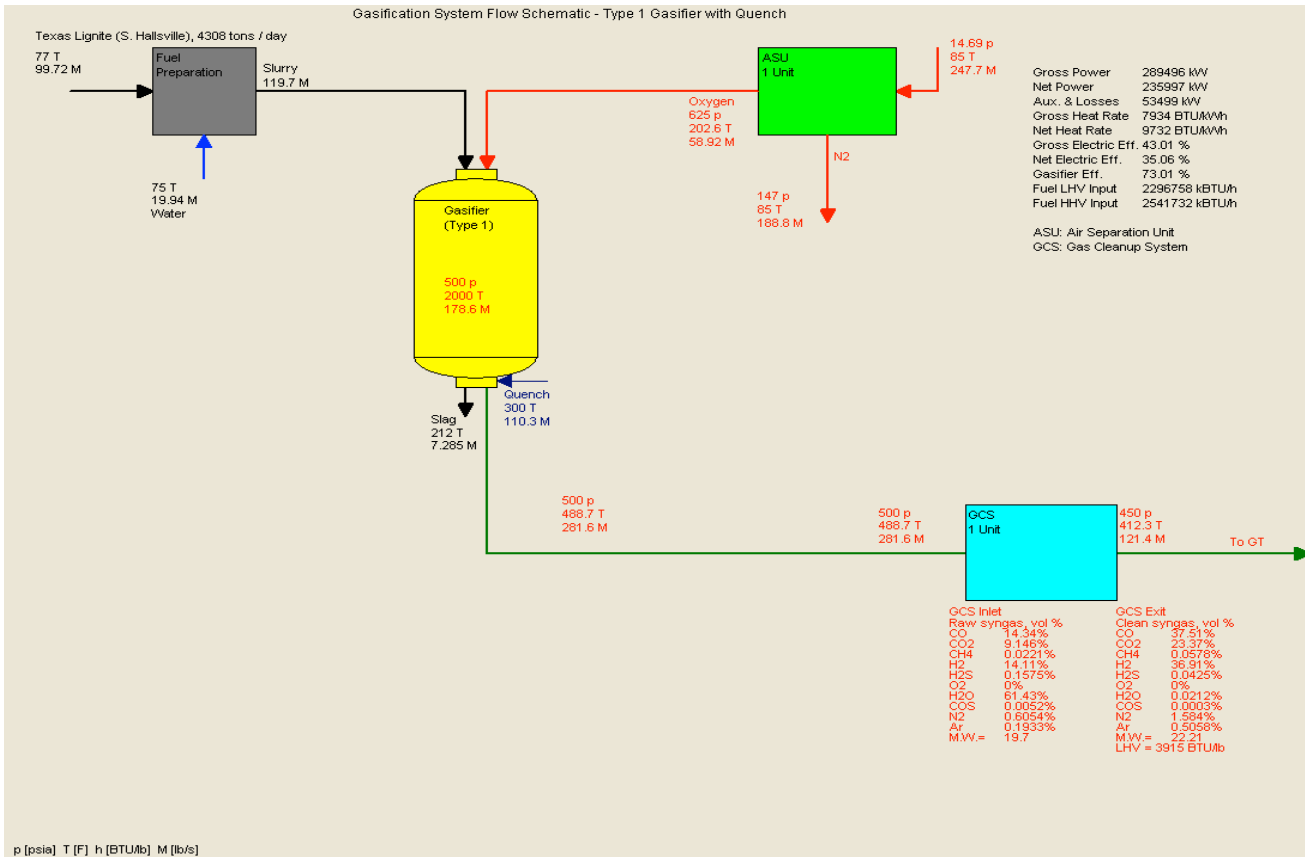

Fig. 4.47 Gasifier design.

4.10.4 Steam Turbine System

For the steam system itself, the HRSG connections and heat exchanger locations are consistent across all cases, both for post-combustion and the baseline, as are the ST layout, the condenser cooling system type, and the deaerator. This is all highlighted in Fig. 4.48. The ST inlet temperature and pressure are fixed at 1100PSI/1000°F (76 bar/538°C) for the subcritical plant, and 2400PSI/1200°F (165.5 bar/650°C) for the supercritical plant. The supercritical plant's turbine inlet pressure is lower than that of a typical PC plant (3500PSI) to avoid material failure and reduce maintenance for the first IGCC system having a supercritical bottom cycle. This is to serve as a stepping stone for moving to higher pressure and temperature supercritical steam conditions in the future. The only difference between the post-combustion CCS plant's steam cycle and that of the baseline is the presence of a ~180lbs/sec mass source at the Intermediate Pressure (IP) boiler exit. Again, this is solely to enforce mass conservation within the HRSG, and to simulate an "external" steam source for the CCS steam, due to software limitations. The HRSG contains two pressure streams: HP and IP, which both provide the steam necessary to provide power via the steam turbine. The HP stream is the main source of steam for the ST inlet, while the IP stream is used to drive plant auxiliaries and processes and also provides additional steam to the ST's reheat stages. All zones within the HRSG are fixed

in all cases, with only temperatures and pressures varying from case to case. In addition, as stated previously, all HRSG connections are consistent for all cases (for instance, the main IP process stream at exchanger IPS1 always provides the water for Acid Gas Removal, the remaining IP stream always connects to the ST reheat section, etc.)

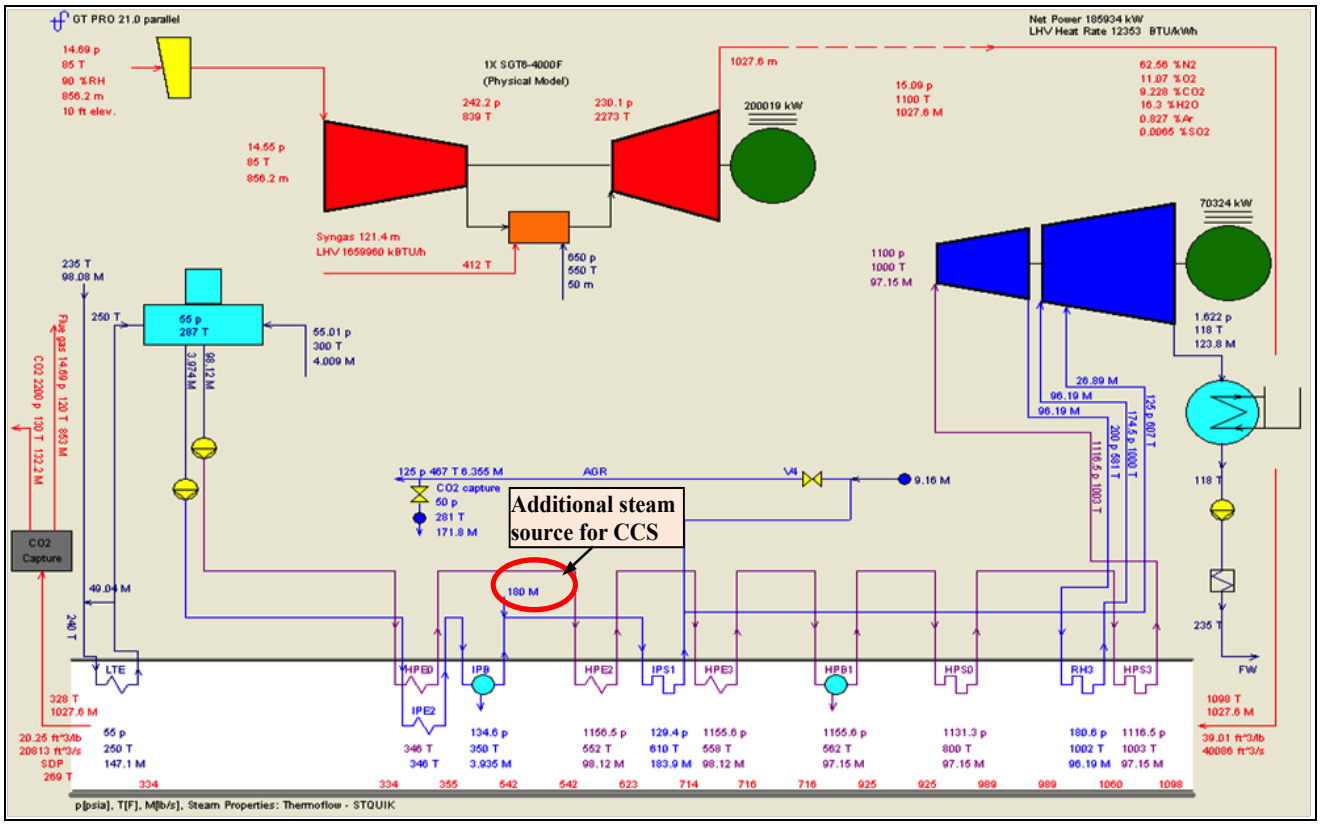

Fig. 4.48 Post-combustion CCS steam cycle, with additional mass source imposed at IPB exit.

The steam turbine itself, as seen in Fig. 4.48, consists of 2 casings, for a total of 3 main stages: one large, high pressure stage and a second, lower pressure stage divided into two separate stages by an IP injection stream containing the leftover steam from the main IP process (acid gas removal for this study). It is a condensing turbine with a reheat section that links the high and intermediate pressure casings together. The temperatures and pressures vary according to which case is being studied. The second casing is split in two, due to the injection of supplementary steam from the IP process stream. The amount injected varies from case to case due to changes in steam demand on other components (CCS and AGR). The conditions were set so that the ST isentropic efficiency could be kept as high as possible in order to maintain the same TIT and TIP. Finally, the steam turbine condenser is connected to a natural draft cooling tower, which makes use of

ambient air in the cooling process. All of the settings on the cooling tower are strictly enforced, and all parameters are fixed in each and every case.

The cleanup system consists of a particulate scrubber supplied with water at 215°F (102°C) for the procedure, a section for Carbonyl-Sulfide (COS) Hydrolysis, a series of coolers and water "drains," and Acid Gas Removal (AGR). The AGR unit is an amine-based system (single-stage), which is based on the Selexol® process and operates at 90% removal efficiency. The NO_x production was based on the emissions specifications from the gas turbine manufacturer: 9ppm for an O_2 reference content of 15% [Kovac, 2008].

4.10.5 Carbon Capture Systems

For all carbon capture processes, the raw CO_2 is handled by simple conservation of mass and species within the program. However, when biomass is involved, the concept of carbon-neutrality must be observed. For this calculation, it was assumed that all biomass feedstock is completely carbon-neutral. This allows for the calculation of the so-called "effective" CO_2 output, which is obtained by taking the total CO_2 and subtracting the biomass's neutral CO_2 from it. Biomass can be assumed to be carbon neutral, again, due to the presence of photosynthesis, which removes carbon from the atmosphere when the biomass was alive. The neutral CO_2 is determined by Eq. 4.79:

$$Neutral\ CO_2(ton/day) = \dot{m}_{feed}\left(\frac{ton}{day}\right) \times BMR \times \%C_{bio} \times \frac{M.W._{CO_2}}{M.W._C} \times 8000\frac{hrs}{year} \times \frac{1\ day}{24\ hrs} \quad (4.79)$$

This equation was derived under the assumptions that (1) all reactions involving carbon eventually result in CO_2 and thus, can be approximated together as a simple combustion equation: $C + O_2 \rightarrow CO_2$, (2) start up and shutdown times are either neglected or assumed to be a part of the plant's recorded 8000 hour operating schedule (the equivalent of a 91.3% capacity factor), making no appreciable difference in the CO_2 emitted as compared to that of normal operating hours, and, finally, (3) the composition of biomass, particularly the carbon content, is constant and uniform, with no variation at any point in time.

4.10.5.1 Post-Combustion CCSs

The plant with post-combustion CCS included is shown in Fig. 4.46 as an insert/addition to the baseline plant. The system makes use of an amine-based solvent to separate the CO_2 from the rest of the GT exhaust. Because of the highly acid nature of the GT exhaust gases due to the presence of SO_x and NO_x, only chemical absorption is applicable in this case. The solvent chosen was Monoethanolamine (MEA), whose price tag was determined to be $1600/ton [Menezes, 2010]. On the whole, adding post-combustion CCS seems to take a drastic toll on the steam cycle's water supply. Among many possible options to provide the steam needed for the amine-based CCS process, the following two options are evaluated:

Option 1 is to tap the steam from the existing HRSG. In this way, the amount of steam delivered to the steam turbine will be reduced and the steam turbine output will suffer. This is a viable option, but will be inconvenient for comparison between non-CCS and CCS-based on similar power output.

Option 2 is to tap the steam from a bigger HRSG by increasing the total steam supply through bigger pumps. The steam that is used to drive the CCS process is thus taken from the IP stream at the same point as that of acid gas removal. This is the lowest pressure point in the system that this water can be taken without directly affecting the steam turbine.

The designed post-combustion system, seen in Fig. 4.49, has quite a demand for steam (171.8 lbs/sec). In an attempt to correct this problem, an additional mass source had to be created to force the steam turbine to operate more closely to that of the baseline case. This mass source was set in place to offset the cost of the CCS system and to make up for the head loss exhibited by the rest of the system, so the injection point in the second stage of the ST could remain close to the baseline case without reversing flow and becoming an extraction point.

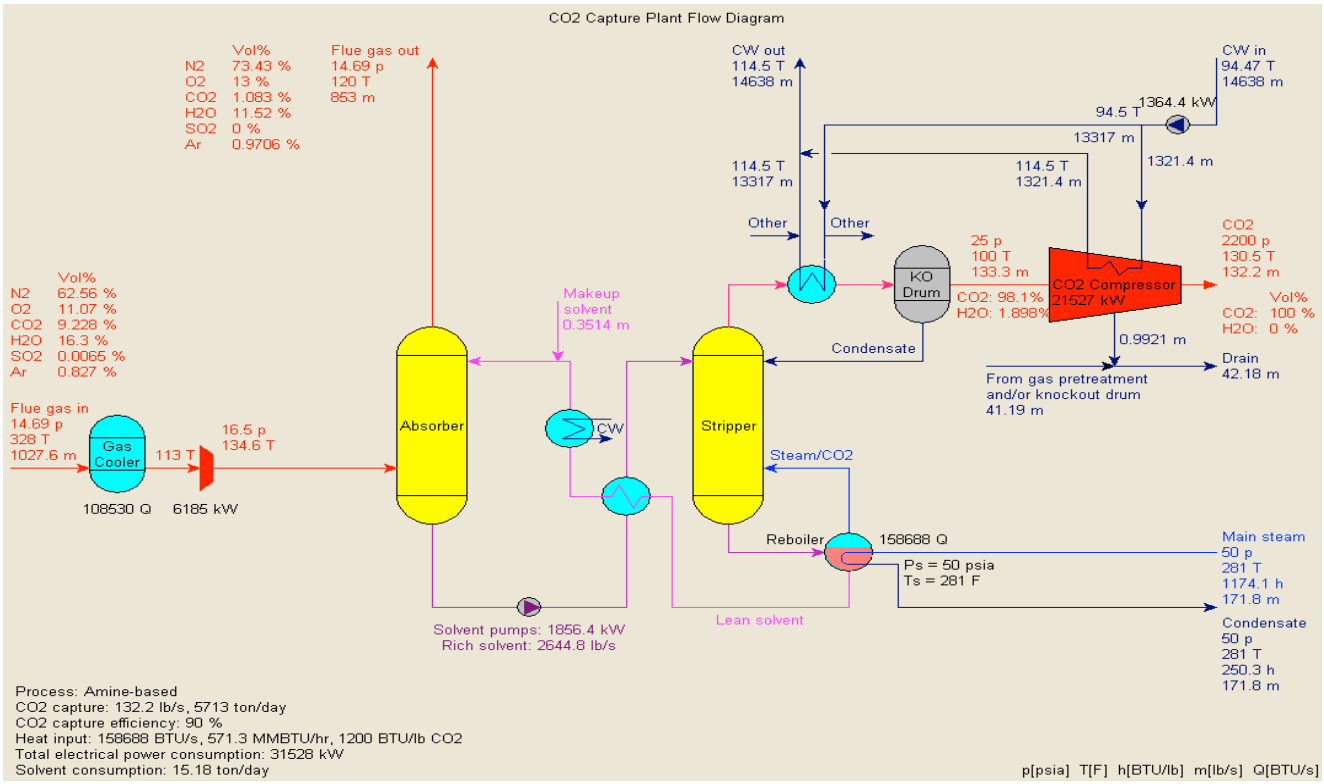

Fig. 4.49 Post-combustion carbon capture system

The carbon capture efficiency is targeted to be 90%. In addition, it should be noted that, due to the nature of chemical absorption, a small portion of the chemical solvent (< 0.01% wt) is lost during the capture process and must be replaced with fresh solvent. This

adds up to a total of about 15 tons/day of solvent, or $24,000 a day in maintenance. Finally, as this system also uses sequestration, a compressor is necessary to push the CO_2 into a proper storage unit. The compressor raises the pressure of the captured CO_2 to 2200 PSI, at a mass flow of about 130-140 lbs/s, with variation attributed to the different system designs and feedstock composition. In total, the CCS system uses around 32MW of electrical power, around 11% of the total expected plant capacity, to maintain operation.

4.10.5.2 Pre-Combustion CCS

For the pre-combustion plants, the content of CO in the syngas is converted to CO_2 and the steam is converted to H_2 via the water-gas shift (WGS) reaction: $CO + H_2O \leftrightarrow CO_2 + H_2$. Subsequently, CO_2 can be separated from H_2 and captured. Depending on whether the WGS reaction takes place before or after the sulfur is removed, the shift process can be further categorized as sour-shift or sweet-shift, respectively. The design of the basic plant layout of pre-combustion CCS is nearly identical to that of the baseline, and the only difference between the main cases outlined here is the location of the CCS plant and CO-shift reactor. The basic plant layout is outlined in Fig. 4.50 with the main figure representing sour-shift CCS and an insert representing sweet-shift CCS. The numbers correspond to the subcritical steam cycle (no biomass in either case).

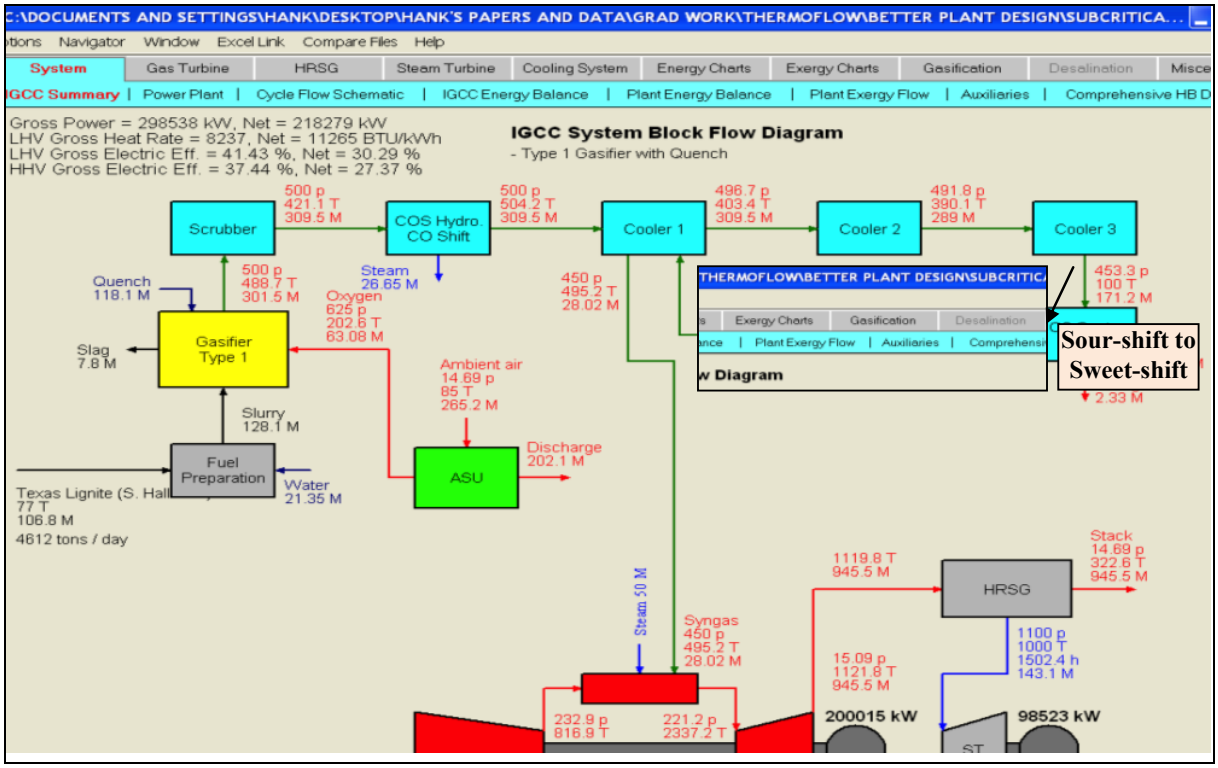

Fig. 4.50 Overall plant layout with sour-shift with no biomass and subcritical steam. An insert shows the sweet-shift arrangement by installing the AGR upstream of the CO-shifter

Since this is pre-combustion CCS, it allows for the use of a physical solvent, as opposed to post-combustion CCS, which demands the use of a chemical solvent. For the Selexol® process, the price for this solvent was assumed to be about $2000/ton.

Figure 4.51(a) shows the layout of sour-shift's gas cleanup system, with Fig. 4.51(b) showing the layout of the complete sour-shift CCS system. The absorbers themselves operate in a cascade-like manner, with the lean solvent first absorbing CO_2 in one absorber, and then sliding down to absorb H_2S in a second absorber. Meanwhile, the syngas enters into the H_2S absorber and flows counter to the solvent, arriving at the CO_2 absorber to undergo carbon capture. This is necessary, because CO_2 and H_2S mix together when under the conditions for AGR, that is, the two compounds will dissolve at the same time. Sequestration implies that the CO_2 will be used for some other purpose, such as advanced oil recovery, which requires an extremely pure stream of CO_2 in order to work properly. Therefore, if H_2S is not removed beforehand, it will require even more work afterward to achieve the right level of CO_2 purity.

The sequestration system makes use of two flash tanks instead of the KO drum from post-combustion CCS. This is because, unlike in post-combustion CCS, the CO_2 absorber isn't directly connected to a stripper column: it will be much easier and less expensive to use flashing to pull the captured CO_2 out of solution, as there are no chemical bonds that need to be broken. In addition, there isn't very much water to separate from the mixture, so there is no need for a KO drum like there is at the end of the H_2S removal stage. The top flash tank strips about 70% of the capturable CO_2 from the solvent, while the lower tank handles the remaining 30% to achieve 90% CO_2 removal (In other words, 10% of the CO_2 is assumed to be uncapturable).

In addition, since this is physical absorption, there is no condensate to be removed before compression (and sequestration), and no additional cooling water needed, since there are no chemical reactions. Since sour shift occurs before AGR, sufficient steam already exists in the syngas stream and there is no additional steam needed to complete the shift: only the catalyst need be added. Hence, no additional steam need be taken from the steam cycle like for post-combustion CCS and sweet-shift CCS.

Figure 4.52 (a), likewise shows the gas cleanup system for the sour-shift cases, while Fig. 4.52(b) shows the layout for the sweet-shift CCS system. Notice from Fig. 4.50, that there is also additional steam (38.95 lbm/s) added to the CO-shift/CCS block for sweet-shift CCS. This is because, since the shifting occurs after the cooling stage, most of the steam that was present has already been condensed out of the syngas. Therefore, additional supplementary steam is necessary to complete the water-gas shift reaction. This is taken from one of the high-pressure (HP) nodes in the HRSG at 1100 psi and 609°F. The HP stream is used in this case because the syngas is already at a very high pressure at this sweet shift point in the cycle. To avoid sacrificing potential GT power or adding unnecessary auxiliary losses by lowering the pressure of the fuel, "HP process" steam must be used for the CO-shift reaction, as shown in Fig. 4.53. Since the CO-shift is

an exothermic process, closed-loop cooling is supplied via water at 250°F (LTE), which is returned to the IP stream (Figs. 4.52 (a) and Fig. 4.53) as it is in the sour-shift plant (indicated in Fig. 4.51(a))

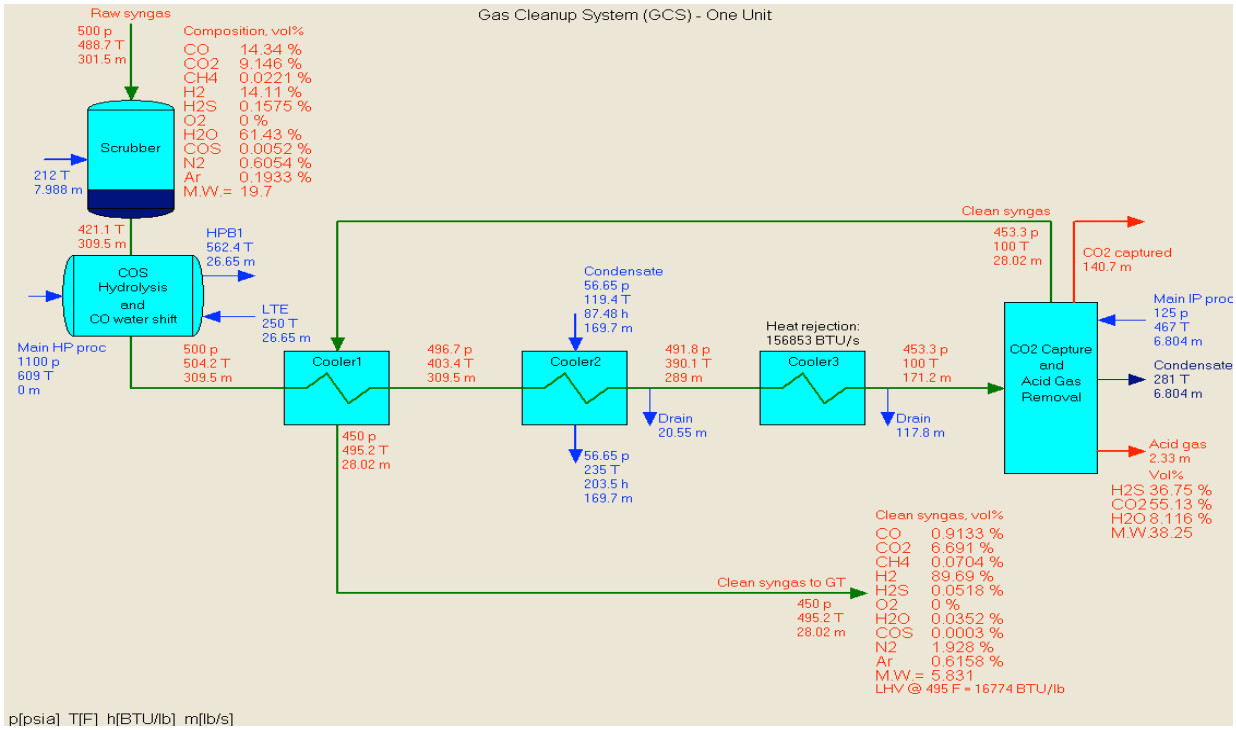

Fig. 4.51(a) Pre-combustion CCS cleanup system with sour-shift.

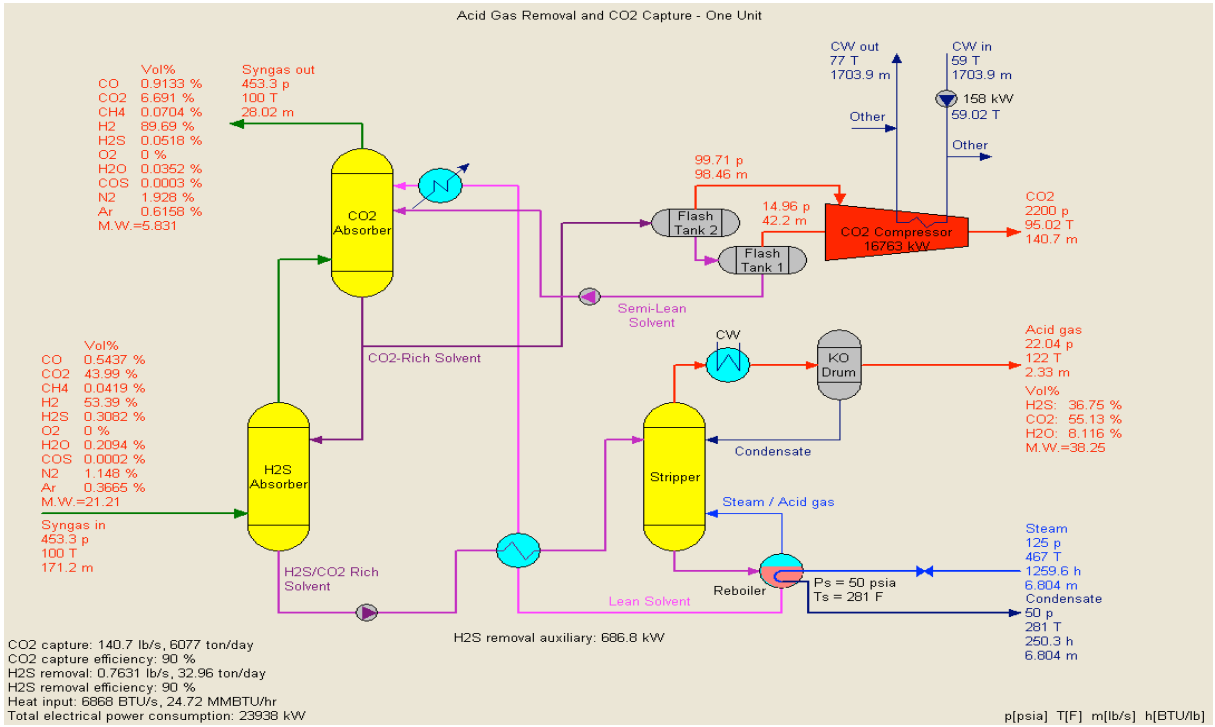

Fig. 4.51(b) Sour-shift CCS system plus AGR plant.

The advantage of sweet shift is that the CO_2 capture plant is more simplistic than sour shift is, so there is less risk of losing some CO_2 during acid gas removal. The CO_2 capture plant for sweet-shift has the same setup and design criteria as those of the CO_2 capture section of the sour-shift plant, with two flash tanks (one stripping 70% of the capturable carbon dioxide and the next handling the remaining 30% to achieve 90% CO_2 capture.), and a CO_2 compressor bringing the pressure to 2200 PSI. The CO_2 compressor, like in the sour-shift case, is used for sequestration purposes. The CO_2 is assumed to be sequestered for a purpose, such as for advanced oil recovery or for permanent storage underground, since this will lead to a more economically viable plant [24], however, since profit margins are not considered in this study, the exact purpose of the CCS is left ambiguous.

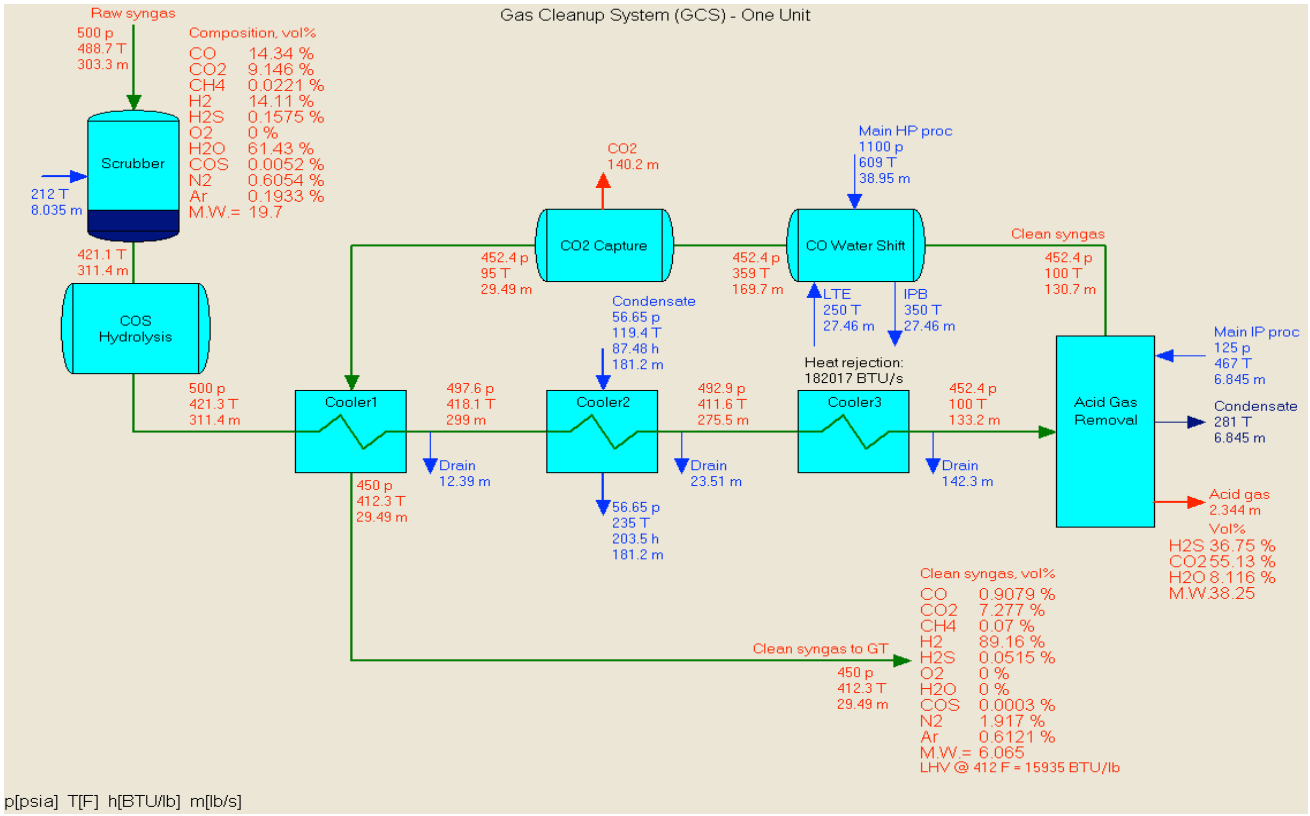

Fig. 4.52 (a) Pre-combustion CCS cleanup system with sweet-shift

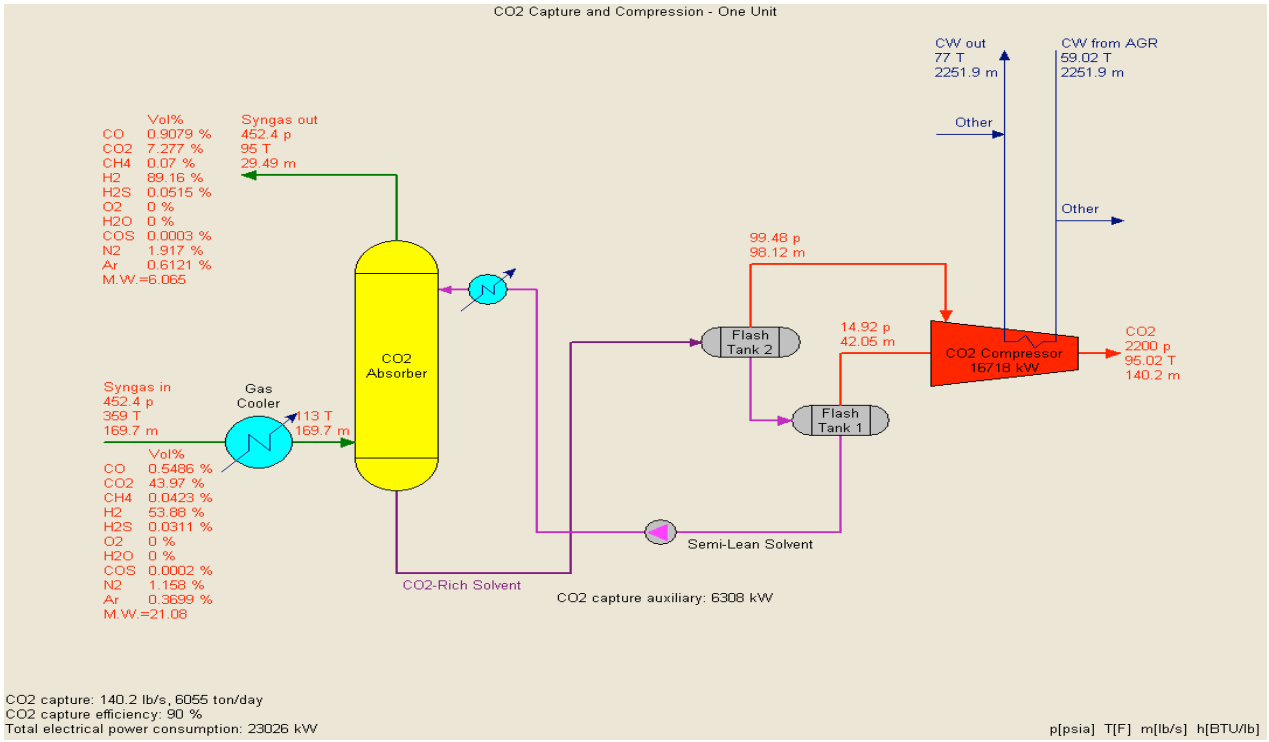

Fig. 4.52 (b) Sweet-shift CCS system

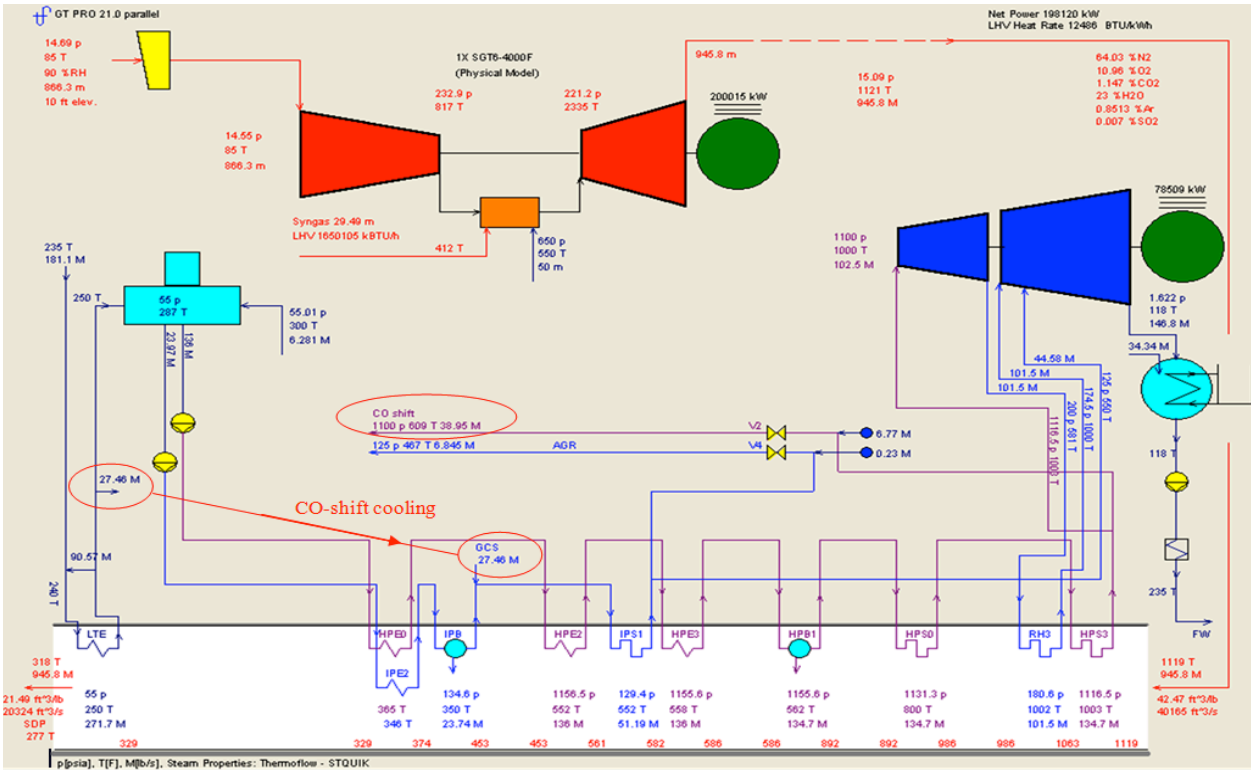

Fig. 4.53 Steam cycle for sweet-shift CCS with CO-shift steam and cooling steam circled

4.10. 6 ECONOMIC ANALYSIS

Beginning with fuel choice, lignite is cheap, and, according to the EIA's report [2010a], lignite from Texas costs approximately $19.00/ton. While sugarcane itself is cheap at only $30.00/ton [USDA, 2010], bagasse is only a portion of the sugarcane. All other by-products like cellulose and hemicelluloses are left behind to be processed into sugar and/or ethanol. On average, about 200 lbs of dry bagasse will be produced from one ton of sugarcane. With this in mind, it becomes easy to make the mistake of assuming that bagasse will be cheaper than sugarcane on a per ton basis. However, this is not the case, as bagasse is often used by farmers in burners to help process the sugarcane. The final price of the bagasse is around $65 per ton of bagasse or $13 per ton of the original weight of sugarcane [Day, 2011].

The price of natural gas for the supercritical plant's duct burner was found to be $4.10 per million Btu ($/mmBtu) based on data from June, 2011, when this study was performed [US DOE, 2011]. In addition, water consumed by the plant was assumed to be based on *utility*, and the price was set at $2.00 per thousand gallons. Finally, overhead and maintenance (O&M) costs were taken from a report by the EIA, where they were determined to be $60.00/kW (fixed) and $0.006/kW-hr (variable) [EIA, 2010b].

With the fuel prices known, the program used demands that the prices be input on a per unit energy basis, so the fuel costs of coal and biomass must be converted over, since all pricing is listed on a per unit weight basis, commercially. This simple conversion for coal is obtained through Eq. 4.80:

$$\frac{\$}{mmBtu(coal)} = \frac{\$}{ton(coal)} \times \frac{1\,ton}{2000\,lbs} \times \frac{1}{LHV_{coal}} \times \frac{10^6 Btu}{1\,mmBtu} \tag{4.80}$$

which comes out to $1.48/mmBtu for coal. Biomass, however, is received wet, so the heating value changes when it undergoes torrefaction and is dried. After the analysis is performed and some terms cancel out, the final conversion for biomass reduces to Eq. 4.81:

$$\frac{\$}{mmBtu(bio)} = \frac{\$}{ton(wet)} \times \frac{1\,ton}{2000\,lbs} \times \frac{1\,lb\,(wet)}{0.7\,lbs\,(dry)} \times \frac{1}{LHV_{dry}} \times \frac{10^6 Btu}{1mmBtu} \tag{4.81}$$

which comes to about $6.92/mmBtu. For all blends of biomass and coal, the two prices obtained from Eqs. 4.80 and 4.81 are linearly combined based on the biomass mass ratio (BMR) in the blended fuel and normalized by the blend's total LHV, which was calculated by the software. This final blend price is given by Eq. 4.82:

$$\frac{\$}{mmBtu(blend)} = \frac{BMR \cdot \frac{\$}{mmBtu(bio)} \cdot LHV_{bio} + (1-BMR) \cdot \frac{\$}{mmBtu(coal)} \cdot LHV_{coal}}{LHV_{blend}}$$

(4.82)

The cost of the blended biomass/coal feedstock is calculated under the assumption that it is linearly proportional to the biomass ratio (BMR). Finally, the energy consumption for coal grinding and drying was estimated to be 40kW-hrs/ton, while biomass, which must undergo torrefaction as well as grinding and drying, was estimated to be 200kW-hrs/ton. The average processing cost for each biomass case was also calculated to be linearly proportional to the BMR.

Finally, as mentioned previously, an overall plant life of 30 years is assumed, with a total operational capacity of 8,000 hours per year. In addition, 30% of the total initial investment is to be taken on *equity,* meaning that the plant owner must pay for these commodities out of his/her own pocket. Taxes on the plant were taken to be around 35%, with 10% flat-interest rates for all plant features. No inflation was considered for this study, so the analysis is based on 2011 USD. Lastly, the total package uses straight-line depreciation, but it was assumed that only 75% of the total investment is available for depreciation for tax purposes.

4,10.7 Results And Discussion

The results are analyzed based first on the effect of biomass within a single system, then upon the effect of the supercritical cycle, and, finally, with respect to the type of CCS used.

4.10.7.1 Power And Efficiency

The results for the power output and plant efficiency can be seen in Tables 4.29 – 4. 32. As seen from these tables, the addition of biomass, even up to 50% by weight in the feedstock has a net positive effect on the efficiency. Beyond 10% BMR, however, the efficiency begins to decrease. This is due to the additional energy costs required to *process* the biomass, as it requires much more energy than raw coal to pre-treat. This added energy consumption is categorized as a part of the "auxiliary losses" in the tables, so the *gross* efficiency is unaffected by this, and, in fact, continues to increase since more gross power is generated. Despite the drop in efficiency, it still remains higher than the efficiency of the coal alone, due to the fact that this type of biomass has a higher heating value, as noted in Table 4.28.

Table 2 Power (kW) and Efficiency (LHV) – Baseline

Biomass/Coal Ratio	0%	10%	30%	50%
Subcritical Plants				
Aux. Losses (kW)	53,499	52,451	55,913	59,277
Net Power	**235,997**	**237,356**	**234,296**	**231,291**
Gross Efficiency	43.01	43.59	43.96	44.31

Net Efficiency	**35.06**	**35.70**	**35.49**	**35.27**
Supercritical Plants				
Aux. Losses (kW)	55,481	54,413	57,873	61,235
Net Power	**267,111**	**268,207**	**265,090**	**262,043**
Gross Efficiency	44.29	44.84	45.18	45.52
Efficiency	**36.67**	**37.28**	**37.08**	**36.89**

Table 3 Power (kW) and Efficiency (LHV) – Post-Combustion CCS

Biomass/Coal Ratio	0%	10%	30%	50%
Subcritical Plants				
Aux. Losses (kW)	84,409	82,668	86,098	89,434
Net Power	**185,934**	**190,260**	**187,369**	**184,610**
Gross Efficiency	40.16	41.06	41.42	41.79
Net Efficiency	**27.62**	**28.62**	**28.38**	**28.15**
Supercritical Plants				
Aux. Losses (kW)	86,731	84,935	88,368	91,702
Net Power	**206,495**	**209,765**	**206,822**	**203,954**
Gross Efficiency	40.93	41.65	41.99	42.33
Net Efficiency	**28.82**	**29.64**	**29.42**	**29.20**

Table 4 Power (kW) and Efficiency (LHV) – Sour-shift

Biomass/Coal Ratio	0%	10%	30%	50%
Subcritical Plants				
Aux. Losses (kW)	80,258	78,444	82,101	85,670
Net Power (kW)	**218,279**	**220,712**	**217,639**	**214,643**
Gross Elect. Eff.	41.43	42.05	42.41	42.76
Net Elect. Eff.	**30.29**	**31.03**	**30.79**	**30.56**
Supercritical Plants				
Aux. Losses (kW)	81,026	79,293	82,977	86,573
Net Power (kW)	**238,077**	**241,559**	**239,387**	**237,309**
Gross Elect. Eff.	42.03	42.72	43.12	43.52
Net Elect. Eff.	**31.36**	**32.16**	**32.02**	**31.89**

Table 5 Power (kW) and Efficiency (LHV) – Sweet-shift

Biomass/Coal Ratio	0%	10%	30%	50%
Subcritical Plants				
Aux. Losses (kW)	80,404	78,586	82,310	85,934
Net Power (kW)	**198,120**	**200,290**	**196,906**	**193,598**
Gross Elect. Eff.	38.42	38.98	39.27	39.56
Net Elect. Eff.	**27.33**	**27.99**	**27.70**	**27.40**
Supercritical Plants				
Aux. Losses (kW)	82,313	80,494	84,221	87,847
Net Power (kW)	**225,406**	**227,536**	**224,130**	**220,819**

Gross Elect. Eff.	39.75	40.29	40.57	40.85
Net Elect. Eff.	**29.12**	**29.76**	**29.49**	**29.22**

The supercritical system has a clearly beneficial effect on the IGCC plant, with a consistent improvement in efficiency of over 1.6 percentage points when compared with the baseline. The efficiency for each amount of biomass also appears to follow the exact same trend as before, with an increase from 0-10% BMR and decreases from 10-50%. The total net power also increases by about 25MW (9.8%) overall compared to the subcritical system. From this, it is clear that using a supercritical cycle provides an overall efficiency benefit for an IGCC plant as a whole.

The sour-shift system, on the other hand, behaves slightly differently for the supercritical cycle than it does for the subcritical cycle. The most obvious change here is that the supercritical cycle *loses* steam power from this case. Where *in the subcritical system, sour-shift increases the total steam power (not shown) by about 10MW compared to the baseline; in the supercritical case, it decreases the power by at least 3 MW*. This change is most likely caused by the fact that the gasification system did not change with the steam cycle, so the quality of water given to the steam cycle (through CO-shift cooling) remains the same, while the grade of steam taken from the IP stream (for AGR) is much higher for the supercritical cycle. This means that the additional water supplied here is not enough to make up for the direct loss of power from sacrificing such high grade steam, whereas, for the subcritical cycle, it was a much better trade. This is also why the efficiency doesn't increase as much between the subcritical and supercritical cycles for the sour-shift cases as it does for the baseline cases: only about 1.0-1.3 percentage points of improvement for sour-shift compared to the previous 1.6 percentage points without CCS.

However, *the supercritical cycle benefits sweet-shift CCS more than any other case set: about 1.8-1.9 percentage points of improvement from the subcritical cycle, making the efficiency higher than that of post-combustion CCS.* Similar to sour-shift, the power output of the sweet shift case is also lost when compared with the baseline: although, still a great deal more than the loss from the sour-shift cases (20MW vs. 40MW). Interestingly enough, the auxiliary losses are not that much higher than those of the sour-shift cases, so the total net power is only about 10MW lower on average than that of sour-shift CCS.

The percentages of auxiliaries and various losses for the pure coal, supercritical baseline plant are shown in Fig. 4.54. It can be seen that the largest amount of parasitic power is consumed by the ASU (68.21%) and the second largest is from coal preparation (12.94%).

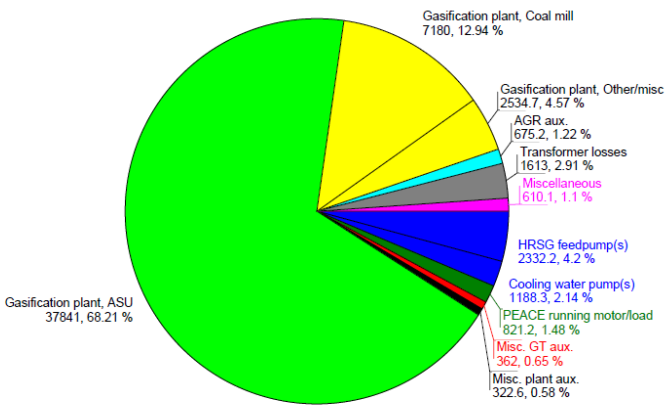

Fig. 4.54 Auxiliaries & losses for supercritical pure-coal plant without CCS

Finally, Post-combustion CCS has a clearly negative impact on overall plant performance. This is not surprising, since CCS costs a significant amount of energy to perform, and offers nothing in the way of power or heat recovery to offset this, and post-combustion CCS seems to reduce the total net efficiency by nearly 8 percentage points in all subcritical cases. Even worse is the fact that the supercritical plant suffers *even greater losses in power* than the subcritical plant. While the subcritical plant lost about 17-19 MW of steam power from the CCS plant, the supercritical plant loses over 30 MW, nearly twice as much. The total net power and efficiency for the post-combustion plants compared to the baseline can be seen in Fig. 4.55 (a) and (b).

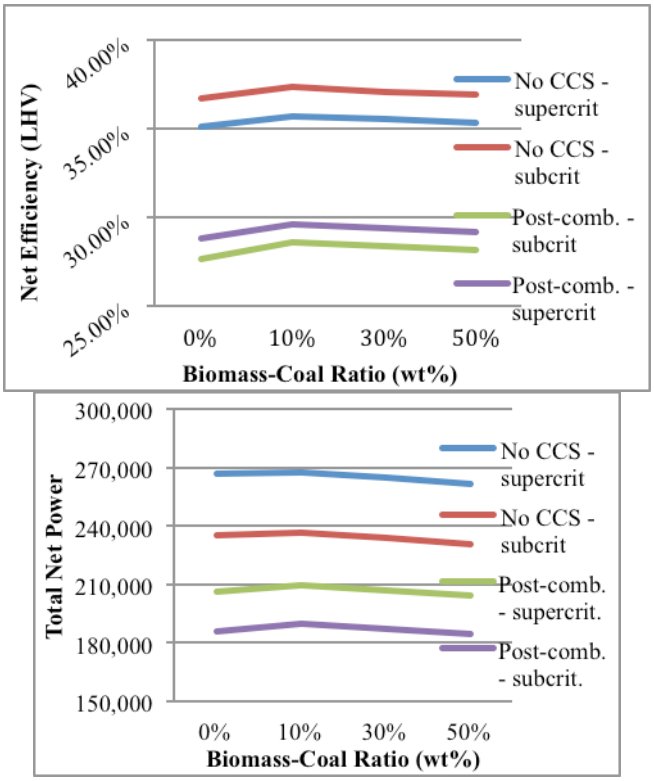

(a) (b)

Fig. 4.55 (a) Net plant efficiency and (b) total net power for baseline and post-combustion plants

The main problem is that *post-combustion CCS requires the use of chemical absorption, and the detriment to the total steam available to provide power is significantly increased, resulting in over 19MW of power directly lost due to reduced steam mass flow.* In addition, the total auxiliary cost increases by about 60% due to the electrical energy consumed in order to maintain the pressure differences in the absorber and stripper columns and to compress the captured CO_2 at the end of the process. The GT power and other specifications not shown are unaffected by this, as all of the changes to the plant do not involve anything to do with the top cycle or the gasification block. However, all of the sour-shift plants are only about 5 percentage points lower than their equivalent baseline cases. An interesting thing to note as well is the fact that *the total steam turbine power (not shown) actually increases for sour-shift when compared to the baseline: about 9-10MW of extra power generated on average.* This may be due to the fact that the CO-shift process makes use of a catalyst to convert extra water into hydrogen for burning. Since CO_2 is removed before it reaches the gas turbine, the loss of mass flow must be made up by pushing additional syngas through the gasifier (thus increasing the gasifier size so it can accept more feedstock.) This translates to extra *energy* to be given to the steam cycle, which, since the ST inlet temperature is constant, demands a higher steam mass flow to keep the same stack temperature. In addition, the sour CO-shift reaction itself requires no additional steam from the HRSG at all to go to completion: all necessary water is already present in the syngas. This water comes from the quench, the slurry water, and the already high moisture content of the coal used. However, this combination of circumstances makes it so that both the TIT constraint and the mass flow constraint on the GT cannot be met at the same time. As such, the TIT condition is held, while the total mass flow rate entering the turbine (air and fuel) is allowed to decrease, resulting in a higher TET.

Finally, sweet-shift appears to be the worst form of CCS in terms of efficiency. While the net power is still above that of post-combustion CCS, the net efficiency is at least one percentage point lower on average than the post-combustion cases. In fact, it consistently decreases the total power output by about 11MW in all instances compared to the baseline. This is due to the fact that, unlike sour-shift, *sweet shift requires additional steam input from the steam cycle directly, resulting in a reduction of steam turbine output of approximately 11MW*. Since it occurs after every other process in the gas cleanup system, the amount of water needed is largely independent of BMR. But, in the long run, this is still enough to cut the efficiency by about 8 percentage points: even more than in post-combustion CCS. See Figs. 4.56 (a) and (b).

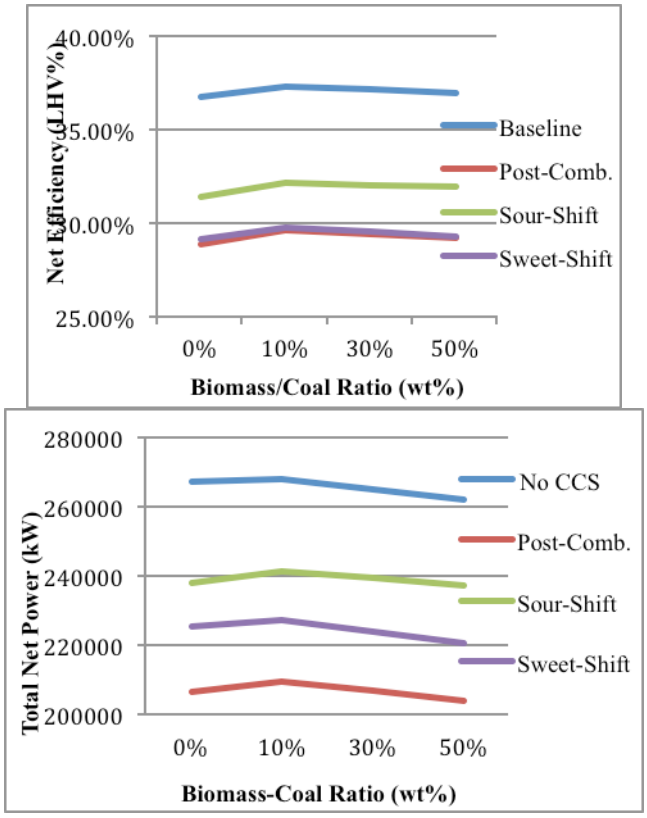

Fig. 4.56 (a) Efficiency and (b) total net power for supercritical plants

4.10.7.2 Syngas Compositions

Tables 4.33 and 4.34 show the syngas compositions for both the subcritical and supercritical plants. The results correspond to the *raw* syngas leaving the gasifier, and, as such, relate to both the baseline case and all CCS cases. This is mainly to demonstrate that the gasification block is virtually untouched by the effect of the supercritical cycle, aside from some scaling to maintain equilibrium. In addition, notice that the addition of further biomass continually increases the amount of CO, H_2, and CH_4, while simultaneously decreasing the amount of CO_2 and H_2O, thus, raising the heating value. The exact data in the tables correspond to those cases without CCS (the baseline).

Table 4.33 Syngas Compositions (vol%) – Subcritical Plants

Biomass/Coal Ratio (wt%)	0%	10%	30%	50%
CO (vol%)	14.34	14.98	15.47	15.97
CO_2	9.146	8.776	8.726	8.670
CH_4	0.0221	0.0274	0.0299	0.0327

H_2	14.11	14.76	14.91	15.06
H_2S	0.1575	0.1434	0.1142	0.0846
H_2O	61.43	60.56	60.03	59.51
COS	0.0052	0.0047	0.0038	0.0029
N_2	0.6054	0.5726	0.5374	0.5016

Table 4.34 Syngas Compositions (vol%) – Supercritical plants

Biomass/Coal Ratio (wt%)	0%	10%	30%	50%
CO (vol%)	14.32	14.98	15.47	15.97
CO_2	9.147	8.776	8.726	8.670
CH_4	0.0221	0.0274	0.0299	0.0327
H_2	14.11	14.76	14.91	15.06
H_2S	0.1575	0.1435	0.1142	0.0846
H_2O	61.42	60.55	60.03	59.51
COS	0.0052	0.0047	0.0038	0.0029
N_2	0.6054	0.5727	0.5374	0.5016

4.10.7.3 Emissions

Table 4.35 shows the emissions data for the baseline cases. Notice that the overall emissions for each type of pollutant universally decrease with the amount of biomass added. However, on a per unit output energy basis (ton/MW-year), the CO_2 emissions actually *increase* for increasing BMR in the supercritical IGCC cases, albeit by a very small amount. The only exception is from 0% to 10% BMR, where there is a sharp decrease just for adding biomass to the feedstock. While the CO_2 emissions beyond this point do increase, note the fact that the emissions for the biomass blends are still *always lower* than they are for pure coal. The *effective CO_2* on the other hand always decreases with increasing BMR. Again, the effective CO_2 is determined by calculating the neutral CO_2 from biomass and subtracting it from the gross CO_2.

The emissions for the post-combustion plants are shown in Table 4.36. In addition to NO_x emissions being virtually eliminated and SO_x emissions being cut by more than 98%, the CO_2 emissions clearly drop by a significant amount. The reduction in SO_x and NO_x occurs because of (1) the fact that post-combustion CCS uses chemical absorption, which allows for the direct removal of SO_x and NO_x and (2) the fact that this form of capture is performed *after* SO_x and NO_x have already formed in addition to performing necessary cleaning beforehand (including Acid Gas Removal). Even the baseline cases make use of AGR, but only the post-combustion cases perform sulfur removal a second time, after combustion occurs. In addition, notice that after just 10% biomass is added, the plant has become carbon-negative. This is true even for the supercritical cycle,

because post-combustion CCS is the only implementation of CCS that can clean the emissions released by the supercritical plants' duct burners.

Table 4.35 Emissions (Tons/MW-year) – Baseline without CCS

Biomass/Coal Ratio	0%	10%	30%	50%
Subcritical Plants				
NO_x	0.994	0.980	0.991	1.002
SO_x	9.14	6.84	6.22	4.57
Gross CO_2	8,942	8,620	8,719	8,819
Eff. CO_2	**8,942**	**7,688**	**5,928**	**4,173**
Supercritical Plants				
NO_x	0.879	0.867	0.876	0.885
SO_x	8.08	6.97	4.37	4.03
Gross CO_2	8,313	7,983	8,064	8,146
Eff. CO_2	**8,313**	**7,159**	**5,598**	**4,045**

Table 4.36 Emissions (Tons/MW-year) – Post-Combustion CCS

Biomass/Coal Ratio	0%	10%	30%	50%
Subcritical Plants				
NO_x	2.69×10^{-8}	2.63×10^{-8}	2.67×10^{-8}	2.71×10^{-8}
SO_x	0.058	0.049	0.039	0.029
Gross CO_2	1,108.1	1,049.0	1,063.5	1,077.7
Eff. CO_2	**1,108.1**	**-113.1**	**-2,426.2**	**-4,756.2**
Supercritical Plants				
NO_x	2.42×10^{-8}	2.38×10^{-8}	2.42×10^{-8}	2.45×10^{-8}
SO_x	0.052	0.045	0.035	0.026
Gross CO_2	1,034.4	987.0	999.5	1,012.0
Eff. CO_2	**1,034.4**	**-67.0**	**-2,162.0**	**-4,356.8**

Tables 4.37 and 4.38 show the emissions data for sour- and sweet-shift CCS, respectively. Notice that in Table 4.37, like in post-combustion CCS, just 10% biomass by weight is enough to make the sour-shift plant carbon-negative. On a per MW-year basis, only the pure coal cases have marginally lower effective CO_2 emissions than the pure-coal post-combustion cases; *all biomass cases are more carbon-negative for the post-combustion cases or, in other words, the post-combustion biomass cases produce about 10% lower CO_2 emissions than those with pre-combustion CCS.* This is due to the increased gasifier size, as, again, the mass flow to the GT cannot be maintained at the same power output without adding additional syngas mass flow. This can only be accomplished by a larger gasifier. Therefore, more CO_2 is being added due to simply having more carbon available from the beginning.

Table 4.37 Emissions (Tons/MW-year) – Sour-shift CCS

Biomass/Coal Ratio	0%	10%	30%	50%
Subcritical Plants				
NO_x	0.842	0.831	0.843	0.855
SO_x	10.58	9.06	7.17	5.28
Gross CO_2	1,070.8	1,040.0	1,072.5	1,105.1
Eff. CO_2	**1,070.8**	**-32.0**	**-2,143.4**	**-4,256.3**
Supercritical Plants				
NO_x	0.763	0.752	0.759	0.766
SO_x	9.59	8.20	6.46	4.73
Gross CO_2	1,312.4	1,280.2	1,311.3	1,342.3
Eff. CO_2	**1,312.4**	**311.1**	**-1,584.3**	**-3,464.3**

Table 4.38 Emissions (Tons/MW-year) – Sweet-shift CCS

Biomass/Coal Ratio	0%	10%	30%	50%
Subcritical Plants				
NO_x	0.937	0.925	0.940	0.955
SO_x	11.73	10.05	7.97	5.88
Gross CO_2	1,284.2	1,236.5	1,258.9	1,281.7
Eff. CO_2	**1,284.2**	**48.6**	**-2,316.7**	**-4,698.3**
Supercritical Plants				
NO_x	0.823	0.814	0.825	0.837
SO_x	10.31	8.84	7.00	5.16
Gross CO_2	1,508.3	1,463.7	1,486.8	1,510.2
Eff. CO_2	**1,508.3**	**418.0**	**-1,654.4**	**-3,732.6**

Even with all this taken into account, post-combustion CCS retains one advantage over sour-shift pre-combustion CCS: handling SO_x and NO_x. Only post-combustion's chemical absorption can process SO_x and NO_x, and only because post-combustion CCS occurs after those compounds are able to form. *The gross CO_2 emissions of the sour-shift CCS cases are about 15% less than the sweet-shift cases in both subcritical and supercritical plants.* When effective CO_2 emissions are examined, for the supercritical plant, the 10% BMR case isn't carbon-negative for either form of pre-combustion CCS. This is directly caused by the presence of the duct-burner, which adds 80,000-100,000 tons of CO_2 per year (or 336-420 tons/MW-year) to the emissions. This is also why the effective CO_2 emissions of other biomass cases in the supercritical cases are less negative than the corresponding subcritical cases. Only post-combustion CCS is capable of cleaning up the CO_2 emissions from the duct burner, which is why post-combustion's 10% biomass case is the only such case for the supercritical cycle that is carbon-negative (all other forms of CCS are still carbon-positive at 10% biomass when used with the supercritical steam cycle). The total effective CO_2 emissions for each type of CCS can be seen in Fig. 4.57. Note that this figure only highlights the data for sub-critical plants.

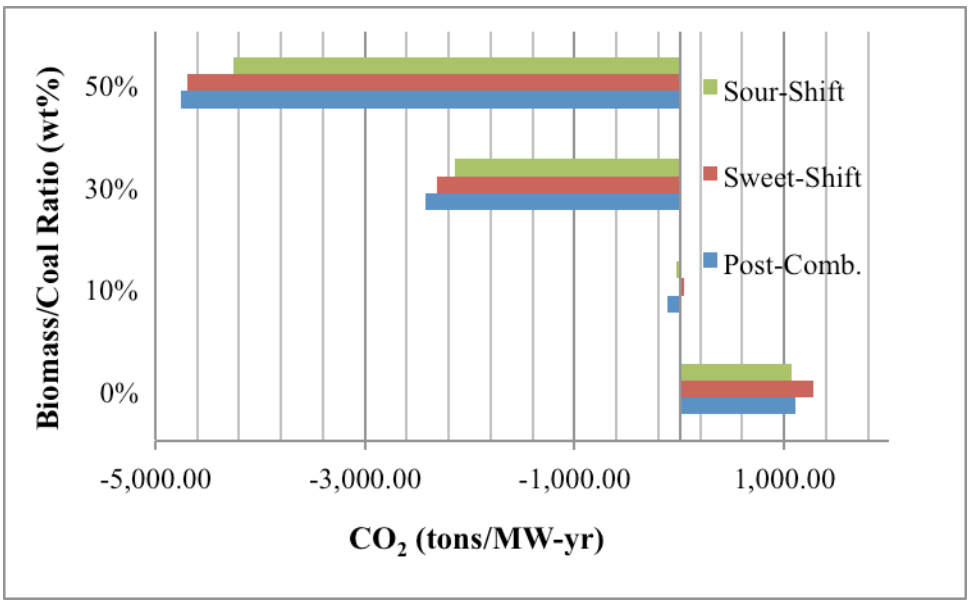

Fig. 4.57 Effective CO_2 for subcritical plants with CCS

4.10.7.4 Economics

Lastly, for the economic impact of these plants, see Tables 12, 13, 14, and 15. Note that the additional $10,000,000 for a torrefaction plant is ~1% of the total capital cost, meaning that it is insignificant compared to the total plant cost. Not to mention, co-gasifying biomass with coal actually *reduces* the total investment by a significant amount. The cost analysis program report (not shown) showed that the biggest saving is in the piping system and the gasifier itself. Not entirely clear at first, but taking into account that the GT inlet temperature and mass flow rate are fixed, this leads to the discovery that using biomass in the gasifier means that *a smaller gasifier can be used* and the plant will still get the same net GT power output. This is possible because of the reduced necessary syngas flow rate to the GT, since the syngas of the biomass blends have higher heating values than that of coal alone. This difference alone accounts for nearly 80% of the price reduction seen in the tables. This results in reductions of the capital cost for both subcritical and supercritical IGCC plants.

The cost of electricity (CoE) actually decreases from 0% to 10% BMR due to the reduced size of the cleanup and gasification islands for both sets of cases. However, it rises again beyond 30% due to the added extra cost of the biomass. As such, *for all cases, 10% BMR is the most optimal ratio, as it boasts the lowest overall CoE (0.4-0.6 cents lower than pure coal and 1.2-1.5 cents lower than 30% BMR).* CoE is calculated based on levelized capital cost, O&M costs, interest, and the costs of water and fuel.

Table 12 Economics – Baseline

Biomass/Coal Ratio	0%	10%	30%	50%
Subcritical Plants				
Capital cost ($Mil)	1,029.8	926.74	911.62	897.44
Capital Cost ($/kW)	**4,363**	**3,904**	**3,891**	**3,880**
CoE ($/kW-hr)	**0.1008**	**0.0979**	**0.1084**	**0.1190**
Supercritical Plants				
Capital cost ($Mil)	1,087.6	983.83	970.95	956.03
Capital Cost ($/kW)	**4,072**	**3,668**	**3,663**	**3,648**
CoE ($/kW-hr)	**0.0972**	**0.0947**	**0.1041**	**0.1133**

Table 13 Economics – Post-Combustion CCS

Biomass/Coal Ratio	0%	10%	30%	50%
Subcritical Plants				
Capital cost ($Mil)	1,490.2	1,374.8	1,359.7	1,345.4
Capital Cost ($/kW)	**8,015**	**7,226**	**7,257**	**7,288**
CoE ($/kW-hr)	**0.1713**	**0.1631**	**0.1763**	**0.1895**
CCS cost ($/kW-hr)	0.0705	0.0652	0.0679	0.0705
CO_2 Removal Cost ($/ton)	**71.99**	**66.86**	**65.02**	**66.12**
Supercritical Plants				
Capital cost ($Mil)	1,539.8	1,422.5	1,407.4	1,392.5
Capital Cost ($/kW)	**7,457**	**6,781**	**6,805**	**6,828**
CoE ($/kW-hr)	**0.1626**	**0.1559**	**0.1678**	**0.1797**
CCS Cost ($/kW-hr)	0.0654	0.0612	0.0637	0.0664
CO_2 Removal cost ($/ton)	**71.88**	**67.75**	**65.67**	**63.22**

Table 14 Economics – Sour-shift CCS

Biomass/Coal Ratio	0%	10%	30%	50%
Subcritical Plants				
Capital cost (million $)	1,164.3	1,043.1	1,027.4	1,011.5
Capital Cost ($/kW)	**5,334**	**4,726**	**4,721**	**4,712**
CoE ($/kW-hr)	**0.1192**	**0.1146**	**0.1269**	**0.1392**
CCS cost ($/kW-hr)	0.0184	0.0167	0.0185	0.0202
CO_2 Removal Cost ($/ton)	**18.70**	**17.31**	**18.34**	**19.17**
Supercritical Plants				
Capital cost (million $)	1,206.2	1,086.8	1,072.3	1,060.0
Capital Cost ($/kW)	**5,066**	**4,499**	**4,479**	**4,467**
CoE ($/kW-hr)	**0.1159**	**0.1114**	**0.1222**	**0.1331**
CCS cost ($/kW-hr)	0.0187	0.0167	0.0181	0.0198
CO_2 Removal Cost ($/ton)	**21.37**	**19.51**	**20.16**	**21.09**

Table 15 Economics – Sweet-shift CCS

Biomass/Coal Ratio	0%	10%	30%	50%
Subcritical Plants				
Capital cost (million $)	1,181.7	1,059.9	1,044.2	1,028.2
Capital Cost ($/kW)	**5,964**	**5,292**	**5,303**	**5,311**
CoE ($/kW-hr)	**0.1316**	**0.1264**	**0.1405**	**0.1547**
CCS cost ($/kW-hr)	0.0308	0.0285	0.0321	0.0357
CO_2 Removal Cost ($/ton)	**32.18**	**29.85**	**31.15**	**32.19**
Supercritical Plants				
Capital cost (million $)	1,241.0	1,119.2	1,103.4	1,087.5
Capital Cost ($/kW)	**5,506**	**4,919**	**4,923**	**4,925**
CoE ($/kW-hr)	**0.1248**	**0.1203**	**0.1326**	**0.1449**
CCS cost ($/kW-hr)	0.0276	0.0256	0.0285	0.0316
CO_2 Removal Cost ($/ton)	**32.45**	**30.38**	**31.44**	**32.50**

Looking at the tables and comparing with the subcritical cycle for all plants, it becomes apparent that *the supercritical cycle universally decreases the capital cost per unit energy ($400/kW) and CoE (0.6-1.0 cents/kW-hr) despite the increase in total cost.* See Fig. 4.58 for a more qualitative comparison. While, for some reason or other, the sour-shift cases' capital cost/kW continues to decrease beyond 10% BMR for both subcritical and supercritical cases, as opposed to those of the other forms of CCS, which increase again for 30% and 50% BMR, the actual difference between the amounts is small ($5-$20/kW) and not worth calling any special attention to.

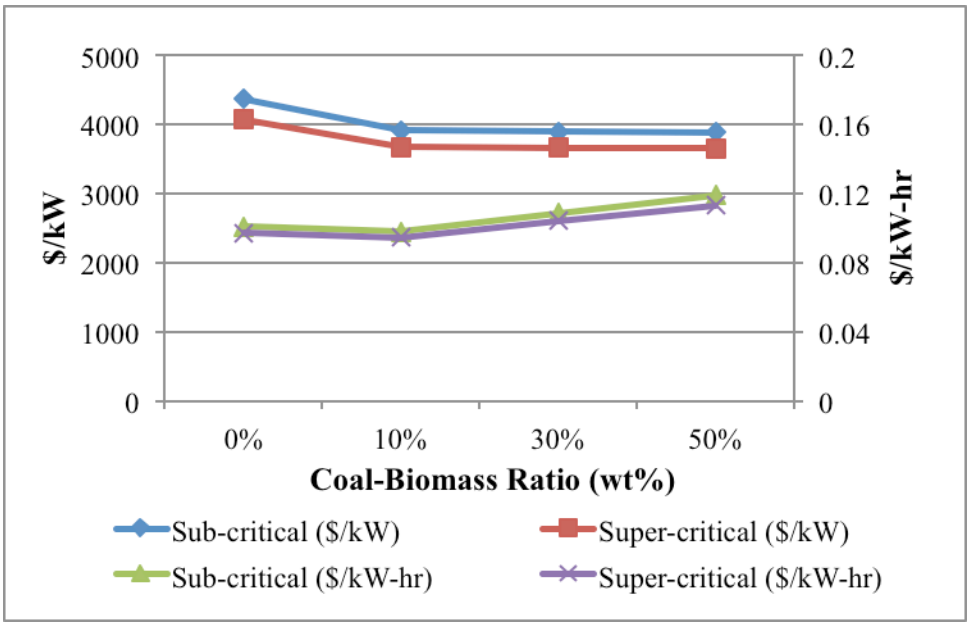

Fig. 4.58 Economics (Baseline plants)

Post-combustion CCS, however, has a clearly adverse effect on both CoE and capital cost. This is not surprising, considering the fact that post-combustion CCS requires the

processing of thousands of tons of exhaust gases a day, all at atmospheric pressure. The unit itself must be hundreds of meters high, and uses up nearly $24,000 worth of makeup solvent alone in a single day. At an **additional** 6-7 cents/kW-hr in CoE and nearly $500/kW in capital costs, using post-combustion CCS may not be viable for this type of plant. The CCS cost follows the same overall pattern as the total CoE does: decreasing at 10% BMR, but increasing beyond this amount. Despite the later increase, the biomass cases still have a lower CCS cost than the pure coal cases. In comparison, the CCS cost for pre-combustion CCS is about 11-12 cents/kW-hr, which is about the same as most of the cases (S1B, L1B, S3B, L3B, and S4B) in the U.S. Dept. of Energy's Vol. 3 report on fossil fuel plants [29], although the capital cost (called "total overnight cost" in the DoE report) is about $1,000/kW more expensive by comparison. This may be due to differing plant sizes (The DoE's plants are more than twice the size of the plants studied here) and year-to-year inflation (This study is based on June 2011 USD. The DoE's report is based on June 2007 USD.)

Sour-shift CCS is the most economical form of CCS in this study, as it has universally lower capital and electrical costs than either other form of CCS: $500/kW cheaper in capital cost than sweet-shift and $2500/kW cheaper than post-combustion, and ~1cent/kW-hr cheaper in CoE than sweet-shift and 5-6 cents/kW-hr cheaper than post-combustion. In other words, post-combustion CCS is the most expensive practice: about 3.7 times more costly than sour-shift CCS. This, again, mainly comes from the easy integration that sour-shift has with existing equipment: sour-shift can easily be retro-fitted onto existing devices, unlike sweet-shift, which requires that two entirely new sections be added to the cleanup system. Also, unlike post-combustion CCS, both forms of pre-combustion CCS use much smaller, less-expensive equipment. Both of these facts are major contributors to sour-shift's much cheaper price tag.

The CCS cost in terms of COE can also be converted to the cost for removing CO_2 (per unit ton basis) using Eq. (4.83):

$$CO2\ Removal\ Cost\ \left(\frac{\$}{ton}\right) = \frac{CoE_{CCS} - CoE_{base}}{\left[\frac{tons_{CO_2}}{MW-yr}\right]_{net}\frac{1MW}{1000kW}\frac{1yr}{8760hrs}}$$

(4.83)

where the "net" tons of CO_2 refers to the difference in effective tons of CO_2 per unit power between the baseline case and the CCS case. The "CO_2 Removal Cost" is also called "CO_2 Avoided Cost" in the U.S. Department of Energy's Volume 3 report mentioned previously [29]. If a "carbon tax" is implemented, the CO_2 Removal Cost can also be referred to as the "Break-even Cost" for avoiding the carbon tax. Only when the carbon tax is higher than the CO_2 removal cost is implementing CCS justified.

As seen in Tables 4.38 – 4.42, a $70/ton carbon tax would only work for those plants that include biomass in the feedstock. For pure coal, a tax of about $72/ton is necessary to justify post-combustion CCS, whereas all of the biomass cases are below $68/ton, with one case as low as $63/ton. The CO_2 removal cost for sweet-shift is only around $30/ton, while sour-shift's is even lower, around $20/ton: once again demonstrating the economic superiority of pre-combustion CCS. For more qualitative data on the plant CoE, see Fig. 4.59.

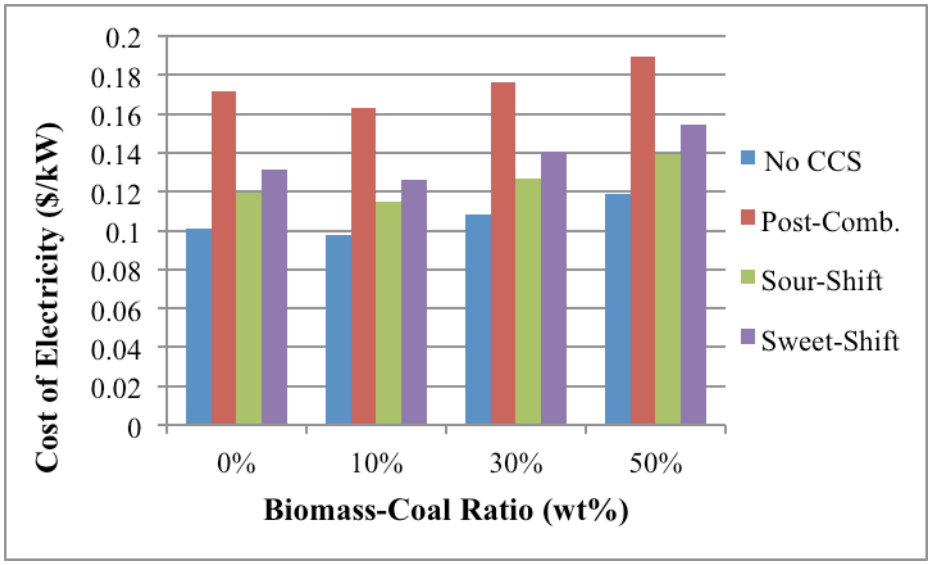

Fig. 4.59 Cost of Electricity for subcritical plants

4.10.8 Conclusions of Biomass/Coal Cogasification IGCC with CCS

In summary, this study was performed using GTPro®, a program from the Thermoflow® software suite. It uses a GE/Texaco gasifier and Siemens SGT6-4000F gas turbine, and the plant was assumed to be constructed in southern Louisiana using Texas Lignite and sugarcane bagasse as fuels. The results show that the net plant efficiency increases at 10% BMR for both sets of cases, but decreases thereafter. However, the efficiency of the blended cases remains higher than that of the pure-coal cases for *all blend ratios.* The emissions (NO_x, SO_x, and effective CO_2) and the capital costs all decrease as the biomass ratio increases. However, the cost of electricity increases with BMR due to how expensive obtaining the biomass is. With these results in mind, the following conclusions can be drawn:

a. The *supercritical* system is universally superior to the subcritical system regardless of which case is taken into consideration. The only difference is in the magnitude of the improvement: sweet-shift CCS benefits the most (1.8-1.9 percentage points of efficiency), due to the greater need for high-quality steam in

more places. Sour-shift, on the other hand, benefits the least (1.1-1.3 percentage points), due to the lower relative quality of the steam generated from the cleanup system. In all cases, about 20-30MW (9-12%) more power is generated. The economic costs, though, have generally the same differences (~$300-$400/kW lower capital and 0.3-0.4 cents/kW-hr lower CoE than the equivalent subcritical cycle.) The net emissions also decrease by 400-500 tons/MW-yr (6-7% less) overall due to the above-mentioned enhanced power output.

b. *Post-combustion carbon capture* is both thermally and economically detrimental to the IGCC baseline: capital costs increase by $3,700/kW (nearly double that of the baseline) and CoE increases by about $0.07/kW-hr. However, the emissions decrease by nearly 7,000 tons/MW-yr through the use of CCS: enough for the plant itself to become carbon-negative using only 10% biomass.

c. CO_2 removal cost is about $72/ton for post-combustion CCS. Blending 10% biomass reduces removal cost about $4-5/ton. The CO_2 removal cost for s*ubcritical, sour-shift* is about $18/ton, *supercritical, sour-shift* is $21/ton, and *sweet-shift* is about $32/ton. Blending 10% biomass can reduce the CO_2 cost by about $4-5/ton for post-combustion, and about $2/ton for both forms of pre-combustion CCS.

d. Sour-shift, pre-combustion CCS is the most optimal form of CCS in the current study: It has the highest efficiency (31-33%, compared to 27-29% sweet or 27.5-28% post-combustion with the lowest CCS impact on efficiency compared to the baseline,) and has the smallest increase in CCS cost compared to the baseline: $1000/kW ($0.018/kW-hr), compared to $1600/kW($0.029/kW-hr) sweet or $3700/kW ($0.068/kW-hr) post-combustion.
e. Sweet-shift, pre-combustion CCS is likewise cheaper to implement than post-combustion CCS (with $2100/kW difference in capital cost), and has lower CoE than post-combustion (by 4-5cents/kW), but, for the subcritical cycle cases, is thermally inferior (0.3-0.5 percentage points in efficiency). However, the supercritical cycle makes sweet-shift the better option due to the improvements from having access to higher quality steam, something that post-combustion CCS does not benefit from as greatly. The net efficiencies are comparable.

f. Biomass blends are always better than pure coal, thermally and economically, but too much biomass (beyond 10% BMR) begins to inhibit power output and efficiency due to pretreatment requirements. Blending 10% biomass tends to

Anthony, D., Howard, J., Hottel, H., and Meissner, H., 1975, "Rapid Devolatilization of Pulverized Coal," *Symposium (International) on Combustion,* Vol.15, pp.1303-1317.

increase the efficiency by about 0.7-1.0 percentage points and the output power by 2-5 MW. The capital costs per kW and CoE also decrease by $400-$800/kW and 0.3-0.8 cents/kW-hr, respectively. However, further biomass beyond 10 BMR decreases the efficiency and the power by up to 0.5 points and 6MW, respectively. The CoE increases by up to 2 cents/kW-hr, with or without CCS, but the capital cost can increase or decrease due to the effect of the CCS system.

REFERENCES

Adanez, J., and Labiano, F., 1990, "Modeling of Moving-Bed Coal Gasifiers*," Industrial & Engineering Chemistry Results*, Vol. 29, pp. 2079-2088.

Ajilkumar, A., Sundararajan, T., and Shet, U., 2009, "Numerical Modeling of a Steam Assisted Tubular Coal Gasifier," *International Journal of Thermal Sciences*, Vol. 48, pp. 308-321.

Ariyapadi, S., Shires, P., Bhargava, M., and Ebbern, D., 2008, "KBR's Transport Gasifier (TRIG™) – an Advanced Gasification Technology for SNG Production from Low-Rank Coals," Presented at the Twenty-fifth Annual International Pittsburgh Coal Conference September 29 – October 02, 2008, Pittsburgh, PA.

Ahmadi, G., Mazaheri, A., Liu, C., and Gamwo, I., 2002, "Computer Modeling of Flow, Thermal Condition and Ash Deposition in a Hot-Gas Filtration Device," 5th International Symposium on Gas Cleaning at High Temperatures, Morgantown, WV (US), 09/17/2002--09/20/2002.

Barroso, J., Ballester, J., Ferrer, L., and Jiménez, S., 2006, "Study of Coal Ash Deposition in an Entrained Flow Reactor: Influence of Coal Type, Blend Composition and Operating Conditions," *Fuel Processing Technology*, Vol.87, pp.737–752.

Bartle, K., Perry, D., and Wallace, S., 1987, "The Functionality of Nitrogen in Coal and Derived Liquids: an XPS Study," *Fuel Processing Technology*, Vol. 15, pp. 351-361.

Beeley, T., Crelling, J., Gibbins, J., Hurt, R., Lunden, M., Man, C., Williamson, J., and Yang, N., 1996, "Transient High-Temperature Thermal Deactivation of Monomaceral-rich Coal Chars," Twenty-Sixty Symposium (International) on Combustion. The Combustion Institute, Pittsburgh, in press.

Benyon P., 2002, "Computational Modelling of Entrained Flow Slagging Gasifiers," PhD thesis, School of Aerospace, Mechanical & Mechatronic Engineering, University of Sydney, Australia.

Bergman, P. C. A. and Kiel, J. H. A., 2005, "Torrefaction for Biomass Upgrading." 14thEuropean Biomass Conference and Exhibition. Paris, France. ECN-RX-05-180.

Bergman, P.C.A., 2005, "Combined Torrefaction and Pelletization: the TOP Process." Renewable Energy in the Netherlands. ECN Biomass: ZG Petten, the Netherlands.

Betta. R. A., Piken, A. G., and Shelef, M., 1974, "Heterogeneous Methanation: Initial Rate of CO Hydrogenation on Supported Ruthenium and Nickel," *Journal of Catalysis*, Vol. 35, pp. 54-64.

Biba, V., Macak, E., Klose, E., and Malenha, I., 1978, "Mathematical Model for the Gasification of Coal under Pressure," *Industrial & Engineering Chemistry Process Design and Development*, Vol. 17, pp, 92-98.

Blander, M., Sinha, S., Pelton, A., and Eriksson,G., 1989, "Calculations of the Influence of Additives on Coal Combustion Deposits,"
https://web.anl.gov/PCS/acsfuel/preprint%20archive/Files/34_2_DALLAS_04-89_0340.pdf

Brewster, M., and Kunitomo, T., 1984, "The Optical Constants of Coal, Char, and Limestone," *Journal of Heat Transfer*, Vol. 106, pp. 678-683.

Bilger, R., 1993, "Conditional Moment Closure for Turbulent Reacting Flow," *Physics of Fluids*, Vol. 5, pp. 436–444.

Beér, J., 2000, "Combustion Technology Developments in Power Generation in Response to Environmental Challenges." *Progress in Energy and Combustion Science*. Vol. 26, pp. 301-27.

Bockelie, M., Denison ,M., Chen, Z., Linjewile, T., Senior, C., and Sarofim, A., 2002, "CFD Modeling For Entrained Flow Gasifiers," Proceedings of the Gasification Technologies Conference 2002, San Francisco, CA.

Bockelie, M., Denison, M., Chen, Z., Linjewile, T., Senior, C., and Sarofim, A., 2002,"CFD Modeling For Entrained Flow Gasifiers in Vision 21 Systems," Proceedings of the Pittsburgh Coal Conference 2002, Pittsburgh, PA.

Bockelie, M.J., Denison, M., Chen, Z., Linjewile, T., Senior, C., and Sarofim, A., "Using Models to Select Operating Conditions for Gasifiers," Proceedings of the Pittsburgh Coal Conference 2003, Pittsburgh, PA.

Boysan, F., Weber, R., and Swithenbank, J., 1983, "Mathematical Modelling of an Entrained Coal Gasifier", 1983 International Gas Research Conference.

Bridgeman, T.G., Jones, J., Shield, I., and Williams, P.T., 2007, "Torrefaction of Reed Canary Grass, Wheat Straw, and Willow to Enhance Solid Fuel Qualities and Combustion Properties." Energy and Resources Research Institute, University of Leeds: Leeds, UK.

Buckius, R., and Hwang, D., 1980, "Radiation Properties for Polydispersions: Application to Coal," *ASME Journal of Heat Transfer*, Vol. 102, pp. 99-103.

Burchill, P., and Welch, L., 1989, "Variation of nitrogen content and functionality with rank for some UK bituminous coals," *Fuel*, Vol. 68, pp. 100.

Cao, Z., Sun, L., Cao, X., and He, Y., 2011, "Study on Fly Ash Adhesion Characteristics and Deposition Mechanism in Shell Coal Gasification Process," *Advanced Materials Research*, Vol. 233 – 235, pp. 789-793.

C.M. van der Meijden, 2010, "Development of the MILENA Gasification Technology for the Production of Bio-SNG," Eindhoven University of Technology Library, ISBN: 978-90-386-2363-4.

Chapyak, E., Blewett, P., and Cagliostro, D., 1983, "Verification Studies of Entrained-Flow Gasification and Combustion Systems with the Simmer-II Code," 10th IMACS World Congress on System Simulation and Scientific Computation.

Chan,P., and Norbeck, J., 2009, "Production of Methane Rich Fuel Gas from Coal using Steam Hydrogasification," Presented at the Twenty-sixth Annual International Pittsburgh Coal Conference September 21 – 24, 2009, Pittsburgh, PA.

Chandrasekhar, S., 1950, *Radiative Transfer*, Oxford University Press, London

Chandel, M., and Williams, E., 2009, "Synthetic Natural Gas (SNG): Technology, Environmental Implications, and Economics," Climate Change Policy Partnership. http://www. netldev netl.doe.gov.

Chodankar, C., Feng, B., and Klimenko, A., 2009, "Numerical Modeling of Underground Coal Gasification Process for Estimation of Product Gas Composition," Paper 25-3, presented at the 26rd International Pittsburgh Coal-Gen Conference, Pittsburgh, Pennsylvania, Sept. 20-23, 2009.

Chen, L., Nolan, R., and Avadhany, S., 2009, "Thermodynamic Analysis of Coal to Synthetic Natural Gas Process," http://www.mit.edu/people/leichen/Thermodynamic_Analysis_of_the_coal_to_SNG_process.pdf

Chen, C., Horio, M., and Kojima, T., 2010, "Numerical Simulation of Entrained Flow Coal Gasifiers," *Chemical Engineering Science*, Vol. 55, pp. 3861-3883.

Chen, M., 2010, "Numerical Simulation Analyses of an Entrained-bed Gasification Reactor," Paper 45-4, presented at the 27th International Pittsburgh Coal Conference, Istanbul, Turkey, October 11 – 14, 2010.

Chen, C., Miyoshi, T., Kamiya, H., Horio, M., and Kojima, T., 1999, "On the Scaling-up of a Two-Stage Air Blown Entrained Flow Coal Gasifier," *The Canadian Journal of Chemical Engineering*, Vol. 77, pp. 745-750.

Chen, C., Horio, M., and Kojima, T., 2000(a), "Numerical Simulation of Entrained Flow Coal Gasifiers. Part I: Modeling of Coal Gasification in an Entrained Flow Gasifier," *Chemical Engineering Science,* Vol. 55, pp. 3861-3874.

Chen C., Horio M., and Kojima T., 2000(b), "Numerical Simulation of Entrained Flow Coal Gasifiers. Part II: Effects of Operating Conditions on Gasifier Performance," *Chemical Engineering Science*, Vol. 55, pp. 3875-3883.

Choi, Y., Li, X., Park, T., Kim, J., and Lee, J., 2001, "Numerical Study on the Coal Gasification Characteristics in an Entrained Flow Coal Gasifier," *Fuel*, Vol. 80, pp. 2193-2201.

Choi, Y., Li, X., Park, T., Kim, J., and Lee, J., 2001, "Numerical Analysis of the Flow Field inside an Entrained-Flow Gasifier," *Korean Journal of Chemical Engineering,* Vol. 18, pp. 376-381.

Chen, W., Hsieh, T., and Jiang, T., 2008, "An Experimental Study on Carbon Monoxide Conversion and Hydrogen Generation from Water Gas Shift Reaction," *Energy Conversion and Management*, Vol. 49, pp. 2801-2808.

Chen, L., Yong, S., and Ghoniem, A., 2012, "Modeling the Slag Behavior in Three Dimensional CFD Simulation of a Vertically-oriented Oxy-coal Combustor," The 37th International Technical Conference on Clean Coal & Fuel Systems, Clearwater FL, June 3-7, 2012.

Choi, Y., and Stenger, H.G., 2003, "Water Gas Shift Reaction Kinetics and Reactor Modeling for Fuel Cell Grade Hydrogen," *Journal of Power Sources*, Vol. 124, pp. 432–439.

Cumber, P., Fairweather, M., and Ledin, H., 1998, "Application of Wide Band Radiation Models to Non-homogeneous Combustion Systems," *International Journal of Heat and Mass Transfer*, Vol. 11, pp. 1573-1584.

Coimbra, C., Azevedo, J., and Carvalho, M., 1994, "3-D Numerical Model for Predicting NOx Emissions from an Industrial Pulverized Coal Combustor," *Fuel*, Vol. 73, pp. 1128–1134.

Costen, P., Lockwood, F., and Siddique, M., 2000, "Mathematical Modeling of Ash deposition in Pulverized Fuel-fired Combustors," *Proceedings of the Combustion Institute*, Vol. 28, pp. 2243–2250.

Couch, G., 1994, "Understanding Slagging and Fouling in pf Combustion." London, IEA Coal Research.

Day, D., 2011, *Louisiana Sugar Cane Institute.* Louisiana State University – Agricultural Center. Private Correspondence.

Denn, M., Wei, J., Yu, W., and Cwiklinski, R., 1982, "Detail Simulation of a Moving-Bed Gasifier," Research Project 1268-1, M.I.T., USA

Dent, F., Moignard, L., Eastwood. A., Blackturn, W., and Hebden, D., 1948, "An investigation into the Catalytic Synthesis of Methane for Town Gas Manufacture," *Gas Res. Board Comm.,* Vol. 20, pp. 106-121.

DeSai, P., Wen, C., Bissett, L., 1978, "Computer Modeling of the Morgantown Energy Research Center's Fixed Bed Gasifier," MERC/CR-78/3, U.S. Department of Energy, Morgantown, WV.

DalSecco, S., Mechitoua, N., and Simonin, O., 1995, "Three-dimensional Modeling of Coal Combustion and NO Formation in a 250MW Coal-fired Furnace," Proceedings of the Third International Conference on Combustion Technology for a Clean Environment Paper 31-2.

DOE/NETL Report, 2007, "Industrial Size Gasification for Syngas, Substitute Natural Gas and Power Production," National Energy Technology Laboratory.

DOE/NETL Report, 2011, "Cost and Performance Baseline for Fossil Energy Plants Volume 3a: Low Rank Coal to Electricity: IGCC Cases," National Energy Technology Laboratory.

DOE Report, 2006, "Practical Experience Gained during the First Twenty Years of Operation of the Great Plains Gasification Plant and Implications for Future Projects," Department of Energy.

Dilip A. Saletore and Wllllam J. Thomson, 1977, "Methanation Reaction Rates for Recycle Reactor Compositions," *Ind. Eng. Chern., Process Des. Dev.,* Vol. 16, pp. 70-75.

Duan, R., Koshizuka, S. and Oka, Y., 2003 "Droplet Breakup Under Impulsive Acceleration Using Moving Particle semi-Implicit Method," 11th International Conference on Nuclear Engineering, Tokyo, Japan, April 20-23, 2003, Paper No: ICONE11-36029.

Edwards, D.K., and Balakrishnan, A., 1973, "Thermal Radiation by Combustion Gases," *International Journal of Heat and Mass Transfer,* Vol. 16, pp. 25-40.

Energy Information Administration (EIA), 2009, "Average Sales Price of Coal by State and Coal Rank." U.S. Dept. of Energy. http://www.eia.gov/cneaf/coal/page/acr/table31.html

Energy Information Administration (EIA), 2010, "Updated Capital Cost Estimates for Electricity Generation Plants." Office of Energy Analysis. U.S. Department of Energy: Washington, DC.

Essenhigh, R., 1981, *Chemistry of Coal Utilization, Second Supplementary Volume*, John Wiley and Sons, New York.

Faltsi-Saravelon, O., and Wild, P.N., 1995, "Prediction of NO Emissions from a Swirling Coal Flame," Proceedings of the Third International Conference on Combustion Technology for a Clean Environment Paper 20-2.

Fernandez-Turiel, J., Georgakopoulos, A., Gimeno, D., Papastergios, G., and Kolovos, N., 2004, "Ash Deposition in a Pulverized Coal-fired Power Plant after High-calcium Lignite Combustion," *Energy & Fuels*, Vol.18, pp.1512-1518.

Field, M., 1970, "Measurements of the Effect of Rank on Combustion Rates of Pulverized Coal," *Combust Flame*, Vol. 14, pp. 237-248.

Fiveland, W., 1988, "Three-dimensional Radiative Heat-transfer Solutions by the Discrete-ordinates Method," *Journal of Thermophysics*, Vol. 2, pp. 309–316.

Fiveland, W., and Wessel, R., 1988, "Numerical Model for Predicting Performance of Three-dimensional Pulverized-fuel Fired Furnaces," *Journal of Engineering for Gas Turbines and Power,* Vol. 110, pp. 117–126.

FLUENT 6.3 User's Guide, September 2006.

Fletcher, T., 1983, "Two-dimensional Model for Coal Gasification and Combustion," PHD Dissertation, Brigham Young University.

Fletcher, T., Kerstein, A., Pugmire, R., and Grant, D., 1990, "Chemical Percolation Model for Devolatilization. 2. Temperature and Heating Rate Effects on Product Yields," *Energy and Fuels*, Vol. 4, pp. 54-60.

Fletcher, T., Smith, P., and Smoot, L., 1984, "Evaluation of a 2-D Coal Combustion Model," Proceedings of 1984 Spring Meeting of the Western States Section of the Combustion Institute, Boulder, CO.

Fletcher, T., and Kerstein, A., 1992, "Chemical Percolation Model for Devolatilization: 3 Direct Use of ^{13}C NMR Date to Predict Effects of Coal Type," *Energy and Fuels*, Vol. 6, pp. 414-431.

Foster, P., and Howarth, C., 1968, "Optical Constants of Carbon and Coals in the Infrared," *Carbon*, Vol. 6, pp. 719-729.

Fairley, P., 2007, "Cheaper Natural Gas from Coal,"

GreatPoint energy, 2008a. http://www.greatpointenergy.com.

Given, P., Marzec, A., Barton, W., Lynch, L., and Gerstein, B., 1986, "The Concept of a Mobile or Molecular Phase within the Macromolecular Network of Coals: a Debate," *Fuel,* Vol. 65, pp. 155-163.

Gibson, M., and Euker, C., 1975, "Mathematical Modeling of Fluidized Bed Coal Gasification," Preprint in AlChE Symposium, Los Angeles.

Gupta, A., and Thodos, G., 1963, "Direct Analogy between Mass and Heat Transfer to Beds of Spheres," *AlChE Journal*, Vol. 9, pp. 751-754.

GreatPoint Energy, 2008b. "GreatPoint Energy announces coal supply partnership with Peabody Energy and enters into agreement to build natural gas manufacturing facilities in Powder River," Basin. http://www.greatpointenergy.com/GPE-Peabody1-25-08.pdf.

Grant, D., Pugmire, R., Fletcher, T., and Kerstein, A., 1989, "Chemical Percolation of Coal Devolatilization Using Percolation Lattice Statistics," *Energy and Fuels*, Vol. 3 pp. 175-186.

Grenoble, D., and Estadt, M., 1981, "The Chemistry and Catalysis of the Water Gas Shift Reaction 1, the Kinetics over Supported Metal Catalysts," *Journal of Catalysis,* Vol. 67, pp. 90-102.

Grosshandler, W., 1980, "Radiative Heat Transfer in Non-homogeneous Gases: a Simplified Approach," *International Journal of Heat and Mass Transfer*, Vol.23, pp. 1447-1459.

Grosshandler W., and Monteiro S., 1982, "Attenuation of Thermal Radiation by Pulverized Coal and Char," *International Journal of Heat Transfer*, Vol. 104, pp. 587-593.

Genetti, B., 1999, "An Advanced Model of Coal Devolatilization Based on Chemical Structure," Master Thesis, Brigham Young University Saxena, S., *Progress in Energy and Combustion Sciences*, Vol. 16, pp. 55-94.

Guenther, C., and Zitney, S., 2005, "Gasification CFD Modeling for Advanced Power Plant Simulation," Proceedings of the 22th International Pittsburgh Coal Conference, Pittsburgh, Pennsylvania, September 12-15, 2005.

Gururajan, V. S., Agarwal, P. K., and Agnew, J. B., 1992, " Mathematical Modeling of Fluidized Bed Coal Gasifiers," *Chemical engineering research & design*, Vol. 70, No. A3, pp. 211-238, ISSN : 0263-8762.

Hirth, T., and Franck, E., 1991, "Oxidation and Hydrothermolysis of Hydrocarbons in Supercritical Water at High Pressures," *Ber. Bunsenges. Phys. Chem*., Vol. 97, pp. 1091-1097.

Higman, C., and M. van der Burgt, *Gasification*, Elsevier, 2003.

Hla, S., Park, D., Duffy, G., Edwards, J., Roberts, D., Ilyushechkin, A., Morpeth, L., and Nguyen, T., 2009, "Kinetics of High-temperature Water-Gas Shift Reaction over Two Iron-based Commercial Catalysts Using Simulated Coal derived Syngases," *Chemical Engineering Journal*, Vol. 146, pp. 148–154

Hobbs, L., Radulovict, P., and Smoot, D., 1992, "Modeling Fixed-bed Coal Gasifiers," *AlChE Journal*, Vol. 38, pp. 681-702.

Hobbs, M., 1990, "Modeling Counter Current Fixed Bed Coal Gasification," PhD Dissertation, Provo. UT., Brigham Young University.

Holgate, H., Webley, P., and Tester, J., 1992, "Carbon Monoxide Oxidation in Supercritical Water: the Effects of Heat Transfer and the Water-Gas-Shift Reaction on Observed Kinetics," *Energy & Fuels,* Vol.6, pp. 586-597

Hohlein, B.; Niessen, H.; Range, J.; Schiebahn, H. J. R.; Vorwerk, M., "Methane from synthesi s gas and operation of high-temperature methanation". *Nuclear Engineering and Design* 1984, 78, (2), 241-250.

Hottel, H., and Howard, J., 1971, "New Energy Technology: Some Facts and Assessments," *New Energy Technology*, Cambridge, MA MIT Press.

Hough, S., 2009, "Supercritical Rankine Cycle." University of Idaho. Technical Paper. ME-517 http://www.if.uidaho.edu/~gunner/ME443-543/HW/rankine.pdf

Hughes, R., Lu, D., Majeski, A., Corber, A., and Anthony, B., 2010, "Entrained Flow Slagging Slurry Gasification and the Development of Computational Fluid Dynamics Models at CanmetENERGY," 2010 International Pittsburgh Coal Conference, Istanbul, Turkey October 11 – 14, 2010.

Hurt, R., and Gibbins, J., 1995, "Residual Carbon from Pulverized Coal Fired Boilers: 1. Size Distribution and Combustion Reactivity," *Fuel*, Vol. 74, pp. 471-482.

Hurt, R., Davis, K., Yang, N., Headley, T., and Mitchell, G., 1995, "Evolution of Char Chemistry, Crystallinity, and Ultrafine Structure during Pulverized-coal Combustion," *Combustion and Flame*, Vol. 100, pp. 31-40.

Hurt, R., and Davis, K., 1994, "Near-extinction and final burnout in coal combustion," Twenty- Fifth (International) Symposium on Combustion, The Combustion Institue, Pittsburgh, Vol. 25, pp. 561-568.

Hottel, H., and Sarofim, A., 1967, *Radiative Transfer*, McGraw-Hill.

Holt, N., 2004, "Gasification Process Selection – Trade-offs and Ironies," Proceedings of the Gasification Technology Conference 2004, Washington, DC.

IM, K., and Ahluwalia, R., 1992, "Radiation Properties of Coal Combustion Products," *International Journal of Heat and Mass Transfer*, Vol. 36, pp. 293-302.

Jesionek, K.; Kantorek, M.; Karcz, H., 2010, "Main Problems Concerning Co-firing Biomass Mixture with Hard Coal in Pulverized-Fuel Boilers." Wroclaw University of Technology. International Pittsburgh Coal Conference, Istanbul, Turkey.

Jones, W.P., and Lindstedt, R.P., 1998, "Global Reaction Schemes for Hydrocarbon Combustion," *Combustion and Flame*, Vol. 73, pp. 233-240.

Johnson, J.L., 1979, *Kinetics of Coal Gasification: a Compilation of Research*, John Wiley and Sons, New York, NY.

Kallio, G., and Reeks, M., 1989, "A Numerical Simulation of Particle Deposition in Turbulent Boundary Layers, International Journal of Multiphase Flow," Vol. 15, No. 3, pp. 433-446.

Kanaar, M., 2006, "Operating Experience of the Buggenum IGCC Plant and Future Plans," presented on the IGCC Panel at ASME Expo Turbo, Barcelona, Spain May 9, 2006.

Karthikeyan, M., Wu, Z., and Mujumdar, A., "Low-Rank Coal Dry Technologies-Current Status and New Developments," *Dry Technology*, Vol. 27, pp. 403-415.

Keiski, R., Salmi, T., Niemisto, P., Ainassaari, J., and Pohjola, V., 1996, "Stationary and Transient Kinetics of the High Temperature Water Gas Shift Reaction," *Applied Catalysis A: General,* Vol. 137, pp. 349-370.

Kelemen, S., Gorbaty, M., and Kwiatek, P., 1994, "Quantification of Nitrogen Forms in Argonne Premium Coals," *Energy & Fuels,* Vol. 8, pp. 896.

Kelemen, S., Gorbaty, M., Vaughn, S., and Kwiatek, P., 1993, "Transformation Kinetics of Organic Sulphur Forms in Argonne Premium Coals During Pyrolysis,"*ACS Division of Fuel Chemistry Preprints*, Vol. 38, pp. 384-392.

Kobayashi, H., Howard, J., and Sarofim, A., 1976, "Coal Devolatilization at High Temperatures," 16th Symp. (Int'l.) on Combustion, The Combustion Institute.

Koryabkina, N., Phatak, A., Ruettinger, W., Farrauto, R., and Ribeiro, F., 2003, "Determination of Kinetic Parameters for the Water–Gas Shift Reaction on Copper Catalysts under Realistic Conditions for Fuel Cell Applications," *Journal of Catalysis*, Vol. 217, pp. 233-239.

Kovac, J., 2008, "Advanced SGT6-5000F Development." Siemens Energy Corporation. *Power-Gen International.* Orlando, FL.

Krevelen, D., 1981, *Coal: Typology, Chemistry, Physics, and Constitution*, Elsevier, New York.

Kusar, H., Hocevar, S., and Levec, J., 2006, "Kinetics of the Water-Gas-Shift Reaction over Nanostructured Copper–Ceria Catalysts," *Applied Catalysis B: Environmental*, Vol. 63, pp. 194–200.

Kuo, K. Y., 1986, *Principles of combustion*, John Wiley and Sons, New York.

Kumar, M., Zhang, C., Monaghan, R., Singer, S., and Ghoniem, A., 2009. "CFD simulation of Entrained Flow Gasification with Improved Devolatilization and Char Consumption Submodels," Proceedings of the ASME International Mechanical Engineering Congress and Exposition, Lake Buena Vista, FL, USA. Nov. 13-19, 2009.

Kumar, M., and Ghoniem, A., 2012, "Multiphysics Simulations of Entrained Flow Gasification. Part II: Constructing and Validating the Overall Model," *Energy Fuels,* Vol. 26, pp. 464-479.

Lang, Y., Zitney, S., and Biegler, L., 2011, "Optimization of IGCC Processes with Reduced Order CFD Models," *Computers & Chemical Engineering,* Vol. 35, pp. 1705-1717.

Lasa, H., and Mok, L.K., 1981, "Entrained Coal Gasifiers: Modeling the Particle Acceleration," *The Canadian Journal of Chemical Engineering*, Vol. 59, pp. 658-661.

Legendre, B.L., Sanders, F.S., Gravois, K.A., 2000, "Sugarcane Production BMPs," Louisiana Department of Natural Resources. Louisiana State University Agricultural Center, Baton Rouge, LA.

Lockwood, F., Papadopoulos, C., and Abbas, A., 1988, "Prediction of a Corner-fired Power Station Combustor," *Combustion Science and Technology*, Vol.158, pp. 5–23.

Long, H. A. and Wang, T., 2011a, "Case Studies for Biomass/Coal Co-gasification in IGCC Applications," GT2011-45512, Proceedings of ASME Turbo Expo 2011, Vancouver, Canada.

Long, H. A. and Wang, T., 2011b, "A System Performance and Economic Analysis of IGCC with Supercritical Steam Bottom Cycle Supplied with Varying Blends of Coal and Biomass Feedstock," IMECE2011-65749, Proceedings of ASME 2011 International Mechanical Engineering Congress and Exposition, Denver, Colorado, U.S.A.

Li, Z., Wei, F., and Jin. Y., 2003, "Numerical Simulation of Pulverized Coal Combustion and NO Formation*," Journal of Chemical Engineering Scie*nce, Vol. 58, pp. 5161-5171.

Luan Y., Chyou, Y., Wang, T., 2011, "Numerical Analysis of Gasification Performance via Finite-rate Model in a Cross-type Two-stage Gasifier," The 28th International Pittsburgh Coal Conference, Pittsburgh, PA, USA, Sept. 12-15, 2011.

Lu, X., and Wang, T., 2013, "Water-Gas Shift Modeling in Coal Gasification in an Entrained-flow Gasifier Part 1: Development of Methodology and Model Calibration," DOI information: 10.1016/j.fuel.2013.02.023, *Fuel*, Vol. 108, pp. 629-638.

Lu, X., and Wang, T., 2013, "Water-Gas Shift Modeling in Coal Gasification in an Entrained-flow Gasifier Part 2: Gasification Application," DOI information: 10.1016/j.fuel.2013.02.024, *Fuel*, Vol. 108, pp. 620-628.

Li, A., and Ahmadi, G., 1992, "Dispersion and Deposition of Spherical Particles from Point Sources in a Turbulent Channel Flow," *Aerosol Science and Technology*, Vol. 16, pp. 209-226.

Linares-Solano, A., Mahajan, O.P., Philip, L., and Walker, P.L., 1979, "Reactivity of Heat-treated Coals in Steam", *Fuel*, Vol. 58, pp. 327-332.

Li, Z., Li, R., and Zhou, L., 2000, "Experimental Study of a High-efficiency and Low Pollution Pulverized-coal Swirl Burner under Cold-state Test Condition," *Journal of Engineering for Thermal Energy & Power* ,Vol. 6, pp. 640–643.

Lee, S., and Tien, C., 1981, "Optical Constants of Soot in Hydrocarbon Flames," *Eighteenth Symp. (Int.) on Combustion*, Combustion Institute, Pittsburgh, pp. 1159-1166.

Lauder, B.E., and Spalding, D.B., *Lectures in Mathematical Modeling of Turbulence*, Academic Press, London, England, 1972.

Lockwood, F., and Shah, N., 1981, "A New Radiation Solution Method for Incorporation in General Combustion Prediction Procedures," *Eighteenth Symposium (International) on Combustion*, Combustion Institute, Pittsburgh, 1981, pp. 1405-1414.

Martula, D., Hasegawa, T., Lloyd, D., and Bionnecaze, R., 2000, "Coalescence-Induced Coalescence of Inviscid Droplets in a Viscous Fluid," *Journal of Colloid and Interface Science,* Vol. 232, pp. 241–253.

McDaniel, J., Hornick, M., Webb, L., Boddiford, D., Davis, T., Pedro, T., Valentine, M., and Hall, B., 2002, "Tampa Electric Polk Power Station Gasification Combined Cycle Project," *Final Technical Report,* Tampa Electric Company. http://www.tampaelectric.com/data/files/PolkDOEFinalTechnicalReport.pdf

Menezes, R., *ICIS Pricing*, 2010, "Ethanolamines: Europe." Ed.:. Reed Business Information Ltd: London, UK. http://www.icispricing.com/il_shared/Samples/SubPage10100082.asp

Modest, M.F., 2003, *Radiative Heat Transfer*, Academic Press.

Mozaffarian, M., and Zwart, R., 2003, "Feasibility of Biomass/waste Related SNG Production Technologies," http://www.ecn.nl/publications.

Mozaffarian, M., Zwart, R., Boerrigter, H., Deurwaarder, E., Kersten, S., 2004, "Green Gas as SNG (synthetic natural gas)-A Renewable Fuel with Conventional Quality," http://www.ecn.nl/ publications.

Mueller, C., and Kremer, H., 1995, "Modeling of an Industrial Scale Gas-burner using 9nite-rate Chemistry-options and Restrictions Resulting from Eddy-Break up Based Models," Proceedings of the third International Conference on Combustion Technology for a Clean Environment Paper 7.1, Lisbon.

Niksa, S., 1995, "Flash chain Theory for Rapid Coal Devolatilization Kinetics. 6. Predicting the Evolution of Fuel Nitrogen from Various Coals ," *Energy and Fuels*, Vol. 9, pp. 467-478.

O'Rourke, P., and Amsden, A., 1987, "The Tab Method for Numerical Calculation of Spray Droplet Breakup," SAE Technical Paper 872089.

O'Rourke, P. J., 1981, "Collective Drop Effects on Vaporizing Liquid Sprays" PhD dissertation, Princeton University, New Jersey.

Qiang, L., Ti-min C., Guo, E., and Chunbo, H., 2006, "Droplet Collision and Coalescence Model," *Applied Math and Mechanics*, Vol. 27(1), pp. 67–73.

Pan, Y. and Suga, K., 2005, "Numerical Simulation of Binary Liquid Droplet Collision," *Physics of Fluids,* Vol. 17, pp. 82-105.

Papadakis, G., and Bergeles, G., 1994, "Prediction of Staged Coal Combustion in Three-Dimensional Furnaces" *Journal of the Institute of Energy*, Vol. 67, pp. 156–167.

Parameswaran, T.; Hughes, P.; Lacelle, R., 2009, "Flame Emission Spectroscopy in a Coal-Biomass Co-fired Boiler." CANMET Energy, Natural Resources Canada. 26th Annual International Coal Conference: Pittsburgh, PA, U.S.A.

Park, N., Kobayashi, T., and Taniguchi, N., 2000, "Application of Flame-wrinkling LES Combustion Models to a Turbulent Premixed Combustion Around Bluff Body," Proceedings of the Third International Symposium on Turbulence, *Heat and Mass Transfer*, Nagoya, Aichi Shuppan, pp. 847–854.

Pope, S., 1985, "PDF Methods for Turbulent Reactive Flows," *Progress in Energy and Combustion Science*, Vol. 11, pp. 119–192.

Philip, L., Walker, P.L., Matsumoto, S., Hanzawa, T., Muira, T., and Ismail, I., "Catalysis of Gasification of Coal-derived Cokes and Chars," *Fuel,* Vol. 62, pp. 140-149.

Probstein, R., Hicks, R., 1982, *Synthetic fuels*. McGraw-Hill, New York.

NETL, 2008, "Gasification Technologies, Development of a Hydrogasification Process for CO-production of Substitute Natural Gas (SNG) and Electric Power from Western Coals Description," http://www.netl.doe.gov/publications/factsheets/project/Proj410.pdf.

Paraskevi P., Dimitris K., and Xenophon V., 2008, "Selective Methanation of CO over Supported Noble Metal Catalysts: Effects of the Nature of the Metallic Phase on Catalytic Performance," *Applied Catalysis A: General*, Vol. 344, pp. 45–54.

Ranz, W. E. and Marshall Jr. W. R., 1952, "Evaporation From Drops Part I," *Chem. Eng. Prog*, Vol. 48, pp. 141-146.

Ranz, W.E., and Marshall, W.R., 1952, "Evaporation from Drops Part 2," *Chem. Eng. Prog*, Vol. 48, pp. 173-180.

Rase, H.F., *Chemical Reactor Design for Process Plants: Volume two – Case Studies and Design Data*, John Wiley and Sons, 1977.

Rabbitts, M., Van Den Houten, G., Glasser, D., and Bryson, A., 1983, "Modelling of Residence Time Distribution in an Entrained Flow Coal Gasifier Reactor," *ChemSA*, Vol. 9, pp. 220-223.

Rehm, M., Seifert, P., Meyer, B., 2009, "Theoretical and Numerical Investigation on the EDC-Model for Turbulence–chemistry Interaction at Gasification Conditions," *Computers & Chemical Engineering*, Vol. 33, pp. 402-407.

Retzlaff, K. M., 1996. "Steam Turbines for Ultrasupercritical Power Plants." General Electric Company. Power Gen – Europe: Budapest, Hungary. GER-3945A.

Rhodes, C., Hutchings, G., and Ward, A., 1995, "WGSR: Finding the Mechanistic Boundary," *Catalysis Today*, Vol. 23, pp. 43-48.

Rhodes, C., and Hutchings, G., 2003, "Studies of the Role of the Copper Promoter in the Iron Oxide/ Chromia High Temperature Water Gas Shift Catalyst," *Physical Chemistry Chemical Physics*, Vol. 5, pp. 2719–2723.

Rinard, I., and Benjamen, B., 1985, "Great Plains ASPEN Model Development: Gasifier Model, Literature Review and Model Specification," Work performed under contract No DE-AC21-82MC19163 for US Department of Energy, Morgantown Energy Technology Centre.

Sarofim, A., and Hottel, H., 1978, "Radiative Transfer in Combustion Chambers: Influence of Alternative Fuels," in Proceedings of the Sixth International Heat Transfer Conference, Hemisphere, Washington, D.C., Vol.6, pp. 199-217.

Shao, Y., 2011, "Investigation of Ash Deposition During Co-firing Biomass/peat with Coal in a Pilot-scale Fluidized-bed Reactor," Ph.D thesis, University of Western Ontario London, Ontario,Canada.

Shi, S., Zitney, S., Shahnam, M., Syamlal, M., and Rogers, W., 2006, "Modelling Coal Gasification with CFD and Discrete Phase Method," *Journal of Energy Institute*, Vol. 79, pp. 217-221.

Salmi, T., and Hakkarainen, R., 1989, "Kinetic Study of the Low-Temperature Water-Gas-Shift Reaction over a Cu-ZnO Catalyst," *Applied Catalysis*, Vol. 49, pp. 285-306.

Sato, T., Kurosawa, S., Smith Jr., R., Adschiri, T., and Arai, K., 2004, "Water Gas Shift Reaction Kinetics under Noncatalytic Conditions in Supercritical Water*," Journal of Supercritical Fluids*, Vol. 29, pp. 113-119.

Schlich, E., and Köhne H., 1977, "Mathematisches Modell für die Vergasung und Verbrennung von Steinkohle unter Druck," *Chemie Ingenieur Technik,* Vol. 55, pp 123-129.

Silaen, A., and Wang, T., 2005, "Simulation of Coal Gasification Process Inside a Two-Stage Gasifier," Paper 20-1, Proceedings of the 22nd International Pittsburgh Coal Conference, Pittsburgh, Pennsylvania, September 19-22.

Silaen, A. and Wang, T., 2006, "Effects of Fuel Injection Angles on Performance of A Two-Stage Coal Gasifier," Proceedings of the 23rd Pittsburgh Coal Conference, Pittsburgh, Pennsylvania, September 25-28,2006.

Silaen, A., and Wang, T., 2009, "Comparison of Instantaneous, Equilibrium and Finite Rate Gasification Models in an Entrained Flow Coal Gasifier," Paper 14-3, proceedings of the 26th International Pittsburgh Coal Conference, Pittsburgh, Pennsylvania, Sept. 21-24, 2009.

Silaen, A., and Wang, T., 2010, "Effect of Turbulence and Devolatilization Models on Gasification Simulation," International Journal of Heat and Mass Transfer, Vol. 53, pp. 2074-2091.

Silaen, A. and Wang, T., 2012, "Investigation of Coal Gasification Process under Various Operating Conditions Inside a Two-Stage Entrained Flow Gasifier," ASME Journal of Thermal Science and Engineering Applications, Vol. 4, 021006/1-11.

Spiro, C. L. and P. G. Kosky, 1982, "Space-filling Models for Coal. 2. Extension to Coals of Various Ranks," *Fuel,* Vol. 61, pp. 1080-1084.

Solomon, P. R., 1981, "Coal Structure and Thermal Decomposition," *In New Approaches in Coal Chemistry*, American Chemical Society, Washington, D.C., Vol. 169, pp 61-71.

Solomon, P., Hamblen, D., Caranglo, R., Sergio, M., and Deshpande, G., 1988, "General Model of Coal Devolatilization," *Energy and Fuels*, Vol. 2, pp. 405-412.

Solomon, P., Serio, M., Carangelo R., and Bassilakis, R., 1990, "Analysis of the Argonne Premium Coal Samples by Thermogravimetric Fourier Transform Infrared Spectroscopy," *Energy & Fuels*, Vol. 4, pp. 319-333.

Saffman, P., 1965, "The Lift on a Small Sphere in a Slow Shear Flow," *J. Fluid Mech.,* Vol. 22, pp. 385-400.

Schulze, K., Scharler, R., and Obernberger, I., 2011, "Development of an Advanced CFD Model for Ash Deposit and Aerosol Formation in Biomass Fired Boilers," 9th European Conference on Industrial Furnaces and Boilers, Estoril, Portugal, 2011.

Siemens-Westinghouse Power Corporation, 1999, "Hawaiian Biomass Gasification Commercialization Project." Final Report, Siemens-Westinghouse Power Corporation, Orlando, FL

Siegel, R., and Howell, J., 1980, *Thermal Radiation Heat Transfer,* Taylor & Francis.

Slezak, A., Kuhlman, J., Shadle, L., Spenik, J., and Shi, S., 2010, "CFD Simulation of Entrained-flow Coal Gasification: Coal Particle density/size Fraction Effects," *Powder Technology*, Vol. 203, pp. 98-108.

Smith, B., Loganathan, M., and Shanatha, M.S., 2010, "A Review of the Water Gas Shift Reaction Kinetics," *International Journal of Chemical Reactor Engineering*, Vol. 8, ISSN:1542-6580.

Smoot, L., and Smith, P., 1985, *Coal Combustion and Gasification*, Plenum Press, New York.

Smith, I., 1978, "The Intrinsic Reactivity of Carbons to Oxygen," *Fuel*, Vol. 57, pp. 409-421.

Smith, K., Smoot, L., Fletcher, T., and Pugmire, R., 1994, *The Structure and Reaction Processes of Coal*, Plenum Press, New York.

Sommerfeld, M., Kohnen, G., and Ruger, M., 1993, "Some Open Questions and Inconsistencies of Lagrangian Particle Dispersion Models," Proceedings of the Ninth Symposium on Turbulent Shear Flows, Paper 5.1, Kyoto, Japan.

Stahl, K., Morris, M., Waldheim, L., Gardmark, and L, Johnsson, U., 2004, "Biomass IGCC at Varnamo, Sweden – Past and Future." GCEP Energy Workshop. Stanford University, Palo Alto, CA.

Sundararajan, A.T., and Shet, U., 2009, "Numerical Modeling of a Steam-Assisted Tubular Coal Gasifier," *International Journal of Thermal Sciences*, Vol. 48, pp. 308-321.

Stegeman, Y., Chesters, A., Vosse, F., and Meijer, H., 1999, "Breakup of (non-) Newtonian Droplets in a Time-dependent Elongational Flow," Proceedings PPS-15's-Hertogenbosch, 1999.

Suuberg, E., Peters, W., and Howard, J., 1979, "Product Compositions and Formation Kinetics in Rapid Pyrolysis of PN Pulverized Coal—Implications for Combustion," The Combustion Institute, Pittsburgh, PA, pp. 117-130.

Solomon, P., Hamblen, D., Carangelo, R., Serio, M., and Deshpande, G., 1988, "General model of coal devolatilization ," *Energy and Fuels*, Vol. 2, pp. 405-422.

Talbot, L., Cheng, R., Schefer, R., and Willis, D., 1980, "Thermophoresis of Particles in a heated Boundary Layer," *Journal of Fluid Mechanics*, Vol. 101, pp. 737-758.

Tampa Electric Polk Power Station Integrated Gasification Combined Cycle Project, Final Technical Report, August 2002.

Tanahashi, M., Yu, Y., and Miyauchi, T., 2000, "Effects of Turbulence Intensity on the Structure of Hydrogen-Air Turbulence Premixed Flames," Proceedings of the Third International Symposium on Turbulence, Heat and Mass Transfer, Nagoya, Aichi Shuppan, pp. 823–830.

Thoesness, C., and Rosza, R., 1976, "Lawrence Livermore Laboratory in-situ Coal Gasification Program: Model Calculations and Laboratory Experiments," Livermore, California, USA, Lawrence Livermore Laboratory.

Twigg, M.V., 1989, *Catalyst Handbook*, second edition, Wolfe Publishing Ltd.

Tunå, Per, 2008, "Substitute Natural Gas from Biomass Gasification," Synopsis of Master Thesis, Department of Chemical Engineering, Lund University, P. O. Box 124, SE-221 00 Lund, Sweden.

Tyrkiel, E., and Cudnok, R., 1981, "Computer Modeling of Coal Combustion and/or Gasification in an Entrained-Bed System,"Specialist Meeting on Coal MHD Power Generation, Sydney.

U.S. Department of Agriculture, 2010a, "Briefing Rooms: Sugars and Sweeteners Recommended Data." Table 13. http://www.ers.usda.gov/Briefing/Sugar/Data.htm

U.S. Department of Agriculture, 2010b, "Briefing Rooms: Sugars and Sweeteners Recommended Data." Table 13. http://www.ers.usda.gov/Briefing/Sugar/Data.htm

U.S. Department of Energy, 2011a, "Natural Gas Weekly Update." Independent Statistics and Analysis. U.S. Energy Information Administration. http://www.eia.doe.gov/oog/info/ngw/ngupdate.asp

U.S. Department of Energy, 2011b, "Cost and Performance Baseline for Fossil Energy Plants." Vol. 3a. *Low Rank Coal to Electricity: IGCC Cases*. National Renewable Energy Laboratory, Pittsburgh, PA. NETL-2010/1399.

Viskanta, R., Ungan, A., and Menguc, M., 1981, "Predictions of Radiative Properties of Pulverized Coal and Fly-ash Polydispersions," ASME paper no. 81-HT-24.

Vannice, M. A, 1975, "The Catalytic Synthesis of Hydrocarbons from H2/CO Mixtures over the Group VIII Metals: II. The Kinetics of the Methanation Reaction over Supported Metals," *Journal of Catalysis*, Vol. 37, pp. 462-472.

Voss, S.and Gould, G., 2001, "The Rankine Cycle: Workhorse of the Coal-fired Industry," Bruns and McDonnell: Public Company Papers.

Wabash River Coal Gasification Repowering Project, Final Technical Report, August 2000.

Waind, T., and Whitty, K., 2010, "Characterization of a Small Scale Slurry-Fed, Oxygen-Blown Entrained Flow Gasifier: How Injector Geometry Affects Flame Stability and Performance," 2010 International Pittsburgh Coal Conference, Istanbul, Turkey October 11 – 14, 2010.

Walker, P., Rusinko, F., Austin, L., 1959, "Gas reactions of carbon," *Advances in Catalysis,* vol. 11, pp. 133-221.

Wallace, S., Bartle, K., and Perry, D., 1989, "Quantification of Nitrogen Functional Groups in Coal and Coal Derived Products," *Fuel*, Vol. 68, pp.1450-1455.

Wang, T., Silaen, A., Hsu, H.W., and Lo, M.C., 2006, "Partial Load Simulation and Experiments of a Small Coal Gasifier," Paper 20-3, proceedings of the 23rd International Pittsburgh Coal-Gen Conference, Pittsburgh, Pennsylvania, Sept. 25-28, 2006.

Wang, T., Silaen, A., Hsu, H.W., and Shen, C.H., 2007, "Effect of Slag Tap Size on Gasification Performance and Heat Losses in a Quench-type Coal," Paper 37-4, proceedings of the 24th International Pittsburgh Coal-Gen Conference, Johannesburg, South Africa, Sept. 10-14, 2007.

Wang, T. and Silaen, A., 2009, "Numerical Investigation of Top Fuel Injection Design in a Coal Gasifier," Paper 26-2, Proceedings of the 26th International Pittsburgh Coal Conference, Pittsburgh, USA, September 20-23.

Wang, T., Silaen, A., Hsu, H.W., and Shen, C.H., 2010, "Investigation of Heat Transfer and Gasification of Two Different Fuel Injectors in an Entrained-Flow Gasifier," *ASME Journal of Thermal Science and Engineering Applications*, Vol.2, pp. 011001/1-10.

Wang, T., Silaen, A., Hsu, H.W., and Shen, C.H., 2011, "Top Fuel Injection Design in an Entrained-Flow Coal Gasifier Guided by Numerical Simulations," *ASME Journal of Thermal Science and Engineering Applications,* Vol. 3, pp. 011009/1-8.

Wang, T., Lu, X., Hsu, H.W., and Shen, C.H., 2011, "Investigation of the Performance of a Syngas Quench Cooling Design in a Downdraft Entrained-Flow Gasifier," Paper 45-2, proceedings of the 28rd International Pittsburgh Coal-Gen Conference, Pittsburgh, Pennsylvania, Sept. 15-18, 2011.

Wade J., Evar W, T., Bryan, L., Sunggyu, L., 2008, "Kinetics of Noncatalytic Water Gas Shift reaction in a supercritical Water Medium," American Institute of Chemical Engineers, AIChE Proceedings of the 2008 AIChE Spring National Meeting, April 2008: paper #139e.

Wiltsee, G., 2000, "Lessons Learned from Existing Biomass Power Plants." Report SR-570-26946. National Renewable Energy Laboratory, Golden, CO.

Wolfstein, M., 1969, "The Velocity and Temperature Distribution of One-Dimensional Flow with Turbulence Augmentation and Pressure Gradient," *Int. J. Heat Mass Transfer*, Vol. 12, pp. 301-318.

Wojtowicz, M., Pels, J., and Moulijn, J., 1995, "The Fate of Nitrogen Functionalities in Coal during Pyrolysis and Combustion," *Fuel*, Vol. 74, pp. 507-515.

Watanabe, H., and Otaka, M., 2006, "Numerical Simulation of Coal Gasification in Entrained Flow Coal Gasifier," *Fuel*, Vol. 85, pp. 1935-1943.

Watanabe, M., Mochiduki, M., Sawamoto, S., Adschiri, T., and Arai, K., 2001, "Partial Oxidation of N-Hexadecane and Polyethylene in Supercritical Water," *J. Supercrit. Fluids,* Vol. 20, pp. 257-268.

Wen, C., Chen, H., and Onozaki, M., 1982, "User's Manual for Computer Simulation and Design of the Moving Bed Coal Gasifier," Work performed under contract No AT21-81MC16474 for Morgantown Energy Technology Centre by West Virginia University, Morgantown, W.VA.

Westbrook, C., and Dryer, F., 1981, "Simplified Reaction Mechanisms for the Oxidation of Hydrocarbon Fuels in Flames," *Combustion Science and Technology*, Vol. 27, pp.31-43.

Wheeler, C., Jhalani, A., Klein, E., Tummala, S., and Schmidt, L., 2004, "The Water-Gas-Shift Reaction at Short Contact Times," *Journal of Catalysis*, Vol. 223, pp. 191–199.

Wu, Y., Zhang, J., Smith, P., Zhang, H., Reid, C., Lv, J., and Yue, G., 2010, "Three-Dimensional Simulation for an Entrained Flow Coal Slurry Gasifier," *Energy Fuels*, Vol. 24, pp. 1156–1163.

WRI, 2008, "Substitute Natural Gas from Coal, Western Research Institute," Laramie, WY, USA. http://www.westernresearch.org/business.aspx?ekfrm=204.

Xu, L., Lee, J., and Kim, H., 2007, "Comparison of Low Temperature Ash Deposition Determined by Theoretical and Experimental Method in Coal Gasifier Condition," World of Coal Ash (WOCA), May 7-10, 2007, Northern Kentucky, USA.

Yong, S., Gazzino, M., and Ghoniem, A., 2012, "Modeling the Slag Layer in Solid Fuel Gasification and Combustion – Formulation and sensitivity analysis." *Fuel*, Vol. 92, pp.162-70.

Yong, S., and Ghoniem, A., 2012, "Modeling the slag layer in solid fuel gasification and combustion – Two-way coupling with CFD," *Fuel,* Vol. 97, pp. 457-466.

Yoon, H., Wei, J., and Denn, M., 1978, "A Model for Moving-bed Coal Gasification Reactors," *AIChE Journal*, Vol. 24, pp. 885-903.

Zhang, H., and Modest, M., 2001, "Evaluation of the Planck-mean absorption coefficients from HITRAN and HITEMP databases," *Journal of Quantitative Spectroscopy and Radiative Transfer,* Vol. 73, pp. 649-653.

Zitney, S., 2010, "Process/equipment Co-simulation for Design and Analysis of Advanced Energy Systems," *Computers & Chemical Engineering*, Vol. 34, pp. 1532-1542.

Zhou, L., 1988, *Coal Combustion*, Hemisphere Publishing, New York.

Zwart, R., Boerrigter, H., Deurwaarder, E., Van der Meijden C., and Van Paasen. S., 2006, "Production of Synthetic Natural Gas (SNG) from Biomass,"

PUBLICATION DIRECTLY SUPPORTED BY THIS PROJECT

Refereed Journal Publications

Wang T. and Long, III H. A, "Performance and Economic Analysis of Biomass/Coal Co-Gasification IGCC Systems with Supercritical Steam Bottom Cycle and Carbon Capture," manuscript submitted to International Journal of Energy Research, 2013

Wang, T., Lu, X., Hsu, H. W., and Shen, C. H., "Design and Performance Evaluation of a Syngas Quench Cooling Section in a Downdraft Entrained-Flow Gasifier," manuscript submitted to ASME Journal of Thermal Science and Engineering Applications, 2013

Mazumder, A.K.M., Wang T., and Khan, J. R,"Design and Simulation of a Hybrid Entrained-Flow and Fluidized Bed Mild Gasifier , Part 1 – Design Considerations and Development of a Multiphase Model," manuscript submitted to ASME Journal of Thermal Science and Engineering Applications, September, 2013

Mazumder, A.K.M., Wang T., and Khan, J. R,"Design and Simulation of a Hybrid Entrained-Flow and Fluidized Bed Mild Gasifier , Part 2 – Case Study and Analysis, "manuscript submitted to ASME Journal of Thermal Science and Engineering Applications, Sept., 2013

Lu, X. and Wang, T., "Investigation of Radiation Models in Entrained-Flow Coal Gasification Simulation," International Journal of Heat and Mass Transfer, vol. 67, pp. 377–3922013

Khan, J.R. and Wang, T., "Implementation of a Demoisturization and Devolatilization Model in Multi-Phase Simulation for a Hybrid Entrained-Flow and Fluidized Bed

Mild Gasifier," International Journal of Clean Coal and Energy, 2013, vol. 2, pp. 35-53, http://dx.doi.org/10.4236/ijcce.2013.23005, Published Online August 2013 (http://www.scirp.org/journal/ijcce)

Chyou, Y.P., Chen, M. H., Luan, Y. T., and Wang, T., "Investigation of the Gasification Performance of Lignite Feedstock and the Injection Design of a Cross-Type Two-Stage Gasifier," Energy Fuels , vol. 27, pp. 3110−3121, dx.doi.org/10.1021/ef400394s, 2013

Lu, X. and Wang, T., "Water-Gas Shift Modeling in Coal Gasification in an Entrained-Flow Gasifier, Part 1: Development of Methodology and Model Calibration," DOI information: 10.1016/j.fuel.2013.02.023, Fuel, vol. 108, pp. 629-638, June 2013

Lu, X. and Wang, T., "Water-Gas Shift Modeling in Coal Gasification in an Entrained-Flow Gasifier, Part 2: Gasification Application," DOI information: 10.1016/j.fuel.2013.02.024, Fuel, vol. 108, pp. 620-628, June 2013

Long, III, H. A. and Wang, T., "A System Performance and Economics Analysis of IGCC with Supercritical Steam Bottom Cycle Supplied with Varying Blends of Coal and Biomass Feedstock," International Journal of Energy Research, Published online in Wiley Online Library (wileyonlinelibrary.com). DOI: 10.1002/er.3022, 2013

Khan, J.R. and Wang, T., "Implementation of a Non-Equilibrium Heat Transfer Model in Stage-Stacking Scheme to Investigate Overspray Fog Cooling in Compressors," International Journal of Thermal Sciences, vol. 68, pp. 63-78, June 2013

Luan, Y. T, Chyou, Y.P., and Wang, T., "Numerical Analysis of Gasification Performance via Finite-Rate Model in a Cross-Type Two-Stage Gasifier," International Journal of Heat and Mass Transfer, vol. 57, pp. 558-566, 2013

Silaen, A. and Wang, T.," Investigation of the Coal Gasification Process under Various Operating Conditions Inside a Two-Stage Entrained Flow Gasifier," ASME Journal of Thermal Science and Engineering Applications, Vol. 4, 021006/1-11, 2012.

Khan, J.R, Wang, T., and Chaker, M., "Investigation of Cooling Effectiveness of Gas Turbine Inlet Fogging Location Relative to the Silencer," ASME Journal of Engineering for Gas Turbine and Power, Vol. 132, 022001/1-9, Feb. 2012

Wang, T., Silaen, A., Hsu, H. W., and Shen, C. H., "Top Fuel Injection Design in an Entrained-Flow Coal Gasifier Guided by Numerical Simulations," ASME Journal of Thermal Science and Engineering Applications, Vol. 3, pp. 011009/1-8, March 2011.

Zhang, Z. and Wang, T., "Simulation of Combustion and Thermal-Flow inside a Petroleum Coke Rotary Calcining Kiln, Part 1: Modeling and Baseline," ASME Journal of Thermal Science and Engineering Applications, Vol. 2, 021006/1-8, 2010

Zhang, Z. and Wang, T., "Simulation of Combustion and Thermal-Flow Inside a Petroleum Coke Rotary Calcining Kiln, Part 2: Effect of Rotation on Tertiary Airflow Pattern and Combustion," ASME Journal of Thermal Science and Engineering Applications, Vol. 2, 021007/1-7, 2010

Wang, T., Silaen, A., Hsu, H. W., and Shen, C. H., "Investigation of Heat Transfer and Gasification of Two Different Fuel Injectors in an Entrained-Flow Gasifier," ASME Journal of Thermal Science and Engineering Applications, Vol.2, pp. 011001/1-10, March 2010

Silaen, A. and Wang, T., "Effect of Turbulence and Devolatilization Models on Gasification Simulation in an Entrained-Flow Gasifier" International Journal of Heat and Mass Transfer, Vol. 53, pp. 2074-2091, 2010

Conference Proceedings and Presentations

Lu, Y. and Wang, T., "Design of a Hybrid Entrained-Flow and Fluidized-Bed Mild Coal Gasifier Guided by Computational Fluid Dynamics," paper 39-4, Proceedings of the 30th International Pittsburgh Coal Conference, Beijing, September 16-19, 2013

Chen, M. H., Chyou, Y. P. and Wang, T. "Modeling of Coal Gasification in a Low-Temperature, High-Pressure Entrained-Bed Reactor" paper 3-2, Proceedings of the 30th International Pittsburgh Coal Conference, Beijing, September 16-19, 2013

Wang T. and Long, III H. A, " Performance and Economic Analysis of Biomass/Coal Co-Gasification IGCC Systems with Supercritical Steam Bottom Cycle, Part 1 – Post-combustion Carbon Capture," ASME paper IMECE 2012-87392, Proceedings of the ASME International Mechanical Engineering Congress & Exposition, November 9-15, 2012, Houston, Texas, USA

Wang T. and Long, III H. A, " Performance and Economic Analysis of Biomass/Coal Co-Gasification IGCC Systems with Supercritical Steam Bottom Cycle, Part 2 – Pre-combustion Carbon Capture," ASME Paper IMECE 2012-87392, Proceedings of the ASME International Mechanical Engineering Congress & Exposition, November 9-15, 2012, Houston, Texas, USA

Lu, X. and Wang, T., "Effect of Radiation Models on Coal Gasification Simulation," ASME Paper IMECE 2012-86997, Proceedings of the ASME International Mechanical Engineering Congress & Exposition, November 9-15, 2012, Houston, Texas, USA

Chyou, Y.P., Hwang, C. P., Luan, Y. T., and Wang, T., "Investigation of the Gasification Performance of Lignite Feedstock and the Injection Design of a E-Gas Like Gasifier," Paper 45-5, Proceedings of the 29th International Pittsburgh Coal Conference, Pittsburgh, Pennsylvania, Oct. 15-18, 2012

Lu, X. and Wang, T., " Investigation of Low Rank Coal Gasification In a Two-Stage Downdraft Entrained-Flow Gasifier, " Paper 27-3, Proceedings of the 29th International Pittsburgh Coal Conference, Pittsburgh, Pennsylvania, Oct. 15-18, 2012

Wang, T., Lu, X., Hsu, H. W., and Shen, C. H., " Investigation of Two-Stage Oxygen Feeding in a Downdraft Entrained-Flow Coal Gasifier, " Paper 21-1, Proceedings of

the 29th International Pittsburgh Coal Conference, Pittsburgh, Pennsylvania, Oct. 15-18, 2012

Long, III, H. and Wang, T., " Case Studies For Various IGCC Parameters Using Blended Coal/Biomass in Entrained-Flow Gasifiers and Supercritical Steam Bottom Cycles," Paper 45-1, Proceedings of the 29th International Pittsburgh Coal Conference, Pittsburgh, Pennsylvania, Oct. 15-18, 2012

Li, X. W. and Wang, T., "A Parametric Investigation of Various Integrated Gasification Combined Cycles with Carbon Capture," ASME paper GT2012-69519, Proceedings of ASME Turbo Expo2012, Copenhagen, Denmark, June 6-10, 2012

Long, III, H. A. and Wang T., "A System Performance and Economics Analysis of IGCC with Supercritical Steam Bottom Cycle Supplied with Varying Blends of Coal and Biomass Feedstock," ASME paper IMECE 2011-65749, Proceedings of the ASME International Mechanical Engineering Congress & Exposition, Nov. 11-17, 2011, Denver, Colorado

Mazumder, A.K.M., Wang T., and Khan, J. R," Design and Simulation of a Hybrid Entrained-Flow and Fluidized Bed Mild Gasifier , Part 1 – Design Considerations and Development of a Multiphase Model," ASME paper IMECE 2011-64473, Proceedings of the ASME International Mechanical Engineering Congress & Exposition, Nov. 11-17, 2011, Denver, Colorado.

Mazumder, A.K.M., Wang T., and Khan, J. R, " Design and Simulation of a Hybrid Entrained-Flow and Fluidized Bed Mild Gasifier , Part 2 – Case Study and Analysis," ASME paper IMECE 2011-64485, Proceedings of the ASME International Mechanical Engineering Congress & Exposition, Nov. 11-17, 2011, Denver, Colorado

Zhang, Z. and Wang T., "Investigation of Combustion and Thermal-Flow Inside a Petroleum Coke Rotary Calcining Kiln with Potential Energy Saving Considerations," ASME paper IMECE 2011-64643, Proceedings of the ASME International Mechanical Engineering Congress & Exposition, Nov. 11-17, 2011, Denver, Colorado

Chyou, Y.P., Hwang, C. P., Luan, Y. T., and Wang, T., "Numerical Analysis of Gasification Performance via Finite-Rate Model in a Cross-Type Two-Stage Gasifier," Paper 32-2, Proceedings of the 28th International Pittsburgh Coal Conference, Pittsburgh, Pennsylvania, Sept. 12-15, 2011

Khan, J.R. and Wang, T., "Development of a Devolatilization Model in Multi-Phase Simulation for a Hybrid Entrained-Flow and Fluidized Bed Mild Gasifier," Paper 32-3, Proceedings of the 28th International Pittsburgh Coal Conference, Pittsburgh, Pennsylvania, Sept. 12-15, 2011

Lu, X. and Wang, T., " Water Gas Shift Modeling of Coal Gasification in an Entrained-flow Gasifer," Paper 45-1, Proceedings of the 28th International Pittsburgh Coal Conference, Pittsburgh, Pennsylvania, Sept. 12-15, 2011

Wang, T., Lu, X., Hsu, H. W., and Shen, C. H., " Investigation of the Performance of Syngas Quench Cooling Design in a Downdraft Entrained Flow Gasifier," Paper 45-2, Proceedings of the 28th International Pittsburgh Coal Conference, Pittsburgh, Pennsylvania, Sept. 12-15, 2011

Long, III, H.A.. and Wang, T., "Case Studies for Biomass/Coal Co-Gasification in IGCC Applications," ASME Paper GT2011-45512, Proceedings of ASME Turbo Expo2011, Vancouver, Canada, June 6-10, 2011

Silaen, A. and Wang, T.," Investigation of Coal Gasification Process under Various Operating Conditions

Inside a Two-Stage Entrained Flow Gasifier," Paper 51-1, Proceedings of the 27th International Pittsburgh Coal Conference, Istanbul, Turkey, October 11-14, 2010

Chyou, Y.P., Hwang, C. P., Luan, Y. T., and Wang, T., "Numerical Simulation of the Gasification Process inside a Cross-Type Two-Stage Gasifier," Paper 51-5, Proceedings of the 27th International Pittsburgh Coal Conference, Istanbul, Turkey, October 11-14, 2010

Zhao, L. and Wang, T., "Simulation of Char Dust Combustion Inside A Pyroscrubber Downstream of a Petroleum Coke Calcining Kiln," Proceedings of the 14th International Heat Transfer Conference, paper IHTC14-23053, August 8-13, 2010, Washington D.C.

Zhang, Z. and Wang, T., "Simulation of Combustion and Thermal-Flow Inside a Petroleum Coke Rotary Calcining Kiln, Part 1: Modeling and Baseline," ASME paper IMECE2009-12634, proceedings of International Mechanical Engineering Congress and Exposition (IMECE), Lake Buena Vista, Florida, Nov. 13-19, 2009.

Zhang, Z. and Wang, T., "Simulation of Combustion and Thermal-Flow Inside a Petroleum Coke Rotary Calcining Kiln, Part 2: Effect of Rotation on Tertiary Airflow Pattern and Combustion," ASME paper IMECE2009-13252, proceedings of International Mechanical Engineering Congress and Exposition (IMECE), Lake Buena Vista, Florida, Nov. 13-19, 2009.

Zhao, L. and Wang, T., "Simulation of Combustion and Thermal-flow Inside a Pyroscrubber," ASME paper IMECE2009-12773, presented at the International Mechanical Engineering Congress and Exposition (IMECE), Lake Buena Vista, Florida, Nov. 13-19, 2009.

Wang, T., Silaen, A., Hsu, H. W., and Shen, C. H., " Numerical Investigation of Top Fuel Injection Design in a Coal Gasifier," Paper 26-2, proceedings of the 26tth International Pittsburgh Coal Conference, Pittsburgh, Pennsylvania, Sept. 21-24, 2009

Silaen, A. and Wang, T., "Comparison of Instantaneous, Equilibrium and Finite Rate Gasification Models in an Entrained Flow Coal Gasifier " Paper 14-3, proceedings of the 26th International Pittsburgh Coal Conference, Pittsburgh, Pennsylvania, Sept. 21-24, 2009

Wang, Q., Liu, P., Xu, X., Wang, B., and Wang., T., " A Parametric Study to Design an Effective Spray Cooling Deployment in an Entrained-Flow Coal Gasifier" paper 49-5, proceedings of the 25th International Pittsburgh Coal-Gen Conference, Pittsburgh, Pennsylvania, Sept. 29-Oct. 1, 2008

Wang, T., Silaen, A., Hsu, H. W., and Shen, C. H., "Investigation of Heat Transfer and Gasification of Two Different Fuel Injectors in an Entrained-Flow Gasifier," Paper 49-4, proceedings of the 25th International Pittsburgh Coal-Gen Conference, Pittsburgh, Pennsylvania, Sept. 29-Oct. 2, 2008

Silaen, A. and Wang,T., " Effect of Turbulence and Devolatilization Models on Gasification Simulation, " paper 19-3, proceedings of the 25th International Pittsburgh Coal-Gen Conference, Pittsburgh, Pennsylvania, Sept. 29-Oct. 2, 2008

Long, III, H. A. and Wang, T., "System Performance and Economic Analysis of a Coal/Biomass IGCC with Supercritical Steam Bottom Cycle," presented at the Industrial Energy Technology Conference (IETC), May 30 –June 1, 2012, New Orleans

Lu, X. and Wang, T., "Simulation of Gasification Process in an Air-Blown Two-Stage Entrained Flow Coal Gasifier," presented at the Industrial Energy Technology Conference (IETC), May 30 –June 1, 2012, New Orleans

Khan, J. R. and Wang, T., "Simulation of Coal Gasification in an Entrained-Flow Gasifier and a Fluidized Bed," presented at the Industrial Energy Technology Conference (IETC), May 18-19, 2011, New Orleans

Long, III, H.A. and Wang, T., "Co-Feeding Biomass and Coal in Integrated Gasification Combined Cycles (IGCC)," presented at the Industrial Energy Technology Conference (IETC), May 18-19, 2011, New Orleans

Wang, T., "Coal Gasification and Its Applications to Clean Energy," Emerging Information and Technology Conference (EITC), Massachusetts Institute of Technology (MIT), Boston, Aug. 5-7, 2009

Silaen, A. and Wang, T., “Analysis of Top-fuel Injectionin an Entrained-flow Coal Gasifier ,” presented at the Annual Technical Review Meeting, Clean Power and Research Consortium (CPERC), Southern University at Baton Rouge, August 28, 2009

Wang, T., "Clean Energy and Power Generation with Low or Negative Carbon Emission," Proceedings of the 2008 Modern Engineering & Technology Seminar, November 17-8, 2008, Taipei, Taiwan, ROC

Silaen, A. and Wang, T., “Investigation of Slag Tap Design and Fuel Injector Heat Transfer in a Coal Gasifier,” presented at the Annual Technical Review Meeting,

Clean Power and Research Consortium (CPERC), University of New Orleans, New Orleans, Oct. 31, 2009

Technical Reports

Lu, X. and Wang, T., "An Applied Numerical Simulation of Entrained-Flow Coal Gasification with Improved Sub-models," ECCC Report 2013-01, Energy Conversion and Conservation Center, University of New Orleans, August 2013

Lu, Y and Wang, T., "Computational Scheme Guided Design of a Hybrid Mild Gasifier," ECCC Report 2012-03, Energy Conversion and Conservation Center, University of New Orleans, August 2012

Wang, T. and Lu, X., "Investigation of Two-Stage Oxygen/Coal Slurry Feeding in a Downdraft Entrained-Flow Gasifier," ECCC Report 2011-02, Energy Conversion and Conservation Center, University of New Orleans, December 2011

Long, III, Henry A. and Wang, T., "Analysis of Biomass/Coal Co-Gasification for Integrated Gasification Combined Cycle (IGCC) Systems with Carbon Capture," ECCC Report 2011-01, Energy Conversion and Conservation Center, University of New Orleans

Kubek, D., Mhadeshwar, A., Rosenthal, J. and Wang, T. , "Progress Towards Cost-Effective H_2 Supply and Energy Sources for CO_2 Activation in Conversion Applications;" May 2011, a techno-economic report delivered exclusively to members of The Catalyst Group Resources' Carbon Dioxide Capture & Conversion (CO_2CC) Program. Details are available at: www.catalystgrp.com/php/tcgr_co2cc.php.

Mazumder, A. K. M. and Wang, T., "Development of a Simulation Model for Fluidized Bed Mild Gasifier," ECCC Report 2010-05, Energy Conversion and Conservation Center, University of New Orleans, November 2010

Silaen, A. K. and Wang, T., "Comprehensive Modeling and Numerical Investigation of Entrained-Flow Coal Gasifiers and Applications," ECCC Report 2010-03, Energy Conversion and Conservation Center, University of New Orleans, May 2010

Bridgeman, W., Chudasama, T. and Phan, S, and Wang, T. "Design of a Hydrodynamic Mild-Gasifier Model," ECCC Report 2010-01, Energy Conversion and Conservation Center, University of New Orleans, May 2010.

Long, H.A. and Wang, T., "Biomass/Coal Co-Gasification for IGCC Applications," ECCC Report 2009-06, Energy Conversion and Conservation Center, University of New Orleans, December 2009.

Li, X. and Wang, T., "A Parametric Investigation of Various Integrated Gasification Combined Cycle (IGCC) with Carbon Capture," ECCC Report 2009-04, Energy Conversion and Conservation Center, University of New Orleans, June 2009.

Khan, J.R. and Wang, T., " Fog Cooling, Wet Compression and Droplet Dynamics In Gas Turbine Compressors," ECCC Report 2009-01, Energy Conversion and Conservation Center, University of New Orleans, May 2009

Silaen, A and Wang, T., "Numerical Investigation of Top Fuel Injection Design in a Coal Gasifier," ECCC Report 2008-05, Energy Conversion and Conservation Center, University of New Orleans, December 2008

Zhao, L. and Wang, T., "Simulation of Combustion and Thermal-flow Inside a Pyroscrubber," ECCC Report 2008-02, Energy Conversion and Conservation Center, University of New Orleans, submitted to Rain CII Carbon, LLC, August 2008.

PATENTS: N/A.

Chapter 5
Louisiana State University (LSU)

Recipient Organization (Sub):	Louisiana State University
Partners:	Nicholls State University (Prime); Southern University; University of New Orleans; Tulane University
Technical Contact (Sub):	Dr. Sumanta Acharya, (225) 578-5809; acharya@me.lsu.edu
Business Contact (Sub):	Winona Ward; (225) 578-2701; wward@lsu.edu

Award Number:	DE-FC26-08NT01922
Project Title:	**Production and Utilization of Next Generation Fuels for Clean Power**
Project Period:	10/1/2008-9/30/2013

LSU is primarily involved in two tasks (identified as Tasks 4 and 5 in the original proposal) and are described below. These tasks are driven by the need for fuel flexibility for land based power generation, and the need to optimize the cooling that, in turn, affects the reliability of turbine components. In terms of fuel flexibility, the two main fuels explored are syngas and a representative biofuel such as ethanol.

Task 5: Fuel Flexibility-Combustion and Emission Characteristics of Next Generation Fuels

Syngas: role of hydrogen, fuel composition variability: *Under this task, we are investigating the effect of fuel composition in premixed combustor rigs and with simulation codes where the role of fuel composition can be effectively studied. Variable concentrations of hydrogen (H_2) and carbon monoxide (CO) in methane will be introduced to study the effect on the performance metrics of flame holding, flashback, auto-ignition, lean blow out, emissions, combustion efficiency and dynamics. Strategies for optimizing these metrics through suitable redesign of the fuel-air delivery system/nozzle will be examined. The research undertaken under this objective followed the taskline below:*

a. *Development of a predictive model for hydrogen combustion and validation*
b. *Numerical study of flashback behavior with hydrogen addition*
c. *Experimental study of lean blowoff with hydrogen addition*

Below, we summarize some key results with respect to the experimental study of LBO.

LBO: This experimental phase of the study focused on LBO (Lean Blow Out), extinction time scales and the factors responsible for the LBO and the detailed mechanistic understanding of this LBO behavior. The experimental study included synchronized OH-PLIF and high speed OH* imaging along with light intensity recording in a swirl-stabilized combustor configuration for both unconfined and confined hydrogen-blended methane flames with hydrogen levels ranging from 0% to 80% by volume. Conditions

close to LBO and during the LBO transient were monitored. The following major conclusions are observed (Zhu and Acharya, 2012, 2013).

1. Hydrogen addition lowers the LBO limit (lower than 0.2 in equivalence ratio), and for a given fuel composition, confined flames can burn at leaner conditions (nearly 0.1 leaner in equivalence ratio) compared to unconfined flames. The calculation of adiabatic flame temperatures and heat release rates based on LHV shows the significant increase in heat retention with hydrogen addition for unconfined flames which contributes to longer extinction times.
2. H_2 addition increases extinction time for unconfined flames, and reduces it for confined flames (Fig.1). These inverse trends appear to be correlated with the RMS fluctuations of OH* (Fig. 2).
3. In unconfined flames, the flames near LBO are stabilized along the inner shear layer between the relatively hot IRZ (Inner Recirculation Zone) and incoming swirling fresh reactant flow for all methane and hydrogen enriched cases tested. Periodic extinction and re-light events are noted for methane flames well ahead of the extinction transient, and are potentially associated with high RMS and straining rates leading to shorter extinction times. For hydrogen-enriched flames, the flame structure is relatively symmetric and stable, leading to reduced RMS of OH*, lowered heat release fluctuation, and therefore longer extinction time.
4. In confined flames, the flame front spans the IRZ for methane flames, and is relatively symmetric and stable in the early phases of extinction. For high hydrogen, the flame is within the IRZ due to the higher molecular diffusivity, and flame structure appears to be columnar with high hydrogen addition. Before extinction, the dominant columnar burning structure appears to be a helical swirling motion which results in high unsteadiness, leading to high OH* RMS, and a shorter extinction time.
5. In all the tested confined and unconfined flames, the final extinction occurs shortly after the reaction zone immediately above the center-body fails, indicating a significant effect of this flame root on the final extinction. It is suggested that the ability to better sustain this flame root might extend the LBO limit to leaner conditions.

The results of this study can provide guidance to a combustion designer. While no design optimization is done here to extend LBO or extinction times, the results of this study indicates that for confined flames, adding additional hydrogen with higher molecular diffusivity than methane causes the flame structure to be located within the IRZ. Thus extinction times are controlled by the flow dynamics in the IRZ. Suitable geometric design changes may be needed to control or alter such behavior.

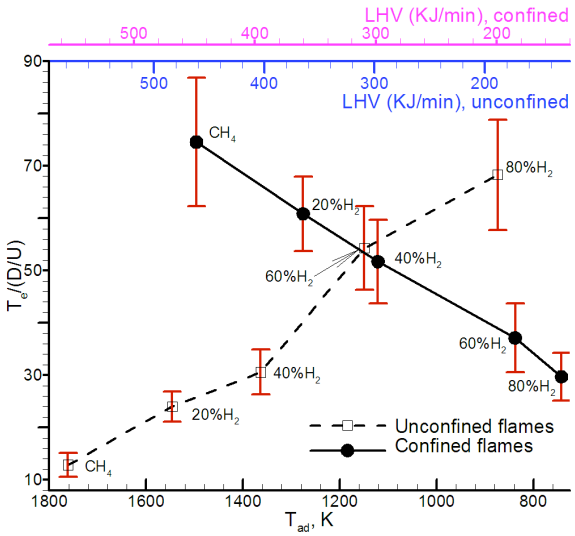

Figure 1. Estimated extinction time T_e normalized by the resident time D/U.

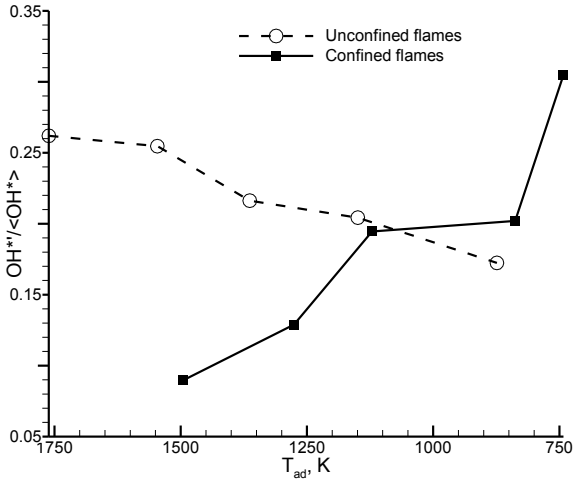

Figure 2. OH fluctuation.*

Biofuel Combustion: *The biofuel combustion study had two major tasks, both dealing with biofuels, and lowering the effective cost of utilization of biofuels to be competitive with the petroleum fuel costs. While the technology for producing biofuel exists today, the cost of production, and the relative cost of the biofuel to petroleum fuel, are the main barriers. The LSU study will focus on these barriers.*

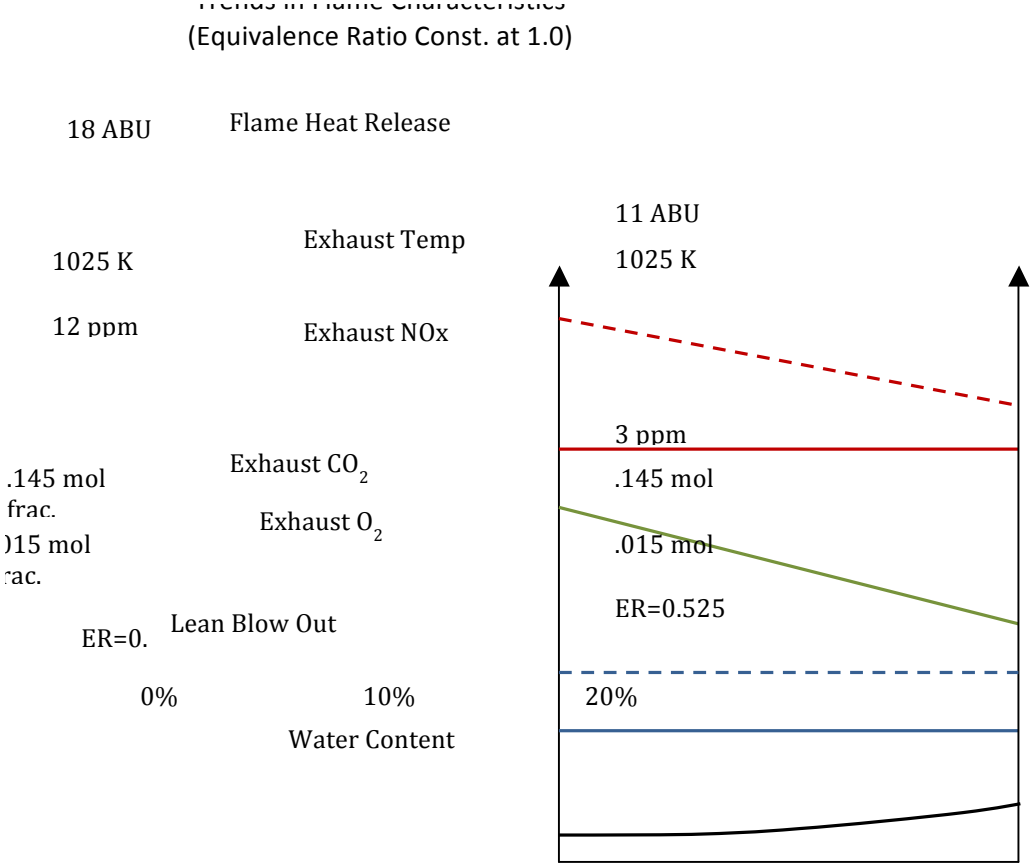

Figure 3: Schematic of the trends of water content on biofuels

Hydrous Biofuel Combustion: In one aspect of the study, we explored the use of hydrous biofuel such as ethanol, and studied the role of different levels of water on the combustion characteristics of ethanol. This was driven by the motivation of reducing bio fuel costs which are exacerbated by the costs associated with removing water.

The main conclusions are summarized below, and also shown in a graphical form in Figure 3.

- *Flame heat release was reduced with increasing water content*
- *Overall combustion efficiency was not adversely affected for fuels up to 20% water*
- *Heat release was more spatially distributed with hydrous fuels*
- *Exhaust temperature was not adversely affected by the addition of water*
- *Exhaust NOx was extremely low for all fuels but was reduced by water addition*

Nano-Metal-Boron Composites and Combustion: In the second aspect of the study, we explored the use of nano-metal additives on the ignition and combustion of boron nanoparticles in an ethanol flame. Adding high-density boron in the form of nano-particles is driven by the motivation of increasing the energy density of the biofuel (Btu/lbm) which is typically 60% of the petroleum fuel. Since the key metric to the consumer is $/Btu, by increasing the Btu/lbm through high-energy additives, it is anticipated that $/Btu will be reduced. As part of the DOE funded effort, easy-to-ignite metal additives were added to Boron to explore the desired goal of early ignition and combustion. By increasing fuel energy density the range of the energy device can be increased (engine can go a longer distance for the same amount of fuel). This can be of

significant cost-savings benefit in transportation applications particularly given the interest of using greater amounts of biofuels.

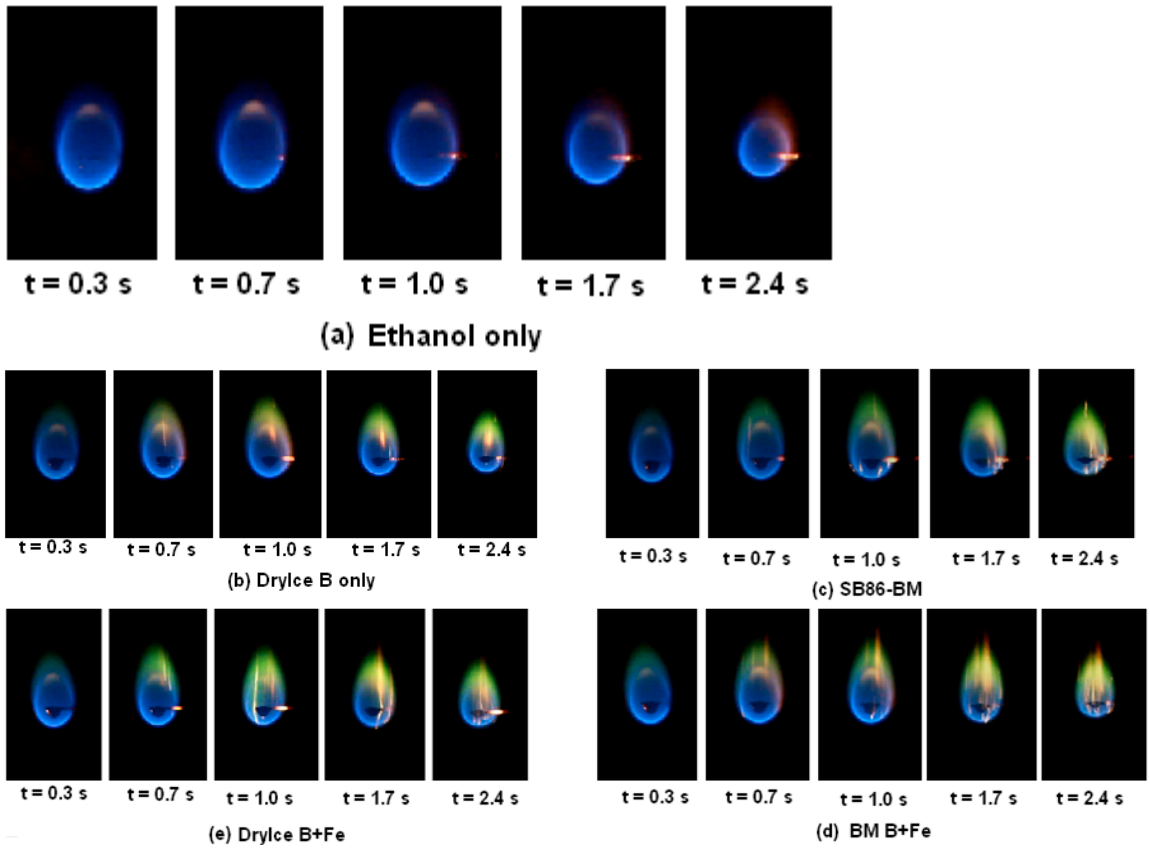

Figure 4: Pictures from the droplet combustion experiment; Ethanol is the blue color, boron is green.

Our initial effort was spent on looking at alternative additives to boron that will further reduce the ignition delay time. To this end, an iron-boron composite has been developed with the premise that iron, which has lower ignition temperature, will burn first leading to higher localized temperatures that are favorable for boron combustion. We have also explored a series of particle composites, with Al-B, Ti-B, Al-Ti-B, and Fe-B, in two different proportions. We have completed testing of these different composites (Karmakar and Acharya, 2013). We report a representative result below where droplet combustion experiments for ethanol only, ethanol plus boron (prepared two ways, straight ball-milled and ball-milled with dry ice that lowers potential surface oxidation), and ethanol plus boron-iron composite. The role of boron (green flame) can clearly be seen, as well as the importance of it's preparation. Also we observe that the presence of iron can be used to accelerate the boron ignition.

TASK B: Improved System Reliability & Performance with Next Generation Fuels

Under this task we have explored strategies for improved cooling and developing advanced material coatings that can extend the life of the components, improve

reliability and reduce the adverse impacts on performance associated with hot spots, thermal oxidation, corrosion, coating spallation, and other damage processes. We are exploring advanced cooling strategies that minimize coolant usage or improve the cooling effectiveness. Since nearly 20 percent to 25 percent of the process air is used for cooling, it represents a significant penalty, and it is of significant benefit to achieve any reduction of the coolant air or the more efficient use of this coolant air to minimize hot spots and the surface temperature, and to reduce temperature variability of the surface to minimize thermal stresses.

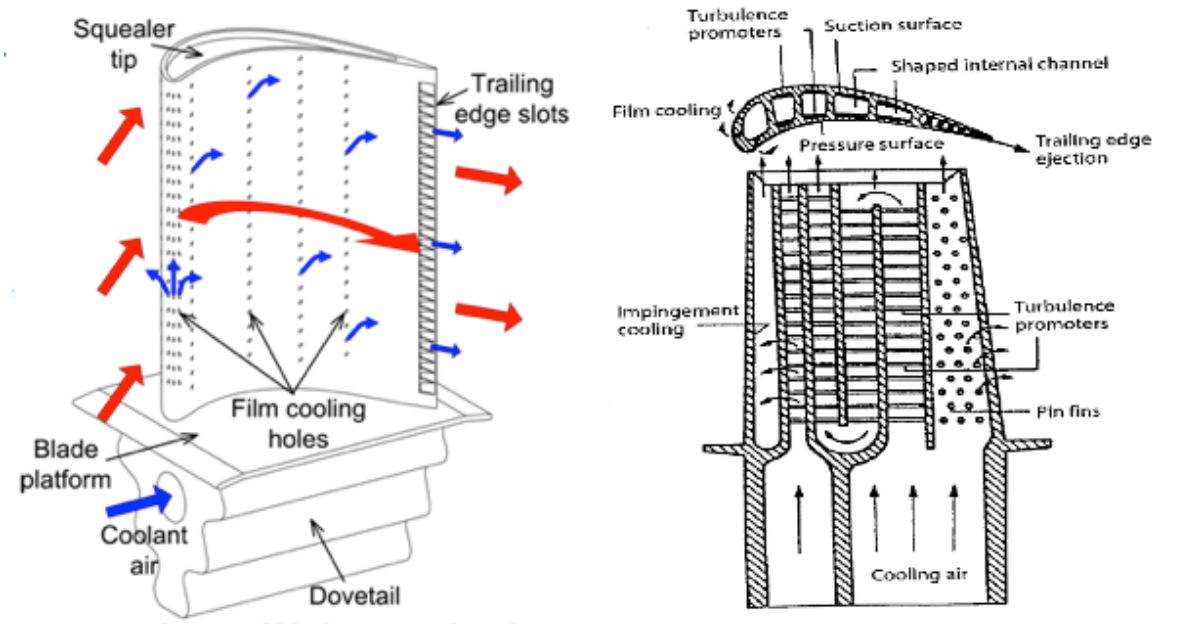

Conceptual view of blade external cooling

(from Liu, Siemens)

Conceptual view of blade internal cooling

(from Han, Texas A & M)

Figure 5: Schematic of Airfoil cooling strategies

In order to cool the airfoil, both internal cooling and external cooling strategies are employed. As shown in the Figure 5, internal cooling involves serpentine passages with rib turbulators or pin fins through which coolant air bypassed from the compressor is circulated. In film cooling, the coolant is discharged through array of coolant holes over the airfoil surface to provide a protective film over the surface.

In addition to cooling the airfoil internally and externally, a major challenge is to cool the endwalls, both along the hub and along the shroud. These regions see significant secondary flows, and therefore, enhanced losses and heat transfer. In the present work, we have explored both external and internal cooling of the airfoil with the key goal of optimizing and minimizing cooling effectiveness. Both numerical and experimental techniques have been explored toward this purpose.

External/Film Cooling of the Airfoil & Endwalls:

Over the last several quarters we have spent considerable effort in getting our simulation methodologies using LES for film cooling for both smooth and rough surfaces. We have convincingly demonstrated that our LES calculations are producing results in excellent agreement with measurements (Leedom, 2009; Leedom & Acharya, 2010; Kalghatgi & Acharya, 2013). This agreement between predictions and experiments are shown in Fig. 6 below.

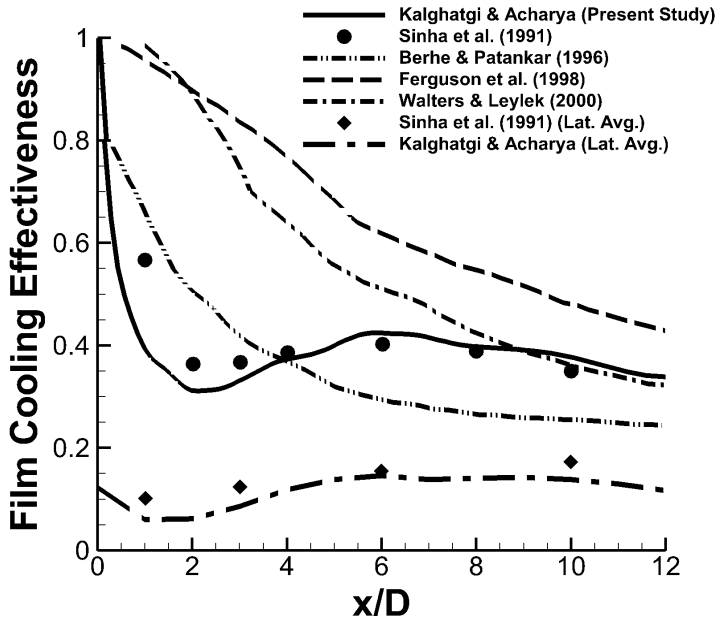

Figure 6: LES flow predictions of centerline cooling effectiveness (or non-dimensional surface temperature) and comparison with experimental data (symbols). Data and predictions for spanwise-averaged cooling effectiveness also shown (lower set of symbols and dash-dot-lines)

Modal analysis of the complete 3D flow and temperature field is carried out using a Dynamic Mode Decomposition (DMD) technique (Kalghatgi and Acharya, 2013). The modal frequencies are identified, and the specific modal contribution towards the cooling wall temperature fluctuation is estimated on the film cooling wall. The low and intermediate frequency modes associated with streamwise and hairpin flow structures are found to have the largest contribution (in-excess of 28%) towards the wall temperature (or cooling effectiveness) fluctuations. This is shown in the power spectral density of the near-wall thermal modes in Fig. 7. The high frequency Kelvin-Helmholtz mode contributes towards initial mixing in the region of film cooling hole away from the wall.

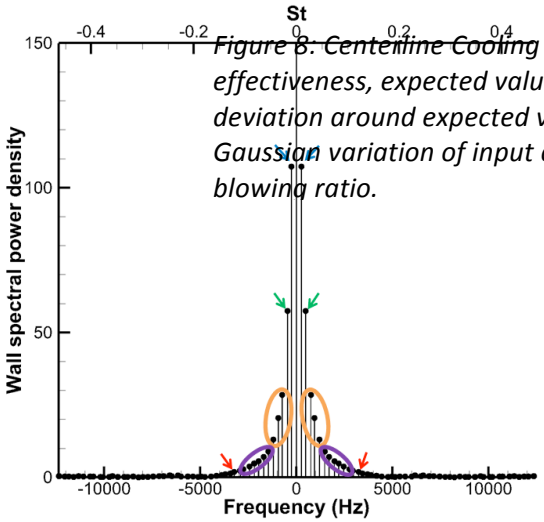

Figure 7: Power Spectral Density of near wall thermal field showing the importance low frequency near-wall modes in controlling surface temperatures.

Rough film-cooled surfaces are also of interest since Synas generated from gasification of coal and/or biomass has particulate contaminations that tend to deposit on hot surfaces and create surface roughness. The rough surface then interferes with the cooling and aerodynamics in the passage, and it is important for the designer to understand this effect. In trying to model roughness, a key problem is that the length scale associated with roughness is very small relative to the geometry, and it is not possible to resolve this roughness with a body fitted grid. Therefore alternative approaches have to be adopted. We have developed a combination of the roughness element model and the immersed boundary method approach (IBM) by which the effect of the surface roughness on the flow field can be effectively simulated. Kalghtagi and Acharya (2009) presented results that demonstrate that high surface roughness may improve film cooling behavior in the near field, but adversely impacts the cooling performance in the far field.

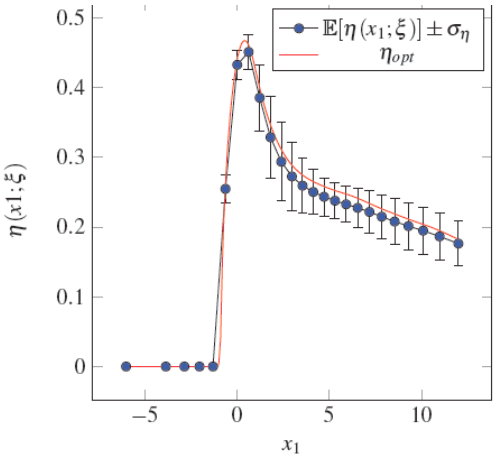

On the computational side, we have also used the response surface approach for quantifying the effect of pulsations on blowing ratio Babaee & Acharya, 2013a), and the role of uncertainty in blowing ratio on film cooling effectiveness (Babaee & Acharya, 2013b). As an example of a key result, the figure on the right shows the film cooling effectiveness (measure of the adiabatic surface temperature) plotted as a function of the downstream distance. Coolant injections is at x=0. The uncertainty bars reflect the variation in the cooling effectiveness resulting from the variation/uncertainty in the blowing ratio (Figure 8).

The other major effort deals with measurements in a realistic hot cascade tunnel consisting of a combustor, and nozzle guide vanes (Fig. 9). The facility is able to deal with about 4-5 lbm/s of air, and combustor exit temperatures in excess of 1200 degrees F. We have made measurements of the endwall temperatures for different blowing ratios with only the thermocouples and heat flux gages, and IR measurements (Post and Acharya, 2010).

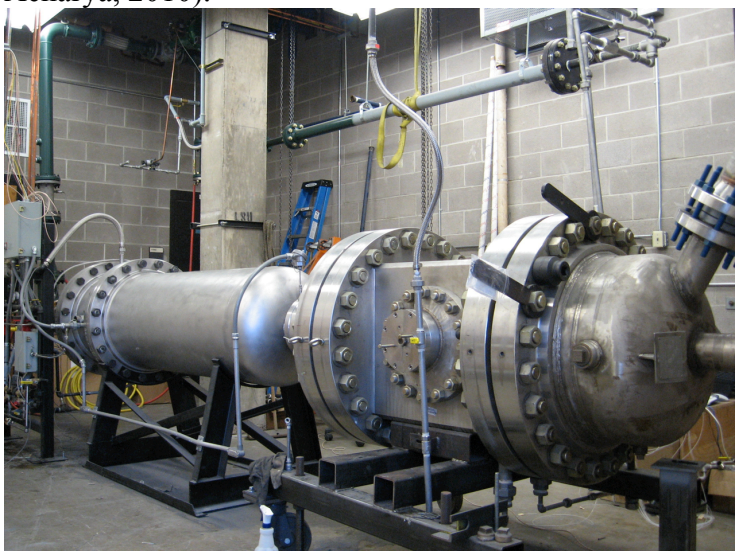

Figure 9: Picture of the hot nozzle-guide vane testing facility

On external cooling, an effort has also been initiated on blade tip cooling. This effort is both experimental and computational. The experimental facility is shown in the figure below (Fig. 10), and consists of a closed loop tunnel that is operated in a transient mode. The figure on the left shows the details of the rotor test section where the shroud is cooled by a distributed set of holes on the shroud.

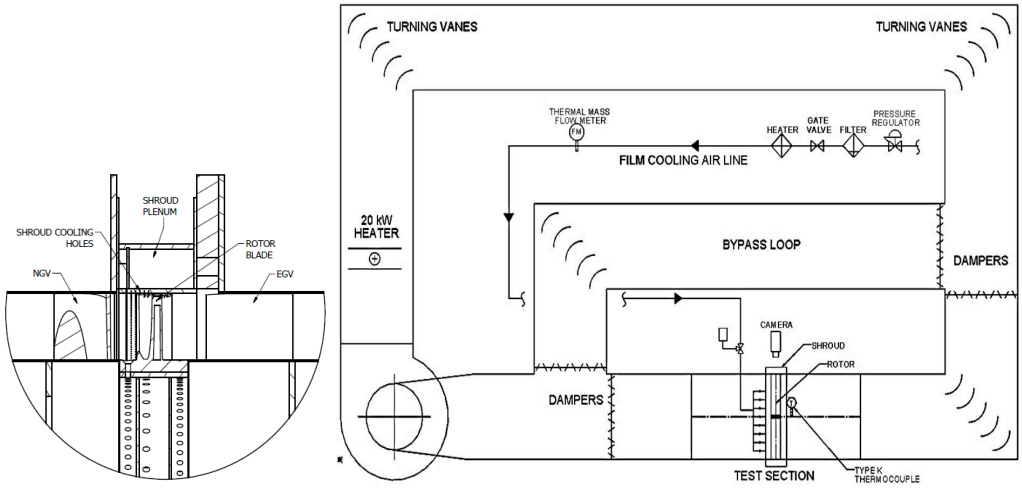

Figure 10: Schematic of the test loop for blade tip cooling with rotation. Figure on left shows the details of the test section.

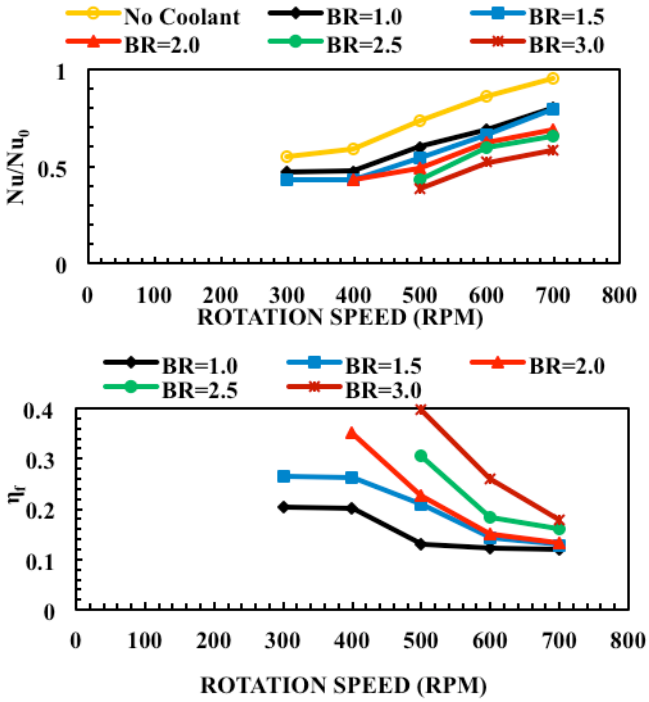

Fig. 11: Area-averaged Nusselt number ratio and cooling effectiveness as a function of the rotation speed and blowing ratio $(rV)j_{et}/(rV)_{crossflow}$ through the shroud holes

The cooling results (Fig. 11) show that increasing the blowing ratio increases the area-averaged film cooling effectiveness in the shroud hole region for all rotation speeds studied. The cooling effect further downstream of the injection hole locations is marginal indicating rapid mix-out of the coolant jets. Furthermore, increasing the blade rotation speed increases the area-averaged Nusselt numbers and decreases the area-averaged film cooling effectiveness in the shroud hole region for all blowing ratios studied. Additional results and discussions are given in Tamunobere et. al. (2014)

The computational part of the study has focused attention on the effect of rotation and tip coolant/PS coolant injection on tip and shroud cooling (Acharya & Moreaux, 2013). In this study it was observed that the relative motion between the blade and tip was the dominant effect and that rotation induced forces only had a secondary effect.

Internal cooling of turbomachinery airfoils:
Turbine airfoils are also internally cooled by circulating coolant air through serpentine passages in the airfoil, and as shown in Figure 5. The passages are turbulated to enhance heat transfer.

We have explored a number of innovations in this area including:

a. The use of swirl injection in the internal coolant passages. Several pitches and configuration of the angled swirl jets were attempted to find the best choice for heat transfer rate at the surface and pressure drop (Segura and Acharya, 2011).
b. The use of angled grooves and angled groove-rib combinations to enhance surface heat transfer (Saha and Acharya, 2013). Figure 12 below shows the significant enhancement in surface heat transfer possible with the angled groove and rib combinations. For a quantitative comparison, Figure 13 shows the Thermal Performance Factor (TPF) which is a ratio of heat transfer enhancement divided by a measure of the pressure drop enhancement for a range of different types of rib turbulators reported in the literature. The groove-rib turbulator proposed here)identified as angled groove-rib, or V-groove-rib) clearly is one of the best performing turbulator among those studied (Fig. 13).

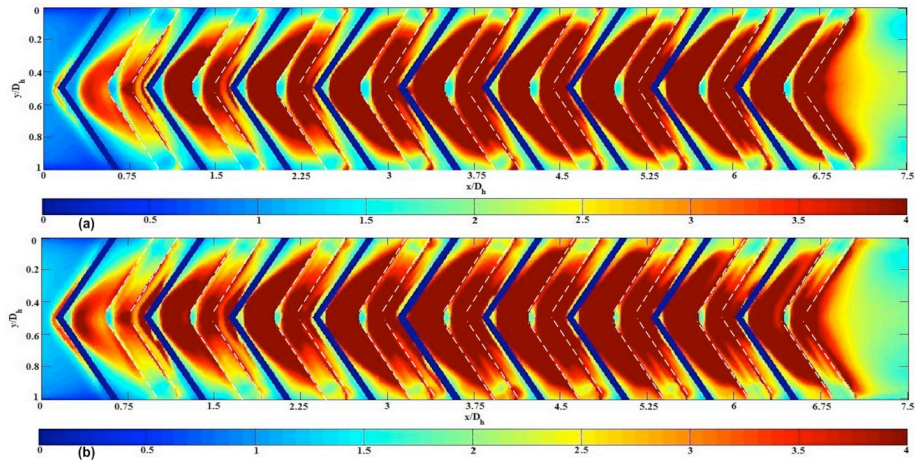

Figure 12: Contour plots of normalized Nusselt number for a V-groove-V-rib configuration at two different Reynolds numbers (top and bottom)

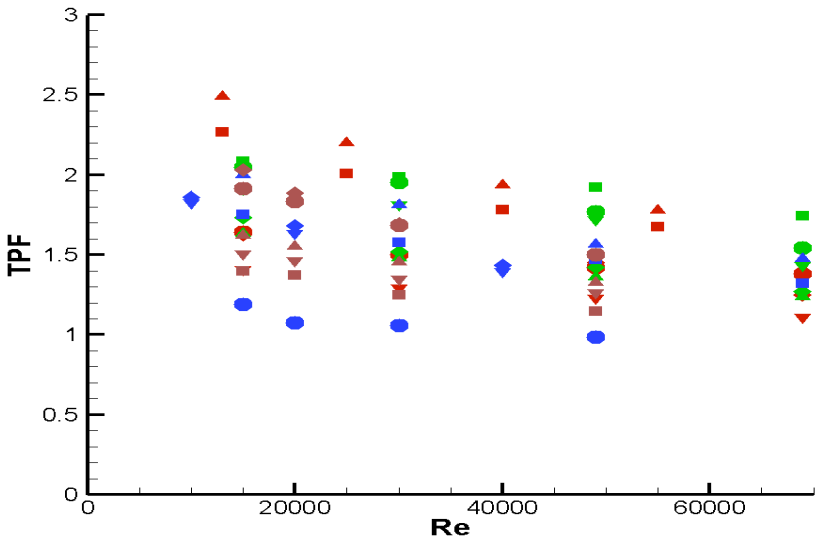

Figure 13: Thermal Performance Factor (TPF) for reported and current internal turbulated configurations. Current configurations are shown by red filled rectangles and red filled triangles.

Concluding Remarks

This report summarizes representative work done at Louisiana State University under the auspices of the DOE funded Clean Power and Energy Research Consortium. The studies were targeted at looking at the role of alternative next generation fuels (syngas, hydrogen, and biofuels) and in improving efficiency and reliability of the energy generation system using gas turbines. Details and related studies have not been included due to the length of the report. Readers can contact the author for additional information.

Archival Publications (also References in the text are included here)

Tuncer, O., Acharya, S., and Uhm, J. H., Dynamics, Flashback and NOx Emissions from Hydrogen-Enriched Methane Flames , *Intl. J. of Hydrogen Energy,* **Vol. 34**, Issue 1, January 2009, Pages 496-506

Sethuraman, E., Nikitopoulos, D., and Acharya, S., Mass/Heat Transfer in Rotating, Smooth High-Aspect Ratio (4:1) Coolant Channels with Curved Walls, *ASME Journal of Turbomachinery,* **Vol. 131**, Issue 2, 2009, pp. 15-24

De, A., and Acharya, S., Large Eddy Simulation of Premixed Combustion with a Thickened Flame Approach, *ASME J. of Engng. for Gas Turbines and Power*, Vol. 31, Issue 6, 2009, pp. 1501-1513

De, A., and Acharya, S., Large Eddy Simulation of a Premixed Bunsen Flame using a Modified Thickened Flame Model at Two Reynolds Numbers, *Comb. Sci. and Tech*., Vol. 181, 2009, pp. 1231-1272

De, A., Zhu, S., and Acharya, S., An Experimental and Computational Study of a Swirl-Stabilized Premixed Flame, *ASME J. of Engng. for Gas Turbines and Power*, Vol. 132, July 2010, No. 7

Kalghatgi, P., and Acharya, S., LES of Film Cooling on Roughened Surfaces, *Heat Transfer Research,* vol. 41, issue 7, 2010, pp. 753-768,

Acharya, S., Film Cooling Simulation and Control, *Heat Transfer Research*, vol. 41, issue 6, 2010, pp. 601-626

Zhu, S., and Acharya, S., An Experimental Study of Lean Blowout with Hydrogen Enriched Fuels In a Swirl Stabilized Premixed Combustor, *ASME J. of Engineering for Gas Turbines and Power*, vol. 134, Issue 4, #041507, April 2012, GTP http://dx.doi.org/10.1115/1.4004742

Zhou, F., and Acharya, S., Heat/Mass Transfer and Flow Structure on Four Dimple Shapes in a Square Internal Passage, *ASME J. of Turbomachinery*, Volume 134, Issue 6, November 2012, #061028 (13 pages) http://dx.doi.org/10.1115/1.4006315

De, A., and Acharya, S., Parametric Study of Upstream Flame Propagation in Hydrogen-Enriched Premixed Combustion: Effects of Swirl, Geometry and Premixedness, *Int. J. of Hydrogen Energy*, Vol. 37, Issue 19, October 2012, pp. 14649-14668, COMB35

De, A., and Acharya, S., Large Eddy Simulation of Flashback in Hydrogen-Enriched Premixed, *Int. J. of Hydrogen Energy*, Volume 37, Issue 22, November 2012, Pages 17294–17309 http://dx.doi.org/10.1016/j.ijhydene.2012.08.019, COMB36

Saha, K., and Acharya, S., Effect of Bend Geometry on Heat Transfer and Pressure Drop in a Two-Pass Turbine Coolant Square Channel, *ASME J. of Turbomachinery*, Volume 135, Issue 2, March 2013, #021035, http://dx.doi.org/10.1115/1.4006665

Breaux, B., Acharya, S., The Effect of Elevated Water Content on Ethanol Combustion, *Fuel*, http://dx.doi.org/10.1016/j.fuel.2012.07.051 Vol. 105, 2013, pp. 90-102

Saha, K., Acharya, S., and Nakamata, C., Heat Transfer Enhancement and Thermal Performance of Lattice Structures for Internal Cooling of Airfoil Trailing Edges, *ASME J. of Thermal Science and Engineering Applications*, Vol.5 Issue 1, March 2013, http://dx.doi.org/10.1115/1.4007277

Leedom, D., and Acharya, S., Large Eddy Simulations of Film Cooling Flows with Plenum Crossflow Effects, *ASME J. of Heat Transfer,* Volume 135, January 2013, Issue 1, 011010 (12 pages) http://dx.doi.org/10.1115/1.4007667

Saha, K., and Acharya, S., Bend Geometries in Internal Cooling Channels for Improved Thermal Performance, *ASME J. of Turbomachinery,* Vol. 135, No. 3, March 2013, # 031028, http://dx.doi.org/10.1115/1.4007582, GTHT62

Acharya, S., and Moreaux, L., Numerical study of the flow past a turbine blade tip: effect of relative motion between blade and shroud, *ASME J. of Turbomachinery,* 136, 031015 (2013) (9 pages), http://dx.doi.org/10.1115/1.4024842, GTHT63

Zhu, S., and Acharya, S., Flame Dynamics with Hydrogen Addition at Lean Blowout Limits, *ASME J. of Engng. For Gas Turbines and Power*, recommended for journal publication, December 2012, COMB 38

Saha, K., and Acharya, S., Heat Transfer Enhancement Using Angled Grooves as Turbulence Promoters, *ASME J. of Turbomachinery*, in press, doi: 10.1115/1.4025733, October 2013, GTHT64

Babaee, H., and Acharya, S., A Hybrid Staggered/Semi-staggered Finite Difference Algorithm for Solving Time-dependent Incompressible Navier-Stokes Equations on Curvilinear Grids", *Numerical Heat Transfer: Part B-Fundamentals*, Vol. 65, Issue 1, pgs. 1-26, 2014, CM23

Babaee, H., and Acharya, S., Effect of Uncertainty in Blowing Ratio on Film Cooling Effectiveness, *ASME J. of Heat Transfer*, Vol. 136, Issue 3, #031701, Nov. 2013, GTHT65

Babaee, H., and Acharya, S., Optimization of Forcing Parameters of Film Cooling Effectiveness, *ASME J. of Turbomachinery*, in press, doi: 10.1115/1.4025732, October 2013, GTHT66

Kalghatgi, P., and Acharya, S., Dynamic Modal Analysis and Flow Features from Large Eddy Simulations of a Film Cooling Jet, *ASME J. Turbomachinery*, accepted Nov. 2013, GTHT67

Articles in Refereed Conferences

Zhou, F., and Acharya, S., Heat Transfer in a Novel Internally-Finned heat Exchange Passage, *ASME Intl. Mech. Engng. Conference & Expo*, 2008, Boston, Nov. 2008, ASME IMECE 2008-68180

De, A., Zhu, S., and Acharya, S., An Experimental and Computational Study of a Swirl-Stabilized Premixed Flame, *ASME Gas Turbine Congress & Expo, 2009,* Orlando, June 2009, ASME GT 2009-60230

Zhou, F., and Acharya, S., Heat/Mass Transfer and Flow Structure on Four Dimple Shapes in a Square Internal Passage, *ASME Gas Turbine Congress & Expo, 2009,* Orlando, June 2009, ASME GT 2009-60240

Kalghatgi, P., and Acharya, S., LES of Film Cooling on Roughened Surfaces, ICHMT Conference on Gas Turbine Heat Transfer (Turbine-09), August 2009, Antalya, Turkey

Zhu, S., and Acharya, S., Role of Hydrogen Addition on Swirl-Stabilized Flame Properties, *ASME Gas Turbine Congress & Expo, 2010,* Glasgow, GT2010-23686, June 2010

Post, J., and Acharya, S., Density Ratio Effects on Endwall and Vane Film Cooling, *ASME Gas Turbine Congress & Expo, 2010,* Glasgow, GT2010-23680, June 2010

Segura, D., Acharya, S., Internal Cooling Using Novel Swirl Enhancement Strategies in a Slot Single Pass Channel, *ASME Gas Turbine Congress & Expo, 2010,* GT2010-23679, Glasgow, June 2010

Saha, K., and Acharya, S., Effect of Entrance Geometry on Heat Transfer in a Narrow (AR= 1:4) Rectangular Two Pass Channel with Smooth and Ribbed Walls, *ASME Gas Turbine Congress & Expo, 2011,* Vancouver, GT2011-46076, June 2011

Zhu, S., and Acharya, S., An Experimental Study of Lean Blowout with Hydrogen Enriched Fuels In a Swirl Stabilized Premixed Combustor, *ASME Gas Turbine Congress & Expo, 2011,* Vancouver, GT2011-46096, June 2011

Segura, D., and Acharya, S., Swirl-Enhanced Internal Cooling of Turbine Blades - Part 1 Radial Flow Entry, *ASME Gas Turbine Congress & Expo, 2011,* Vancouver, GT2011-46160, June 2011

Segura, D., and Acharya, S., Swirl-Enhanced Internal Cooling of Turbine Blades- Part 2 - 90 Degree Flow Entry, *ASME Gas Turbine Congress & Expo, 2011,* Vancouver, GT2011-46652, June 2011

Breaux, B., and Acharya, S., The Effect Of Elevated Water Content On Ethanol Combustion: A Feasibility Study, *Proceedings of the ASME 2011 Power Conference*, July 12-14, 2011, Denver, Colorado, POWER 2011-55301

Babaee, H., Acharya, S., A Semi-Staggered Numerical Procedure for Solving the Incompressible Navier-Stokes Equations on Curvilinear Grid, *ASME IMECE Conference, Denver,* CO, IMECE 2011-6331

Breaux, B., Karmakar, S., Zhu, S., and Acharya, S., Evaluation of Hydrous Ethanol Combustion in a Swirl-Stabilized Combustor, *ASME IMECE Conference, Denver*, CO, IMECE 2011-63688

Saha, K., and Acharya, S., Bend Geometries in Internal Cooling Channels for Improved Thermal Performance, *ASME Gas Turbine Congress & Expo, 2012,* Copenhagen, GT2012-69190, June 2012

Acharya, S., Moreaux, L., Numerical Study of Flow Past a Turbine Blade Tip: Effect of Relative Motion between Blade and Shroud, *ASME Gas Turbine Congress & Expo, 2012,* Copenhagen, GT2012-69192, June 2012

Zhu, S., and Acharya, S., Dynamics of Lean Blowout in Premixed Combustion with Hydrogen Addition, *ASME Gas Turbine Congress & Expo, 2012,* Copenhagen, GT2012-69189, June 2012

Saha, K., and Acharya, S., Heat Transfer and Pressure Drop in a Straight Lattice Structure with Coolant Bleeds, *ASME Summer Heat Transfer Conference*, Puerto Rico, July 8-12, 2012

H. Babaee, and Acharya, S., Optimization of Forcing Parameters of Film Cooling Effectiveness, *ASME Gas Turbine Congress & Expo, 2013,* San Antonio, GT2013-95636, June 2013

Saha, K., and Acharya, S., Heat Transfer Enhancement Using Angled Grooves as Turbulence Promoters, *ASME Gas Turbine Congress & Expo, 2013,* San Antonio, GT2013-95818, June 2013

Zhu, S., and Acharya, S., Flame Dynamics with Hydrogen Addition at Lean Blowout Limits, *ASME Gas Turbine Congress & Expo, 2013,* San Antonio, GT2013-95822, June 2013

Babaee, H., and Acharya, S., Effect of Uncertainty in Blowing Ratio on Film Cooling Effectiveness, *ASME Summer Heat Transfer Conference, 2013*, Minneapolis, HT 2013-17159, July 2013

Kalghatgi, P., and Acharya, S., Dynamic Modal Decomposition Analysis of Simulations for an Inclined Film Cooling Jet, *ASME Summer Heat Transfer Conference, 2013*, Minneapolis, HT 2013-17160, July 2013

Karmakar, S., and Acharya, S., Role of nano-metal composites in promoting Boron combustion in ethanol flames, 11th ISHMT/ASME Heat and Mass Transfer Conference, Kharagpur, India Dec 28th-31st 2013.

Kalghatgi, P., and Acharya, S., Improved Film Cooling Effectiveness With A Round Film Cooling Hole Embedded In Contoured Crater, *ASME Gas Turbine Congress & Expo, 2014, Dusseldorf,* GT2014-26600, June 16-20, 2014

Saha, K., Acharya, S., Effect Of Entrance Geometry and Rotation On Heat Transfer In A Narrow (AR=1:4) Rectangular Internal Cooling Channel, *ASME Gas Turbine Congress & Expo, 2014, Dusseldorf,* GT2014-26602, June 16-20, 2014

Tamunobere, O., Drewes, C., and Acharya, S., Heat Transfer to an Actively Cooled Shroud with Blade Rotation, *ASME Gas Turbine Congress & Expo, 2014, Dusseldorf,* GT2014-27103, June 16-20, 2014

CHAPTER SIX
Southern University, Baton Rouge
ADVANCED MATERIAL COATINGS FOR GAS TURBINE

Technical Contact: Professor Patrick F. Mensah, 225-771-4193 Fax: 225-771-4877, patrick_mensah@subr.edu
Business Contact: Brian Bell, 225-771-3722, brian_bell@subr.edu
Southern University and A&M College

SUMMARY

The overall objective of the project tasks at Southern University was to study the effects of addition of oxygen reactive elements (RE) nanoparticles such as hafnium (Hf) in the bond coat materials as well as addition of refractory element such as gadolinium to Yttria-stabilized zirconia (YSZ) powder in forming specialized air plasma spray (APS) TBC top coat microstructures. The goal was to develop coating materials that could be used to enhance the superalloy substrate material (IN738) for increased power output and efficiency in advanced gas turbine using next generation fuels. Thus, during the project period 2008-2013, the focus of research activities has been on the development, property characterization and performance testing of plasma spray processed TBCs coating microstructures. The developed and processed TBCs were tested for their thermo-physical, oxidation, and mechanical properties to investigate minimizing insulation capability maximizing endurance properties. The effects of thermal cycling of the processed TBCs in this work were also tested at elevated temperatures for reliability and durability. Three tasks undertaken by researchers at Southern University in collaboration with researchers at Louisiana State University were: i) Development of APS advanced novel thermal barrier coatings, ii) Thermo-physical properties experimental characterization, and iii) Characterization of effects of microstructures and comparative thermal cycling and spallation studies. The investigations undertaken in this project included education and training of undergraduates and graduate students as well as post-doctoral research associates. The outcomes of the research activities include the following:

Refereed publications:

- A computational approach to more accurately model and simulate thermal transport through thin micro-scale materials such as TBCs was developed based on hyperbolic heat diffusion and published in the Transactions of The ASME Journal of heat Transfer[1];
- A study on high temperature oxidation interfacial growth kinetics in TBCs with bond coatings of NiCoCrAlY+Hf published in Journal of Material Science and Engineering A^2 focuses on the potential use of Hf to retard the growth of alumina layer in TBCs.

Education and workforce development outcomes:

- Two post-doctoral research associates have been engaged in the research activities.

- One PhD graduate and six master of engineering graduates successfully completed their dessetation[34] and thesis [35-40]research work. Their work also resulted in several conference proceeding publications and presentations. Several undergraduates were also engaged in this work as well as postdoctoral research associates.

WORK STATEMENT

The higher inlet temperatures required for improved efficiency in advanced gas turbines can be engineered by the use of processed thermal barrier coatings (TBCs) on directionally solidified or single crystal blades produced by advanced casting techniques. Processed TBCs generally consist of a ceramic top coating, a metallic bond coating, and a thermally grown oxide (TGO) layer deposited on a super alloy. The bond-coat is typically a platinum-modified nickel aluminide or an M–Cr–Al–Y (where "M" represents, Co, Ni, Fe, or mixed combination), employed to improve the adhesion between the ceramic top-coat and the substrate. Although significant advances have been made in improving the durability of TBCs for turbine engine components, such coatings are still susceptible to various types of damage, including objects ingested by the engine, erosion, oxidation, and attack from environmental contaminants. It is therefore, necessary to modify the chemical composition or coating microstructure of TBCs to improve its' durability to withstand erosion, high temperature oxidation and impact loading. There is also a need for TBCs with reduced thermal conductivity for insulation.

In an effort to achieve an enhanced prime reliant TBC system that will boost propulsion and energy systems' capability and efficiency, the research group at southern University proposed studying the effects of addition of oxygen reactive elements (RE) nanoparticles such as hafnium (Hf) in the bond coat materials as well as addition of refractory element such as gadolinium to Yttria-stabilized zirconia (YSZ) powder in forming specialized air plasma spray (APS) TBC microstructures. Therefore, the **objective** of this task focuses on investigating issues dealing with the development, thermo-physical properties measurements and performance characterization of the effects of nano-particulate YSZ powder used in air plasma spray (APS) coated microstructures This project was conducted in three phases given below.

First and second phases10/1/2008 -12/31/2010

Task 6 Advanced Material Coatings

Subtask 6.1 Development of Air plasma spray (APS) advanced novel thermal barrier coatings

Subtask 6.2 Thermo-physical properties experimental characterization

Subtask 6.3 Characterization of effects of microstructures and comparative thermal cycling and spallation Studies

Third Phase 1/1/2011-9/30/2013

Task 8 Advanced Material Coatings

Subtask 8.1 Development of APS advanced novel thermal barrier coatings
Subtask 8.2 Thermo-physical properties experimental characterization and in-service performance modeling.
Subtask 8.3-Characterization of effects of microstructures and comparative thermal cycling and spallation studies.
The above tasks are in line with prior stated activities in proposed plan of studies conducted in this research.

Task 6: Advanced Material Coatings

INTRODUCTION

Since the advent of TBCs over forty years ago, users have constantly strived to improve performance of air plasma sprayed coatings. In particular, the role of TBC microstructures in contact with deleterious by products of combustion has been of significant interest in order to increase the life, insulating, and reliability of materials used in turbine hot path components for advanced applications at elevated temperatures.
This project focuses on the development, performance, and testing of plasma spray processed TBCs coating microstructures of novel thermal barrier coatings materials in collaboration with Louisiana State University. Proposed plasma spray processed TBCs using yttria stabilized zirconia with additions of alumina, hafnia, and gadolinium for minimizing oxidation and thermal conductivity have been tested for thermal-physical properties evaluations, and microstructural characterizations. Thermal cycling endurance studies at elevated temperature have also been conducted to investigate reliability/durability of these TBC materials. Thermal performance modeling and simulation has also been undertaken as part of this project.

In what follows are extended abstract versions of some of the accomplishments. The details can be found in refereed publications, conference proceedings, PhD dissertation, and master's thesis documents of our students listed at end of this report. The results on the approach undertaken to develop, process and characterize the properties of gadolinium zirconate functionally gradient nano-structured thermal barrier coatings on Inconel superalloy substrate (IN738) are presented. Part **A** discusses thermo-mechanical properties and thermal cycling behavior of gadolinium zirconate $Gd_2Zr_2O_7$ (GZ) based thermal barrier coatings (TBCs) investigated in this study in comparison to conventional yttria-stabilized zirconia (YSZ) coatings. It also presents results focusing on coefficient of thermal expansion (CTE) measurements, thermal cycling tests, measured elastic properties and porosity of the multilayered GZ/YSZ TBCs deposited by atmospheric plasma spraying (APS) on an Inconel 738 (IN738) superalloy substrate. In part **B** thermo-physical properties at elevated temperatures of potential YSZ+GZ double layer TBC coatings being developed by the investigators at Southern University are presented. The

thermo-physical properties (thermal diffusivity, thermal conductivity and specific heat capacity) of test samples are measured as functions of specimen temperature (400 to 1100^{o}C) using the Laser Flash.

A. Thermo-mechanical study of the role of $Gd_2ZR_2O_7$ (GZ) in improving life of YSZ AND GZ double layered thermal barrier coatings

Due to the sintering and phase transformation at higher temperatures YSZ is limited to work under 1200^{o}C **[**1, 2, and 3**]**. Furthermore, TBC failure is known to typically occur by spallation of the ceramic, at the bond coat – TBC interface independent of processing technology [4 - 5]. Therefore the local stress state at the interface plays an important role in TBC life time. Two important factors affecting this stress state are; growth stresses due to bond coat oxidation and thermal expansion mismatch between the bond coats, thermally grown oxide (TGO) and the ceramic top coat [4-6]. Other factors include: global loading conditions, geometrical factors (such as interface roughness and imperfections) and mechanical properties of bond coat. Finite element models focusing on various combinations of these factors have been studied and shown that although the coefficient of thermal expansion plays a huge role in the interface stresses, failure is complex; influenced by a combination of many factors still being studied.

Rare-earth zirconates with general formula $M_2Zr_2O_7$ (M=rare earth) with lower thermal conductivity and higher phase stability than YSZ appear to be promising candidates as alternative TBC ceramics. Gadolinium Zirconate ($Gd_2Zr_2O_7$, GZ) shows high thermal stability and can maintain lower thermal conductivity (1.6 W. (m.K)$^{-1}$at 700^{o}C) compared to YSZ (2.3 W. (m.K)$^{-1}$at 700^{o}C) [1]. However due to lower coefficient of thermal expansion (CTE) of GZ (8.1~10.5 x10^{-6}K^{-1} at 200~1000^{o}C) [7] than YSZ (11.5 x10^{-6}K^{-1} at 200~1000^{o}C) [8] the thermal cycling life of GZ TBCs is much shorter than YSZ TBCs. The primary objective of this study is to investigate and analyze the thermal cycling life and mechanical properties of functionally graded YSZ+GZ double layer TBC coatings and compare them to single layer GZ and YSZ TBCs for advanced gas turbine applications at elevated temperatures.

In a preceding study, this research group conducted studies that focused on the thermal cycling tests on pure GZ coatings, GZ and YSZ composite coatings, double layered GZ/YSZ coatings, and pure YSZ coatings prepared [9]. The results showed better thermal cycling life of the GZ/YSZ double layer structure compared to other tested GZ based TBCs. That study however was not comprehensive in varying amount of GZ /YSZ composition. In addition, the thermo-mechanical properties were not characterized. Properties like coefficient of thermal expansion (CTE), hardness and young's modulus which leads to thermal stresses should be carefully investigated before a material is used for the top coat application.

EXPERIMENTAL

Materials: The samples used in this study are prepared using atmospheric plasma spray (APS) standard (STD) coating process instrumentation available at Materials Solution International, Houston, TX. The Bond coat NiCrAlY-Hf and the top coat YSZ/GZ - $Gd_2Zr_2O_7$ powder (-325 MESH) were sprayed on grit blasted and tumbled disc shaped IN738 superalloy substrates 12.7 mm in dia. x 3 mm thickness. The bond coat composition used for the preparation of these samples was standard Sulzer Metco powder of nominal composition Ni-22Co-17Cr-12.5Al-0.25Hf-0.4Si-0.6Y (weight %). The top coat powders used were variations of 7.65wt%Y_2O_3-ZrO_2 and $Gd_2Zr_2O_7$ mixtures. Single and multilayer TBC samples of different compositions of YSZ and GZ were used to prepare the functionally graded top layer of multilayer samples for the experimental studies as shown in Table 1.

Plasma Spray Processing Parameters: All the samples were sprayed using a SG-100 air plasma spray gun with internal powder feed injection. The samples were sprayed using a FANUC 710i robot for precise gun-to part motion and for repeatability of process. The TBC systems were used for measurements of CTE values, elastic property measurements and thermal cycling behavior. The test specimens in our processing of APS TBC systems have included two different batches of 300 μm and 600 μm total top coat thickness; and an additional 1200 μm thickness of top coats used for CTE measurements as per instrument operating specifications.

The symbols in Table1 indicate (a) 1200μm thickness topcoat samples used for CTE testing, (b) 600 μm thickness top coat samples used for elastic property measurement testing and (c) 300 μm thickness top coat samples used for thermal cycling tests. All the double layered TBC systems have a bottom layer of 100% YSZ and a top layer of functionally graded GZ/YSZ ceramic coating of different GZ compositions.

TABLE 1: TEST MATRIX FOR APS COATINGS FOR DOUBLE LAYERED YSZ AND GZ TBC SPECIMENS

Coating Type- Single Layer
(1) 100% YSZ Top Coating (a, b, c)
(2) 100% GZ Top Coating (a, b, c)

Coating Type – Double Layer [Bottom layer of each system is 100% YSZ] [Top layer of each system is α % GZ/ 100- α % YSZ]	
(3) 10%GZ/YSZ (c)	Top Layer : 10%GZ+90%YSZ
	Bottom Layer : YSZ
(4) 25%GZ/YSZ (b, c)	Top Layer : 25%GZ+75%YSZ
	Bottom Layer : YSZ
(5) 30%GZ/YSZ (a)	Top Layer- 30%GZ+70%YSZ
	Bottom Layer : YSZ
(6) 50%GZ/YSZ (a, b, c)	Top Layer : 50%GZ+50%YSZ
	Bottom Layer : YSZ
(7) 70%GZ/YSZ (a)	Top Layer : 70%GZ+30%YSZ
	Bottom Layer : YSZ
(8) 75%Gz/YSZ (b)	Top Layer : 75%GZ+25%YSZ
	Bottom Layer : YSZ

Coefficient of Thermal Expansion (CTE) Measurements

To facilitate further studies on TBC failure, the CTEs of topcoats were measured. The samples studied were: 100%YSZ, 100% GZ, 30%GZ/YSZ, 50%GZ/YSZ, and 70%GZ/YSZ ceramic topcoats. The sizes were approximately 1.2 mm thicknesses with a 0.25 inch diameter. The CTEs of the TBC ceramics were measured using a high-temperature dilatometer (Netzsch DIL402C). The samples were held in place by a 12 mm alumina spacer that was used initially to calibrate the dilatometer. The measurements were made from room temperature (20°C) up to 1250°C at a heating rate of 5°C/ min in argon atmosphere. The CTE was measured on three different samples of the same material, and the average of all three at each temperature was taken. The result at each temperature is displayed in 1/K.

Elastic Properties Measurements

Hardness and Young's modulus property measurements were carried out with TI-900 Tribo-indenter using a 3 segment Quasi-static load function with respect to force and time selection considering the begin force, end force, segment time. Each test indentation is performed on the polished cross section specimens. Also the TBCs specimens after the thermal cycling testing were evaluated by SEM microstructural evaluations along with porosity characterization using Poremaster characterization equipment. Results are presented and analyzed to study the role of double layered TBC specimens.

Thermal Cycling Apparatus and Procedures

Thermal cycling tests were carried out in a CM 1700 bottom-loading programmable furnace using a 1.45 hour thermal cycle with ramping from room temperature to 1100^{o}C in 30 minutes, and isothermal soaking at 1100^{o}C for 60 minutes, followed by cooling to room temperature in 15 minutes as shown in Figure 6.1.

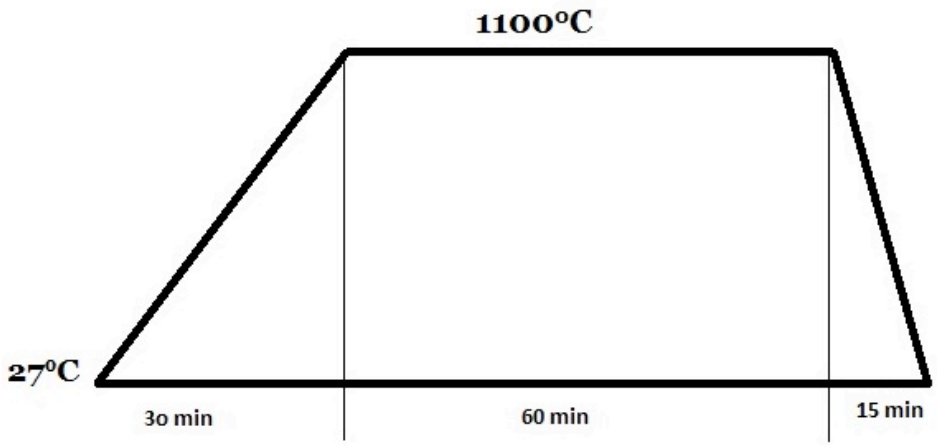

Figure 6.1: Temperature profile of the thermal cycling tests

Porosity Measurements and Structural Characterization

The voids in the test samples are filled with another probe material, either gas (helium or nitrogen) or a liquid (mercury or water) by method called intrusion porosimetry. Potentially, the probe material's volume is measured as a function of the filling pressure. The instrument's ability to calculate the porosity values is based on mercury intrusion porosimetry which involves the intrusion of a non-wetting fluid (mercury) into the specimen's void by increasing the fluid pressure up to 33,000 psi. This instrument is capable of measuring the total volume of mercury intruded into the sample and the bulk volume of the sample using the following equation (Poremaster-33 equipment manual, 2006-2007):

$$Porosity\ (\%) = \frac{V_t}{V_b}\ x\ 100$$

Where V_t is the total volume of mercury intruded and V_b is the bulk volume of the sample. The SEM evaluations were carried out to analyze the failure behavior on selected cross-sections of TBC samples after thermal cycling at 1100^{o}C.

RESULTS AND DISCUSSION

Results of Coefficient of Thermal Expansion (CTE) Measurements

Coefficient of thermal expansion (CTE) values of the tested specimens in Figure 6.2 show results of the experimental characterization of CTE properties of samples processed in this study. Trends of the data in Figure 6.2 are summarized as follows:

100% YSZ sample starts out with the lowest CTE at 22°C and gradually increases to the highest CTE for temperature range: ~200°C - 600°C. The 50%GZ/YSZ (double layer) starts out higher than 100%YSZ but does not become comparable until temperatures ~400°C - 800°C beyond which it overtakes 100%YSZ up to 1250°C. The 70%YSZ/GZ behaves similar to 50%GZ/YSZ starting out with the lowest CTE until 800°C where it catches up to YSZ and beyond which it overtakes YSZ as well as 50%GZ/YSZ.

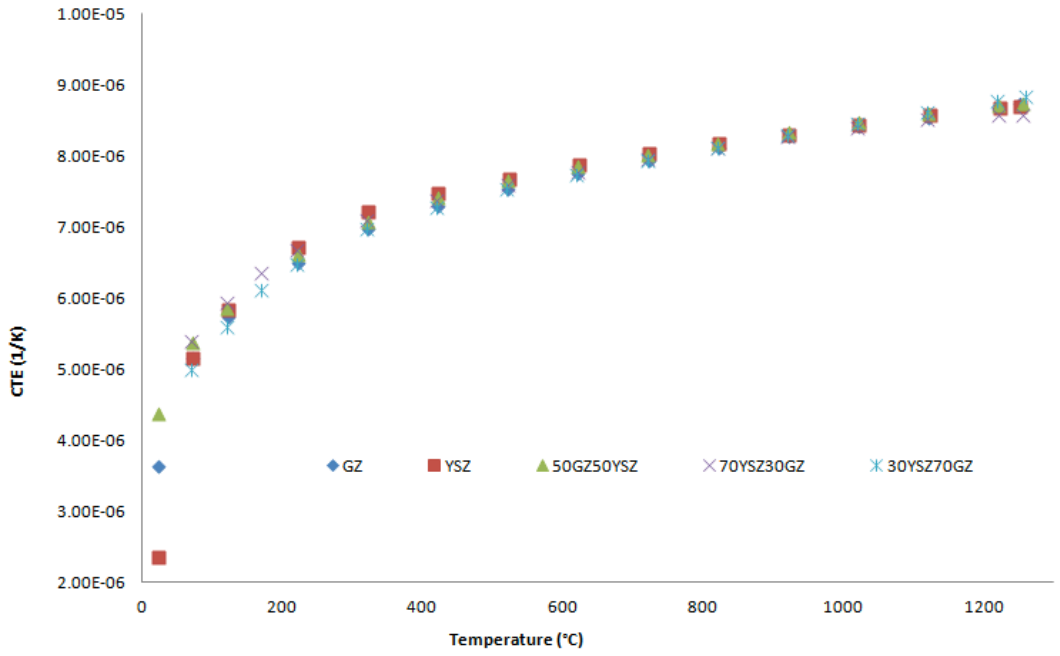

Figure 6.2: Measured Coefficient of Thermal Expansion of various TBC Ceramics

Results of Elastic Properties Measurements

The measurements of hardness and Young's modulus for selected TBC systems are reported in Figure 6.3a and Figure 6.3b. The results indicate a trend of increasing hardness and Young's modulus from pure GZ coatings to higher additions of GZ in GZ/YSZ double layered coatings.

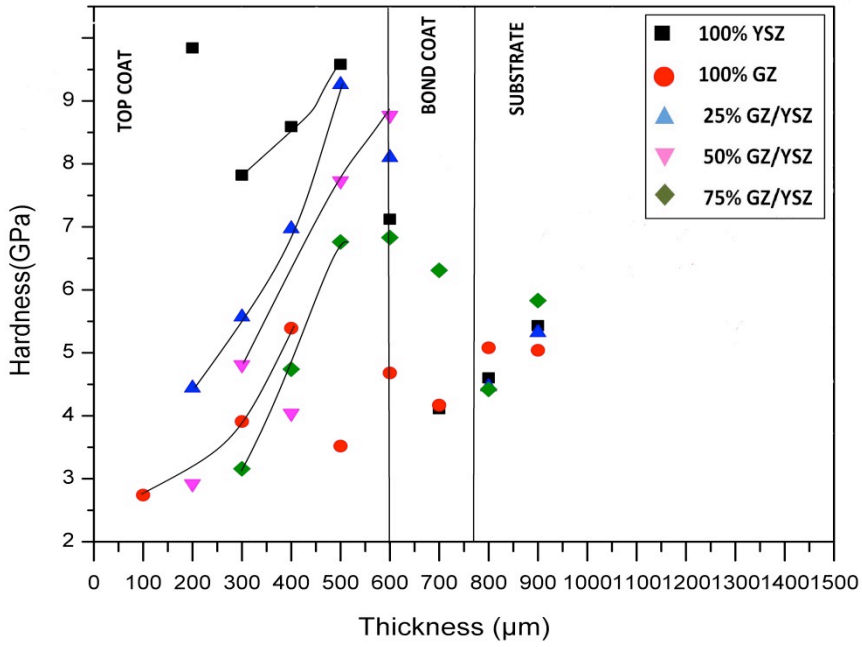

Figure 6.3a: Hardness of different TBC systems tested on Tribo-Indenter

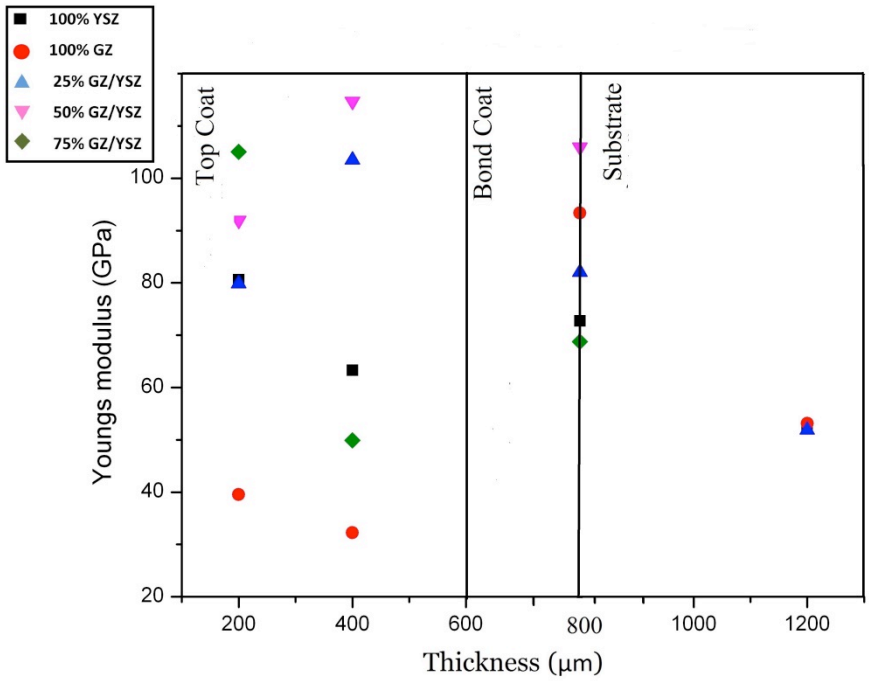

Figure 6.3b: Young's modulus of different TBC systems tested on Tribo-Indenter

The measured hardness and Young's modulus values of all the five TBC systems are provided for cross-sections of samples that were cut across the thickness and polished. Among the tested TBC systems, YSZ has the high hardness while GZ has the lowest hardness. Note that the hardness of 25%GZ/YSZ and 50%GZ/YSZ double layered systems is greater than that of pure GZ TBCs. The Young's modulus of 25%GZ/YSZ and 50 % GZ/YSZ is greater than that of pure GZ TBCs. From the pattern followed by these tested TBC systems it is seen that the double layered functional TBCs with decreasing GZ percentage increases the elastic properties of the GZ based TBC system. It is expected that a higher elastic modulus and yield stresses would contribute to high resistance to damage from particle attacks or wear during gas turbine operation when the TBCs are not subjected to critical failure caused by TGO formation. As the hardness and Young's modulus of 25% GZ/YSZ DL layered system is similar to that of YSZ we can say that these GZ based functionally graded double layered TBC systems are expected to show superior thermal cycling life when compared to pure GZ TBCs while maintaining lower thermal conductivity than YSZ systems.

Results of Thermal Cycling, Porosity and SEM Characterization

Results of the thermal cycling behavior test at 1100^{o}C of selected test compositions are shown in Figure 6.4.

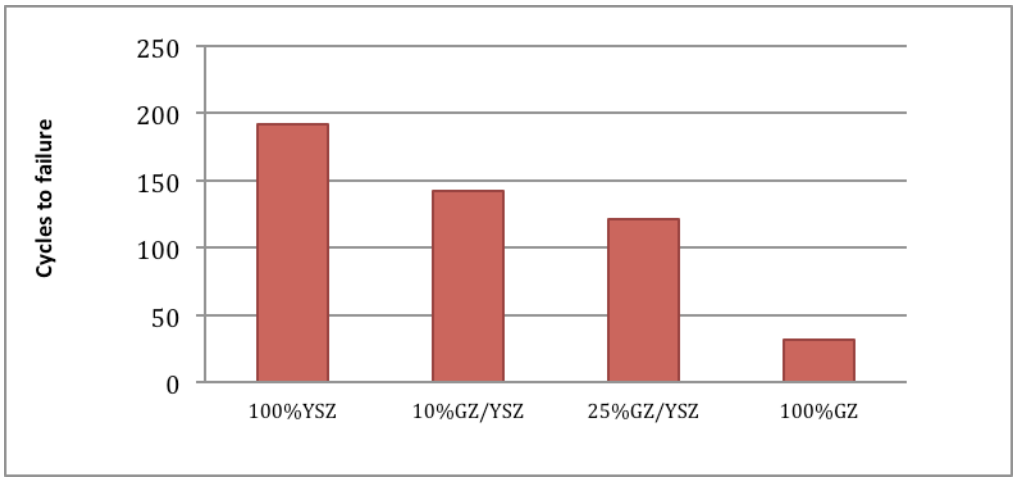

Figure 6.4: Thermal cycling behavior using 1.45-hour thermal cycles at 1100^{o}C

The thermal cycling results show that functionally graded double layered TBC systems show improved thermal cycling life compared to 100% GZ as shown in Figure 6.4. Reductions in the amount of GZ in the mixture yield higher thermal cycling life to failure and 10%GZ/YSZ closest cycling life to failure at 1100^{o}C compared to the pure YSZ samples.

Measured density and porosity values as obtained from porosimetry are given in following Table 2 of selected TBC samples produced using APS-STD process.

Table 2 Measured Density and Porosity Values of TBCs Studied

Sample	Density (Kg/m^3)	Porosity
YSZ (600µm)	4795.6	18.1%
GZ (600µm)	5860.9	22.4%
25%GZ/YSZ (600µm)	4555.1	23.5%
50%GZ/YSZ(600µm)	5612.7	25.8%
75%GZ/YSZ(600µm)	5202.1	20.3%

From the elastic properties measurement graphs (Figure 6.3a and Figure 6.3b) it is noticed that 25% GZ/YSZ double layered TBC system shows significant improvement in the hardness and Young's modulus values when compared to pure GZ TBC systems. Thus functionally graded double layered coatings can improve the thermal cycling life of GZ based TBCs as the enhanced elastic properties contribute to higher resistance of the TBC systems. The thermal cycling results can be correlated with the elastic properties measurements as the double layered TBC systems showed significantly higher life time when compared to pure GZ coatings.

Summary of this work

The role of GZ in double layered TBCs has been investigated. The evaluations of selected TBC systems have been made of CTE values, elastic properties, and thermal cycling life at 1100^{o}C alongwith study of porosity and microstructural effects. Measurements of CTE data indicate increasing values with increase of temperature and lowest CTE values starting at 22 ^{o}C, which would impact the thermal cycling behavior. Measurements of hardness and Young's modulus characteristics using TriboIndenter have been analyzed for the effects of GZ in double layered TBC systems. The hardness test results indicated a trend of possible benefits of GZ addition up to 25% in the double layered TBC specimens. Functionally graded double layer TBC systems show improved thermal cycling life compared to 100% GZ**.** There is further need to configure the optimum GZ in these functionally graded TBCs. Addition of GZ in the double layered TBC systems should lower the thermal conductivity thereby providing beneficial insulating properties of these TBC systems for high temperature applications. In our structure and porosity measurements, the failure is observed in the bond coat/ top coat interface in all the tested samples. Furthermore, the porosity can be interrelated to lower thermal conductivity and higher insulating behavior of these TBCs.

This study has focused on the isothermal testing which is the prevalent approach in thermal cycling of TBCs. However this approach does not capture the temperature gradient and other environmental effects TBCs are exposed to in actual gas turbine systems.

B. Processing gadolinium zirconate functionally gradient nano-structured thermal barrier coatings

Materials: Multilayer TBC samples with Gadolinium particles in the top coat YSZ coating were processed on IN738 substrates. All the samples in this work are prepared using air plasma spray (APS) standard (STD) coating type. The Bond coat MCoCrAlYHf and the top coat YSZ/GZ were sprayed on disc shaped IN 738 superalloy 12.54 mm in dia. x 3 mm thick samples. The bond coat composition used for the preparation of these samples was standard Sulzer Metco powder of nominal composition Ni-22Co-17Cr-12.5Al-0.25Hf-0.4Si-0.6Y (weight %). The top coat powders used were 7.65wt%Y_2O_3-ZrO_2 and $Gd_2Zr_2O_7$. The first layer of the functionally graded top coat was made up of three compositions of YSZ and GZ, namely, 70%YSZ+30%GZ, 50%YSZ+50%GZ and 30%YSZ+70%GZ and the bottom layer was made up of 100%YSZ to form multi-layer samples for thermo-physical properties and thermal cycling tests. The total thickness of the top coat was around 600 ±100 μm with YSZ-GZ combination around 300±50 μm and bottom layer YSZ around 300 ±50 μm. The IN 738 substrate samples are 12.54 mm dia x 3mm disc samples that have been electro-discharged machined (EDM) machined and tumbled - to be bond coated and top coated as specified above. The GZ powder is of

$Gd_2Zr_2O_7$ powder (-325 MESH) that was used for preparation of above specimens. All the samples used in this work were fabricated by Materials Solution Inc., Houston TX.

Thermo-physical properties measurements

***Apparatus and procedures**:* The thermal conductivity is measured by using laser flash method. The thermal diffusivity (α_i) for each material was measured as a function of specimen temperature (in the range 100 to 1100°C) in inert gas (Argon) atmosphere. Prior to thermal diffusivity measurements, the front face of the specimens were coated with a thin layer (~10 A^o) of platinum and then sprayed with graphite[10]. The back face was only coated a thin layer of graphite spray. This was done to prevent direct transmission of the laser beam through the translucent TBCs. The precision of the thermal diffusivity measurements is within ±5%.

Results and Discussion

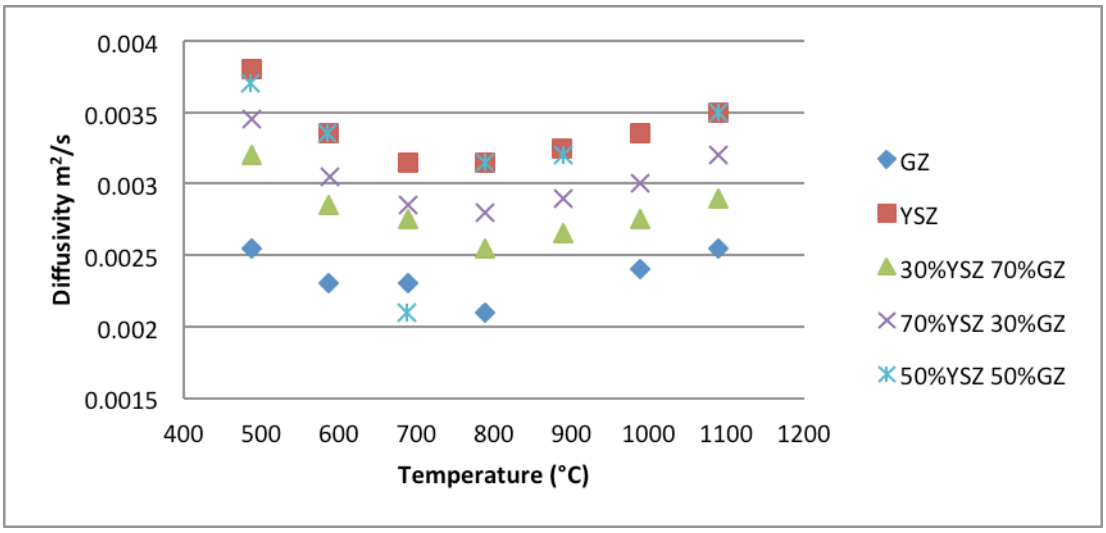

Figure 6.5 Thermal Diffusivity Measurements

Figure 6.5 depicts that the diffusivity of the TBC samples decrease with increasing temperature up to approximately 800°C. The high temperatures cause sintering in the ceramics consequently leading to increasing diffusivity with temperature beyond this point. For TBC application purposes, materials with low thermal diffusivities are desirable for better insulating ability. Pure YSZ is shown to have the highest diffusivity of the samples tested while GZ exhibits the lowest diffusivity values. The double layered YSZ and GZ samples exhibit diffusivity properties between the pure YSZ and GZ samples as expected.

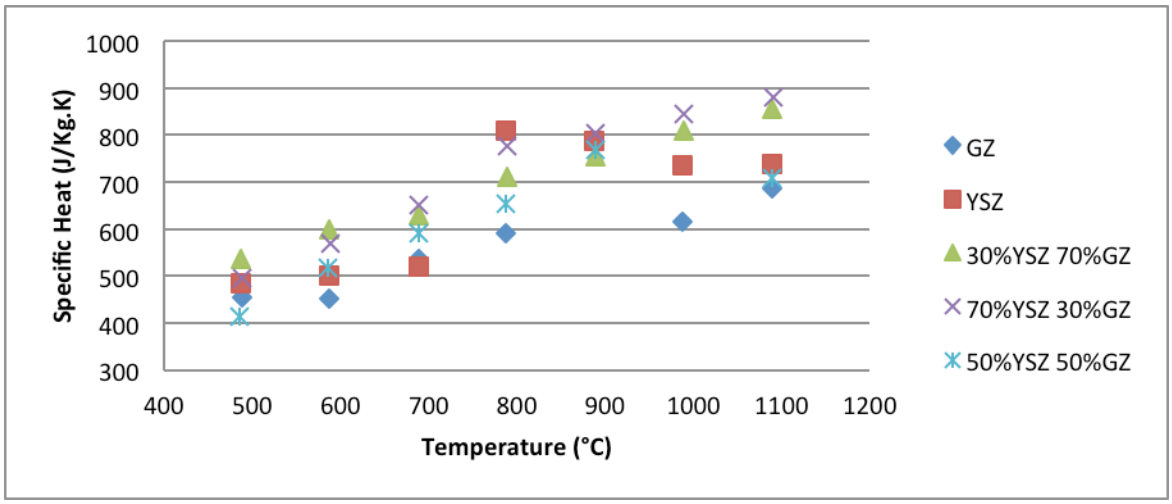

Figure 6.6 Specific Heat Capacity Measurements

Similarly the results for the Specific Heat measurements of each material are shown in Fig 6.6. The specific heats of the different samples generally increase with increasing temperature. It is important to recall the inverse relationship between the specific heat and diffusivity of a material given by:

$$\alpha = k/\rho c_p \qquad (1)$$

where: α is thermal diffusivity; k is thermal conductivity; ρ is the density and c_p is the specific heat. The bulk densities of the different YSZ and GZ samples were determined and used as an input in the laser flash method. Note that the density of pure GZ is approximately 1.14 times the density of pure YSZ.

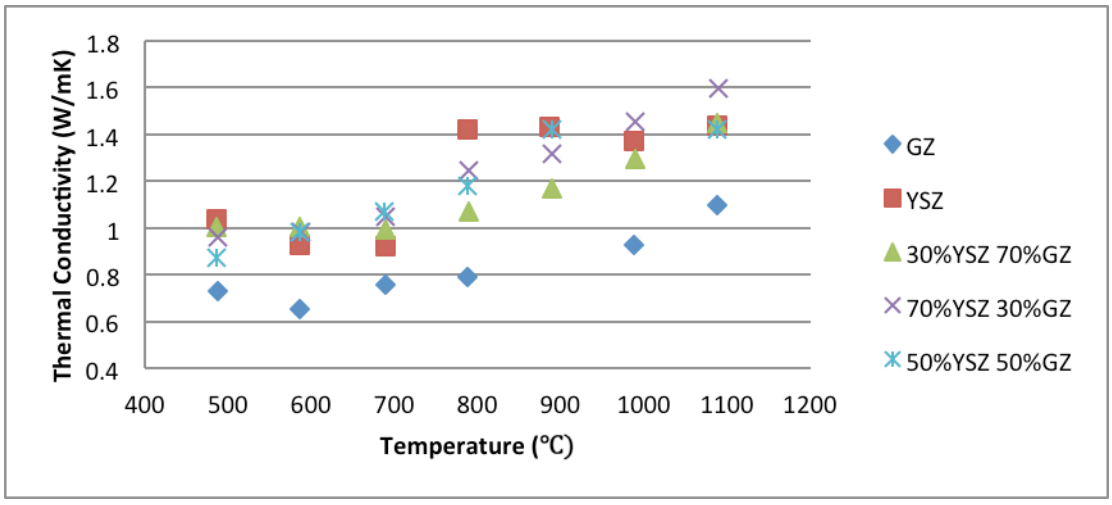

Figure 6.7 Comparison of Thermal conductivities

The thermal conductivity of each sample was determined from the measured density, thermal diffusivity and specific heat measurements using the laser flash method. Figure 6.7 shows the comparison of thermal conductivities. Thermal conductivity of each

material decreases with temperature until sintering, and then increases with temperature beyond the sintering temperature around 600^{o}C.

Summary of this work

The thermo-physical comparisons of varying composition of GZ in double layer TBCs have been investigated. Increasing the amount of GZ in the YSZ top layer resulted in significant reductions in thermo-physical properties measured. It is concluded that **a**ddition of GZ in the double layer YSZ TBC coating should potentially lower the thermal conductivity thereby providing beneficial insulating TBC properties for high temperature applications. A novel testing of thermal cycling behavior of TBCs under conditions of selected temperature gradients and controlled environments is also in progress and will be used to elucidate impact of reduction of thermo-physical properties on thermal cycling behavior.

REFERENCES

1. Jie Wu, Xuezheng Wei, Nitin P. Padture, Paul G Klemens, Maurice Gell, Eugenio Garcia, Pilar Miranzo, and Maria I. Osendi, "Low-Thermal-Conductivity Rare-Earth Zirconates for Potential Thermal-Barrier-Coating", Application, *J. Am. Ceram. Soc.,85[12] 3031-35 (2002)*

2. Carlos G. Levi, Emerging materials and processes for thermal barrier systems, *Curr. Opin. Solid State Mater.Sci ., Vol 8, 2004, p 77-91*

3. R.VaBen, F.Traeger, D. Stover, "New Thermal Barrier Coatings Based on Pyrochlore/YSZ Double-Layer Systems", *Int. J.Appl.Ceram Technol.,Vol 1 (4), p 351-61 (2004)*

4. J. Schwarzer, D. Lohe, O. Vohringer. "Influence of the TGO creep behavior on delaminationn stress development in thermal barrier coating systems." Materials Science and Engineering A. (2004): 692-695.
5. J. Rosler, M. Baker, M. Volgmann. "Stress state and failure mechanisms of thermal barrier coatings: Role of creep in Thermally Grown Oxide." Acta mater 49. (2001): 3659-3670. Print.
6. A.M. Freborg et al. "Modeling oxidation induced stresses in thermal barrier coatings." Materials Science and Engineering A245. (1998): 182-190.

7. Lehmann H., Pitzer D., Vassen R., "Thermal conductivity and thermal expansion coefficient of the lanthanum rare-earth-element zirconate system", J.Am. Ceram. Soc., 86[8], 2003, 1338-1334.

8. Cao XQ, Vassen R., Sstover D., "Ceramic materials for thermal barrier coatings", J.Eur. Ceram. Soc. 2004; 24.

9. L. Wang, S. Nandikolla, M. H. Habibi, P. F. Mensah, R. Diwan, and S. M. Guo," Thermal Cycling Behavior of $Gd_2Zr_2O_7$ Based Thermal Barrier Coatings," Materials Science & Technology 2011 Conference, October 16-20, 2011, Columbus , OH

10. Ogad Agu, Ravinder Diwan, Patrick F. Mensah, Monica B. Silva, and S.M. Guo, "Porosity and Thermal Cycling Behavior of Plasma Sprayed and EBPVD Thermal Barrier Coatings", Proc. of ASME Turbo Expo: Power for Land, Sea and Air GT June 14-18, 2010, GT 2010- 22433, (2010)

Publications/Presentations

Peer Reviewed Journals

1. S. Akwaboa, P. Mensah, E. Beyazouglu, and R. Diwan, "Thermal Modeling and Analysis of a Thermal Barrier Coating Structure Using Non-Fourier Heat Conduction," ASME J. of Heat Transfer, Vol 134 (11) pp. 111301-1-12, November 2012
2. W. Soboyejo, P. Mensah, R. Diwan, J. Crowe and S. Akwaboa, "High Temperature Oxidation Interfacial Growth Kinetics in YSZ Thermal barrier Coatings with bond coatings of NiCoCrAlY," Mater. Sci. Engr. A, 528 (2011) 2223-2230, Available online December 22, 2010

Conference Proceeding/ Presentations

3. Stephen Akwaboa and Patrick Mensah, "Numerical Analysis of Dual-phase-lag Heat Transfer in a Micro-Scale Thermal Barrier With an interfacial Resistance," ASME MNHMT2013-22269, Hong Kong, China, 11-14, December 2013 (Manuscript in press)
4. S. Akwaboa, P. Mensah, and Y. Dag, "Study Of Heat Transfer in a Thermal Barrier Coatings System Using The Dual Phase Lag Model Based on Mean Value Finite Volume Method," (In Press), IMECE2013-66060, San Diego, CA 2013
5. S. Kodiyalam, M. Benissan, S. Akwaboa, A. Jana, D. Bagayoko, and P. Mensah, "Parallel molecular dynamics simulations and immersive visualization of TBC components: TGO and YSZ," (In Press), IMECE2013-66060, San Diego, CA 2013
6. Michael Benissan, Patrick Mensah, and Stephen Akwaboa, "Modeling of Thermally Grown Oxide (TGO) Layer Growth as a Moving Boundary Problem," HT2013-95917, ASME Summer Heat Transfer Conference, July 2013, Minneapolis, MN
7. Patrick F. Mensah, Ravinder Diwan, Swamy Nandikolla and Omotola Coker "Thermo-Mechanical Study of the Role of $Gd_2Zr_2O_7$ (GZ) In Improving Life of YSZ and GZ Double Layered Thermal Barrier Coatings". IMECE 2012-88279, Houston, TX. 9-15, November 2012
8. Michael Benissan, Stephen Akwaboa and Patrick Mensah, "A two-dimensional multi-scale thermal model for in-service performance of thermal barrier coatings," (Abstract Accepted) IMECE2012-89714, Houston TX, 2012
9. Michael Benissan, Stephen Akwaboa and Patrick Mensah, "Experimental Measurement of Nusselt Number Correlations on Flat Plate And NACA 0010 Section Surfaces, ASME Summer Heat Transfer Conference, HT2012-58340, Puerto Rico, USA, July 8-12, 2012
10. L. Wang, S. Nandikolla, M. H. Habibi, P. F. Mensah, R. Diwan, and S. M. Guo," Thermal Cycling Behavior of $Gd_2Zr_2O_7$ Based Thermal Barrier Coatings,"

Materials Science & Technology 2011 Conference) October 16-20, 2011, Columbus , OH

11. N. Polasa, M. B. Silva, S. Akwaboa, R. Diwan, P. F. Mensah , and S.M. Guo, "High Temperature Oxidation Studies of NICoCrAlY and NICoCrAlY– HF bond coats," Materials Science & Technology 2011 Conference) October 16-20, 2011, Columbus , OH

12. Monica. B. Silva, S. M Guo, Patrick Mensah, and Ravinder Diwan, "Thermal Conductivity Prediction For Thermal Barrier Coatings," IMECE 2010-38728, ASME IMECE, November 12-18, 2010, Vancouver, British Columbia, Canada

13. Edwin Igiede, Patrick F. Mensah, and Stephen Akwaboa, "High Temperature Endurance of FRP Composites with Polymeric Thermal Barrier Coatings," IMECE 2010-40720, ASME IMECE, November 12-18, 2010, Vancouver, British Columbia, Canada

14. Stephen Akwaboa, Patrick Mensah, and Ravinder Diwan, "A Comparison Study of Heat Transfer Through Electron Beam Vapor Deposition (EBPVD) and Air Plasma Sprayed (APS) Coated Gas Turbine Blades," IHTC14-2296, Proceedings of 4th International Heat Transfer Conference, Washington DC, August 2010

15. Daniel Ofori, Patrick F. Mensah, Mayank Tyagi and Samuel Ibekwe, "Modeling of The Multiphase Heat Transfer Enhancement In A Heat Exchanger Surface With Different Patterns of Micro-Pin Fins: A Volume of Fluid Modeling Approach," 7th International Conference on Heat Transfer, Fluid Mechanics and Thermodynamics (HEFAT 2010), Antalya, Turkey, 19-21 July 2010

16. Monica. B. Silva, Ogad Agu, Patrick Mensah, Ravinder Diwan, and S. M Guo, "Porosity and thermal cycling behavior of plasma sprayed and EBPVD thermal barrier coatings", IGTI 2010-22433, ASME Turbo Expo: Power for Land, Sea and Air, June 14-18, 2010, Glasgow, UK

17. Stephen Akwaboa, Patrick Mensah, and Ravinder Diwan , "Effects of Thermal Radiation On Air Plasma Spray (APS) Coated Gas Turbine Blade," GT2010-23660, ASME Turbo Expo: Power for Land, Sea and Air, June 14-18, 2010, Glasgow, UK

18. E. Beyazouglu, S. Akwaboa, and P. Mensah , "Multiscale Study on The Thermal Model Of The Thermal Barrier Structure", ASEE GSW Conference, McNeese State University, Lake Charles, LA March 25-26, 2010

19. A. Jana, K. Sekeroglu, D. Jerro, P. Mensah, S. Ibekwe, and S. Kodiyalam, "Enhancement of ME Laboratories with Interdisciplinary Emerging Technologies," ASEE GSW Conference, McNeese State University, Lake Charles, LA March 25-26, 2010

20. Ogad A. Agu, Patrick F. Mensah and Ravinder Diwan, "Effects of Thermal cycling and Porosity on Novel Thermal Barrier Coatings (TBCs)." ASEE GSW Conference, McNeese State University, Lake Charles, LA March 25-26, 2010

21. Stephen Akwaboa, Patrick Mensah, Monica. B. Silva, Ravinder Diwan, Douglas E. Wolfe, and S. M Guo, "Thermal Properties and Porosity Comparison of APS and EBPVD TBCs Deposited on MCrAIY Hf Bond Coated IN738", IMECE 2009-11901, ASME IMECE, November 13-19, 2009, Lake Buena Vista, Florida

22. W. Soboyejo, P. Mensah, and R. Diwan, "Interfacial Kinetics of High Temperature Oxidation in YSZ Thermal barrier Coatings with NiCoCrAlY Bond

Coat," ASME IMECE2009-11556, November 13-19, 2009, Lake Buena Vista, Florida

23. Monica. B. Silva, S. M. Guo, Nalini Uppu, Ravinder Diwan, and P. F. Mensah, "The Study of Thermal Properties Measurements of YSZ-Al2O3 ceramic composites," ASME IGTI GT2009-59496
24. Monica. B. Silva, S. M. Guo, Nalini Uppu, Ravinder Diwan, and P. F. Mensah, "Porosity Effects on Thermo-physical Properties of Standard and Vertically Cracked Thermal Barrier Coating Samples," ASME IGTI GT2009-59826
25. P. Mensah, N. Uppu, and R. Diwan, "Performance of Dense Vertical Cracked Air Plasma Spray Processed Thermal Barrier Coatings: Thermo-Physical Properties Measurements, and Effects of Thermal Stress On Thermal Cycling Failure," ASME Heat Transfer Conference, HT2008-56354, Jacksonville, Florida, August 2008

Extended Abstracts

26. S. Kodiyalam, M. Benissan, S. Akwaboa, P. Mensah, A. Jana, "Molecular dynamics simulations of thermal conduction in alumina perpendicular to the R-plane," Proceedings of the Louisiana EPSCoR RII LA-SiGMA 2013 Symposium, Baton Rouge, Louisiana, July 29 2013, pp. 117-120.
27. Omotola Coker, Stephen Akwaboa, Patrick F. Mensah, Ravinder M. Diwan and Samuel Ibekwe, "Comparison of Thermo-physical properties FOR PERFORMANCE EVALUATION of $GD_2Zr_2O_7$ powders in YSZ thermal barrier coatings," 21st Annual International Conference on Composites/Nano Engineering, ICCE-21 July 21-27, 2013 in Tenerife, Spain
28. M. Benissan, S. Akwaboa Amitava Jana, and P. Mensah "Microscale Modeling of Thermally Grown Oxide (TGO) Layer Growth as a Moving Boundary Problem" IMECE-2012-94060, Houston TX, 9-15, November 2012 **(Won ASME Travel Grant Sponsorship to present at the conference)**
29. Stephen Akwaboa, S. Kodiyalam, Amitava Jana, P. Mensah, R. Diwan, "Computation And Stereographic Visualization of Temperature And Heat Flux in a Thermal Barrier Coating of a Turbine Blade," 19th Annual International Conference on Composites/Nano Engineering, ICCE-18 July 24-30, 2011 in Shanghai, China
30. Ravinder M. Diwan, Patrick F. Mensah, Naresh Polasa, and Douglas E. Wolfe, "Mechanical Properties of Hot Corrosion Tested APS and EB-PVD Multilayer Thermal Barrier Coatings Using Nano Indentation," 19th Annual International Conference on Composites/Nano Engineering, ICCE-18 July 24-30, 2011 in Shanghai, China
31. S. Kodiyalam, B. Mukerji, S. Akwaboa, P. Mensah and A. Jana, "Visualizing Simulated Multi Scale Data: temperature and Heat Flux in a Turbine Blade Cross-Section and its Thermal Barrier Coating," Proceedings of 2010 RII Cybertools-Science Drivers Symposium, Baton Rouge, August 2010
32. Ravinder M. Diwan, Patrick F. Mensah, Naresh Polasa and Douglas Wolfe, "Hot Corrosion And Thermal Oxidation Studies of EB-PVD and APS Thermal Barrier Coatings",18th Annual International Conference on Composites or Nano Engineering, ICCE-18 July 4-10, 2010 in Anchorage Alaska, USA

33. Ravinder M. Diwan, Patrick F. Mensah, Ogad Agu and Douglas E. Wolfe "Thermal Oxidation Cycling Studies of APS and EB-PVD Composite TBC Microstructured Coatings", 17th Annual International Conference on Composites or Nano Engineering, ICCE-17 July 26-31, 2009 in Hawaii USA

PhD Thesis

34. Monica B. DeSilva, Study of Microstructural Effect on the Thermal Properties of Yttria-Stabilized Zirconia Thermal Barrier Coatings Made by Atmospheric Plasma Spray and Pressing Machine, Ph.D. Mechanical Engineering, LSU May 2010

Master's Thesis

35. Michael Benissan, Thesis title "Finite Difference Thermal Model for a Thermal Barrier Coating with Alumina Growth, Master of Engineering December 2012
36. Omotola Coker, thesis title "Coefficient of Thermal Expansion Dependent Thermal Stress Analysis of Thermal barrier Coatings Using finite Element Model." Master of Engineering, December 2012
37. Swamy Nandikolla , "Investigation of the Role of $Gd_2Zr_2O_7$ (GZ) Powders in Thermal Cycling Behavior of Thermal Barrier Coatings.", Master of Engineering, July 2012
38. Naresh Polasa, A Study of High Temperature Oxidation and Hot Corrosion Effects of Advanced Multilayer Thermal Barrier Coatings (TBCs)," Master of Engineering December 2010
39. Ogad A. Agu, Patrick F. Mensah and Ravinder Diwan, "Effects of Thermal cycling and Porosity on Novel Thermal Barrier. Coating (TBCs)." Master of Engineering July 2010
40. Ebubekir Beyazoglu, Multi-scale Modeling of Thermal Performance of Ceramic Thermal Barrier Coatings," Master of Engineering May 2010